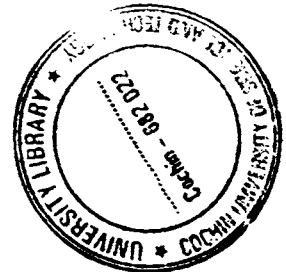# NON-DESTRUCTIVE EVALUATION OF
ION-IMPLANTED SEMICONDUCTOR THIN FILMS
USING
PHOTOTHERMAL DEFLECTION SPECTROSCOPY

Thesis submitted to
Cochin University of Science and Technology
for the award of the degree of

DOCTOR OF PHILOSOPHY

By

M. PAULRAJ

Applied Optics Laboratory
Department of Physics
Cochin University of Science and Technology
Cochin – 682 022
Kerala, India

December 2004

DR. K. P. VIJAYAKUMAR
Professor

Department of Physics
Cochin University of Science
and Technology
Cochin – 682 022
INDIA

PH. (OFF) : 91 0484 – 2577404
(RES): 91 0484 – 2577103
(FAX) : 91 0484 – 2577595
E-MAIL : kpv@cusat.ac.in

CERTIFICATE

Certified that the work presented in this thesis entitled *"Non-Destructive Evaluation of ion-implanted semiconductor thin films using Phototothermal Deflection Spectroscopy"* is based on the bonafied research work done by Mr. M. Paulraj under my guidance in the Department of Physics, Cochin University of Science and Technology, Cochin – 682 022, and has not been included in any other thesis submitted previously for the award of any degree.

Cochin – 22

30-12-2004

Prof. K. P. VIJAYAKUMAR

(Supervising Guide)

DECLARATION

Certified that the work presented in this thesis entitled *"Non-Destructive Evaluation of ion-implanted semiconductor thin films using Photothermal Deflection Spectroscopy"* is based on the original research work done by me under the guidance of **Prof. K. P. Vijayakumar**, Department of Physics, Cochin University of Science and Technology, Cochin – 682 022, and has never been included in any other thesis submitted previously for the award of any degree.

Cochin – 22

30-12-2004

M. PAULRAJ

Acknowledgment

No way could any thesis work be done in isolation, without any help from teachers and colleagues, this one is not an exception. If your were one among them who helped me realize this work possible, I thank you first.

My heartfelt thanks to my supervising guide, Prof. K. P. Vijayakumar for his sincere, invaluable guidance, suggestions and encouragement given during the whole phase of my work, which I felt had always put me along the right track. I am equally indebted to Dr. C. Sudha Kartha, for her constant encouragement and technical guidance throughout the course of my work.

I wish to thank Prof. V.C. Kuriakose, HOD, Department of Physics and the former HOD's, Prof. Sabir, Prof. Rajajapan Nair, Prof. Elizabeth Mathai, for their help.

I specially thank, Dr. K. G. Muraleedharan Nair, (Co-ordinator, IUC DAEF, Materials Science Division, Indira Gandhi Center for Atomic Research (IGCAR), Kalpakkam) for the support he had given me during ion beam studies at IGCAR. Late Dr. Kanwar Kishan, (Former Head, Materials Science Divison, IGCAR) has got great respect in my heart, because I could still remember the tireless effort he had put in, to make IUC-DAEF a successful collaborative work.

I also thank Shri. Mugudapathy, Scientist, Particle irradiation facility (IGCAR), who used to stay with us, if there was any problem with the ion implanters. Dr. A. K. Tyagi, Dr. Sitaram Dash, Dr. C. Sundar, Dr. Kesavamoorthy and Dr. Rajagopalan were always available for me, for any technical discussion during my stay at IGCAR.

Dedicated to My Appa & Amma

Contents

Chapter 2 ION IMPLANTATION STUDIES

Chapter 3 STUDIES ON DOPED AND ION IMPLANTED CdS THIN FILMS

Chapter 4 STUDIES ON INDIUM SULPHIDE THIN FILMS

Chapter 5 STUDIES ON UNDOPED AND ION IRRADIATED ZnO THIN FILMS

Chapter 6 PDS FOR INDUSTRIAL APPLICATION

Preface

Materials and equipment which fail to achieve the design requirements or projected life due to undetected defects may require expensive repair or early replacement. Such defects may also be the cause of unsafe conditions or catastrophic unexpected failure, and will lead to loss of revenue due to plant shutdown. Non-Destructive Evaluation (NDE) / Non Destructive Testing (NDT) is used for the examination of materials and components without changing or destroying their usefulness. NDT can be applied to each stage of a system's construction, to monitor the integrity of the system or structure throughout its life.

Photothermal Deflection Spectroscopy (PDS) technique has found a place as a modern NDT technique. It works on the principle of thermal wave detection in the sample due to the sample's non-radiative process taking place following optical excitation. Moreover, this has proved to be a powerful technique for the analysis of optical, thermal and even electrical properties of solids especially semiconductors. Its ability to monitor sub-surface damage in materials well beyond the optical penetration depth has secured its position as an ideal NDT technique. We used this in-house built PDS setup to characterize all our samples. **Chapter 1** describes the principle of PDS technique and the methods adopted, to measure the thermal and transport properties of semiconducting thin films. Depth profiling done using only laser beam leaves the sample safe. Brief review of work done by others are also given.

Ion implantation is now a days, a popular technique for doping. The most important effect caused due to ion implantation is the alteration of chemical composition of a material. This can lead to modification of the electrical conductivity and / or the optical property of the material. In order to achieve high reliability in semiconductor devices, on miniaturized scale, and to ensure high performance, knowledge of the defects / damages created by energetic ion in a semiconductor is becoming increasingly necessary. **Chapter 2** gives an overview of the effects due to implantation in semiconductor material. Path of the ion in both amorphous and crystalline material are studied. Ion range calculation using various theoretical methods is discussed, giving emphasis to TRIM (TRansport of Ion in Matter) calculation. Working principle of ion implanters and the analytical techniques used for materials characterisation are described in brief.

CdS is well known for its tendency to form nonstoichiometic compound, having excess cadmium, leading to n-type conductivity. Intrinsic CdS film is extensively used as window material in solar cells, having $CuInSe_2$ or $CuInS_2$ or CdTe as absorber layer. Pure or undoped CdS films generally show high electrical resistivity. So doping is adopted to modify its electrical and optical properties. **Chapter 3** give the results obtained from Cu doped (using vacuum evaporation) CdS and ion implanted (Cu^+, Ar^+ and He^+ ions) CdS thin film samples. In case of doped samples, depth of diffusion of the metal atoms into the target was determined. Similarly, for ion implanted samples, the depth of ion penetration into the sample was determined. Projectile range of these ions in CdS was also compared with SRIM calculation. Two-dimensional image mapping was done to study the depthwise

damage caused due to ion implantation and the defect levels were also investigated using Photoluminescence (PL) technique.

β-In$_2$S$_3$ is a semiconductor with a band gap of 2.0 – 2.8 eV having excellent photoconducting and photoluminescent properties that makes it a promising optoelectronic material. Cu(In,Ga)Se$_2$ based solar cell having chemically deposited In$_2$S$_3$ as a buffer layer, could reach efficiencies up to 15.7%. **Chapter 4** gives results of studies conducted on In$_2$S$_3$ thin films prepared using chemical spray pyrolysis (CSP) technique using two different solutions (chloride and nitrate) and also using SILAR (Successive Ion Layer Adsorption and Reaction) method. These samples were characterized to study their thermal and transport properties. In$_2$S$_3$ samples prepared by spraying different volumes of solution were also investigated to measure the film thickness and carrier mobility. Measured values of thickness were compared with that obtained from Stylus method.

ZnO is used as a transparent conducting electrode in photovoltaic and other optoelectronic devices. It plays an important role in realizing blue and ultraviolet light-emitting diodes and lasers. They are n-type in nature and p-type conversion is possible by elemental doping technique. **Chapter 5** gives results of studies conducted on ZnO thin film samples (pristine and ion irradiated) prepared using CSP technique. Mobility and thickness of the samples were calculated and compared with the results from other techniques. ZnO samples irradiated using 120 Mev Au$^+$ ions were studied to know the changes in their optical and thermal properties due to irradiation induced damage.

Chapter 6 describes methods for using PDS technique for industrial application. Non destructive and non-contact evaluation of welded joint has been attempted on industrial point of interest. Online thickness monitoring of paint is of great value in automobile industries. Hence, a simple work in this direction is just demonstrated. Thermal properties of doped polymer materials were studied; they find application in rubber industries.

Finally, **chapter 7** is a summary of the work carried out. Scope for future work is also detailed.

List of papers publications in journals and international / national conferences

1. Characterisation of undoped and Cu doped CdS thin films using photothermal and other techniques.

   M. Paulraj, S. Ramkumar, K. P. Varkey, K. P. Vijayakumar, C. Sudha Kartha, K. G. M. Nair, *Phys. Stat. Sol. (a)*, 1– 10 (2004) / **DOI** 10.1002/pssa.200406918.

2. Studies on Ar^+ implanted CdS films using photothermal deflection technique.

   M. Paulraj, S. Ramkumar, K. P. Vijayakumar, C. Sudha Kartha, P. Magudapathy, K. G. M. Nair and B. Viswanathan, *Nucl. Instr. And Meth. In Phys. Res. B*, **122(1-2)** (2004) 123-129.

3. Measurement of film thickness and carrier mobility of semiconductor thin films using Photothermal deflection technique.

   M. Paulraj, S. Ramkumar, Teny Theresa John, P. M. Ratheeshkumar, C. Sudha Kartha, K. P. Vijayakumar, K. G. M. Nair and Y. Yasuhiro (Communicated - Semiconductor Science and Technology).

4. Photothermal imaging of He^+ ion implanted CdS.

   M. Paulraj, S. Ramkumar, C. Sudha Kartha, K. P. Vijayakumar, and K. G. M. Nair, *Journal de Physique IV* - Proceedings of "13th International conference on photoacoustic and photothermal phenomena", held at Rio de Janeiro - Brazil, (July 2004).

5. Characterisation of In_2S_3 and ZnO thin films for photovoltaic application using photothermal deflection technique.

   M. Paulraj, S. Ramkumar, Teny Theresa John, P. M. Ratheeshkumar, C. Sudha Kartha, K. P. Vijayakumar, and K. G. M. Nair, *Journal de Physique IV* - Proceedings of "13th International conference on photoacoustic and photothermal phenomena", held at Rio de Janeiro - Brazil, (July 2004).

6. Determination of thickness and mobility of In_2S_3 and ZnO thin films using photothermal deflection technique.

   M. Paulraj, S. Ramkumar, Teny Theresa John, P. M. Ratheeshkumar, C. Sudha Kartha, K. P. Vijayakumar, and K. G. M. Nair, Proceeding in Regional Conference on Photoacoustics in Condensed matter physics and NDT, held at Madurai Kamaraj University (School of Physics) (March 2004).

7. Photothermal studies on pure and doped ZnO thin films prepared using spray pyrolysis - Optical property.

   M. Paulraj, S. Ramkumar, P. R. Amjith, P. M. Ratheesh Kumar, C. Sudha Kartha, K. P. Vijayakumar, K. G. M. Nair, Proceeding of VIII (International Union of materials Research societies) International conference on advanced materials, The materials Research society of Japan, held at Yokohama, Japan, (Oct 2003).

8. Photothermal Evaluation of He$^+$ implanted CdS thin film.

   M. Paulraj, S. Ramkumar, C. Sudha Kartha, K. P. Vijayakumar, K. G. M. Nair, Proceeding of II International conference on Advanced Vibrational spectroscopy, held at Nottingham, UK, (Aug. 2003).

9. Photothermal studies on Pure and doped ZnO thin films prepared using spray pyrolysis - Electrical properties.

   M. Paulraj, S. Ramkumar, P. R. Amjith, P. M. Ratheeshkumar, C. Sudha Kartha, K. P. Vijayakumar and K. G. M. Nair, Proceedings for Tenth International conference on Composites / Nano Engineering, held at New orleans, Louisiana, USA, (July 2003).

10. Determination of thermal diffusivity of polymethane doped with various fillers by photothermal deflection method.

    M. Paulraj, S. Ramkumar, V. G. Jayakumari, S. Kusuma Kumari, C. Sudha Kartha, K. P. Vijayakumar, Proceeding of International Seminar on Advances in

    Polymer technology - CUSAT, held at Cochin, India (Dec 2002).

11. Photothermal deflection spectroscopy for studying defects due to implantation on solar cell material.

    M. Paulraj, S. Ramkumar, K. P. Vijayakumar, C. Sudha Kartha, K. G. M. Nair and T. S. Radhakrishnan, Proceeding of World Renewable Energy Congress VII, held at Cologne, Germany (July 2002).

12. Defects due to implantation by photothermal deflection spectroscopy.

    M. Paulraj, S. Ramkumar, K. P. Vijayakumar, C. Sudha Kartha, K. G. M. Nair, T. S. Radhakrishnan - Proceedings of "12th International conference on photoacoustic and photothermal phenomena", held at Toronto - Canada, (June 2002).

13. Photothermal deflection spectroscopy for ion implanted thin films.

    M. Paulraj, S. Ramkumar, A. Jayaprasad, K. P. Vijayakumar, C. Sudha Kartha, K. G. M. Nair, T. S. Radhakrishnan - Proceedings of DAE Solid state physics Symposium, held at Mumbai - India, (Dec 2001).

Chapter 1

PHOTOTHERMAL DEFLECTION SPECTROSCOPY STUDIES

1.1 Introduction

The "Photothermal Deflection Spectroscopy (PDS)" technique was first introduced in the early 1980 by Boccara, Fournier and Badoz. [1]. It was subsequently developed by Aamodt and Murphy. [2, 3], and later by Jackson *et al* [4]. It had been a very useful tool for measuring optical absorption coefficient, thermal conductivity, thermal diffusivity, imaging and as scanning microscopy in solids [5, 6, 7 and 8]. Compared with the optical absorption / transmission measurement, PDS is far more sensitive as it can detect even a defect concentration below parts per million level. But optical transmission measurement is not sensitive enough as it is strongly affected by light scattering [9]. This reason makes PDS advantageous over other techniques for the measurement of weak subgap optical absorption.

PDS is based on the excitation and detection of thermal waves in condensed matter, and this is distinguished by two intriguing properties. One, is that the dissipation of the energy of optically excited electronic states into thermal energy providing means to explore non-radiative de-excitation channels in matter. The other is monitoring the time and spatial dependence of oscillating temperature field that offers a unique possibility to obtain depth resolved information on optical and thermal parameters. Part of the energy from the pump beam is absorbed by the sample and is transformed into a

temporal variation of temperature. This variation of temperature of the solid results in a local refractive index gradient of the surrounding fluid that is detectable by a probe beam passing through it. This photothermal signal (amplitude and phase lag) contains information about,

(i)   the thermal diffusivity of each layer in a sample

(ii)   its absorption coefficient and

(iii)   the thickness of each layer.

The PDS amplitude reflects not only the heat propagation but also the intensity of the heat generation, as given by,

$$\Phi = \frac{\partial n}{\partial T}\left(\frac{2\beta PL}{\rho C\sqrt{\omega\alpha_c}}\right),\dots\dots\dots\dots\dots\dots\dots\dots\dots\dots\dots\dots(1.1a)$$

Where,

Φ – Deflection amplitude

$\dfrac{\partial n}{\partial T}$ – Rate of change of refractive index with temperature,

β – Absorption per unit length of sample,

ρ – Density of sample,

ω – modulation frequency,

L – Sample thickness,

P – Power density of incident beam

C – Specific heat,

α_c – Thermal diffusivity of coupling fluid,

The heat generation is a function of the light absorption which is strongly affected by the defects and band to band excitation. On the other hand, phase

of the PDS signal reflects only the heat propagation time from the heat source to the sample surface defined by;

$$\delta\phi = \left(\frac{\pi\omega}{\alpha}\right)^{\frac{1}{2}} l, \quad \dots\dots\dots\dots\dots\dots\dots\dots\dots\dots\dots\dots\dots\dots\dots\dots\dots\dots(1.1b)$$

Where

    ϕ – Phase or PDS signal delay against the reference signal,

    α – Thermal diffusivity of the material,

    l – Length of heat propagation path,

Therefore, if we measure the photothermal signal as a function of the modulation frequency of the incident light and employ an appropriate data analysis, it is possible to extract the thermal properties of the layered materials [10]. Main advantages of PDS are its sensitivity and the ability to provide information, in a non contact manner, over a wide frequency range of thermal waves. The possibility of thermal characterization of materials to a resolution of micrometer and submicrometer scale has also been proved possible [11, 12].

Thermal diffusivity is the physical quantity which characterizes the heat diffusion process due to conduction. All methods allow one to estimate the diffusivity by studying the temperature induced when sample is heated using pulsed or periodical methods. The use of laser as heating source improved these methods, giving rise to a contactless point of heating due to optical absorption. In fact, PDS can detect very precisely small temperature rises ($<10^{-6}$ K). This technique has been successfully applied as a quantitative tool for non-destructive characterization of inhomogeneous material. Presently such techniques are widely used to evaluate different types of inhomogeneity,

whether macroscopic subsurface defects present in a homogeneous material, or microscopic structural modifications which produce local thermal conductivity changes. In last few years, there is growing interest in techniques to measure heat or thermal structures on micrometer and nanometer scales. The necessity arise due to the continuous reduction of size of semiconductor device associated with an increase of the dissipated power densities. Thermal wave inspection on small scales can provide information on adhesion between different constituents. In nanocrystalline materials, the grain boundaries between the grains, of size in the range 5 to 100 nm, govern the physical properties of the materials which can be analysed by thermal wave based techniques.

Among conventional thickness measurements techniques, ellipsometry and interferometry are prominent non destructive technique since they use visible light for both input and output. However, their application is limited to transparent films. But PDS method is applicable to non contact measurements in gases and liquids and opaque materials since it uses visible light for both input (excitation beam) and non radiative (thermal) as output. The tunable penetration depth of modulated heat flow in the sample of interest allows to extract subsurface information about the thermal properties of the sample from the frequency dependence of the surface temperature oscillations [13].

Thermal waves infact penetrate inside the sample. At high chopping frequency, the induced thermal waves have a short penetration and give information of the surface thermal properties. On the contrary, at low frequency the thermal waves have high penetration depth and give information of deeper layers. Obviously the whole thermal depth profile may be reconstructed by considering the photothermal signal in the whole frequency

range [14]. The interrelation between microstructure and local thermal properties in a solid makes the nondestructive and noncontact depth profiling of the microstructure by means of thermal waves possible [15]. The frequency-dependent and consequently depth-dependent photothermal signals carry information on local thermal properties of the material. To reconstruct their depth profile one has to use theoretical methods to reconstruct the measured signal for the corresponding frequencies. But this procedure requires knowledge on the solution of the heat diffusion equation with space-dependent coefficients. PDS has found applications in the estimation of coating thicknesses, the characterization of layered samples and also has been used successfully to detect hidden patterns inside opaque and strongly scattering samples. Applications in the areas of photobiology, photochemistry, photophysics and reaction dynamics can also be realized if the effects of thermal energy release can be understood.

Another area of PDS application is in "photothermal imaging" that includes nondestructive evaluation of materials and components with pattern sizes in the mm range, as well as with sub-µm resolution. Table 1.1 gives the resolution values for various photothermal methods presently used.

Photothermal Techniques	Record Resolution till date	Reference
Scanning probe thermal microscope	> 50 nm	[16]
Photothermal reflectance microscope	> 1 μm	
Photothermal infrared microscope	> 10 μm	
Electron acoustic scanning microscope Laser acoustic scanning microscope	> 100 nm	

Table 1.1 gives the resolution values for various photothermal methods presently used.

The PDS measurement could also be performed at 77 K by using liquid nitrogen as cooling and deflection medium [17]. Photothermal diffraction is the preferred apparatus for measuring heat evolution in short lived, transient species or ultrafast process. Resolutions of ~100 femtosecond is currently achievable by using femtosecond excitation with optically delayed femtosecond probe time for the population and thermal refractive index change components [18]. Photothermal infrared microscope is better suited for the investigation of soft materials, such as food, textile materials and biological samples.

1.2 Brief review of earlier works using PDS techniques

Boccara *et al* [1, 4] were the first to report the measurement of spectral dependence of subband gap optical absorption coefficient using PDS in 1980.

They also observed that PDS technique was quite insensitive to the spurious scattering induced by rough surfaces. Calibration was done with carbon black as reference sample. They could perform room temperature and low temperature measurements using this setup. Sensitivity of detection scheme was almost equal to 10^{-9} rad/$\sqrt{Hz}$ when modulated at a few tens of Hz. The lowest measurable temperature of the sample surface deduced was $T_{min} \approx 10^{-4}$ K. They recorded spectra of $Cs_3Cr_2Cl_9$ powdered sample and of $Nd_2(MoO_4)_3$ monocrystal. They were able to detect absorption and dichroism spectra of $^4I_{9/2}$ $\rightarrow$ $^2H_{1\frac{1}{2}}$ transition of Nd^{3+} in $Nd_2(MoO_4)_3$ sample. Simultaneously, Patel *et al* [21] developed pulsed photoacoustic spectroscopy which was also one among the photothermal techniques. The setup could measure small absorption coefficients of «10^{-1} cm^{-1}. Using this, they could study optical absorption spectra of H_2O and D_2O. They were also able to determine absorption strength and profiles of high harmonics of the vibrational modes in transparent organic liquids such as benzene. Quantitative absorption spectra of thin liquid films of thickness ranging between 1 to 10 μm, solids and finely powered crystals were also studied. Kizirnis *et al* [22] and Rose *et al* [23] later developed pulsed PDS and used it for combustion diagnostics for measurements of species concentrations in a solution [24, 25], to determine the local temperature within a system [24] and to determine flow velocity in a flame [25]. Joshua [26] studied picosecond thermal expansion of an absorbing surface, after irradiating with 1-picosecond laser pulses, as short heating source on Si, by adapting the method of PDS. The results were compared with thermoelastic model. At a typical average pump power of 2 mW, the temperature rise was calculated to be ~1K that resulted in a peak deflection of ~5 μrad. The picosecond time resolution was obtained by varying the relative delay of the pump and the

probe beam. Jonathan *et al* [27] modified the PDS setup to study liquid samples within a cylindrical capillary using a tunable dye laser. The sample container was a quartz capillary of internal diameter 75 µm. HeNe laser beam focused to 40 µm dia was used as the optical probe beam. Maximum signal to noise ratio was achieved when the excitation beam was modulated at a frequency of 205 Hz. They were able to achieve spectral absorption peak near 575 nm for 1×10^{-3} M Nd^{3+} in aqueous solution. Gibson *et al* [28] studied the bound exciton systems in silicon by using photothermal ionization spectroscopy. They could measure extremely low-defect concentrations (about $<10^{10}$ cm^{-3}) in the far-IR region. Hodgkinson *et al* [29] studied the self referencing technique compared to a closed cell photothermal detector that used water meniscus as the pressure sensor. Deflection of the meniscus was measured using an optical fibre Fabry-Perot interferometer. They also observed that for anthracene (at 254 nm), the limit of detection was approximately 5-10 ppb.

Mandelis [30] developed a detailed analytical model for signal-to-noise ratio in conventional frequency domain and time domain photothermal measurement methodologies. The developed model was compared with the "rate window photothermal method" using both theoretical and experimental data. He observed that the lock-in-amplifier rate window measurement mode and the digital lock-in-amplifier mode exhibits superior signal to noise ratio to both conventional frequency domain and time domain photothermal measurement.

Tilgner *et al* [31] studied the influence on the thermal response of sample under photothermal investigation when real absorbing layers were used as the source of thermal waves. They studied glass and Cu samples covered by

various absorbing layers. The same group [32] studied the influence of buried layer within a sample, on the propagation of thermal waves, by measuring the phase and amplitude of the photothermal signal. Fujimori *et al* [33] studied film thickness dependence of the deflection amplitude using PDS. The calculated results showed that thicknesses in a range from skin depth to the thermal diffusion length of the opaque film could be determined from deflection amplitude. They estimated the thickness of an oxide film by comparing the calculated values with the measured ones for NiO and SiO_2 films.

Walther *et al* [34] theoretically estimated thermal properties and performed thermal depth profiles from laterally resolved radiometric measurements. They studied the effects of scattering of the heating beam from the rough sample surface and of infrared diffraction at the collecting optics using the photothermal signal. Glorieux *et al* [35] obtained the thermal conductivity depth profiles of thermally inhomogeneous materials derived from time dependence of the surface temperature. A neural network method, which was trained to recognize the correlation between depth profiles and the surface temperature on the basis of studies on many samples, was used. Depth profiles derived from simulated noisy signals and the average reconstruction errors were analysed for different circumstances. The neural network training can be easily adapted to take into account the influence of apparatus and non-opaqueness of the material. These effects were found to be reproducible and that they can be modeled in the forward calculation. They observed that neural network, once trained, gives immediate reconstructions. Paoloni *et al* [13] reconstructed thermal conductivity depth profile of case hardened steel samples by a neural network method. The reconstruction quality was very

good for shallow regions and moderately good up to 500 μm depth. The reconstruction agreed very well with profiles reconstructed from other experimental data obtained on the same samples. Bai *et al* [36] evaluated the subsurface defects in composite materials such as carbon fibre reinforced polymers in aircraft structures. They also developed a photothermal model in order to investigate the behaviour of thermal waves in homogeneous and layered plates with finite thicknesses. The model was then utilized to predict the phase differences produced by multi-layer subsurface defects. The theoretical results were compared with the experimental values. Nagasaka *et al* [10] developed a new apparatus to evaluate thermal diffusivity distributions of functionally graded materials by photothermal radiometry. Distribution of thermal diffusivity was determined for a layered Ni/ZrO_2 sample at room temperature. Salazar *et al* [37] developed a complete theoretical work for PDS technique for thermal diffusivity measurements in solids. They also found that the thermal diffusivity factor depended on thermal and optical properties of the sample. Isaac *et al* [38] measured temperature dependence of the thermal diffusivity of high temperature superconductor Bi-Sr-Ca-Cu-O with varying Pb doping levels, using a photoacoustic technique. Pb doping stabilized the superconducting phase around 110 K. It was found that above a critical temperature T_c, the thermal diffusivity decreased as the Pb concentration increased and below T_c it had a trend to saturate at low Pb concentrations. Bertolotti *et al* [39] used the PDS method to measure the low thermal diffusivity materials. They could also compare experimental results with computer simulated values. Langer *et al* [40] measured thermal conductivity of nickel and gold films of thickness 0.4-8 μm, grown on quartz, using modulated thermoreflectance technique. They also observed that the measured value on

films with various thicknesses revealed a thermal conductivity close to bulk value for nickel while gold films exhibited a reduced conductivity with decreasing film thickness. Borca *et al* [41] measured the temperature of electrically heated fine wire of 127 µm diameter by photothermal radiometry. Temperature of the wire was derived from the ratio of photothermal emission signals at two different wavelengths. The measured values were compared with the thermocouple readings at different laser modulation frequencies. Zammit *et al* [42] studied the thermal conductivity and the optical absorption coefficient of ion implanted Si and GaAs using photoacoustic measurements. The values obtained were in good agreement with the reported in literature values.

Sablikov *et al* [43] developed a theory for the photoelectric effect in semiconductors near fundamental absorption, taking into account the generation of free electrons and holes, their diffusion and recombination. They could determine diffusion length of carriers, surface recombination velocity, and bulk lifetime along with light absorption coefficient. They applied the conventional Rosencwaig and Gersho (RG) theory in their calculation. Dadarlat *et al* [44] studied electrical properties of vacuum evaporated PdSe films. They could determine spatial electrical conductivity and Peltier effect profiles. Purpose of these measurements was to find the spatial conductivity profile and to identify the type of majority carriers. Marin *et al* [45] used photoacoustic technique for the measurement of surface recombination velocity at the interface between semiconductor substrates and epitaxial layers, grown on their surfaces. They also derived a theoretical model to calculate the photoacoustic signal for various systems such as SiN(H)/Si, AlGaAs/GaAs and GaInAsSb/GaSb.

1.3 Instrumentation

1.3.1 Experimental setup

An intensity modulated light beam generates periodic thermal wave due to optical heating. Thermal wave, otherwise called "diffusion wave", generated will propagate into solid and the surrounding media according to usual diffusion process, creating a thermal gradient. The wave-like disturbances involve oscillations of diffusing energy or particles [46]. Their generation and detection in condensed matter, form the basis of the measurement and understanding of optical, electronic and thermal properties of the material. Angstrom initiated the study on diffusion waves. In the case of semiconductors, incident light also generates a photo excited carrier population. Photo excited minority carriers will also diffuse away from surface layer, where they are generated and set up a population gradient, determined by the carrier diffusion. Recombination of the carriers will further influence the thermal gradient. Both thermal gradient and free carrier gradient will induce a change in the local index of refraction of the solid and the surrounding media [47].

Fig. 1.1 is the schematic of the PDS experimental setup we used for our studies. Pump beam used were from;

(a) 488 nm, 30 mW from an Ar^+ ion laser,

(b) 532 nm, 30 mW from a semiconductor diode pumped Nd-YAG laser and

(c) 632 nm, 10mw and 15mW from a He-Ne laser.

The wave length so selected was to study the low, middle and far end in the visible region. For a continuous wavelength scanning we used 150 watts, Xe arc lamp (Oriel) filtered by a ¼-m monochromator (Oriel) with a resolution of

13 nm. Pump beam stability was studied and it was found that the beam stabilizes after 20 minutes. So the experiment was started only after keeping laser switched on for 30 minutes. Pump beam was focused to a diameter of 60 μm using a combination of focusing lens and was directed perpendicular to the sample surface. A probe laser beam, passing close and parallel to the sample surface through the refractive index gradient, generated due to optical absorption, experienced deflection of amplitude (Φ) from its path [1]. Probe beam we used was a low power (1 mW, 543.5 nm) He-Ne laser beam. We also optimized the position and the focal length of the lens which focused the probe beam on the position sensor placed at 10cm from the point of the pump-probe beams interaction.

As the PDS technique is often limited by noise [48] and the noise sources such as mechanical vibrational pickup, motion of the fluid in which the refractive index is created and oscillating intensity of the laser beam, should have to be minimized for good detection regime. In order to minimize noise and to increase signal to noise ratio (S/N), the sample was placed within a sample cell, filled with double-distilled carbon tetrachloride (CCl_4) solution. The whole setup was mounted on a vibration isolation table, so as to reduce vibration from ground pickup. Photothermal data was recorded only after the intensity of laser beam was stable. Electronic noise of detector also affects the sensitivity. Hence a low noise-high gain operational amplifier (OPA111-Burr Brown) was used in an instrumentation amplifier circuit. A Bi-cell photodiode (EG&G UV-140 BQ-2) was used to measure the deflection. The amplified signal was then fed to a dual input lock-in-amplifier (Stranford SR 830) to collect the phase and amplitude of the thermal wave generated. All the samples were characterized in this in-house built photothermal deflection setup.

Laser light sources are used for sample excitation and to probe the resulting refractive index changes, due to their high optical irradiance, monochromaticity, and coherence properties. As excitation sources, higher
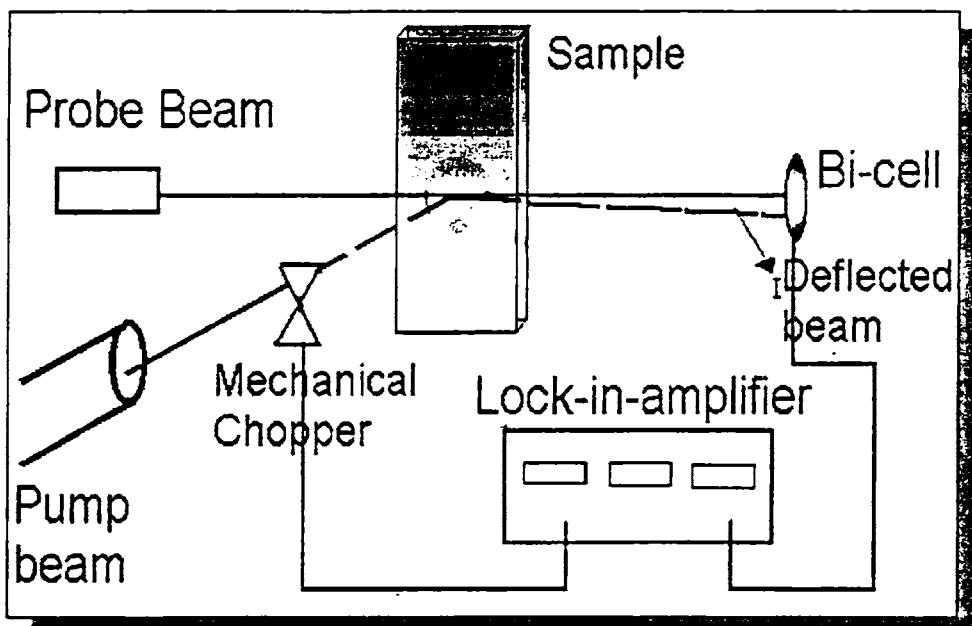
Fig. 1.1 Schematic layout of the PDS experimental setup.

irradiance and ability to focus coherent laser beams to small area, both result in larger signals than those able to be obtained with incoherent light sources. In brief, increased temperature results from higher optical power and smaller excitation volumes. As probes of the resulting refractive index changes, the coherence and monochromatic properties of laser sources allow highly sensitive analysis of the optical phase shifts. The resolution of the system is related to the size of the pump beam and to the sampling step: one way to magnify the resolution is to focus the pump beam on the surface and to reduce

the sampling step. CCl_4 was used as the deflection medium, as it absorbs only below 250 nm and had high (dn/dT), dn being the change in refractive index corresponding to a change dT in temperature of the medium due to the heat generated by induced light absorption [1, 4].
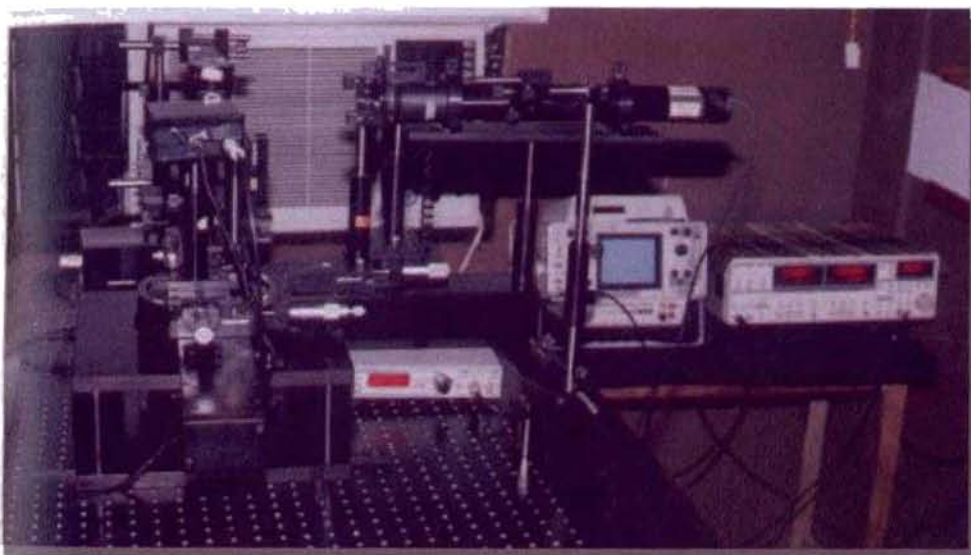
Fig. 1.2 Inbuilt PDS experimental setup mounted over a three arm unit with 638nm, 10mW He-Ne laser(Melles Griot) serving as the pump beam. Driver for mechanical chopper. Cathode Ray Oscilloscope and Lock-in-amplifier are also seen.
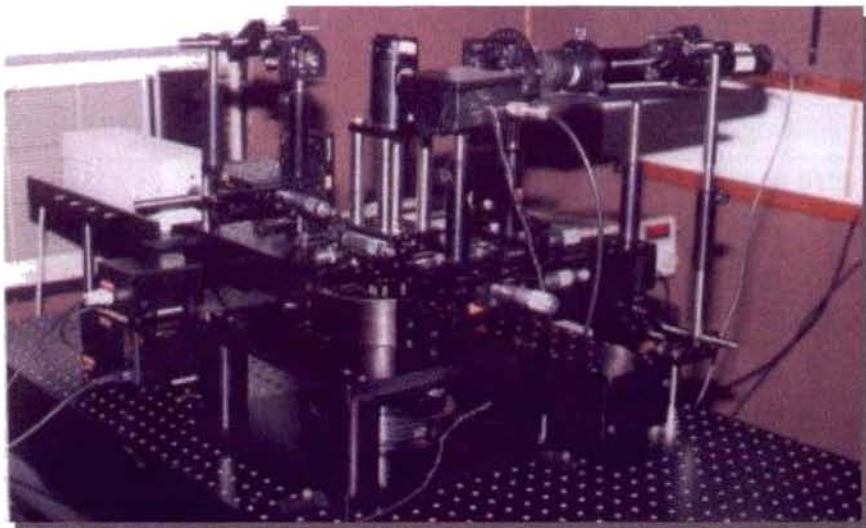
Fig. 1.3 Side view of the above PDS experimental setup.
The whole system is mounted over an optical bread board,
which is inturn placed over a vibration isolation table.

Fig. 1.4 Inbuilt PDS experimental setup mounted over a
three arm unit with 150 W Xe-arc lamp (Oriel) as a
broad band source. Monochromator (Oriel) seen in the
foreground was used to separate the broad band into
monochromatic beams that were used as the pump beam.

Fig. 1.5 Side view of the above PDS experimental setup.

1.3.2 Detection

The probe beam was initially centered on a bi-cell photodetector, such that deflection signals could be measured as a difference in voltage between the two halves of the detector. The ambient medium through which the probe beam passed was usually air. We used double distilled CCl_4 to increase the deflection signal. The deflection of the probe beam was measured synchronously using a dual input lock-in-amplifier (Stranford SR 830) with respect to the chopping of the pump laser beam.

For small temperature changes, the angular deflection of an infinitesimally small probe beam passing through a region of non-uniform temperature is given by.

$$M = -\int \frac{1}{n}\frac{dn}{dT}\nabla T(r) \times dr, \dots\dots\dots\dots\dots\dots\dots\dots\dots\dots\dots\dots\dots\dots\dots\dots\dots\dots\dots(1.2)$$

Where,

n – index of refraction of the medium, and the integral is evaluated along the path of the probe beam.

Due to the fact that the photon noise of the heating beam was not seen by the photothermal detector, the signal to noise ratio could be considerably enhanced by increasing the heating beam intensity [50, 51]. Oscillatory temperature fields were analysed in the frequency domain, using a synchronous lock-in amplifier.

Signal amplitude was proportional to excitation irradiance and hence the use of more powerful lasers resulted in the increase of detection limits. However, the higher irradiances might also result in nonlinear effects, which might be due to temporary changes in the sample matrix, resulting in refractive index perturbations only during excitation source irradiation. Absorption based nonlinear effects might be due to dynamic quantum state effects such as optical saturation, bleaching, or multiple photon excitation. Most of nonlinear effects became more problematic on using short pulsed excitation lasers where instantaneous irradiances were high and the excitation time scales became short, compared to excited state relaxation. Thus we fixed the intensity of the pump beam to a maximum of 30 mW for all our experiments.

1.3.2a Detector response

To understand the signal generated in PDS, oscillation of probe laser beam that impinged on the active area of a standard detector, after passing through the refractive index gradient, was to be understood. Initially the laser beam was centered between the bi-cell photodiode. Fig. 1.6 is the schematic

representation of the probe beam oscillation on the position sensing bi-cell detector. Dashed squares represent the bi-cell.

Let us consider the beam to be oscillating between two imaginary diaphragms. A small deflection of the beam between the diaphragms could produce a decrease in the detectable intensity of the radiation. Thus, the detector response became the measure of deflection of the probe laser beam. In Fig. 1.6, the solid circle represents the area of the impinging beam over the bi-cell photodiode and the dashed circle represents the position of oscillating beam after time t. The detectable intensity of the light (under the area ABCD) is given by [44];

$$\Phi(t) = 2H_0 r^2 [\arcsin \sqrt{1 - a^2(t)} - a(t)\sqrt{1 - a^2(t)}], \quad \dots\dots\dots\dots\dots\dots(1.3)$$

where,

r – radius of the probe beam

H_0 – Radiation density of the probe laser beam that is assumed to be uniform,

$$a(t) = \frac{(1 + \sin \omega t)}{2}, \dots\dots\dots\dots\dots\dots\dots\dots\dots\dots\dots\dots\dots\dots\dots(1.4)$$
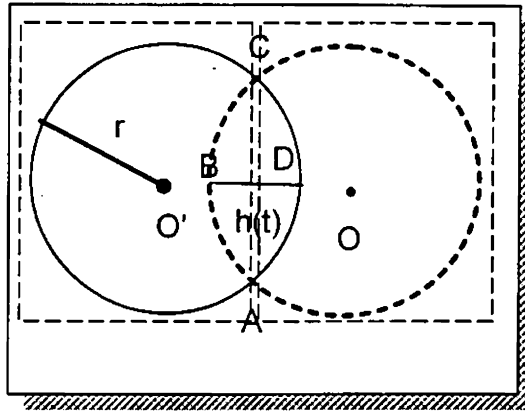
Fig. 1.6 Schematic representation of the probe beam oscillation on the position sensing bi-cell detector. Dashed squares represent the bi-cell.

As the centre of the beam oscillates between two extremes positions O' and O then,

$$h(t) = r \left[\frac{1 - \sin \omega t}{2} \right], \dots\dots\dots\dots\dots\dots\dots\dots\dots\dots\dots\dots\dots\dots\dots\dots(1.5)$$

The detector response is directly proportional to the deflection and therefore to the heat which produced this deflection. The distance between the sample and the detector was 10 cm. Deflection of 0.3 cm of the probe beam on the detector yielded an amplitude of 1 volt, when observed using a cathode ray oscilloscopy (CRO). The PDS amplitude and phase signals obtained from the lock-in amplifier were fed into a personal computer for further calculation. Fig. 1.7 is the schematic representation of the local refractive index gradient due to

20

modulated pump beam that was detected using a bi-cell position sensing detector [52].
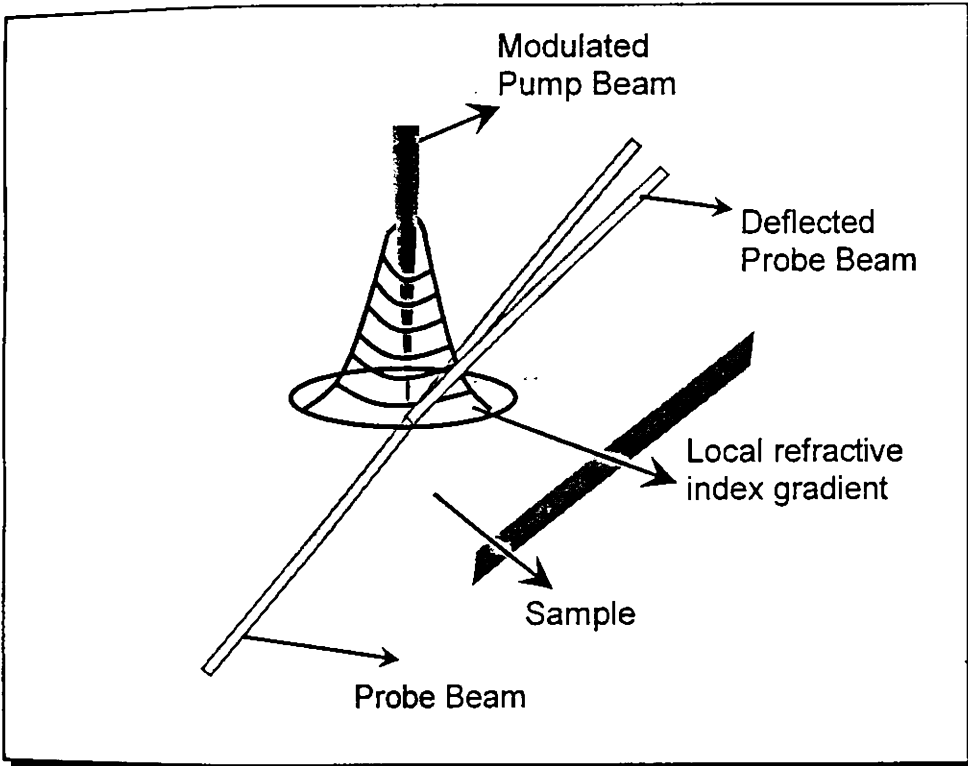
Fig. 1.7 Schematic representation of the local refractive index gradient due to modulated pump beam and detected using a bi-cell position sensing detector.

1.3.3 Theory

1.3.3a Analysis of signal amplitude

Exact description of the photothermal signal formation requires consideration of the thermal wave generation, its propagation within the sample, and its scattering from thermal inhomogeneities [53]. In one dimensional geometry, PDS signal is given by [54],

$$\Phi = T_r \left(\frac{1}{n_o} \right) \frac{dn}{dT} L \frac{dT(z_o)}{dz} e^{i\omega t}, \dots\dots\dots\dots\dots\dots\dots\dots\dots\dots\dots\dots\dots\dots\dots(1.6)$$

where,

T_r – The detector transducer factor,

$\left(\dfrac{1}{n_o} \right) \dfrac{dn}{dT}$ – Relative index of refraction change with temperature

of the deflecting medium,

L – Interaction length between pump and probe beam,

ω – Modulation frequency,

z_o – Distance of the probe beam from the sample surface,

$T(z_o)$ – Ambient temperature in the deflection medium,

$T(z)$ – Rise in temperature in the deflection medium,

$$T(z) = Q e^{-\sigma_m z}, \dots\dots\dots\dots\dots\dots\dots\dots\dots\dots\dots\dots\dots\dots\dots\dots\dots\dots\dots\dots\dots\dots(1.7)$$

Here

Q – ac temperature rise at the sample surface.

In the case of samples with buried interface layers, we considered three layers, namely the top layer (1), the interface layer (2) and the bottom layer (3). Thus a three layer model was developed as shown in Fig. 1.8,
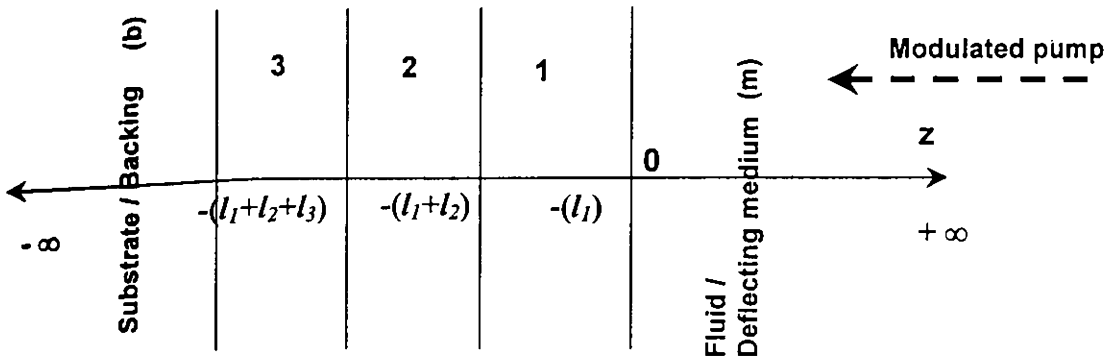
Fig. 1.8 Schematic representation of one dimensional geometry for a three layer sample.

Here, 1, 2 and 3 are the absorbing layers of the sample coated over a substrate or a backing medium. Then the sample had three layers over the substrate. The whole sample was immersed in the fluid.

Heat diffusion equation in different media is given by,

$$\frac{\partial^2 T}{\partial z^2} = \frac{1}{\alpha_m}\frac{\partial T}{\partial t}, \qquad\qquad 0 \le z \le \infty \dots\dots\dots\dots\dots\dots(1.8)$$

$$\frac{\partial^2 T}{\partial z^2} = \frac{1}{\alpha_1}\frac{\partial T}{\partial t} - \frac{\beta_1\eta_1 I_o}{2k_1}e^{\beta_1 z}\left(1+e^{i\omega t}\right), \quad -l_1 \le z \le 0 \dots\dots\dots\dots\dots(1.9)$$

$$\frac{\partial^2 T}{\partial z^2} = \frac{1}{\alpha_2}\frac{\partial T}{\partial t} - \frac{\beta_2\eta_2 I_o}{2k_2}e^{(\beta_2 z - \beta_1 l_1)}\left(1+e^{i\omega t}\right),$$

$$-(l_1 + l_2) \le z \le -l_1 \dots\dots\dots\dots(2.0)$$

$$\frac{\partial^2 T}{\partial z^2} = \frac{1}{\alpha_3}\frac{\partial T}{\partial t} - \frac{\beta_3 \eta_3 I_o}{2k_3} e^{(\beta_3 z - \beta_1 l_1 - \beta_2 l_2)}\left(1 + e^{i\omega t}\right),$$

$$-(l_1 + l_2 + l_3) \leq z \leq -(l_1 + l_2) \; ...(2.1)$$

$$\frac{\partial^2 T}{\partial z^2} = \frac{1}{\alpha_b}\frac{\partial T}{\partial t},$$

$$-\infty \leq z \leq -(l_1 + l_2 + l_3) \; ....(2.2)$$

Where,

α_j – Thermal diffusivity,

And, $\alpha_j = \dfrac{k_j}{c_j \rho_j}$, (where j = m,1,2,3 and b)

k_j – Thermal conductivity,

c_j – Specific heat,

ρ_j – densities,

β_1 – Optical absorption coefficients,

l_n – Thicknesses of the layer,

η_n – efficiencies of nonradiative processes,

I_o – Intensity of light source,

The solutions for the ac components of the temperature rise in the media is given by,

$$T(z,t) = Q e^{-\sigma_m z} e^{i\omega t},\qquad\qquad 0 \leq z \leq \infty \; .... (2.3)$$

$$T(z,t) = (R e^{\sigma_1 z} + S e^{-\sigma_1 z} - E e^{\beta_1 z})e^{i\omega t},\qquad -l_1 \leq z \leq 0 \; .... (2.4)$$

$$T(z,t) = (T e^{\sigma_2 z} + U e^{-\sigma_2 z} - F e^{\beta_2 z})e^{i\omega t},\qquad -(l_1 + l_2) \leq z \leq -l_1 .... (2.5)$$

$$T(z,t) = (V e^{\sigma_3 z} + W e^{-\sigma_3 z} - G e^{\beta_3 z}) e^{i\omega t},$$

$$-(l_1 + l_2 + l_3) \leq z \leq -(l_1 + l_2) \,...(2.6)$$

$$T(z,t) = Z e^{\sigma_4 z} e^{i\omega t}, \qquad\qquad -\infty \leq z \leq -(l_1 + l_2 + l_3) \,.........(2.7)$$

Where,

$$E = \frac{\eta_1 \beta_1 I_o}{2k_1 \left(\beta_1^2 - \sigma_1^2\right)};$$

$$F = \frac{\eta_2 \beta_2 I_o e^{-\beta_1 l_1}}{2k_2 \left(\beta_2^2 - \sigma_2^2\right)}; \quad G = \frac{\eta_3 \beta_3 I_o e^{-(\beta_1 l_1 + \beta_2 l_2)}}{2k_3 \left(\beta_3^2 - \sigma_3^2\right)};$$

$$\sigma_j = (1+i)a_j; \quad a_j = \left(\frac{\omega}{2\alpha_j}\right)^{\frac{1}{2}}$$

Applying the continuity conditions for the temperature and heat flux at the various media boundaries, one obtains a set of equations from which a big expression for Q, which is the heat flux at the surface of the sample can be obtained (equation. 2.8).

$$Q = \cfrac{
\begin{aligned}
&\{2I_o\eta_3\beta_3 b_1 b_2 \exp[-(\beta_1 l_1 + \beta_2 l_2)]/k_3(\beta_3{}^2 - \sigma_3{}^2)\}[(r_3 - 1)(b_3 + 1)\exp(\sigma_3 l_3) \\
&-(r_3 + 1)(b_3 - 1) \times \exp(-\sigma_3 l_3) + 2(b_3 - r_3)\exp(-\beta_3 l_3)] \\
&+ I_0\eta_2\beta_2 b_1 \exp(-\beta_1 l_1)/k_2(\beta_2{}^2 - \sigma_2{}^2)] \times \\
&[(r_2 - 1)[(b_2 + 1)(b_3 + 1) \times \exp(\sigma_2 l_2 + \sigma_3 l_3) + (b_2 - 1)(b_3 - 1) \\
&\exp(\sigma_2 l_2 - \sigma_3 l_3)] - (r_2 + 1)\{(b_2 - 1)(b_3 + 1)\exp[-(\sigma_2 l_2 - \sigma_3 l_3)] \\
&+ (b_2 + 1)(b_3 - 1)\exp[-(\sigma_2 l_2 + \sigma_2 l_3)]\} + 2\exp(-\beta_2 l_2)[(b_2 - r_2)(b_3 + 1) \times \\
&\exp(\sigma_3 l_3) + (b_2 + r_2)(b_3 - 1)\exp(-\sigma_3 l_3)] + [I_0\eta_1\beta_1 / 2k_1(\beta_1{}^2 - \sigma_1{}^2)] \\
&[(r_1 - 1)\{(b_1 - 1)[(b_2 + 1)(b_3 - 1) \times \exp(\sigma_1 l_1 - \sigma_2 l_2 - \sigma_3 l_3) \\
&+ (b_2 - 1)(b_3 + 1)\exp(\sigma_1 l_1 - \sigma_2 l_2 + \sigma_3 l_3)] + (b_1 + 1)[(b_2 - 1)(b_3 - 1) \times \\
&\exp(\sigma_1 l_1 + \sigma_2 l_2 - \sigma_3 l_3) + (b_2 + 1)(b_3 + 1)\exp(\sigma_1 l_1 + \sigma_2 l_2 + \sigma_3 l_3)]\} \\
&-(r_1 + 1)[(b_1 + 1) \times \{(b_2 + 1)(b_3 - 1)\exp[-(\sigma_1 l_1 + \sigma_2 l_2 + \sigma_3 l_3)] \\
&+ (b_2 - 1)(b_3 + 1)\exp[-(\sigma_1 l_1 + \sigma_2 l_2 - \sigma_3 l_3)]\} \\
&+ (b_1 - 1)\{(b_2 + 1)(b_3 + 1)\exp[-(\sigma_1 l_1 - \sigma_2 l_2 - \sigma_3 l_3)] \\
&+ (b_2 - 1)(b_3 - 1)\exp[-(\sigma_1 l_1 - \sigma_2 l_2 + \sigma_3 l_3)]\}] \\
&+ 2\exp(-\beta_1 l_1)[(b_1 + r_1)\{(b_2 + 1)(b_3 - 1)\exp(-[\sigma_2 l_2 + \sigma_3 l_3]) \\
&+ (b_2 - 1)(b_3 + 1)\exp(-[\sigma_2 l_2 - \sigma_3 l_3])\} + (b_1 - r_1)\{(b_2 - 1)(b_3 - 1) \times \\
&\exp(\sigma_2 l_2 - \sigma_3 l_3) + (b_2 + 1)(b_3 + 1)\exp(\sigma_2 l_2 + \sigma_3 l_3)\}]])
\end{aligned}
}{
\begin{aligned}
&[(g + 1) \times [(b_1 - 1)\{(b_2 + 1)(b_3 - 1)\exp(\sigma_1 l_1 - \sigma_2 l_2 - \sigma_3 l_3) \\
&+ (b_2 - 1)(b_3 + 1)\exp(\sigma_1 l_1 - \sigma_2 l_2 + \sigma_3 l_3)\} \\
&+ (b_1 + 1)\{(b_2 - 1)(b_3 - 1)\exp(\sigma_1 l_1 + \sigma_2 l_2 - \sigma_3 l_3) \\
&+ (b_2 + 1)(b_3 + 1)\exp(\sigma_1 l_1 + \sigma_2 l_2 + \sigma_3 l_3)\}] \\
&-(g - 1) \times [(b_1 + 1)\{(b_2 + 1)(b_3 - 1)\exp(-[\sigma_1 l_1 + \sigma_2 l_2 + \sigma_3 l_3]) \\
&+ (b_2 - 1)(b_3 + 1)\exp(-[\sigma_1 l_1 + \sigma_2 l_2 - \sigma_3 l_3])\} \\
&+ (b_1 - 1)\{(b_2 + 1)(b_3 + 1)\exp(-[\sigma_1 l_1 - \sigma_2 l_2 - \sigma_3 l_3]) \\
&+ (b_2 - 1)(b_3 - 1)\exp(-[\sigma_1 l_1 - \sigma_2 l_2 + \sigma_3 l_3])\}]]
\end{aligned}
}$$

....(2.8)

Where

$$b_1 = \frac{k_2 a_2}{k_1 a_1};$$

$$b_2 = \frac{k_3 a_3}{k_2 a_2};$$

$$b_3 = \frac{k_b a_b}{k_3 a_3};$$

$$g = \frac{k_m a_m}{k_1 a_1};$$

$$r_n = (1-i)\frac{\beta_n}{2a_n};$$

In equation (2.8) by setting to zero the thickness of any of the three layers one obtains the result for two layer sample and by setting to zero any two of the three layers the result for a one layer sample is obtained.

Then the photothermal amplitude is given as,

$$\Phi = T_r \left(\frac{1}{n_o}\right)\frac{dn}{dT} L a_m \sqrt{\left(Q_R^2 + Q_I^2\right)} \times e^{-a_m z_o},$$

.... (2.9)

The phase lag measured is given by,

$$\varphi = \tan^{-1}\left(\frac{Q_I}{Q_R}\right) - a_m z_o - \frac{\pi}{4},$$

.... (3.0)

Where, Q_R and Q_I are the real and imaginary part of Q.

Fig. 1.9 is the amplitude versus chopping frequency curve generated for the parameters given in Table 1.2. This is for "1000" In_2S_3 thin film samples (See chapter 4, section 4.4.2.2c for details).
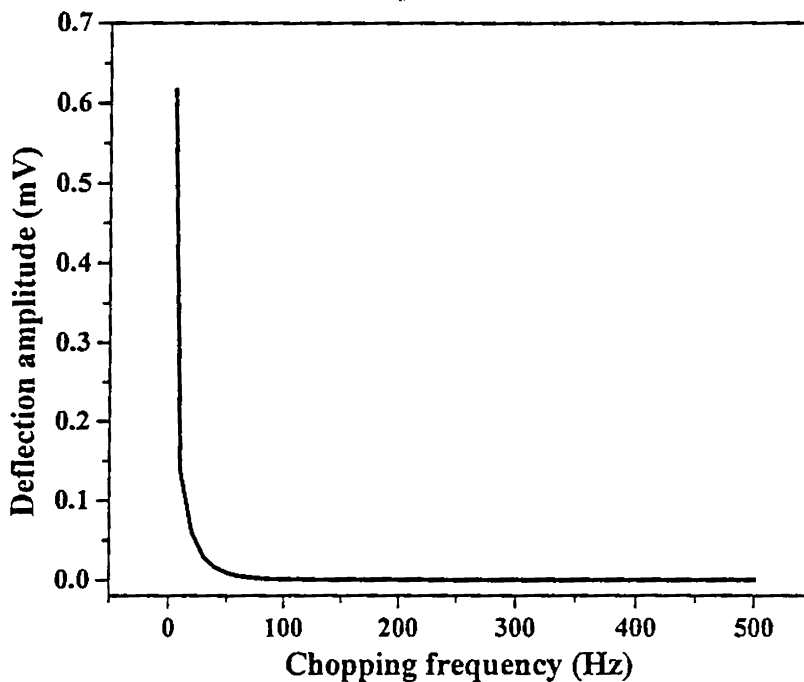
Fig. 1.9 Amplitude versus chopping frequency curve generated using equation (2.9)

Input parameters	Values
T_r (Detector transducer factor)	65
n_o (Refractive index of CCl$_4$)	1.46
L (Interaction length, between pump and probe beam)	2.0 (μm)
z_o (Distance of probe beam from sample surface)	2.3 (μm)
ω (Chopping frequency)	Varies from 5 Hz to 500 Hz

Table 1.2 Input values used to generate deflection amplitude versus chopping frequency plot (Fig. 1.9) using equation (2.9) for a frequency range from 5 Hz to 500 Hz.

1.3.3b Analysis of signal amplitude in case of semiconductors

Time dependent deflection of a narrow probe beam propagating through an inhomogeneous medium at a given distance x is given by [55],

$$\Phi(x,t) = \frac{l}{n}\frac{\partial n(x,t)}{\partial x}, \dots\dots\dots\dots\dots\dots\dots\dots\dots\dots\dots\dots\dots(3.1)$$

Here, the inhomogeneous medium is the local refractive index change occurring in the coupling medium, as heat generated inside the sample is transferred to the coupling medium in contact with the sample surface and x is the distance between the probe beam and sample surface.

The parameters in equation (3.1) are,

Φ – the angular deflection,

l – Interaction length between the pump and the probe beam,

n – local index of refraction,

$\dfrac{\partial n(x,t)}{\partial x}$ – Refractive index change,

29

For semiconductors, refractive index change is also due to free carrier contribution, thus equation (3.1) can be rewritten as,

$$\frac{\partial n(x,t)}{\partial x} = \frac{\partial n}{\partial T}\frac{\partial T(x,t)}{\partial x} + \frac{\partial n}{\partial N}\frac{\partial N(x,t)}{\partial x}, \dots\dots\dots\dots\dots\dots\dots\dots\dots\dots\dots(3.2)$$

where,

$T(x,t)$ – Time dependent temperature,

$N(x,t)$ – Minority carrier density distribution.

The thermal term is composed to two components. One is due to the thermal wave from the surface heating that is due to the immediate thermalization of carriers. The other is due to non radiative recombination of the photoexcited carriers which diffuse away from the irradiated region. Probe beam wavelength does not play a major role as it only passes parallel and above the sample surface.

1.3.3b(i) Thermal contribution

The equation describing the thermal contribution follows from the standard heat diffusion equation with a source term due to carrier recombination and a surface source boundary condition, which is given by,

$$D_{th}\frac{d^2T}{dx^2} = \frac{dT}{dt} - \frac{E_G D_{th}}{k}\frac{N(x,t)}{\tau}, \dots\dots\dots\dots\dots\dots\dots\dots\dots\dots\dots(3.3)$$

Where,

D_{th} – Thermal diffusivity term,

k – thermal conductivity,

E_G – Energy band gap of the semiconductor,

N – Carrier density,

τ – Minority carrier lifetime.

with the boundary condition,

$T(x,0) = 0$, and

$$-k\frac{dT}{dx}(0,t) = sN(0,t)E_G + \frac{h\upsilon - E_G}{h\upsilon}\phi_0 e^{i\omega t}, \dots\dots\dots\dots\dots\dots\dots\dots\dots(3.4)$$

Where,

   $h\upsilon$ – Photon energy,

   ϕ_0 – Light flux,

   s – surface recombination velocity,

1.3.3b(ii) Free carrier contribution

The carrier population distribution is given by the non-homogeneous diffusion equation.

$$D\frac{d^2N}{dx^2} = \frac{dN}{dt} + \frac{N}{\tau}, \dots\dots\dots\dots\dots\dots\dots\dots\dots\dots\dots(3.5)$$

Where,

D – Minority carrier diffusion,

The boundary conditions are,

$N(x,0) = 0$, and

$$D\frac{dN}{dx}(0,t) = -\frac{\phi_0}{h\upsilon}e^{i\omega t} + sN(0,t), \dots\dots\dots\dots\dots\dots\dots\dots\dots(3.6)$$

The steady state solution for the temperature distribution is given by,

$$T(x,t) = \mathrm{Re} \left(\frac{\left(\phi_0 E_G / \lambda_{el}\right)\left(\dfrac{e^{-x/\lambda_{th}}}{1/\lambda_{th}} - \dfrac{e^{-x/\lambda_{el}}}{1/\lambda_{el}}\right)e^{i\omega t}}{h\upsilon\tau Dk(s/D+1/\lambda_{el})\left[1/\tau D + i\left(\omega/D\right) - i\left(\omega/D_{th}\right)\right]} + \left(\frac{\phi_0 E_G s}{h\upsilon Dk(s/D+1/\lambda_{el})} + \frac{\left(h\upsilon - E_G\right)\phi_0}{h\upsilon k}\right)\lambda_{th}e^{-x/\lambda_{th}}e^{i\omega t} \right), \quad \ldots\text{(3.7)}$$

Where,

$$1/\lambda_{th} = \sqrt{i\omega / D_{th}},$$

$$1/\lambda_{el} = \sqrt{(1+i\omega\tau)/D\tau},$$

This yields the thermal gradient,

$$\frac{dT}{dx}(x,t) = \mathrm{Re} \left(\frac{\phi_0 E_G / \lambda_{el}}{h\upsilon\tau Dk(s/D+1/\lambda_{el})\left[1/\tau D + i\left(\omega/D - \omega/D_{th}\right)\right]} \times e^{-x/\lambda_{el}}e^{i\omega t} - \left(\frac{\phi_0 E_G / \lambda_{el}}{h\upsilon\tau Dk(s/D+1/\lambda_{el})\left[1/\tau D + i\left(\omega/D - \omega/D_{th}\right)\right]} + \frac{\phi_0 E_G s}{h\upsilon Dk(s/D+1/\lambda_{el})} + \frac{\left(h\upsilon - E_G\right)}{h\upsilon}\frac{\phi_0}{k}\right)e^{-x/\lambda_{th}} \right)$$

$$\ldots\ldots\ldots\ldots\ldots\ldots\ldots\ldots\ldots\ldots\ldots\text{(3.8)}$$

Similarly for minority carrier distribution we obtain,

$$N(x,t) = \mathrm{Re} \left(\frac{\phi_0 e^{-x/\lambda_{el}}}{h\upsilon D(s/D+1/\lambda_{el})}e^{i\omega t} \right), \ldots\ldots\ldots\ldots\ldots\ldots\ldots\ldots\text{(3.9)}$$

The thermal gradient due to the recombination of photogenerated carriers is given by,

$$\frac{dN}{dx}(x,t) = \mathrm{Re} \left(\frac{-\phi_0 / \lambda_{el}}{h\upsilon D(s/D+1/\lambda_{el})}e^{-x/\lambda_{el}}e^{i\omega t} \right), \ldots\ldots\ldots\ldots\ldots\ldots\text{(4.0)}$$

Equation (3.8 and 4.0) can be combined with equation (3.2) and on simplification one gets,

$$\frac{d\Phi}{dx} = \left[C_1^{th}\right]e^{-x\sqrt{i\omega/D_{th}}} + \left[C_2^{th}\right]e^{-x\sqrt{(1+i\omega\tau)/D\tau}} + \left[C_3^{FC}\right]e^{-x\sqrt{(1+i\omega\tau)/D\tau}}, \ldots\ldots\ldots\ldots(4.1)$$

$$= \left[C_1^{th}\right]e^{-x\lambda_{th}} + \left[C_2^{th}\right]e^{-x\lambda_{el}} + \left[C_3^{FC}\right]e^{-x\lambda_{el}}, \ldots\ldots\ldots\ldots\ldots\ldots\ldots\ldots\ldots(4.2)$$

Where,

C_1^{th} and C_2^{th} – the coefficients of the thermal contribution,

C_3^{FC} – Coefficient of the free carrier contribution.

Thus, from the above equation, it is clearly seen that there should be three general regions. The first one is due to "purely" thermal behaviour. The second is dominated by electronic behaviour which is associated with the photogenerated carriers. The third is for the intermediate region for intermediate frequencies, where occurs a complex interaction that is highly sensitive to carrier lifetime and surface recombination.

At low frequencies, the first term dominates as ω tends to zero, where $D \gg D_{th}$. The electronic behaviour dominates at high frequencies. The exponential dependence is emphasized by plotting the logarithm of the deflection amplitude as a function of the square root of the modulation frequency ω.

For low frequencies, $\omega\tau \ll 1$, $\lambda_{el} \to \sqrt{D\tau}$, while λ_{th} increases. Hence the thermal properties dominate and then the equation (4.2) can be reduced to,

$$|Signal| \alpha \left|\frac{d\Phi}{dx}\right|, \ldots\ldots\ldots\ldots\ldots\ldots\ldots\ldots\ldots\ldots\ldots\ldots\ldots\ldots\ldots\ldots\ldots\ldots\ldots(4.3)$$

$$\left|\frac{d\Phi}{dx}\right| = Const\left(e^{-x\sqrt{i\omega/2D_{th}}}\right), \ldots\ldots\ldots\ldots\ldots\ldots\ldots\ldots\ldots\ldots\ldots\ldots(4.4)$$

$$\log\left|\frac{d\Phi}{dx}\right| = Const - x\sqrt{\omega}\left(\frac{1}{\sqrt{2D_{th}}\,(\ln 10)}\right),\dots\dots\dots\dots\dots\dots\dots\dots\dots(4.5)$$

Thus, D_{th} can be determined from the slope of log deflection amplitude versus square root of frequency in the low frequency region.

For high frequencies, $\omega\tau \gg 1$ and $\lambda_{el} \to \sqrt{(D/i\omega)}$, and the electronic properties dominate. Then equation (4.2) reduces to

$$\left|\frac{d\Phi}{dx}\right| = Const\left(e^{-x\sqrt{\omega/2D}}\right),\dots\dots\dots\dots\dots\dots\dots\dots\dots\dots\dots\dots(4.6)$$

$$\log\left|\frac{d\Phi}{dx}\right| = Const - x\sqrt{\omega}\left(\frac{1}{\sqrt{2D}\,(\ln 10)}\right),\dots\dots\dots\dots\dots\dots\dots\dots\dots(4.7)$$

Thus, D can be determined from the slope of log deflection amplitude versus square root of frequency in high frequency region. And the mobility can be calculated from the Einstein-Smoluchowski relation, which couples the mobility μ and the diffusion coefficient D;

$$\boxed{D = \frac{kT}{e}\mu,}\qquad \dots\dots\dots\dots\dots\dots\dots\dots\dots\dots\dots\dots\dots\dots(4.8)$$

Where

   μ – Mobility,

   e – electronic charge,

Fig 1.10 is the plot for log amplitude versus square root of chopping frequency for "1000" In_2S_3 thin film sample. As suggested by the theoretical predication, for low frequency (between 2.5 $\sqrt{Hz}$ and 20 $\sqrt{Hz}$) the graph has a steep linear

decrease, while at intermediate frequency (between 20 √Hz and 25 √Hz) there occurs a "hump", which is due to complex interaction of photogenerated carriers that separates "purely thermal" from electronic contribution.
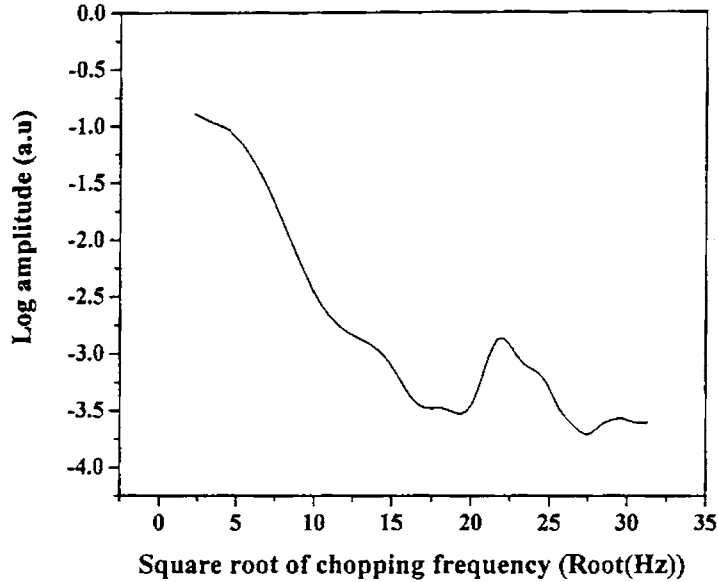
Fig 1.10 Graph showing variation of log amplitude versus square root of chopping frequency for "1000" In_2S_3 thin film sample.

1.4 Depth Profiling

The propagation of thermal waves in solids is strongly influenced by the material's microscopic properties, by its physical microstructure, and especially by the distribution of inner interfaces [56]. Along with this, the fact that the penetration depth of thermal waves can be controlled by the variation of modulation frequency, make a novel nondestructive photothermal depth profiling possible. The possibility to deduce depth dependent information is

based on the measurement of the time of flight of heat. For short flying time, the detected heat originates from near surface regions and for long flying time, from regions far below the surface. In the frequency domain, for periodically modulated excitation, short and long flying time correspond to high and low modulation frequencies, respectively.

To determine the sample thickness, the sample was first theoretically modeled and the heat propagation inside the sample was solved using the heat diffusion equation as suggested in section (1.3.3a). Curve fitting was done using theoretical values. Thickness was derived from parameters of best fit curve the solved equation (equation (2.9)).

1.5 Thermal diffusivity and mobility determination

1.5.1 Determination of thermal diffusivity

Principle of photothermal method is to provide a local temperature increase by the absorption of a focused laser beam and thermal diffusion removes heat from the region excited by the laser in the characteristic thermal diffusion time (t_c). This increase in temperature depends on the heat-conductive properties of the sample [57]. Refractive index perturbations due to the "purely thermal" term is called "temperature effects".

Thermal diffusivity for the sample in our case, was calculated from data obtained by linear curve fitting in the low frequency region, (which is due to "purely" thermal contribution), in the log amplitude versus square root of the chopping frequency plot for the respective samples and by evaluating D_{th} from the equation (4.5).

Although specific volume changes affect the density, they are called "specific volume effects" to discriminate them from the temperature dependent density change terms. The final goal of such a nondestructive inspection technique is to obtain information about the location, the shape and the kind of structural and therefore thermal subsurface inhomogeneities from measured values.

1.5.2 Determination of mobility

Mobility is calculated from data obtained from the slope of the curve in the high frequency region (which is due to electronic contribution) from the log amplitude versus square root of the chopping frequency plot for the respective samples. One gets D from this using the equation (4.7) and Mobility (μ) can be calculated from equation (4.8).

1.6 Imaging

The aim of photothermal imaging techniques is to obtain information about the depth of optically invisible inhomogeneities within the sample. This helps in knowing the shape of distribution and the density of defects.

We performed two dimensional imaging of the sample by scanning the pump beam over an area of 500 x 500 μm^2. Layout of the experiment is shown in Fig. 1.11.
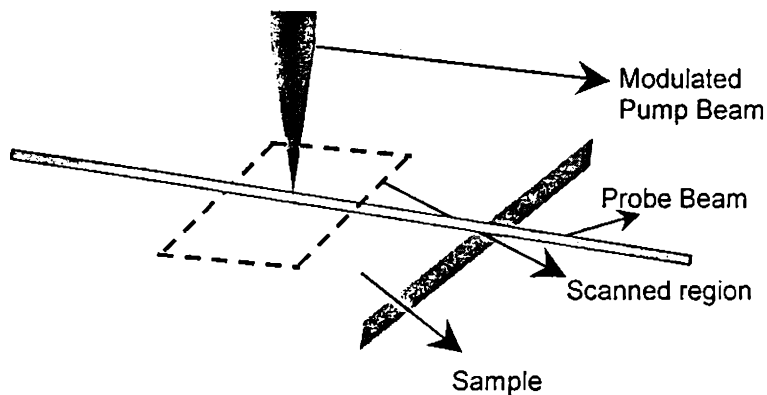
Fig. 1.11 Schematic of layout for imaging measurements.

Data obtained from photothermal deflection method is plotted as deflection amplitude versus scanned distance. The "contrast" in PDS imaging is the detectability of weak thermal inhomogeneities with respect to the background signal of the homogeneous material [53]. PDS techniques have also been established as successful methods for imaging microscopic structures thermally. Optically invisible patterns like buried defects or inhomogeneities become "visible" thermally in PDS technique [58, 59]. For samples having low absorption coefficient the PDS signal has the form,

$$S \propto \left(\alpha_s + \alpha_d d \right), \dots\dots\dots\dots\dots\dots\dots\dots\dots\dots\dots\dots\dots\dots\dots\dots\dots\dots\dots(4.9)$$

Where,

α_s and α_d are the surface and bulk absorption coefficients, respectively.

1.7 Conclusion

PDS technique has been gaining advantage over other optical techniques due to its versatility and sensitive nature. As this technique fully uses optical beam, the samples under investigation can be evaluated without making any contacts. Due to its non-destructive nature, this technique could be used on very thin samples and even for analysis of soft biological samples. We built this tool in our laboratory and used it for thin film analysis. As this technique is not affected by light scattering, the thermal and optical properties for even less absorbing samples could be found out. We could measure variation in electrical properties on Cu doped CdS thin films and also depth of Cu penetration into CdS thin film layer. Ion implantation causes change in optical, structural, thermal and electrical properties of the material. Variation in thermal and optical properties could be determined. Depth of penetration of energetic ions into thin film sample were also determined. Due to its sensitivity, feeble optical absorption could be detected that helps in studying even transparent samples. So we could study the thickness of transparent conducting oxide such as ZnO having various thicknesses, and the values were coinciding with those obtained from stylus method. Transport property such as mobility was also calculated and were found to coincide with the Hall measurements. This technique was also applied to non-destructively evaluate the quality of welded joint and to measure the thickness of painted layer over a substrate.

References

[1] A.C. Boccara, D. Fournier and J. Badoz, *Appl. Phys. Lett.*, **36(2)** (1980) 130.

[2] J.C. Murphy and L.C. Aamodt, *J. Appl. Phys.*, **51** (1980) 4580.

[3] L.C. Aamodt and J.C. Murphy, *J. Appl. Phys.*, **52** (1981) 4903.

[4] W.B. Jackson, N.M. Amer, A.C. Boccara, and D. Fournier, *Appl. Opt.*, **20** (1981) 1333.

[5] A. Mandelis, *J. Appl. Phys.*, **54** (1983) 3404.

[6] L.C. Aamodt and J.C. Murphy, *J. Appl. Phys.*, **58** (1983) 54.

[7] K.R. Grice, L.J. Inglehart, L.D. Favro, P.K. Kuo, and R.L. Thomas, *Appl. Phys.*, **54** (1983) 6245.

[8] F. Lepoutre, D. Fournier, and A. C. Boccara, *J. Appl. Phys.*, **57** (1985) 100.

[9] R.S. Sussman, J.R. Brandon, G.A. Scarsbrook, C.G. Sweeney, T.J. Valentine, A.J. Whithead and C.J.H. Wort, *Diamond Relat. Mater.*, **3** (1994) 303.

[10] Y.Nagasaka, T.Sato and T.Ushiku, *Meas. Sci. Technol.*, **12** (2001) 2081.

[11] A. Rosencwaig, *"Non-Destructive Evaluation"* Ed. A. Mandelis (New Jersey: PTR Prentice-Hall) (1994) pp 1-22.

[12] F.Lepoutre, D. Balageas, P. Forge, S. Hirschi, J. L. Joulaud, D. Rochais, F.C. Chen, *J. Appl. Phys.*, **78** (1995) 2208.

[13] S.Paoloni, P.Mayr, C.Glorieux, R.Li Voti, H.Bentefour, J.Thoen, *Analytical sciences.*, **17** (2001) 406.

[14] R.Li Voti, G.L.Liakhou, S.Paoloni, C.Sibilia and M.Bertolotti, *Analytical Sciences*, **17** (2001) 414.

[15] G.Busse and H.G.Walther, *"Progress of Photothermal and Photoacoustic*

Science and Technology", Ed A.Mandelis, 1 (Elsevier, 1992) 205.

[16] Network news, *European thematic network*, Issue No. 3 (1999) pp 16.

[17] S. Nonomura, T. Nishiwaki and S. Nitta, *Philos. Mag. B*, 69 (1994) 335.

[18] M. Takezaki, N. Hirota, M. Terazima, *J. Chem. Phys.*, 108 (1998) 4685.

[19] N.M. Amer and W.B. Jackson, *Semicond. Semimet. B*, 21 (1984) 83.

[20] *"Amorphous silicon and Related Materials"*, Ed. H. Curtins and M. Favre, H. Fritzsche World Scientific, Singapore (1988) p.329.

[21] C.K.N. Patel and A.C. Tam, *Rev. Modern Phys.*, 53(3) (1981) 517.

[22] S.W. Kizirnis, R.J. Brecha, B.N. Ganguly, L.P. Goss, and R. Gupta, *Appl. Opt.*, 23, 3873 (1984).

[23] A. Rose and R. Gupta, *Proceedings of the Combustion Institute*, 20 (1985) 1339.

[24] A. Rose and R. Gupta, *Opt. Commun.*, 56 (1986) 303.

[25] A. Rose and R. Gupta, *Opt. Lett.*, 10 (1985) 532.

[26] Joshua E. Rothenberg, *Optics letters*, 13(9) (1988) 713.

[27] Jonathan D. Spear, Gregory L. Klunder and Richard E. Russo, *Rev. Sci. Inst.*, 69(6) (1998) 2259.

[28] M. Gibson, E. McGlynn and M.O. Henry, *Physica B*, 273-274 (1999) 1011.

[29] Jane Hodgkinson, Mark Johnson, John P. Dakin, *Sensors and Actuators B*, 67 (2000) 227.

[30] Andreas Mandelis, *Rev. Sci. Instrum.*, 65(1) (1994) 3309.

[31] R. Tilgner, J. Baumann, and M. Beyfuss, *Can. J. Phys.*, 64 (1986) 1287.

[32] J. Baumann and R. Tilgner, *Can. J. Phys.*, 64 (1986) 1291.

[33] Haruo Fujimori, Yamato Asakura, Kazumichi Suzuki and Shunsuke Uchida, *Jpn. J. Appl. Phys.*, 26(10) (1987) 1759.

[34] H.G.Walther, and T. Kitzing, *J. Appl. Phy.*, **84(3)** (1998) 1163.

[35] C. Glorieux, R. Li Voti, J. Thoen, M. Bertolotti and C. Sibilia, *J. Appl. Phys.*, **85(10)** (1999) 7059.

[36] W. Bai and B.S. Wong, *Meas. Sci. Technol.*, **12** (2001) 142.

[37] A. Salazar, A. Sanchez-Lavega, and J. Frenandez, *J. Appl. Phys.*, **65** (1989) 4150.

[38] Johney Isaac, J. Philip, M.T. Sebastian and A. D. Damodaran, *Physica C*, **199** (1992) 247.

[39] M. Bertolotti, R.Li Voti, G. Liakhou, and C. Sibilia, *Rev. Sci. Instrum.*, **64(6)** (1993) 1576.

[40] G. Langer, J. Hartmann and M. Reichling, *Rev. Sci. Instrum.*, **68(3)** (1997) 1510.

[41] T. Borca-Tasciuc and G. Chen, *Rev. Sci. Instrum*, **68(11)** (1997) 4080.

[42] U. Zammit, M. Marinelli, F. Scudieri and S. Martellucci, *Appl. Phys. Lett.*, **50(13)** (1987) 830.

[43] V.A. Sablikov and V.B. Sandomirskii, *Phys. Stat. Sol. (b)*, **120** (1983) 471.

[44] D. Dadarlat, M. Chirtoc and Rodica M. Candea, *Phys. Stat. Sol. (a)*, **98** (1986) 279.

[45] E. Marin, I. Riech, P. Diaz and H. Vargas, *Anal. Sci.*, **17** (2001) s288.

[46] Andreas Mandelis, *Phys. Today*, **1** (2000) 29.

[47] Daniele Fournier, Claude Boccara, Andrew skumanich, and Nabil M. Amer, *J. Appl. Phys.*, **32** (1999) L 125.

[48] Michael D. Morris and Konan Deck, *Anal. Chem*, **58** (1986) 811A.

[49] M. Commandre and P. Roche, *Appl. Opt.*, **35** (1996) 5021.

[50] L.B. Kreuzer, *J. Appl. Phys.*, **42** (1971) 2934.

[51] Mladen Franko, Chieu D. Tran, *Rev. Sci. Inst.*, **67** (1996) 1.

[52] L.C. Aamodt and J.C. Murphy, *J. Appl. Phys.*, **54(2)** (1982) 581.

[53] K. Friedrich, K. Haupt, U. Seidel, and H.G. Walther, *J. Appl. Phys.*, **72(8)** (1992) 3759.

[54] U. Zammit, M. Marinelli and R. Pizzoferrato, *J. Appl. Phys.*, **69(5)** (1991) 3286.

[55] L.W. Casperson, *Appl. Opt.*, **12** (1973) 2434.

[56] J.W.Vandersande and C.Wood, *Contemp. Phys.*, **27** (1986) 117.

[57] Kerstin Friedrich and Heinz-Guenter Walther, *J. Appl. Phys.*, **70(9)** (1991) 4697.

[58] G. Busse, *Phys. Acoustics*, **18** (1988) 403.

[59] H.G. Walther, K. Friedrich, K. Haupt, K. Muratikov, and A. Glazov, *Appl. Phys.Lett.*, **57** (1990) 1600.

Chapter 2

ION IMPLANTATION STUDIES

2.1 Introduction

Use of ion beam dates back to 1948 for developing the first transistor - a breakthrough in the past for the present modern electronics. By 1956, potential of ion implantation, for introducing electrically active dopants in a controlled fashion, was realized and a number of patents were filed.

Ion implantation is a key technological process in modern microelectronics, that was introduced as an alternative to diffusion, for the semiconductor doping process. Implantation of impurity atoms for doping semiconductor wafers offered many advantages such as rapidity, accuracy, wide range of doses, flexibility of profile depth, and control over the amount of ions in a specific region. One main disadvantage of ion implantation process is damage introduced into semiconductor, resulting from the energetic nature of the process, which has a significant influence on the electrical and optical properties of the semiconductors [1]. But the development of laser annealing technique solved this difficulty very much. Moreover, the advantages of this doping technology really forced researchers to use this for fabricating semiconductor devices of smaller dimensions [2-4].

With rapid development in scaling down semiconductor devices, detailed information on impurity profiles which follows ion implantation has significant technological importance. Thus a rigorous understanding of projected range (R_p), longitudinal range straggling (ΔR_p), skewness (γ),

kurtosis (β), and transversal range straggling (ΔR_t) of implanted ions in solids is of great value [5].

The technique makes use of ions with energy in the range of keV to a few MeV that bombard the target. These ions then slow down due to the interaction with the solid target and finally come to rest at a depth normally referred to as the *"Range"*. The concentration and depth of penetration of implanted impurities can be controlled by controlling the ion current, time of implantation and beam energy. Being a non-equilibrium process, there is no solubility constraints and any type of atom can be implanted in any target. The defects produced during irradiation are normally annealed out by suitable thermal treatments.

2.2 Brief review on ion implantation

Over the past few decades, use of energetic ion beams, to implant electrically active atoms into semiconductors, has become an area of intensive research and is an advanced technological tool useful for fabricating highly reliable semiconductor devices on an increasingly miniaturized scale. Ohl (1952) [6] was the first person who tried to change the electrical properties of semiconductor devices by ion irradiation. He implanted silicon point contact diodes with various ions and found improvement in the reverse current-voltage curve. Cussins (1955) [7] implanted germanium with a wide variety of ions. Shockley (1957) [8] by the time, had filed a patent "Forming Semiconductor Devices by Ionic Bombardment", (Filed Oct. 28, 1954; Granted April 2, 1957). Alvager and Hanse (1962) [9] made the first nuclear detector by implanting phosphorus in highly resistive silicon, at 10 keV, followed by annealing at

°C. McCaldin and Widmer (1963) [10] prepared p-n junctions by cesium implantation. Gibbons (1968) [11] and Gibbons, Moll, and Meyer (1965) [12] implanted rare earth elements into semiconductors to produce electroluminescent layers. King *et al.* (1965) [13] and Martin, Harrison, and King (1966) [14] also made nuclear detectors and for the first time, the solar cells.

Formation of noble metal nanoclusters in transparent materials, through ion implantation, was used to colorize glasses [15-17]. Control of cluster morphology in a material allowed tailoring and tuning of optical bandgap. Colouration in uncoloured beryl has also been done using ion implantation with ion species such as V, Cr, Mn or Fe [18]. Swift-heavy-ion (SHI) implantation is of very recent interest [19]. It is a process in which ions of kinetic energy in MeV range are implanted in the target and advantage of a strongly reduced surface recession by sputtering is exploited. A method of enhanced nanoparticle formation in silica glass, under co-irradiation by laser and heavy ions, improved the optical quality of implanted substrates by decreasing the defect absorption of implanted silica glass [20,21]. Post-treatment of the metal-polymer bi-layer system by ion implantation/ion beam mixing process is expected to make the polymer harder, more conductive, and more resistive to mechanical wear and chemicals. These materials find application in surface acoustic wave (SAW) detectors, long wavelength infrared detectors, and biosensors. It is also used to fabricate carbon-based micro-electromechanical systems (MEMS) [22]. Implanted hydrogen in semiconductor interacts with defects to passivate them, thereby improving the device performance [23]. In large scale integrated circuit fabrication using GaAs, nitrogen implantation is used to form isolated GaN buried layer [24].

Carbon ions with energy of 30 keV was implanted in amorphous In_2O_3 thi films at doses of $10^{15}–10^{16}$ ions cm^{-2} and electrical resistivities of carbo implanted films decreased due to increase in carrier concentration [25]. Gree and red emissions were obtained in Ca implanted GaN samples [26]. Ion beam synthesis was applied to form carbides, silicides and nitrides for differen purposes ranging from surface property modification to formation o conducting layers for electronic devices [27-35]. Ion implantation is also ver effective for improving surface properties of polymer such as surface electrica properties, hardness and wear resistance [36-38]. Many studies were carrie out to prepare nanoparticles by ion implantation and have revealed thei luminescent [39] and non-linear optical properties [40-43]. Optical propert changes in silica glass induced by Cu and O multiple – energy implantatio with successive annealing were studied, and formation of copper or coppe oxide nanoparticles was revealed. Formation of Cu nanoparticles wa enhanced by the multi – energy ion implantation.

Impurity doping has also been widely performed by ion implantation in order to create photocatalysis for operating under visible light irradiation [44, 45]. Here, oxygen vacancies in the photocatalyst act as recombination centre of electron hole pairs and as electron trap [46]. Modification of TiO_2 coatings for photoinduced hydrophilicity under weak UV illumination was also recently studied by Ar ion beam irradiation [47].

2.3 Ion implantation effects in materials

Ions, when accelerated through a large potential difference and allowed to strike a solid surface, get embedded in the solid, there by changing its

chemical composition. By displacing atoms from their normal positions, the energetic ion can alter structure and physical properties of the solid also. This results in alteration of chemical composition, which can lead to modification of its electrical conductivity in the case of a semiconductor. At high ion concentration, presence of electrical defects such as interstitial impurities, dislocations, grain boundaries, and inhomogeneities are predominant that can lead to strong degradation of electrical features of the materials. It is this degradation that must be dealt with, during ion implantation for device fabrication.

During stopping of an ion, the primary defect structure is mainly created by recoiling lattice atoms, which quickly lose their energies through binary collisions with neighbouring atoms. This leads to a number of collision cascades along the ion track with relatively high defect densities. The resulting primary defect profile can be computed rather reliably by Monte Carlo method. However, final damage profile might be quite different due to dynamical processes taking place in subsequent thermal spike phase, which lasts much longer than the primary collisional phase. During this second phase, non-thermal processes within cascade volume can lead to rearrangements, which can result in formation of dislocations, point defect clusters and amorphized regions. In addition, sharp density fluctuations at the periphery of cascade volume are expected to accompany the thermal spike phase [48], which might create additional defect structures in surrounding lattice. At higher ion fluences, further complications are introduced by radiation induced annealing effects. Relative importance of these mechanisms depends strongly on forces that bind the atoms in their lattice positions. Total amorphization is normally found after high dose irradiation of covalent materials. However,

such total destruction of the crystal structure is not found in metals, where displaced atoms rearrange themselves into extended defects, preserving much of the original lattice structure. In an ionic crystal, as in metal lattice, structure is not totally destroyed by high dose ion implantation, as most of the damage is accommodated in dislocations. But, defect structure does not consist of a pure dislocation network. Channelling results also indicate the existence of highly disturbed regions. In general, it is found that most of the radiation damage is removed after annealing at temperatures of the order of 1000 °C. After annealing, metallic precipitates are observed for gold [49,50], silver [51], platinum [52], indium [53] and sodium implantations [54], while in the case of iron, a large fraction of implanted atoms move into substitutional lattice positions. Experimental results of this study indicate a mixed defect structure, consisting of severely disordered areas in coexistence with regions where original lattice structure, although distorted by extended defects, is still maintained. Such a mixed structure was confirmed by annealing studies, which showed that one type of defect could be removed by heating at temperatures between 600 and 800 °C while remaining defects could only be removed at much higher temperatures [55]. The major problem with ion implantation is elimination of the damage created during slowing down of projectiles in the target. Violent collision of the ions with the target atoms displace them from their equilibrium lattice sites. In case of a silicon atom to be displaced, the minimum energy, that should be transferred to, is about 15 eV. If the knocking atom has enough energy, it can create other displacements, giving rise to a collision cascade process. The primary damage after implantation is a complex function of parameters such as, ion mass, energy, dose rate, target temperature, substrate orientation, and dopants / impurities present in the substrate. The

atoms transfer rapidly their high vibrational excitations to those in the surrounding material, and in just few picoseconds, the system cools. The material is then subjected to a rapid thermal quenching of the order of 10^{14} – 10^{15} K/s [56]. A different phase can result and a small volume of "hot" atoms may become a small amorphous region, surrounded by a crystalline matrix.

2.3.1 Wafer heating during ion irradiation

Energy of beam that strikes the target is dissipated into heat. Chemical reactions can occur as temperature of the target increases. Disorder created by the implant depends crucially on substrate temperature. It can be from amorphous zones to a highly defective crystal. If temperature rises during implantation, formation of amorphous structure might be prevented at high dose, due to dynamical annealing.

The heat flow equation can be written as,

$$LC_p\rho\frac{dT_w}{dt} = \frac{P_B(t)}{A_s} - h(T_w - T_{wH}) - 2\sigma \in_w (T_w^4 - T_s^4), \dots\dots\dots(2.1)$$

Where,

L – Layer thickness,

C_p – Specific heat,

ρ – Density,

P_B – Beam power,

A_s – Area scanned by the beam,

h – Cooling coefficient,

$\in_w$ – Wafer emissivity,

T_w – Wafer temperature,

T_{wH} – Temperature of wafer holder,

T_s – Temperature of surrounding ambient,

σ – Stefan – Boltzmann constant (5.67 x 10^{-8} $Wm^{-2}K^{-4}$),

The Second term on the RHS in equation (2.1) is for the front and bac surface of the wafer. Wafer temperature is measured by infra radiometry or t temperature stickers.

Thermal process is necessary to activate the dopant electrically and (eliminate damage. Residual damage in the form of extended defects lik dislocation line, dislocation loops and stacking fault, may still be there i annealed wafers. After annealing, these secondary defects, if present i particular regions of the device, can be detrimental. The device yield can b impaired and main trend in this field is to understand methods to reduc density of defects and to increase the yield.

According to Murphy's Law, the yield (Y) of good devices on a wafe depends on product of average defect density (D_o) and area (A) of the chip a per the relation [57]:

$$Y = [(1-e^{-ADo})/D_oA]^2, \dots\dots\dots\dots\dots\dots\dots\dots\dots\dots\dots\dots\dots\dots\dots(2.2)$$

For example, in the case of a 16 Mbit DRAM, defect densities les than 0.5 defect/cm^2 have to be achieved. Strategies and remedies for the reduction of defect densities, especially in the ion implantation related

processes are the prominent task in mass production of VLSI and ULSI devices.

As any other equipment, implanters also generate particulates that are deposited on wafer surface and this reduces drastically the yield of devices. These particles shield the covered portion of device from implant. Implantation depths are usually in 0.05-1μm range and linewidth is also in 0.5 – 1.0 μm range. These defects are called "killer", because they impair the device. With the shrinkage of devices the density of defect must also be reduced considerably to maintain a reasonable yield. For yield levels above 50%, in case of a 4Mbit DRAM, defect densities less than 1. defect/cm^2 should be achieved at end of several hundred process steps [58].

2.4 Theory

Knowledge of fundamentals of interaction of an energetic ion with a semiconductor and way in which this interaction can be used in device fabrication is becoming increasingly necessary for a material engineer. Applications of ion implantation in other fields are rapidly diversifying.

Process of ion implantation relies on possibility of injecting energetic ions deeply into a solid. In achieving this deep penetration, ions will have to collide, individually or collectively, with atoms of the solid. During these collisions, energy will be exchanged between moving ion and initially stationary lattice atoms, resulting in considerable energy loss by the ions and energy gain by the atoms. The energy loss causes slow down of the ions and eventually to rest in the lattice. Energy gain results in creation of defects or disorder in the lattice. In addition to energy loss, injected ion will suffer

deflections at each separate or multiple collision and sequence of these deflections will determine its detailed trajectory in the solid. Similarly, the trajectories of lattice atoms, that gain sufficient energy to be displaced from their normal position, will be dictated by their energy transfer and deflection sequences. Thus overall pattern of lattice disorder will depend upon individual collision events. Since the ion and atom collision events occur sequentially and are separable, the central problem in predicting ion penetration and lattice disorder, therefore, totally depends on understanding of the dynamics of collision between a moving ion and an initially stationary atom. Fig. 2.1 shows the path traveled by the incident ion before it comes to rest.
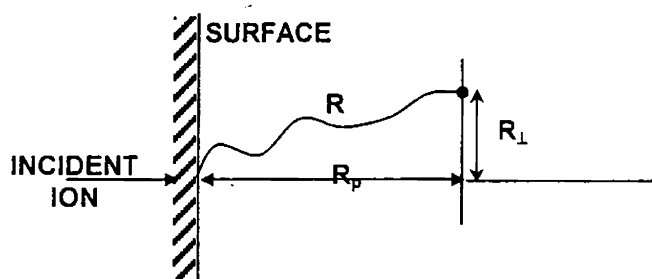
Fig. 2.1 Schematic representation of the path traveled by the incident ion before it comes to rest.

Stopping power or specific energy loss ($-dE/dx$) is an important factor for the determination of range of embedded ion in the target. Here E is the ion energy and x is the distance inside the target and is usually measured along the direction of incidence of ions.

Distribution of implanted ions depends on several parameters such as ion mass energy, target mass and beam direction. Number of collisions

experienced by an ion per unit path length and the energy lost per collision are random variables, as all the ions having the same incident energy do not stop at the same location. There is, instead, a distribution, in space, of stopping points, that is described by a range distribution function. The perpendicular distance from the straight line path or the lateral spreading is characterized by a zero mean value and by a non-zero straggle, $\Delta R_{\perp}$. The transverse spreading is caused by multiple collisions of ions and it increases with depth into the target, being a function of ratio of target and ion masses respectively. Thus, range calculations require knowledge of rate of energy loss or stopping cross section of incident projectiles.

$$S = -\frac{1}{N}\left(\frac{dE}{dx}\right),\dots\dots\dots\dots\dots\dots\dots\dots\dots\dots\dots\dots\dots\dots\dots\dots\dots\dots(2.3)$$

Where,

E – Energy dissipated and

x – Distance into the target,

N – atomic density of target (eV/cm^2)

In classical scattering theory, interaction of the moving ions with target atoms, is described, assuming two separate processes. One is collision with nuclei, which is due to the coulombic repulsion between the ion and the target nuclei and the second, collision with the electrons. Electronic energy loss is an inelastic process, in which the incident ion moves through the cloud of electrons of a target atom. The electrons can be excited to higher discrete energy levels, or can be excited in the collective motion of plasmons. The prevalence of one contribution over the other depends on the ion velocity (v)

with respect to that of target electrons, stopping cross section or rate of ener

loss,

Thus, the stopping cross section or rate of energy loss can be then sp

into nuclear and electronic stopping,

$$S = S_n + S_e, \dotfill (2.$$

Where,

S_n – Nuclear stopping term,

S_e – Electronic stopping term,

$$S_n + S_e = -\frac{1}{N}\left(\frac{dE}{dx}\right)_n - \frac{1}{N}\left(\frac{dE}{dx}\right)_e, \dotfill (2.$$

In a binary collision, if elastic collision occurs with a target ato

initially at rest, (as shown in Fig. 2.2), then conservation of energy ar

momentum yields a transferred energy,

$$T = \frac{4M_1 M_2 E_i}{\left(M_1 + M_2\right)^2}\sin^2\frac{\theta_c}{2}, \dotfill (2.6$$

Where,

E_i – initial energy,

θ_c – Scattering angle in the center of mass.

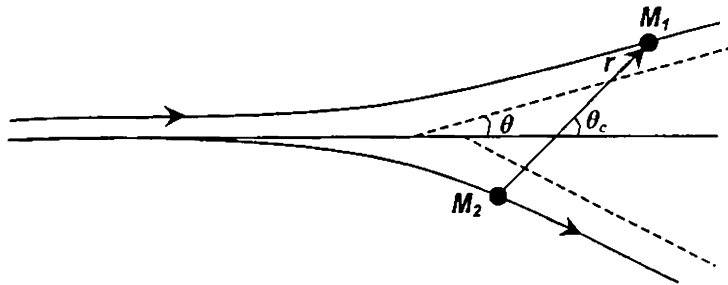M_1 – Mass of ion, M_2 – Mass of target,

Fig.2.2 Schematic of the collision between a projectile of mass M_1 and a target atom of mass M_2.

Maximum energy transfer is obtained in a head on collision, when $\theta_c = 180°$.

The scattering angle θ_c related to the interatomic potential $V(r)$ is,

$$\theta_c = \pi - 2p \int_{R_{min}}^{\infty} \frac{dr/r^2}{\sqrt{1 - V(r)/E_r - p^2/r^2}}, \dots\dots\dots\dots\dots\dots\dots\dots(2.7)$$

Where

p – impact parameter,

R_{min} – minimum distance of approach,

r – Interatomic distance,

E_r – energy in the center of mass system, and

$E_r = M_2 E_i/(M_1 + M_2),$

Probability for scattering in a direction θ_c is given by the differential cross section.

$$d\sigma(\theta_c) = 2\pi p dp, \dots\dots\dots\dots\dots\dots\dots\dots\dots\dots\dots\dots\dots\dots\dots(2.8)$$

$$= -2\pi p \left[\frac{dp}{d\theta_c}\right] d\theta_c, \dots\dots\dots\dots\dots\dots\dots\dots\dots\dots\dots(2.9)$$

$$= -\frac{p}{\sin\theta_c}\left[\frac{dp}{d\theta_c}\right] d\Omega, \dots\dots\dots\dots\dots\dots\dots\dots\dots\dots(3.0)$$

Where

$d\Omega$ – Solid angle,

$= 2\pi \sin\theta_c \, d\theta_c$ and $dp/d\theta_c < 0$.

In low velocity region, electronic energy loss is proportional to ion velocity. Interaction arises from scattering of electrons that are no longer attached to any specific atom but form a gas in which positive charges are embedded. Electronic stopping power is proportional to ion velocity and reaches a maximum when ion velocity is comparable to the average velocity of outer electrons, so that the interaction time is highest possible and maximum transfer of energy occurs between projectile and the target electrons.

The stopping cross section varies non – monotonically with target atomic number. At higher velocities, excitations and ionization of core electrons dominate and collective excitations of the electron gas take place. Electronic stopping power is inversely proportional to the square of the velocity.

$$\frac{dE}{dx} = \frac{Z_1^2 e^4 N}{mv^2 4\pi\varepsilon_0} B, \dots\dots\dots\dots\dots\dots\dots\dots\dots\dots\dots\dots\dots\dots\dots\dots(3.1)$$

Where,

Z_I – Atomic number of the ion,

m – Electronic mass,

B – Measure of the penetration of incident ion through electron shell.

The Ziegler Biersack Littmark (ZBL) [59] treatments adopted in the popular Transport of Ion in Matter (TRIM) [60] program is based on stopping power of protons. Every change of the projectile charge state generally reduces the projectile's kinetic energy. As a matter of fact, the stopping cross sections are predicted not better by 10% and errors even exceed 30%.

R_p and ΔR_p are the projected range and the standard deviation of the projected range (or straggle) along the normal to the sample surface. A Boltzmann transport equation is set up to solve the statistical problem of final ion distribution. Transport equations can be solved to determine the moments of this distribution and the shape of the curve (giving concentration versus depth) is determined. In comparison with experiments, the projected ranges calculated according to Lindhard Scharff Schiott (LSS) treatment deviate by a factor two at the lowest energies, while the agreement is good to ~10%, at the higher energies. For the implanted dose N_0 the implanted profile is given by,

$$C(x) = \frac{N_0}{\sqrt{2\pi}\Delta R_p} \exp\left[\frac{-(x - R_p)^2}{2(\Delta R_p)^2}\right], \quad\text{...(3.2)}$$

where, x – is the distance from the target surface, measured along the axis of the incident beam.

R_p – average penetration depth

ΔR_p – standard deviation.

Shape of the distribution is characterized by the parameters skewness and Kurtosis. Skewness (γ) is a measure of distribution that is tilt away from symmetry about the mode of first moment. Kurtosis (β) is measure of pointed or flat tapering of the distribution. These two quantities a dimensionless. The depth resolution is few hundred Å. Light ions, in the encounters with target atoms, will experience a relatively large amount backward scattering and hence distribution will be mostly filled on the surfa side. Heavy ions, on the other hand, will experience a large amount of forwa scattering and their distribution is mostly filled on the deep side of the profile

Channelling is a simple steering effect, resulting from Coulomb repulsion between positive charged projectiles and target atoms along the ro or planes. Fig. 2.3 shows the channelling process, for ion beam incident at angle, on the target. If ion beam direction is at small angles with the targ atoms, the ions suffer a series of gentle collisions and if it is almost parallel a plane in a crystal, the projectile ions suffer a minimum path deviation. Clo encounters with the target atoms are strongly prevented so that all process that require small impact parameters are greatly reduced. As a consequence, channelled ion does not displace target atoms and experiences a reduc energy loss not by elastic nuclear encounters but by electronic interaction multiple scattering by various defects and by vibrating lattice atoms until the are dechannelled. Particles there after see crystal as a random medium. It w discovered accidentally by Monte Carlo simulations of the range of heavy io implanted in solids [61] and by profile measurements of keV heavy ions polycrystalline metal targets [62].
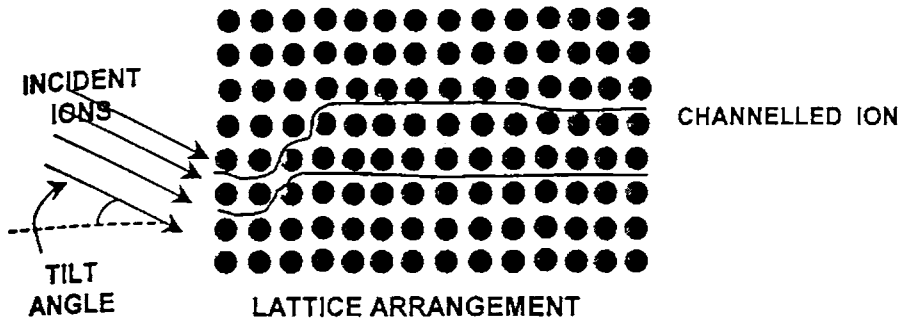
Fig. 2.3 Schematic representation of channelling process

2.5 Theoretical Simulation

Monte Carlo (MC) and Boltzmann Transport Equation (BTE) methods are widely used to simulate ion implantation in solids. In BTE approach [63], scattering processes of ions in the target are described by changes in statistical momentum distribution. Calculation of range and damage distribution are regarded as transport problem describing motion of the ions during their slowing down process to zero energies. Monte Carlo methods are based on the simulation of individual particles trajectory through their successive collisions with target atoms. This applies two main approaches for a detailed calculation. First "Binary Collision Approximation" (BCA) and second "Molecular Dynamics" (MD) [64]. MD approach studies movement of atoms in solid as a function of time and takes into account, the interaction with all neighbouring atoms. All moving atoms are followed in small steps of time so that their collisions are automatically included. For these reasons, MD based programs are used to describe sputtering, low energy processes and in cases where multicollisions must be considered. In BCA program, movement of ions in

solid is described by a series of successive binary collisions. It breaks down at low energies, when many body effects become important.

Final result is based on summation of nuclear and electronic scattering events occurring in a large number N(N>1000) of simulated ion trajectories. By following N histories, distributions for range parameters of primary and recoiled ions, and associated damage can be obtained. Each history begins with a given energy, position and direction of incident ion. The ion is assumed to change trajectory at each elastic collision with target atom and to move in straight free path between elastic collisions. The ion loses energy continuously between elastic collisions by inelastic scattering with electrons.

The most popular program to describe slowing down of an ion into an amorphous target is TRIM (Transport of Ions in Matter) code [65]. It uses liquid model to describe target structure. Entire trajectory of a single ion into an amorphous target, range and depth distribution of incident ions can be obtained. Collision cascades determined by recoiled target atoms can also be obtained. First version of TRIM allowed only calculation of the incident ion trajectory. TRIM.SP (TRIM SPuttering) [66] is an extension of the earlier TRIM, and is a three dimensional program considering projectiles and recoils. In non-crystalline or amorphous materials, energetic implanted ions have Gaussian distribution. But in case of single crystal, ions entering in certain directions often do not make random sequence of collisions but rather get steered by a succession of correlated interactions with atoms. Simulation of ion trajectory in crystalline targets requires knowledge of the atom locations. These positions can be constructed by three translation vectors starting from a basis of one or more atoms according to elementary crystal structure. Another

version of TRIM code (CTRIM) has been developed to consider crystal structure [67].

Stanford University Process Engineering Modeling Program (SUPREM) [68] is a program that can describe all processes used in microelectronic industry for fabrication of devices.

Fig. 2.4 (a) shows TRIM calculated path traveled by 100 keV Ar ions in CdS and Fig. 2.4 (b) shows the TRIM calculated path traveled by 100 keV He ions in CdS. For light atoms, mean free path between successive elastic collisions is larger than interatomic distance, and thus the collision cascade will result in a dilute distribution of defects. Heavy ions at low energy can have a mean free path comparable with interatomic distance and a dense cascade will be generated.
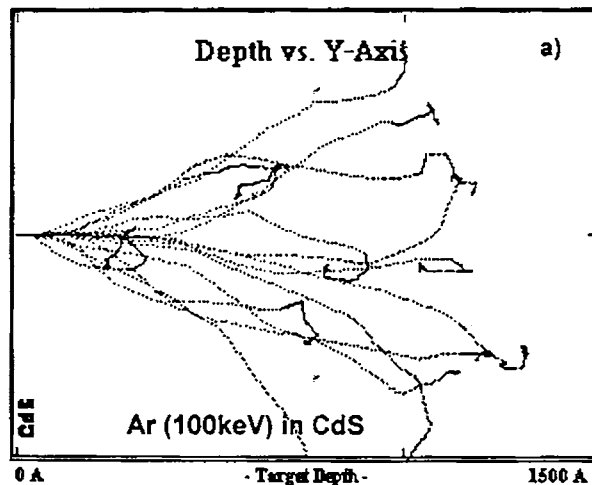

Fig. 2.4 (a) TRIM calculated projectile path traced for 100 keV Ar ion in CdS.
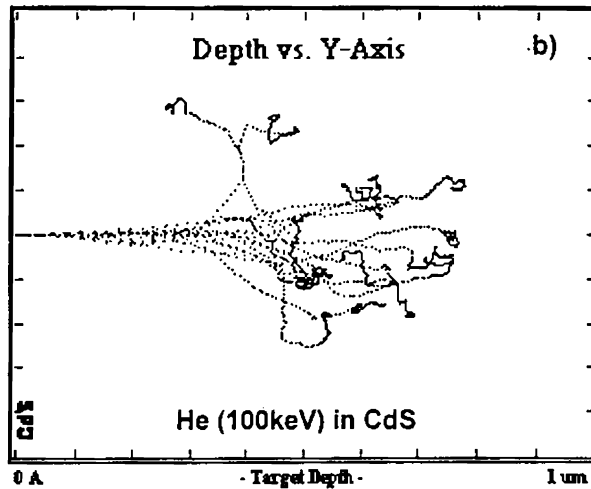
Fig. 2.4 (b) TRIM calculated projectile path traced for
100 keV He ion in CdS.

A typical cross section of an implanted sample, if analyzed by TEl
reveals a variety of extended defects; amorphous zone, stacking faul
dislocation loops, twins, clusters etc. The visibility is limited to defects
dimensions above 1-2 nm.

2.6 Annealing effect

Atoms displaced during implantation, may at a later stage, return
their usual positions. This process may occur over a short time scale. Duri
this period, collision cascades could be moving through lattice or over mu
longer periods following completion of implantation, called "self annealing".

Ion implantation, therefore, must be followed by one or mc
annealing processes for semiconductor to recover its crystallinity and l

doped impurity to become active. In general, thermal annealing in a conventional furnace is currently used to activate doping such that thermal diffusion takes place, leading to a large redistribution of impurity atoms. This redistribution then causes enlargement of the junctions, which may be prohibitive for the optimal operation of the device. Moreover, these implantation-induced defects strongly modify recombination properties of semiconductor that may affect the operation of devices and p-n junctions.

Rapid Thermal Annealing (RTA) methods have been introduced to minimize redistribution of impurities. This procedure uses light or electron beams to reduce annealing duration, while maintaining a sufficiently high temperature, to activate the doping species. Most commonly used technique is so called lamp RTA process in which thermal heating of sample is ensured by heat dissipation of halogen lamps surrounding the wafers. These lamp RTA machines provide very fast heating pulses (~1-10sec) that allow temperature to range from 1000 to 1100 °C without significant thermal diffusion.

2.7 Accelerators

Conventional accelerators could not be operated at voltages higher than 8 MV and this is a fundamental drawback since half the possible targets in Periodic Table are beyond practical limits set to scattering experiments by coulomb barrier effects at that energy.

Charged particles are accelerated whenever subjected to action of an electric field. After traversing a potential difference of V volts, a particle with charge Z times that of electron will have a kinetic energy of ZV electron volts, and is then implanted into target. A series of cavities that are polarized by a

radio frequency voltage in linear accelerators, act as a resonance device in which electric component of time varying RF electromagnetic field acts on charged particles to produce acceleration. Frequencies of ~ 5 MHz are used to drive electrodes. One such 150 keV low energy ion accelerator (Sames J - 15) installed at Indira Gandhi Centre for Atomic research (IGCAR), Kalpakkam, was used for our present studies. Fig. 2.5 shows the schematic layout of the ion implanter setup, while Fig. 2.6 is the photograph of the accelerator. Fig. 2.7 is the photograph of the target chamber showing the Cu block over which the sample was mounted before implantation.
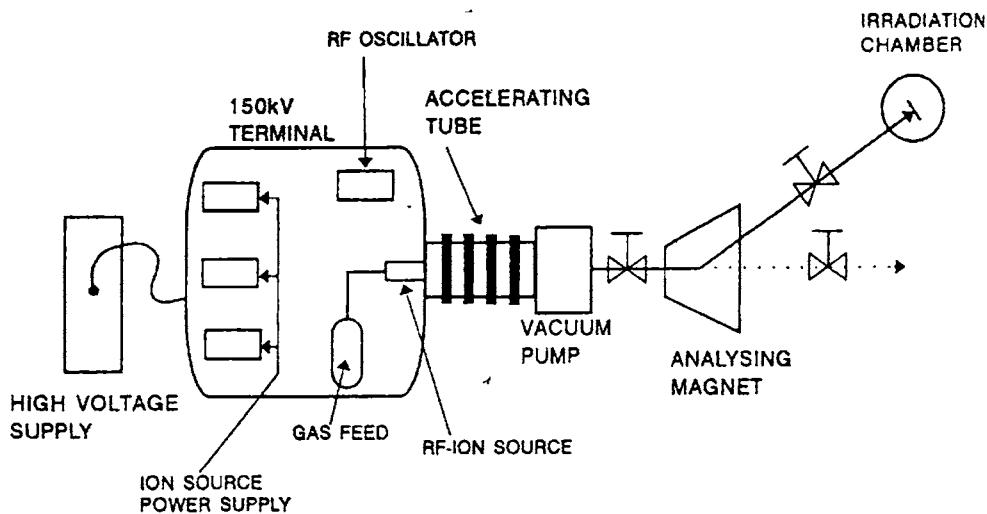
Fig. 2.5 Layout of 150 keV low energy accelerator.

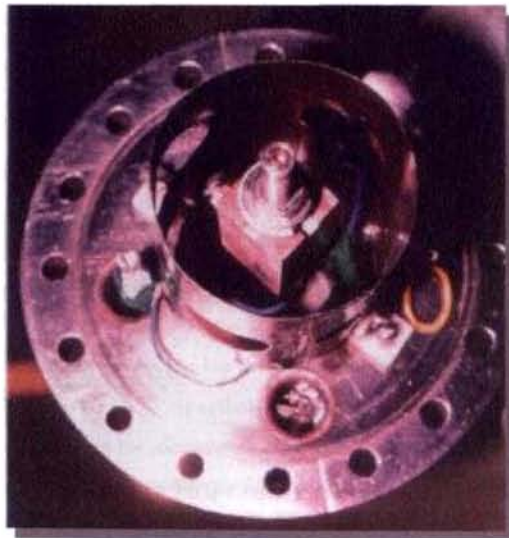Fig. 2.6 Photograph of the 150 keV accelerator installed at IGCAR. Kalpakkam - INDIA.

Fig. 2.7 Photograph of the target chamber encasing the copper block on which the sample was mounted.

Van de Graaff accelerator is another class of accelerator machine, that can deliver very high voltage by mechanically driving charges into a conductor and to target. Spark is the most serious source of trouble in Van de Graaff generators. This would readily exhaust the charge available. Stable operation can only be achieved below the limit set by sparks. Sparking field in dry air, at atmospheric pressure, is 3×10^6 V/m. Dry nitrogen at 16 atmospheres can withstand voltage gradients as high as 200 kV/cm without electric breakdown. Then dimension of Van de Graaff generator would increase (roughly) linearly with the ultimate voltage desired. Unlike Van de Graaff generator, Cockcroft – Walton or Cascade Generator (1932) works based on movement of electric charges through an array of condensers. Their limitations are only the maximum voltage which the rectifier, condensers and transformer can stand. Present day selenium rectifiers set a practical limit at 100 kV. Ripple voltage is of course an extremely undesirable feature. By early 1959 the first 12 MeV tandem accelerator was put in operation at Chalk River Laboratories of Atomic Energy of Canada Ltd.

In conventional, single stage accelerator, positive ions are produced inside high voltage terminal and subsequently accelerated to ground potential. But for high-energy operation there are two stages. First, negative ions are produced at ground potential and pre-accelerated to ~20-100 keV after which these are separated by a magnet and injected into acceleration tubes inside the tank. Negatively charged ions are then accelerated towards the central terminal, where they are stripped of some of the electrons in a striping canal, filled by a gas. Then they are accelerated again towards other end, at ground potential, thereby suffering an additional acceleration. The same voltage is used twice. The total final energy will be,

$$E = qV_o + qV_T \, (1+n), \dots\dots\dots\dots\dots\dots\dots\dots\dots\dots\dots\dots\dots(3.3)$$

Where,

V_o – Pre-acceleration potential,

V_T – terminal voltage,

n – charge state of ions produced in stripper.

Charge states from +1 to +3 are easily produced in the stripper so that energies from 300 keV to 6.9 MeV can be obtained with considerable current ~20 – 100 µA.

Two kinds of tandem systems exist; Pelletrons and Tandetrons. In pelletrons the high voltage is obtained through the charging of several moving chains while in tandetrons acceleration is produced by a solid state Walton – Cockroft system. The tank is filled by the insulating gas SF_6 to a pressure of ~ 8 bar. In the present work we used Pelletron accelerator at Institue of Physics, Bhubaneswar (IOPB) for some of our studies, and photograph of the accelerator system, is shown in Fig. 2.8.

Fig. 2.8 Photograph of a 3 MV Pelletron accelerator system.

2.8 Accessories

The implanters are classified according to the beam intensity:

1. Low current ~0.1 mA.

2. Medium current ~1.0 mA.

3. High current ~10 mA.

4. Very high current ~100 mA.

An ion implanter consists of the following major components:

An ion source contains the species to be implanted either as solid or a liquid or as gas and an ionizing system to ionize species. Lifetime of an ion source varies between several tens of hours to a few hundred of hours, and it is dependent on operation conditions.

In an extracting and ion analyzing mechanism, the ions are extracted from source by a small accelerating voltage and then injected into the analyze magnet. The extraction voltage ranges usually between 15 and 40 kV.

In an accelerating column, selected ions are injected into the accelerating column. Others are stopped by presence of suitable screens. In the absence of external forces, beam cross section would tend to increase Accelerating system should therefore provide an external force, so as to constrict the beam along the axis known as "focussing". The selected ions are accelerated by a static electric field that focuses and shapes the ion beam which are then in column, ready to be implanted with an energy up to 80-40 keV. In case of high energy accelerators final energy is given by $(1+n)qV$. Where,

n – charge state of stripped positive ions,

V – terminal voltage,

q – charge.

Magnetic mass analyzers are used to separate desired ionic species from all the other charged species which are contaminants from residual air, hydrocarbons from vacuum pumps and impurities from solid components of the source. Vacuum is usually maintained by three pumping systems, one for ion sources, another for scanner system and the third one for wafer chamber. In a scanning system, ions are distributed uniformly over a target by electrical fields varying in x and y directions in a saw-tooth fashion or by a mechanical shift of target.

Current measurements of dose is done usually by placing a current integrator between target and ground by counting the total collected current from incident ions. Thus the dose is given by;

$$Dose = \frac{Q_{tot}}{q_{ion}} = \frac{1}{q_{ion}} \int_0^T I_B dt, \dots\dots\dots\dots\dots\dots\dots\dots\dots\dots\dots(3.4)$$

Where,

I_B – beam current measured for time T(seconds)

Electrical current can be easily measured to an accuracy of a tenth of a percent or less and can be measured over a very large dynamical range, from nAmp to Amp. When ion beam impinges upon the target, secondary electrons, sputtered and ionized atoms, photons, and absorbed gas molecules are emitted. The yield of secondary electrons ranges between 2 and 20 per incident ion.

2.9 Application

Ion beams have also been used to stimulate events occurring within reactor materials and many years of equivalent reactor operation can be closely simulated by perhaps only a few hours of ion implantation. Other applications of ion implantation are production of low friction and wear resistant metal surfaces, conversion of surface layers to oxide and nitrides, introducing catalysts into surface layers and many more. The technique is primarily used in semiconductor technology, though it also finds applications in several other areas like surface modification for improvement of hardness, wear and corrosion resistance etc. Optical properties of surface layers of many materials can be altered by implantation. By changing refractive index, it is possible to produce waveguides for optical integrated circuits. Magnetic bubbles in thin magnetic garnet films are currently under investigation because of their great potential as memory storage systems. It has been found that ion implantation can modify properties of such films and bubbles they contain.

2.10 Characterisation of implanted samples

Implantations are usually performed on structured wafers with insulating layers such as oxide, nitride and photoresists. Building up of charges transported by the beam at these layers can be detrimental because of damage and of electrical break down. Wafer charging can also affect beam propagation and may cause even a blow up with a deterioration of uniformity.

Influence of wafer charge on the device yield is more pronounced for thin oxide layer (~10 nm) as adopted in VLSI and ULSI. The structure to determine the effect of charge is usually a MOS capacitor. After implantation

two different tests are performed. One is Breakdown Voltage (BV) and the other is J-T testing. In BV, voltage across the capacitor is increased in time, until current through the device exceeds a fixed value. Failure point is usually 1μA. Voltage at which current reaches this value is the breakdown voltage. In good Silicon oxide it is of the order of 10 MV/cm. In J-T, the current through capacitor increases with time and failure is indicated by a sudden drop in voltage. This technique measures the charge, as the time integral of the current density to breakdown.

Four point contacts measurements could also be done on thin implanted layer, whose conductivity is opposite to that of substrate. Current (I) is carried through outer two contacts and voltage drop (V) is measured across the internal probes. Sheet resistance is given by,

$$R_s = K \frac{V}{I}, \dots\dots\dots\dots\dots\dots\dots\dots\dots\dots\dots\dots\dots\dots\dots\dots\dots\dots\dots\dots(3.5)$$

Where,

K – Constant that depends on configuration, position and orientation of the probes.

Value of R_s ranges usually between 10^3 Ω/□ to 10 Ω/□. Low dose regime from 2×10^{11} ions/cm^2 to 5×10^{12} ions /cm^2 requires a high resistivity substrate.

Large scale application of ion implantation process is based on accurate control of dopant over the wafer. Uniformity of implant over the wafer and reproducibility of dose from wafer to wafer and from batch to batch are the main issues in an industrial environment, being directly related to device yield and reliability.

2.11 Analytical techniques

2.11.1 Thermal wave technique

Thermal Wave apparatus is a method based on optical thermal response of layer damaged by the implant [69,70]. The technique is contact less, nondestructive and does not require thermal treatment. It can map samples implanted over dose range 10^{10} ions/cm^2 to 10^{16} ions/cm^2 [71]. Fig. 2.9 shows the schematic representation of the thermal wave method used for quality checking of ion implanted wafers. In the commercial thermal wave system, change in the reflectance is monitored [72] by Ar$^+$ laser, which is modulated at a frequency of 1-10 MHz and response is detected in phase. Absorbed energy produces periodic waves of photo-induced heat (thermal wave) and of plasma wave (electron-hole pairs) too [73]. The thermal and plasma waves propagate several micrometers (~3μm in Si) beneath the surface and interact with defects or damage. Because the diffusion of thermal and plasma waves is modified by defects, point to point surface temperature and surface plasma density vary according to the defect sites, and corresponding variation of probe laser reflectance is used as a mechanism for imaging the in-depth defects. The spatial resolution depends on the probe spot and is of the order of ~0.8 μm.
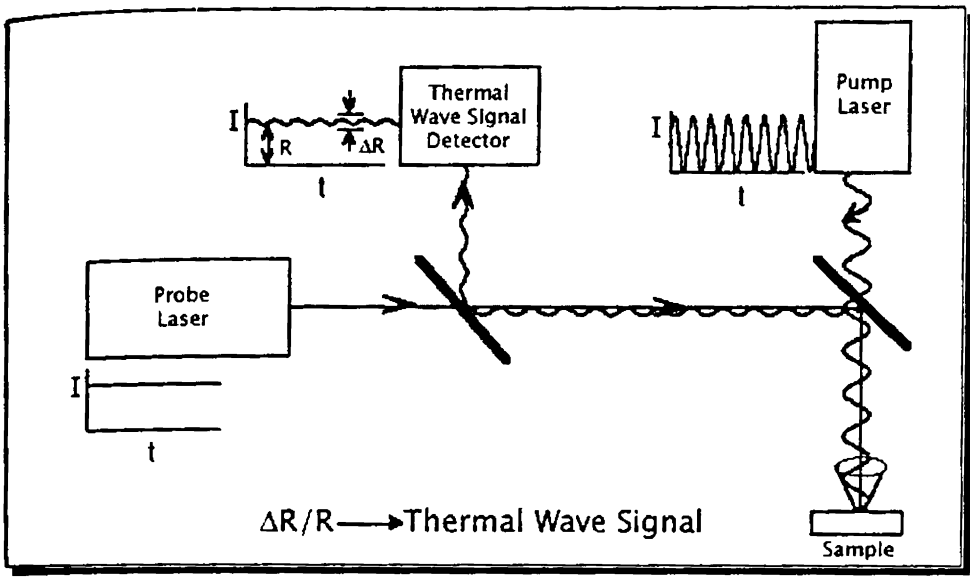
Fig. 2.9 Layout of thermal wave technique
used for analysis of ion implanted wafers.

2.11.2 X-ray analysis

Any analysis by X-ray diffraction of ion-implanted layers is based on modifications of the lattice parameters of initially perfect single crystalline substrate. Fig. 2.10 is the layout of X-ray detection.
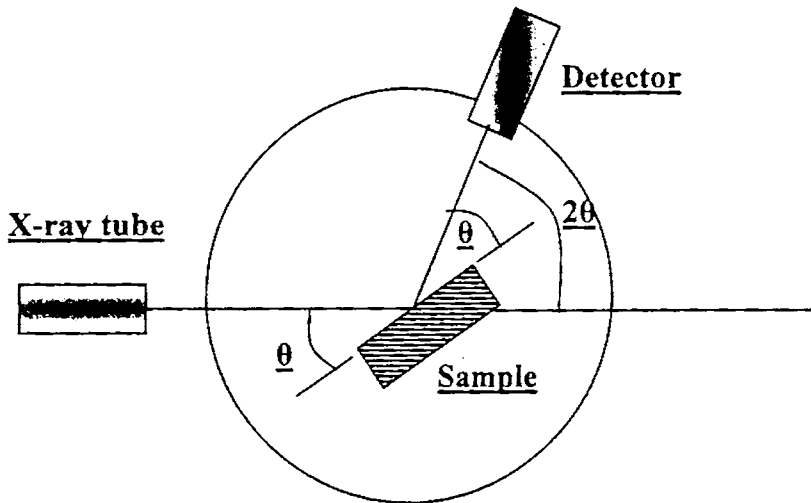
Fig.2.10 Layout of the X-ray detection.

Due to ion implantation there will be relative change of netplane distance $(\Delta d/d)$. The well known Bragg equation that describe diffraction process can be written as,

$$2d\ sin\Theta_B = n\lambda, \dots\dots\dots\dots\dots\dots\dots\dots\dots\dots\dots\dots\dots\dots\dots\dots\dots\dots (3.6)$$

where,

        d – distance of the diffraction netplanes,

        Θ_B – Bragg angle,

        n – Order of diffraction (n = 1,2,3,....)

        λ – wavelength of X ray used.

Perfection of a lattice can be described by the statistical random displacement of atoms from their position. Every defect distorts the lattice over

a certain finite region, and accumulation of defects increases mean square displacement of atoms.

Statistical distribution of the displacement of any atom according to a spherically symmetrical Gaussian form is given by,

$$W = (8\pi^2 / \lambda^2)\sin^2\Theta_B \times U^2, \dots\dots\dots\dots\dots\dots\dots\dots\dots\dots\dots(3.7)$$

where,

W – Static Debye-Waller factor,

U – Depends on the random displacement standard deviation.

Perfection P of a crystal lattice is described by exp(-W). It goes to zero in the case of amorphization.

2.11.2a Determination of grain size

Grain size of film can be a calculated using the Debye-Scherrer formula,

$$D = \frac{0.9\lambda}{\beta Cos\theta}, \dots\dots\dots\dots\dots\dots\dots\dots\dots\dots\dots\dots\dots\dots(3.8)$$

Where,

D – the diameter of the crystallites,

λ – the wavelength of CuKα line (1.5145 Å),

β – the FWHM of the XRD peak in radians and

θ – the Bragg angle.

2.11.2b Determination of lattice strain

Williamson-Hall [74] approach allows us to separate two differen causes for a line broadening. It is usually assumed [75] that the broadening β of a Bragg reflection (*hkl*) originating from the finite grain size of ι polycrystalline material follows the Sherrer equation.

$$\beta_\tau = \frac{\lambda}{\tau \cos \Theta_{hkl}}, \dots\dots\dots\dots\dots\dots\dots\dots\dots\dots\dots\dots\dots\dots\dots\dots\dots\dots(3.9)$$

Where

λ – The X-ray wavelength,

Θ_{hkl} – Bragg angle,

τ – Mean 'effective' size of the coherent scattering region normal to the reflecting planes.

Additional stress-induced in the lattice could also contribute to broadening β_ι of the line, which is given by the Wilson formula:

$$\beta_\varepsilon = 4\varepsilon \tan \Theta_{hkl}, \dots\dots\dots\dots\dots\dots\dots\dots\dots\dots\dots\dots\dots\dots\dots\dots(3.10)$$

Here,

ε – strain, which is a dimensionless value.

It is assumed to be proportional to the square root of density of dislocations.

Thus, for total reflection width β_{hkl},

$$\beta_{hkl} = \beta_\tau + \beta_\varepsilon$$

$$= \frac{\lambda}{\tau \cos \Theta_{hkl}} + 4\varepsilon \tan \Theta_{hkl}, \dots\dots\dots\dots\dots\dots\dots\dots\dots\dots\dots\dots(3.11)$$

From the plot of measured value $\beta_{hkl} \cos\Theta_{hkl}$ as a function of $4\sin\Theta_{hkl}$, one could estimate the strain (ε) as the slope of the straight line and τ from its intersection with the vertical axis.

2.12 Conclusion

Eventhough, implantation of impurity atoms for doping semiconductor wafers offers many advantages such as rapidity, mass separation for purity requirements, accuracy and a wide range of doses, flexibility of profile depth and control over the amount of ions in a specific region, the amount of damage caused due to energetic ions influence the chemical, electrical and optical properties of the material. The consequence of ion bombardment is the amorphization of the semiconductor surface. At high ion concentrations, the presence of electrical defects such as interstitial impurities, dislocations, grain boundaries, and inhomogeneties are dominant. This implantation-induced disorder, leads to strong degradation of the electrical features of the materials and also strongly modify the recombination properties of the semiconductor that may affect its operation. As the size of electronic device decreases to submicron levels, it becomes an important issue to understand the effects of ion implantation.

Accelerators exists for various ranges so as to provide the user with the required acceleration of ions. Eventhough, high energy-accelerators of energy more than GeV (10^9 eV) is not presently very popular, a meaningful energy range for materials science is from 1 keV to 10 MeV. However, there are few machines in the world that are capable of creating high-current heavy ions in the continuous mode. For materials engineering, not only the high energy but

also the high current density is an important factor. The high number densi

provides a technological merit, so that atoms can be efficiently implanted in

a solid for a short period. Also, the higher energy ions, of MeV range, are n

sensitive to surface charging.

Optical, structural, thermal and electrical changes that occur aft

implantation could be analysed using optical absorption, X-ray analysi

thermal wave analysis or photothermal deflection spectroscopy, which are a

non-destructive techniques.

References

[1] J.W. Mayer, L. Eriksson and J.A. Davies, *Ion implantation in semiconductors*, Academic press (1970).

[2] J.F.Ziegler, *Nucl. Instr. And Meth. in Phys. Res. B*, **6** (1985) 270.

[3] A.N. Saxena, D. Pramanik, *Mater. Sci. Eng. B*, **2** (1989) 1.

[4] C. McKenna, C. Russo, B. Pedersen, D. Downey, *Semicond. Int.*, (1986) 101.

[5] Jenq-Horng Liang, *Nucl. Instr. And Meth. in Phys. Res. B*, **180** (2001) 216.

[6] R. Ohl, *Bell Syst. Tech. J.*, **31** (1952) 104.

[7] W.D. Cussins, *Proc. Phys. Soc. London B*, **68** (1955) 213.

[8] W. Shockley, *U.S. Patent No.*, 2 **787** (1957) 564.

[9] T. Alvager and N.J. Hansen, *Rev. Sci. Instr.*, **33** (1962) 567.

[10] J.O. McCaldin and A. E. Widmer, *J. Phys. Chem. Solids*, **24** (1963) 1073.

[11] J.F. Gibbons, *Proc. IEEE*, **56** (1968) 295.

[12] J.F. Gibbons, J.L. Moll, and N.I. Meyer, *Nucl. Instrum. Meth.* **38** (1965) 165.

[13] W.J. King, J.T. Burrel, S. Harrison, and F. Martin, and C.M. Kellet, *Nucl. Instrum. Meth.*, **38** (1965) 178.

[14] F.W. Martin, S. Harrison, and W. J. King, *IEEE Trans. Nucl. Sci.*, **NS-5-13** (1966) 22.

[15] G.N. Van den Hoven, *J. Mater. Res.*, **12** (5) (1997) 1401.

[16] C.J. McHargue, *Mater. Res. Soc. Symp. Proc.*, **27** (1984) 385.

[17] T. Kobayashi, T. Terai, *Nucl. Instr. and Meth. B*, **141** (1998) 441.

[18] J.C.R. Mittani , S. Watanbe,M. Matsuoka, D.L. Baptista, F.C. Zawislak, *Nucl. Instr. and Meth. B*, **218** (2004) 255–258.

[19] Y. Takeda, C.G. Lee, N. Kishimoto, *Nucl. Instr. And Meth. B*, **191** (2002) 422.

[20] N. Kishimoto, N. Okubo, N. Umeda, Y. Takeda, *Nucl. Instr. and Meth. B*, **191** (2002) 115.

[21] N. Kishimoto, N. Okubo, N. Umeda, Y. Takeda, *Proc. SPIE*, **4636** (2002) 88.

[22] Y.Q. Wang, M. Curry, E. Tavenner, N. Dobson, R.E. Giedd, *Nucl. Instr. and Meth. B*, **219–220** (2004) 798.

[23] P.C. Srivastava, U.P. Singh, *Bull. Mater. Sci.*, **19** (1996) 60.

[24] D. J. Friedman, J. F. Geisz, S. R. Kurtz, D. Myers, J. M. Olson, *J. Cryst. Growth*, **195** (1998) 409.

[25] K. Hanamoto, M. Sasaki, H. Miki, Y. Nakayama, *Nucl. Instr. and Meth. in Phys.Res. B*, **184** (2001) 371.

[26] T. Monteiro, C. Boemare, M.J. Soares, E. Alves, C. Liu, *Physica B*, **308-310** (2001) 42.

[27] H. Weishart, H. J. Steffen, W. Matz, M. Voelskov, W. Skorupa, *Nucl. Instrum. Meth. Phys. Res. B*, **112** (1996) 338.

[28] H. Du, Z. Yang, M. Libera, D. C. Jacobson, Yu.C. Wang, R.F. Davis, *J. Am.Ceram. Soc.*, **76** (1993) 330.

[29] Z. Yang, H. Du, M. Libera, I.L. Singer, *J. Mater. Res.*, **10** (1995) 1441.

[30] J. Bentley, L.J. Romana, L.L. Horton, C. J. McHargue, *Mater. Res. Soc. Symp. Proc.*, **235** (1992) 363.

[31] R. G. Vardiman, *Mater. Sci. Engg. A*, **177** (1994) 209.

[32] R. S. Bhattacharya, A.K. Rai, J.M. Williams, *J. Appl. Phys.*, **65** (1989) 1885.

[33] S. Minagawa, K. Baba, M. Ikeyama, k. Saitoh, S. Nakao, Y. Minagawa,

Nucl.Instrum. Meth. Phys. Res. B, **127-128** (1997) 651.

[34] R. Capelli, A. Miotello, P.M. Ossi, *J. Appl. Phys.,* **81** (1997) 146.

[35] N. Laidani, M. Bonelli, A. Miotello, L. Guzman, L. Calliari, M. Elena, R. Bertoncello, A. Glisenti, R. Capalletti, P. Ossi, *J. Appl. Phys.,* **74** (1993) 2013.

[36] C.J. Sofield, S. Sugeen J. Ing, L.B. Bridwell, Y.Q. Wang, *Vacuum,* **44** (3/4) (1993) 285.

[37] H. Tsuji, H. Satoh, S. Ikeda, N. Ikemoto, Y. Gotoh, J. Ishikawa, *Surf. Coat.Technol.,* **103/104** (1998) 124.

[38] C.M. Lopatin, T. L. Alford, V. B. Pizziconi, M. Kuan, T. Laursen, *Nucl. Instrum. Meth. B,* **145** (1998) 522.

[39] T.S. Iwayama, S.Nakao, K.Saitoh, *Appl. Phys. Lett.,* **65** (1994) 1814.

[40] K. Uchida, S.Kaneko, S.Omi, *J.Opt. Soc. Am. B,* **11** (1994) 1236.

[41] K.Fukumi, A.Chayahara, K.Kadono, *J.Appl.Phys.,***75** (1994) 3075.

[42] M.Ando, K.Kadono, M.Haruta, T.Sakaguchi, M.Miya, *Nature,* **374** (1995) 625.

[43] Y.Takeda, V.T.Gritsyna, N.Umeda, C.G.Lee, N.Kishimoto, *Nucl. Instrum.Methods B,* **148** (1999) 1029.

[44] T. Umebayashi, T. Yamaki, H. Ito, K. Asai, *J. Phys. Chem. Solids.,* **63** (2002) 1909.

[45] H. Yamashita, M. Harada, J. Misaka, M. Takeuchi, K. Ikeue, M. Anpo, *J. Photochem. Photobiol. A,* **148** (2002) 257.

[46] N. Sakai, A. Fujishima, T. Watanabe, K. Hashimoto, *J. Phys. Chem. B,* **105** (2001) 3023.

[47] M. Takeuchi, Y. Onozaki, Y. Matsumura, H. Uchida and T. Kuji, *Nucl. Inst. Meth.Phys. Res. B,* **206** (2003) 259.

[48] R.S.Averback, T.Diaz de la Rubia and R.Benedek, *Nucl. Instr. And Meth.* *in Phys. Res. B*, **33** (1988) 15.

[49] J.A.Sawicki, G.Abouchacra, J.Serughetti and A.Perez, *Nucl. Instr. And Meth. in Phys. Res. B*, **16** (1986) 355.

[50] G.Abouchacra, G.Chassagne and J.Serughetti, *Radiat. Eff.*, **64** (1982) 189

[51] G.Abouchacra and J.Serughetti, *Nucl. Instr. And Meth. in Phys. Res. B*, **1«** (1986) 282.

[52] Hj.Matzke, A.Turos and P.Rabette, *Radiat. Eff.*, **65** (1982) 1.

[53] A.Perez, M. Treilleux, L. Fritsch and G. Marest, *Radiat. Eff.*, **64** (1982) 199.

[54] M. Treileux, J.P. Dupin, G. Fuchs and P. Thevenard, *Nucl. Instr. And Meth. in Phys. Res. B*, **19/20** (1987) 713.

[55] E.Friedland , *Nucl. Instr. And Meth. in Phys. Res. B*, **116** (1996) 136.

[56] *"Surface Modification and Alloying"*, Ed. J.A. Davies, J. M. Poate, G. Foti and D. C. Jacobson, Plenum, New York (1983) p. 189.

[57] B.T. Murphy, *Proc. IEEE*, **52** (1964)1537.

[58] M.I. Current, L. A. Larson, *Mat. Res. Soc. Proc.*, **147** (1985) 365.

[59] *"The Stopping and range of ions in solids"*, J.F. Ziegler, J.P. Biersack, U. Littmark, Pergamon Press, New York (1985).

[60] J.P. Biersack, L.G. Haggmark, *Nucl. Instr.Meth.*, **174** (1980) 257.

[61] G.R. Piercy, F. Brown, J.A. Davies, M.McCargo, *Phys. Rev. Lett.*, **10** (1963) 399.

[62] M.T. Robinson, O.S.Oen, *Phys. Rev.*, **132** (1963) 2385.

[63] L.A. Christel, J.F. Gibbons, S. Mylroie, *J. Appl. Phys.*, **51** (1980) 6176.

[64] T. Diaz de la Rubia, R.S. Averback , H. Horngming, R. Benedek, *J. Mater. Res.*, **4** (1989) 579.

[65] J.P. Biersack, L.G. Haggmark, *Nucl. Instr. Meth.*, **174** (1980) 257.

[66] J.P. Biersack, W. Eckstein, *Appl. Phys.*, **34** (1982) 73.

[67] C. Rosselt, *"Radiation Effect and Defect in Solid"*, **129** (1993).

[68] O.A. Antoniadis, R.W. Dutton, *IEEE J. Solid State Circuits SC*, **14** (1979) 412.

[69] A.Rosencwaig, *Photoacoustic and Thermal wave phenomena in Semiconductors*, A. Mandelis ed., Elsevier New York (1987) p.78

[70] J.Opsal, A. Rosencwaig, *MRS Bulletin*, Vol. **XIII**, (1988) p. 28

[71] W. L. Smith, A. Rosencwaig, D. C. Willenborg, J. Opsal, M. W. Taylor, *Solid State Technology*, **29** (1986) 85.

[72] R. Martini, C. Wichard, W. L. Smith, M. W. Taylor, *Solid State Technology*, **30** (1987) 89.

[73] A. Rosencwaig, *"VLSI Electronics: Microstructure Science"*, N.G. Einspruch ed. Academic Press, New York (1985) p. 227

[74] G. K. Williamson and W. H. Hall, *Acta. Metall.* **1** (1953) 22.

[75] H. P. Klug and L. E. Alexander, *"X-Ray Diffraction Procedures for Polycrystalline and Amorphous Materials"*, (New York: Wiley) (1974).

Chapter 3

STUDIES ON DOPED AND ION IMPLANTED CdS THIN FILMS

3.1 Introduction

Cadmium sulfide had long been used widely in opto electronics and microelectronics due to its good optical and electrical properties. Pure and doped monocrystals and thin layers of this material are often used in photoconducting, photovoltaic and optoelectronic devices [1]. CdS is well known for its tendency to form nonstoichiometic compound, having excess cadmium, leading to n-type conductivity. The kind and number of defects and hence the electric, optical and luminescent properties of the material depend on the technique of sample preparation and its thermal history [2]. Thin films of CdS have been prepared by several techniques such as sputtering [3], evaporation [4], serigraphy [5], chemical vapor deposition [6], chemical spray pyrolsis [7] and chemical bath deposition [8, 9]. Production of large surface area CdS thin films by easy and low cost techniques for industrial use is of great importance. Chemical spray pyrolysis method has proved to be a reliable technique for this [10-13].

Even though electrical and optical properties strongly depend on the preparation conditions, pure or undoped CdS films generally show high electrical resistivities. Thus, it is difficult to produce undoped CdS films with good electro-optical properties, just by controlling the preparation conditions. However intrinsic CdS film is extensively used as window material in solar cells, having $CuInSe_2$ or $CuInS_2$ or CdTe absorber layer [14]. One of the

factors affecting the efficiency of thin-film solar cells is the electrical properties of the buffer layer, which in turn, depend mainly on the presence o different trap levels [15]. The basic requirements of thin films for solar cel applications are controllable optical and electrical properties with better crystallinity. An effective way to obtain CdS films with the desired parameter is to introduce dopants, and there have been many reports on this sort of work [16-18].

Fabrication of homojunction in CdS layer has great practical application, in the case of solar cells with CdS forming the buffer layer. Then one can imagine tandem cell structure with a homojunction in the top CdS layer. This homojunction can absorb photons of higher energy, while photons of lower energy can be absorbed by the lower junction. It has been generally concluded that formation of p-type CdS is very difficult because of self compensation effects due to sulfur vacancies [19] and hence conventional doping technique is ineffective. Copper is a well known luminescence activator [20] and acts as a deep acceptor, strongly influencing optical and electrical properties [21]. Therefore, it is important to study the effect of doping CdS with Cu by analysing the interaction between the Cu centers and the host material [22].

Ion implantation has been used for doping semiconductors. Conversion of n-type CdS into p-type by ion implantation with impurities such as P^+, Bi^+ and N^+ has been proved to be possible [23]. Ion implantation has several advantages over other techniques such as, precise control of the depth and concentration of dopants. It is also not limited by solubility constraints. However this technique introduces considerable amount of lattice defects that will modify optical and electrical properties of the material. Effect of low

energy ions such as, Ar^+, Kr^+, Bi^+, Ne^+ implantation in CdS crystals were also studied [24].

Photothermal deflection spectroscopy (PDS) is a highly sensitive and non-destructive technique developed in 1980 [25]. It has become an important tool for subband gap absorption study in both thin films and bulk material of semiconductors. Its non contact nature for probing optical [26], thermal [27], electrical [28] properties has placed it high amongst other analytical techniques. It allows the study of excess charge carrier lifetime, minority diffusion constant, and surface recombination velocity of a p-type material [29]. Since it is not affected by diffuse reflectance or light scattering, weak optical absorption coefficient can also be easily determined [30].

In this work, we used PDS technique to study Cu doped (through thermal diffusion and ion implantation) CdS. Ion species used were Ar^+, He^+ and Cu^+. For studying the defects, caused exclusively due to ion implantation, we selected He^+ and Ar^+ for our study, as Cu^+ electrically is active in CdS. Due to Ar^+, which is heavier compared to He^+, a comparative study of the amount of damage created by heavy and light ions was also possible.

3.2 A brief review of earlier works

3.2.1 Research on CdS thin films

Reynolds *et al* [31] were the first to observe photovoltaic effect in single crystal CdS with various metal electrodes. This gave a kick start for the work on single crystal CdS. Bube [32] observed photoconductivity and crystal imperfections in CdS crystal. He calculated the speed of response of photoconductivity for high intensity light excitation. High conductivity CdS

crystal, with chloride impurity, showed only a very low dependence of photosensitivity on temperature with a maximum near 173 K and low a conductivity for pure CdS crystals showed much greater variation of photosensitivity with temperature [33]. Ashour *et al* [34] had investigated the morphology of evaporated cadmium sulphide films. They observed that as-grown film, of thickness less than 30 nm, exhibited protrusions which were identified with films grown along *c*-axis. Structure of the deposited film was analysed using XRD pattern, with particular emphasis to the effects of preparation condition on the orientation, crystallite grain size and residual microstrain. Hernandez *et al* [35] reported the thermal annealing studies of CdS thin films prepared using chemical bath deposition (CBD). They reported variation of optical and electrical properties of thin films, before and after annealing in sulphur atmosphere, and found that the absorption edge shifted towards higher wavelength when the annealing temperature was increased. This was attributed to structural transformation. Kale *et al* [36] studied electrical and optical properties of the films prepared by chemical method. They studied the effects due to variation in deposition temperature and dipping time. Depending on condition of deposition, chemically deposited CdS thin films showed a blue shift as high as 0.35 eV in the optical band gap. It was found that as the deposition temperature decreased from 358 K to 273 K, the band gap increased from 2.4 eV to 2.7 eV.

Spray pyrolysis technique is very economic and gives highly reproducible samples having large area. Chamberlin and Skarman [37] were the first to develop chemical spray method for producing large area films of CdS and CdSe by spraying the solution onto a heated substrate. In their work on Cu_2S–CdS photovoltaic cell, they achieved electron density of

10^{15}-10^{16} cm^{-3} and electron mobility as high as 90 cm^2 V^{-1} s^{-1}. Wu and Bube [38] investigated electrical transport properties of sprayed CdS films. They found that photoconductivity of solution sprayed film was caused primarily by an increase in electron mobility. The variation in electrical transport properties of sprayed CdS films, as a function of substrate temperature, was correlated with variation in orientation, cubic/hexagonal phase ratio and its morphology [39]. Palafox et al [40] prepared pure and Indium doped thin films by chemical spray method. They acheived the lowest resistivity of 3x10^{-2} Ωcm for CdS:In thin films. Chow et al [41] had studied the chemically sprayed CdS thin films for their physical properties and preparation conditions. They observed the substrate temperature playing a vital role in determining the grain structure and the transport property. Films prepared by spray over a hot substrate maintained around 300 °C exhibited photovoltaic grade property with orderly structures and fairly well defined crystal grains.

It has generally been observed that the formation of p-type CdS is very difficult, because of self compensation effect due to sulfur vacancies [42, 43] and the depth of the acceptor level in CdS (~1 eV) [44]. There are only very few reports on conversion of CdS into p-type. Woods et al [45] were able to achieve p-type conduction in CdS through Cu diffusion. Grimmeiss et al [46] prepared p-type CdS by depositing thin films of CdS and Cu followed by annealing at high temperature. This resulted in diffusion of Cu atoms into CdS layer, giving rise to p-type conduction. They also achieved photovoltaic effect on these films. Kashiwaba et al [17] had also reported achievement of p-type characteristic of Cu doped CdS thin films. They found that Cu could easily diffuse into CdS film when it was deposited on a thin Cu film at 200 °C. Hall measurement and positive Seebeck coefficient confirmed p-type

characteristics. The same group [47] later fabricated thin film diodes composes of Cu-doped p-type CdS(CdS(Cu)) and undoped n-type CdS films o CdS(Cu)/CdS structure and observed light emission of blue green (500 nm) green (600 nm) and red (700 nm) colour under a forward current at 77 K Sebastian [48] could prepare p-type CdS thin films using CBD by doping copper ions in the bath. He observed p-type CdS thin films formed when CuC solution was added to the bath containing cadmium acetate triethanolamine ammonia solution and thiourea. Mathew *et al* [49] achieved p-type conversion of CdS prepared using CSP technique and doping copper atoms by allowing to diffuse into the CdS thin films after annealing the Cu/CdS bilayer system. Ho probe and Hall effect measurements were used to confirm n-type CdS film converted into p-type. Resistivity of these films was quite high for low C₁ concentration while further addition of Cu caused a drastic decrease in it resistivity.

Khawaja [50] had studied the optical properties of evaporated CdS films. They obtained optical constants (n and k) of these films. Optica absorption studies on the CdS:Cu as a function of Cu concentration hat revealed deep levels in the energy gap of CdS [51]. Absorption coefficient nea the edge was also found to be modified. Sunny *et al* [52] studied optical an surface properties of spray pyrolysed CdS thin films using Spectroscopi ellipsometry to identify the conditions for preparing polycrystalline CdS film having better electrical and optical properties. They studied the variation o real and imaginary parts of the refractive index with preparation conditions an found the optical constants (n and k) to increase with increase in substrat temperature. They also evaluated surface roughness and found that it decrease with increase in substrate temperature and reached a minimum in the rang

280-300 °C. Zeenath *et al* [15] studied trap levels in n-type and p-type chemical spray pyrolysed CdS thin films, using thermally stimulated current and dark conductivity measurements. For n-type CdS, they obtained activation energy of sulphur vacancy using short period of light excitation and for a longer excitation they could find out activation energies of both Cd and S vacancies. In case of Cu doped p-type CdS, they observed both S vacancy and Cu impurity irrespective of period of light excitation.

Another method of doping CdS thin film was by ion implantation of various acceptors, such as phosphorous, nitrogen, and bismuth ion species [23, 53, 54, 55]. These studies gave rise to p-type characteristics of CdS thin films. Anderson [56] implanted high-energy phosphorous ions into CdS and had shown evidence of conductivity type conversion after annealing. Type conversion was confirmed by thermal probe measurements done on the implanted surface. Diode fabricated from these implanted material showed good rectification characteristics and low voltage electroluminescence at room temperature. In this case, phosphorous substituted anion in II-VI compounds acted as an acceptor impurity [54] that resulted in p-type conductivity. Effect of implantation of Bi and Cu ions into CdS was studied by Tell *et al* [57]. They observed that variation in optical absorption, photovoltage and photoluminescence occurred due to implantation effect. Ratnasagar *et al* [58] studied amorphisation of CdS thin films due to argon ion irradiation. Kitagawa and Yoshida [59] studied defect recovery in CdS crystals irradiated with 10 MeV electron at 77K and observed three stages of recovery between 80 K and 410 K. Ruxandra *et al* [60] performed electron irradiation in thin polycrystalline CdS layer. Influence on electrical properties and modification of trap distribution were studied. A uniform trap distribution appeared after

first session of irradiation and for the second session an exponential trap distribution was induced in the band gap of CdS layer. Dawar *et al* [61] studied the effect of laser irradiation on structural and electrical properties of CdS thin films deposited by resistive heating technique. XRD studies revealed that crystallites of these films were improved on laser irradiation. Narayanan *et al* [53] studied the effects of 130 keV N^+ ion implantation in CBD CdS. They observed an increase in electrical conductivity of these films with increase in nitrogen ion concentration. Hot probe measurements confirmed p-type conductivity in implanted samples and n-type conductivity in pristine samples. The same group [63] carried out depth profiling studies using positron annihilation on 140 keV Ar^+ ion implanted CBD CdS films of 1 μm thickness, grown over glass substrate. They observed that, for increase in Ar^+ ion dose, there occurred formation of antisite defects in the surface region. At sample depths corresponding to peak damage layer there was no large vacancy clusters formed. Senthil *et al* [64] investigated 100 keV N^+ ion implanted in vacuum evaporated CdS. They observed the formation of Cd metallic nanocluster of size 5.3 nm from low frequency Raman scattering measurements. Yakushev *et al* [65] investigated 2.5 keV D^+ ion implanted in $Cu(InGa)Se_2$ thin films coated over a 30 nm CdS layer and studied the passivating effects on electrically active defects using D^+ ion.

Basol *et al* [66] reported that chemically prepared CdS films performed better as window material in thin film solar cells. They used very thin layer (~50 nm) of CdS, as the window material in $CdS/CuInSe_2$ solar cells and had observed that this structure of solar cell lead to high efficiency. Varkey *et al* [67] fabricated homojunction using spray-pyrolysed CdS thin films followed by thermal evaporation of Cu and annealing the CdS/Cu bilayer film. Fill

factor and efficiency observed were 0.44 and 0.73% respectively. H.L. Kwok [68] analysed the electronic properties of chemically sprayed CdS films and solar cells. His observation was that although theoretically the mobility was found to be proportional to the ratio of grain to intergranular dimensions, this dependence alone was insufficient to explain the measured changes in mobility in case of chemically sprayed CdS films. He used an equivalent circuit model to explain the photovoltaic effects. Dressner *et al* [69] studied structural and electrical properties on evaporated films. They observed that electronic mobility had dependence on orientation of the crystallites and resistivity of the high mobility films could be controlled by addition of Cl or Ga at the proper stage of processing. Tomas *et al* [70] found that resistivity of the film reduced due to annealing in hydrogen atmosphere. A process to reduce the resistivity of the film was to passivate chemisorbed oxygen at the grain boundaries. Narayanan *et al* [9] also reported the drastic reduction in resisitivity on cadmium sulphide thin films, prepared by CBD, when annealed in flowing air. Observed reduction in resistivity happened only when substantial quantity of CdO phase was formed.

3.2.2 Studies on semiconductor materials using PDS technique

Yuang *et al* [71] used photothermal deflection spectroscopy (PDS) for studying time dependence of optically induced degradation in CdS and CdSe semiconductor doped glasses. They observed absorption peaks in PDS experiment and used a theoretical model, to evaluate average radii of semiconductor microcrystals. It was observed that the estimated average radii of quantum dots were consistent with that obtained from other methods and they found this technique as an alternative tool for study of optical properties

of semiconductor microcrystals. Grus etal [2] studied CdS polycrystalline powder, doped with Cu, using photoacoustic spectroscopy and observed change in the density of states in the energy gap. Kuo *et al* [27] measured thermal diffusivities of solids using this technique. They compared data of various pure elements with those of compound semiconductor materials from two other laboratories. The values obtained were also in good agreement with those in literature. Salazar *et al* [72] used PDS to measure thermal diffusivity in solids and also developed theoretical equation for determination of thermal parameters. Madhusoodanan *et al* [73] used photoacoustic spectroscopy to study the variation of optical energy gap and also measured thermal diffusivity of $Ge_xSe_{100-x}(10 \leq x \leq 38)$ glasses. Thermal diffusivity was found to be maximum for the stoichiometric composition x=33. They also studied the optical absorption in the subband gap region. Bertolotti *et al* [74] did an extensive study of materials, having low thermal diffusivity, using PDS. Determination of thermal diffusivity was done using computer simulation, by solving heat diffusion equation along with experimental results. Kyrill *et al* [75] measured thermal parameters of bulk materials, thin films, and multilayered structures by using PDS. Fournier *et al* [28] used PDS technique to investigate transport properties of semiconductors. They had also developed a theoretical model that was used to quantitatively describe the transport parameters such as mobility, life time, surface recombination velocity and carrier concentration in a semiconductor material. They demonstrated purely thermal behaviour using silver coated thick glass slab and photogenerated carriers in semiconductors due to photoexcitation alone using p-type Si crystal. Friedrich *et al* [76] published a rigorous theoretical work on photothermal imaging quantitatively by means of a point spread function (PSF). This represented image of a buried

thermal point defect, and provided a non destructive subband gap imaging of thermal point defects in a material or a semiconductor. Grauby *et al* [77] developed a high resolution photothermal imaging technique for high frequency phenomena, using a charge coupled device camera associated with a multichannel lock-in scheme. Spatial resolution was better than 1 μm. Joule and Peltier heating effect was photothermally imaged for a 2.5 kΩ polycrystalline silicon resistor across which a sinusoidal current was flowing. Kawahara *et al* [78] performed non contact imaging of buried structures in open air atmosphere by using photothermal deflection method. They could image optically opaque buried structures in layered samples. Material parameters such as thermal diffusivity were also calculated. Tilgner *et al* [79] used two layer model for studying a thin absorber layer coated over substrates such as glass and copper. The same group [80] developed a three layer model for determining thickness and thermal properties of buried layers much thinner than their thermal diffusion length. Fujimori *et al* [81] developed a non contact technique for the measurement of film thickness using photothermal deflection, from theoretical and experimental results employing the deflection amplitude alone. The calculated results showed the thickness in a range from skin depth to the thermal diffusion length of an opaque film that could be determined from the deflection amplitude. Velinov *et al* [82] used one dimensional model for studying influence of optical, thermal, elastic and thermoelastic parameters, as well as to derive the thickness of absorbing layer using amplitude of the photothermal wave. Walther *et al* [83] proposed a new approach for estimation of depth profile by combining lateral scanning and frequency variation. For this, the heating beam was focussed and the surface temperature was measured at different distances apart from the heating spot.

These measurements had to be repeated at different modulation frequencies for better signal to noise ratio. Nagasaka *et al* [84] used three dimensional heat flow in the low frequency range and solved heat conduction equations for multi-layered samples. They determined distributions of thermal diffusivity, for a four layered Ni/ZrO$_2$ (functionally graded material) at room temperature.

3.3 Experimental Details

3.3.1 Preparation of CdS thin films over SnO$_2$ layer

Chemical Spray Pyrolysis (CSP) technique was used for preparing CdS thin film samples for the present work. Glass coated with SnO$_2$ layer (of thickness ~500nm) was used as the substrate, which had optical transmission of 80% and resistivity of 25×10^{-6} Ωm. CdS thin film was deposited by spraying an acqueous solution of cadmium chloride (0.02M) and thiourea (0.02M) on the SnO$_2$ coated glass substrate kept at a temperature of 300 °C with compressed air as carrier gas. The droplets underwent pyrolytic decomposition to form stoichiometric CdS film having thickness ~1μm. The growth on oxide semiconductors took place as soon as the droplets reached the hot surface. Sample preparation was discussed in detail elsewhere [67]. Schematic of the sample is represented in Fig. 3.1. This sample is named "Type I".

CdS layer (~1μm)

SnO$_2$ (~0.5μm)

Substrate (Glass)
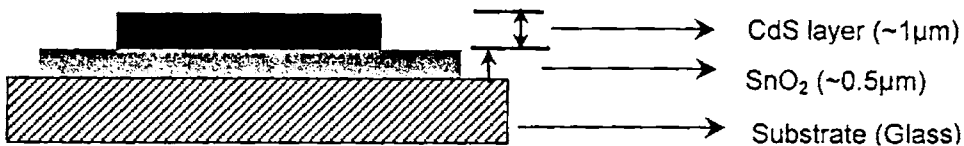
Fig.3.1 Schematic representation of the sample.

3.3.2 Cu doping in "Type I" CdS thin film samples

Cu was deposited using vacuum evaporation technique, at pressure of 10^{-5} torr over a masked area on "Type I" sample. This bilayer sample was annealed in vacuum (10^{-5} torr) at 300 °C for 45 minutes. This formed "Type II" sample. At annealing temperatures above 500 °C oxygen reacted with the CdS lattice at a relatively high rate, and a CdO layer, whose thickness depended on the temperature and O_2 concentration [40], would be formed. So we chose to keep the annealing temperature below 500 °C. In order to increase quantity of Cu diffused into CdS layer, more copper was deposited. Thus "Type III" sample were prepared with more Cu doping. For this a second layer of copper was vacuum evaporated on the same position on "Type II" sample and was again annealed under same condition for 45 min. This process was repeated on "Type III" sample in order to obtain "Type IV" sample. Annealing for 45 min in vacuum ensured complete diffusion of Cu. Thickness of vacuum evaporated copper layer, before diffusion, was approximately 25 nm for all the cases. Fig. 3.2 shows the Cu layer above the "Type I" sample before diffusion.

Cu layer(~25nm)
CdS layer (~1μm)
SnO_2 (~0.5μm)
Substrate (Glass)
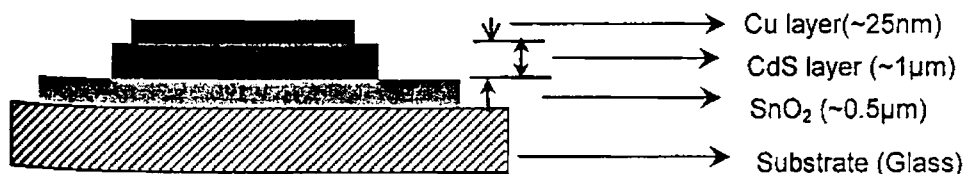
Fig. 3.2 Schematic representation of Cu
evaporated CdS sample before annealing.

3.3.3 Ar^+ ion implantation in CdS thin film samples

Mass analysed beam of Ar^+ ions from a low energy accelerator (J-15 Sames 150 kV accelerator) was used for implanting one set of "Type I"

samples. Beam current was maintained around 0.5 to 0.8 µA, to avoid heating effect during ion implantation. Samples were irradiated to various dosages in the range 10^{15} to 10^{17} Ar^+ ions/cm^2 for an accelerating voltage of 100 keV. Implantation was carried out at room temperature at 10^{-5} torr. SRIM calculations were done to get an idea of ion penetration into CdS sample. The modelling of ion implantation in semiconductors is usually accomplished by approximating the ion distribution using standard mathematical formulae. Pure Gaussian forms were used initially and the expression for ion distribution is given by,

$$\text{Ion distribution } (Y) = C \exp[(X-X_0)^2 / 2\sigma^2], \dots\dots\dots\dots\dots\dots\dots(3.1)$$

Where,

X_0 – the initial position of the ion at the surface,

X – the peak position or projected range due to ion distribution into the material and

σ – the straggling or width of the distribution,

C – Constant.

This was soon found to be inadequate and dual Gaussians were introduced such that, one was good for the left side and the other for the right side of the distribution. The whole work was to reproduce experimental data. Fig.3.3 is the (calculated using SRIM) pictorial representation for 100 keV Ar^+ ions into CdS. The Ar^+ ion distribution was found to be almost Gaussian and the maximum penetration depth was around 800 Å. Table 3.1 is the tabulated value of SRIM data. This also shows that the projected range is 0.08 µm.
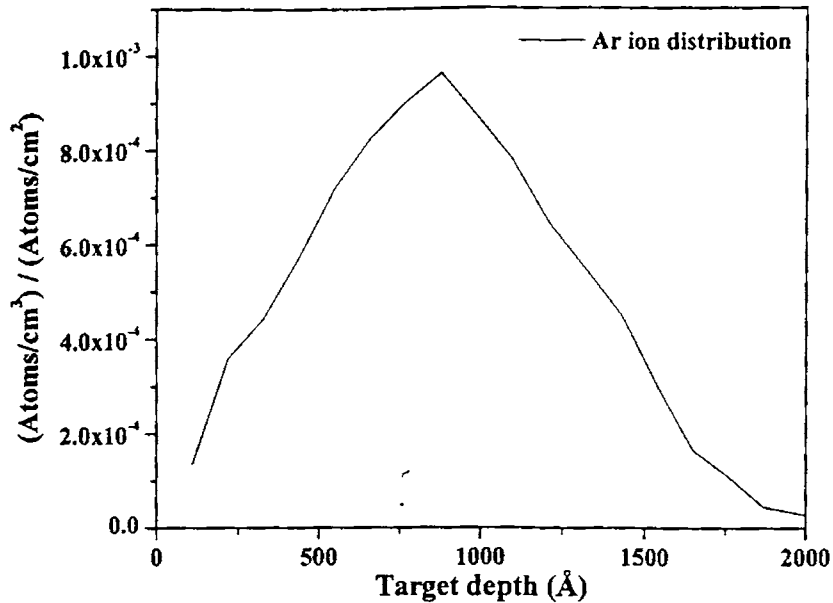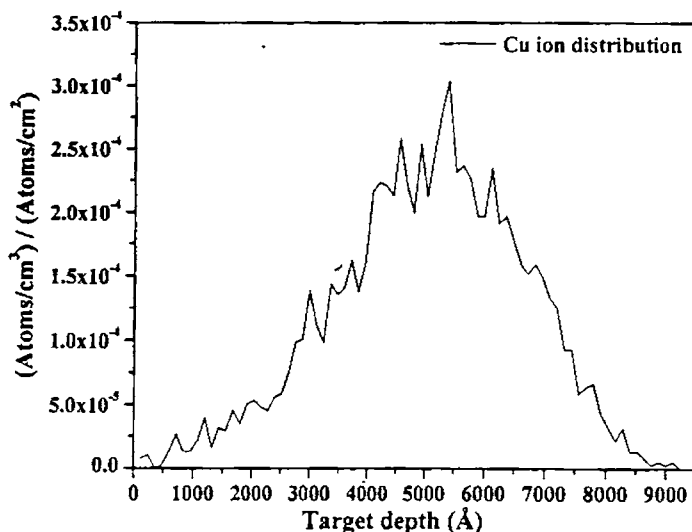
Fig. 3.3 Graph depicting Ar^+ ion distribution in CdS for an accelerating voltage of 100 keV; SRIM calculation.

Ion energy	(Electronic Stopping) dE/dx	(Nuclear Stopping) dE/dx	Projected Range (μm)	Longitudinal Straggling (μm)	Lateral Straggling (μm)
100 keV	0.6748	1.053	0.0800	0.0451	0.0333

Table 3.1 Values obtained from SRIM calculation for Ar^+ ions into CdS sample for accelerating voltage of 100 keV. The Projected range tabulated here is used in our calculation for non destructive depth profiling using PDS.

3.3.4 Cu⁺ ion implantation in CdS thin film samples

In order to implant Cu into CdS film, mass analysed beam of 1 MeV Cu^+ ions from a high energy accelerator (Pelletron accelerator) was used. Beam current was maintained around 0.5 to 0.6 µA, to avoid heating effect during ion implantation. Samples were irradiated to various dosages in the range 10^{13} to 10^{15} Cu^+ ions/cm². Implantation was carried out at room temperature in vacuum (10^{-6} torr). Fig.3.4 is the pictorial representation (calculated using SRIM) for 1 MeV Cu^+ ions into CdS. It was found that Cu ion distribution into CdS was not uniform as in the case of Ar ion. As Cu ion is heavier than Ar ion, the cascade damage caused due to its immediate stopping could be more. Moreover, much higher energy was used to get it implanted into CdS. The penetration depth was found to be around 5000 Å and Table 3.2 is the tabulated value of SRIM data.

Fig. 3.4 Graph showing Cu^+ ion distribution in CdS for an accelerating voltage of 1 MeV; SRIM calculation.

Ion energy	(Electronic Stopping) dE/dx	(Nuclear Stopping) dE/dx	Projected Range (μm)	Longitudinal Straggling (μm)	Lateral Straggling (μm)
1 MeV	2.186	1.249	0.4915	0.1711	0.1359

Table 3.2 Values obtained (from SRIM calculation) for Cu^+ ions implanted in CdS sample using accelerating voltage of 1 MeV. The Projected range tabulated here was used in our calculation for non destructive depth profiling using PDS.

3.3.5 He^+ ion implantation in CdS thin film samples

He$^+$ ions were also implanted in another set of "Type I" sample, using a low energy accelerator (J-15 Sames 150 kV accelerator) for various accelerating voltages from 60 keV, 80 keV, 100 keV and 120 keV maintaining a constant dosage of 5×10^{16} He$^+$ ions/cm^2. Beam current was maintained around 0.5 to 0.8 μA, to avoid heating effect during ion implantation. Implantation was carried out at room temperature in vacuum (10^{-5} torr). The idea of increasing the acceleration energy of the ions is to penetrate deeper into the material. SRIM calculations were done to get an idea of ion penetration into of CdS sample. Fig.3.5 depicts result of SRIM calculation for 60 keV, 80 keV, 100 keV and 120 keV He$^+$ ions into CdS thin film samples. It is clearly seen that the range distribution shows a shift to deeper depths into the sample with increase in acceleration energy of the ions. Table 3.3 gives the details of variation of different parameters with acceleration voltages. The projected range increases from 0.36 μm (for 60 keV) to 0.62 μm (120 keV) and the average shift is ~ 0.085 μm.
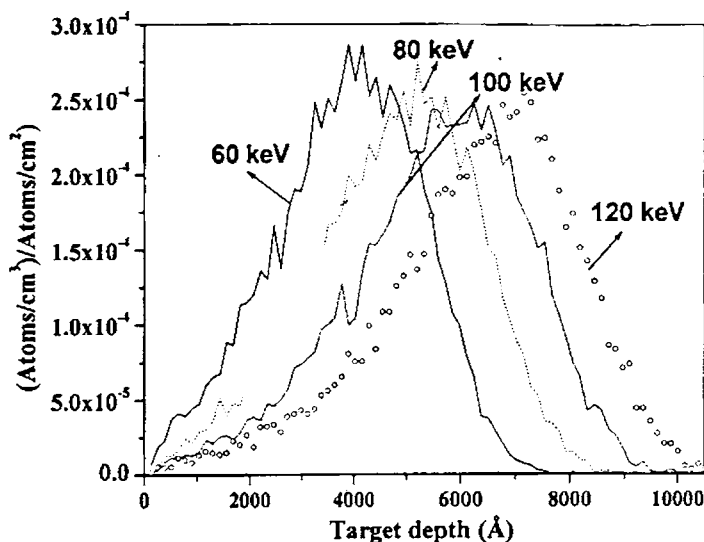
Fig. 3.5 SRIM calculated plot for He$^+$ ion distribution into CdS for accelerating voltages of 60 keV, 80 keV, 100 keV and 120 keV.

Ion energy	(Electronic Stopping) dE/dx	(Nuclear Stopping) dE/dx	Projected Range (μm)	Longitudinal Straggling (μm)	Lateral Straggling (μm)
60 keV	0.0302	8.761	0.3639	0.1899	0.1663
80 keV	0.0309	7.384	0.4569	0.2084	0.1884
100 keV	0.04117	6.42	0.5418	0.2223	0.2060
120 keV	0.04565	5.714	0.6204	0.2331	0.2207

Table 3.3 Values obtained from SRIM calculation for He$^+$ ions into CdS sample for accelerating voltages of 60 keV, 80 keV, 100 keV and 120 keV. The Projected range tabulated here was used in our calculation for non destructive depth profiling using PDS.

3.4 Results and Discussion

3.4.1 Cu thermally evaporated and diffused into CdS Sample

3.4.1.1 Optical absorption studies

As CdS was a direct band gap material, energy band gap was calculated from $(\alpha h v)^2$ versus hv curve. There was an increase in energy band gap initially for "Type II" sample and a steep decrease on further Cu doping. Fig. 3.6 shows the variation in Eg due to Cu doping in CdS thin film for "Type I", "Type II", "Type III" and "Type IV" samples.
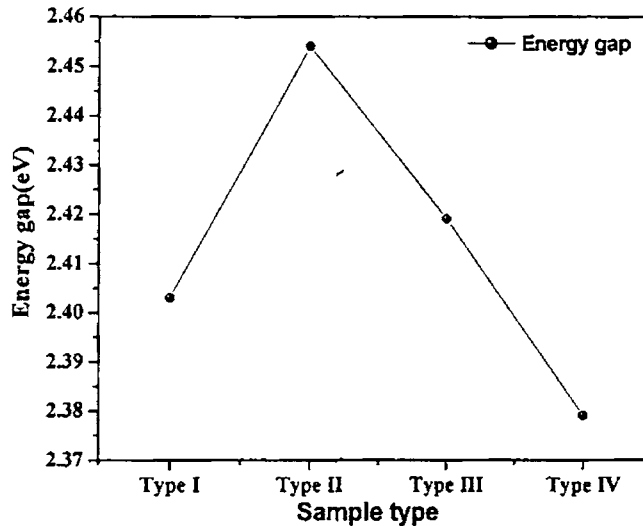
Fig. 3.6 Energy band gap variation for Cu doped CdS samples

Pristine sample showed a band gap value of 2.4 eV. It was found to increase to 2.45 eV on Cu doping in case of "Type I" sample. On further Cu doping, the band gap showed a sharp decrease to 2.38 eV. Fig. 3.9 shows the grain size value calculated from the XRD data. It was found that the grain size shows a

decrease for "Type II" and was found to increase with further increase in Cu doping. The decrease in band gap, due to the increase in Cu concentration, could be possibly due to increase in grain size. Kale *et al* [36] observed decrease in band gap with increase in annealing temperature, which was due to the grain growth. Mahuya *et al* [100] observed an increasing nature of band gap for ball-milled Bi_2O_3 powder due to reduction of grain size. Here also grain size of "Type II" sample decreased and this supports increase in band gap for this sample.

3.4.1.2 X-Ray Diffraction studies

X-ray diffraction (XRD) pattern for "Type I", "Type II", "Type III" and "Type IV" sample indicated that there existed 7 peaks corresponding to (100), (002), (101), (110), (103), (112) and (203) planes. Fig. 3.7 shows XRD pattern for CdS(Cu) samples for various quantity of copper doping. The peaks indicated that CdS had hexagonal orientation and there were no peaks corresponding to any copper compounds like Cu_xS or CuO. It was evident that Cu merely diffused into CdS and did not form any chemical reaction with sulphur to form new compounds. Abe *et al* [85] reported similar result in case of evaporated CdS over Cu layer. The *c*-axis of crystallites was mostly oriented perpendicular to the substrate. From the XRD pattern, it was found that peak corresponding to (112) and (203) planes showed very sharp increase and then decreased with increase in Cu doping.
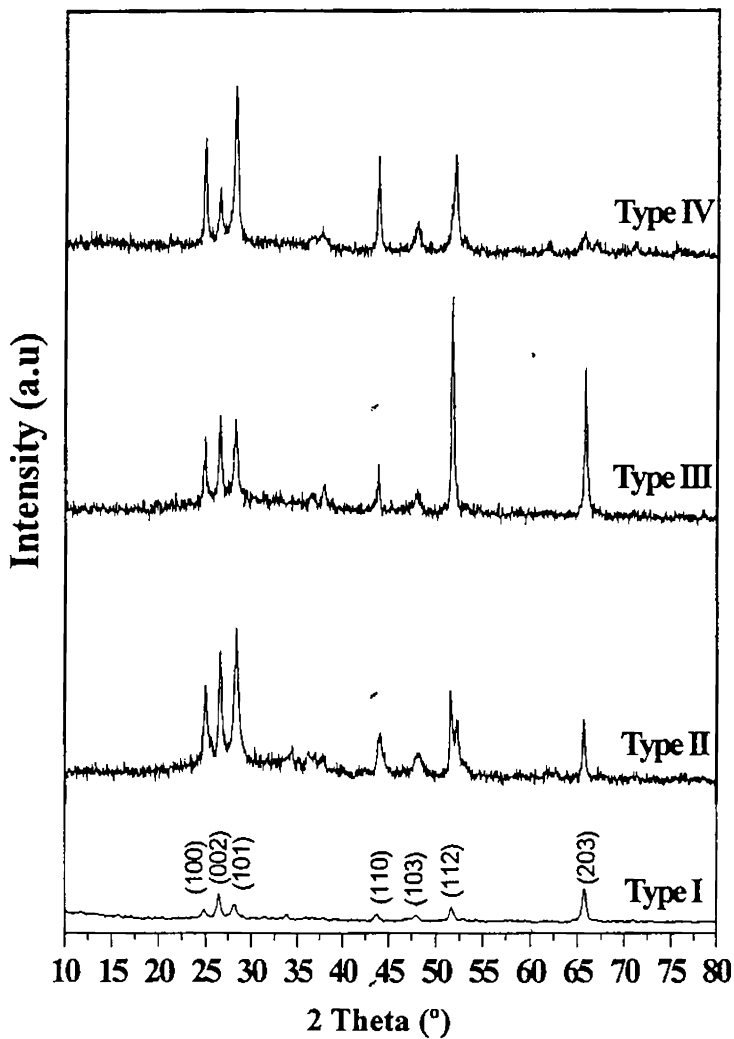
Fig. 3.7 XRD pattern for variation of Cu doped CdS samples

Lattice strain of copper diffused samples was calculated from the XRD pattern, from line broadening. Fig.3.8 shows lattice strain. Lattice strain was least for "Type II" sample and was observed to increase with Cu doping. Since Cu atom had smaller atomic radii than a Cd atom, small quantity of Cu doping could result in occupying interstitial site and for heavy Cu doping it was also possible to have Cu atoms in the interstitial / grain boundaries. This could be the reason for relaxation of lattice strain for "Type II" sample and an increase in lattice strain for further Cu doping. Similar kind of effect was observed by Susumu *et al* [86]. They had reported that, an infinitesimally small number of Cu atoms in CdS film occupy the Cd sites and a greater number of Cu atoms were probably distributed at the grain boundary. Thus our reasoning goes well with the above result.
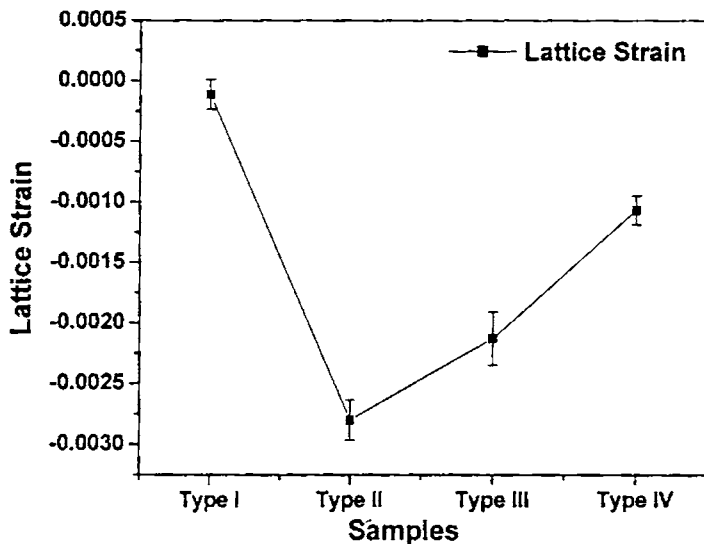
Fig. 3.8 Lattice strain variation of Cu doped CdS samples

Grain size calculated using Debye-Scherrer formula for the (112) peak from the XRD pattern is plotted in Fig. 3.9. It was observed that there occurred a decrease in grain size from 16.89 nm for "Type I" sample to 12.36 nm for "Type II" sample. On increasing the quantity of Cu doping, it showed an increase and attained a value of 15.84 nm for "Type IV" sample. This grain growth could also be the reason for decrease in energy band gap for heavy Cu doping. In that case, stuffing of Cu atoms into a unit cell could lead to variation in cell dimension. Thus we calculated unit cell volume from "*a*" and "*c*" lattice parameters. Fig. 3.10 gives variation of the unit cell volume for different Cu doped CdS sample.
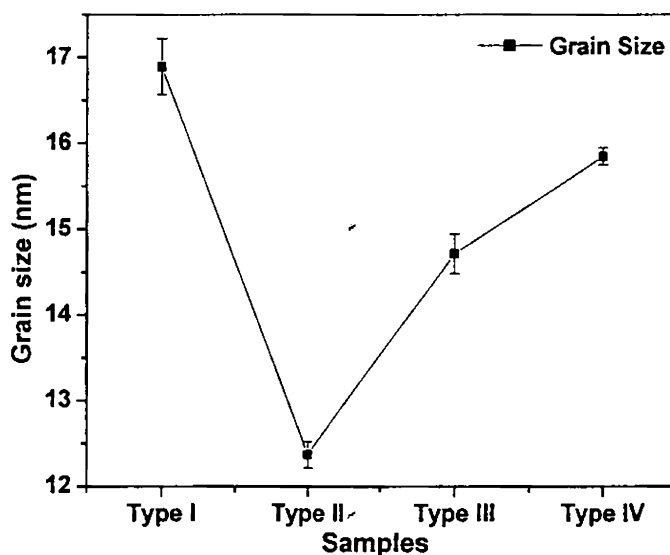
Fig. 3.9 Grain size variation for Cu doped CdS samples

The unit cell volume was maximum for "Type II" sample and decreased for further Cu doping. The observed increase in unit cell dimension

for "Type II" sample was very small and this could be due to the positioning of Cu atoms at interstitial positions while for "Type III" and "Type IV" sample Cu atoms might have gone to grain boundaries causing a increase in grain size.
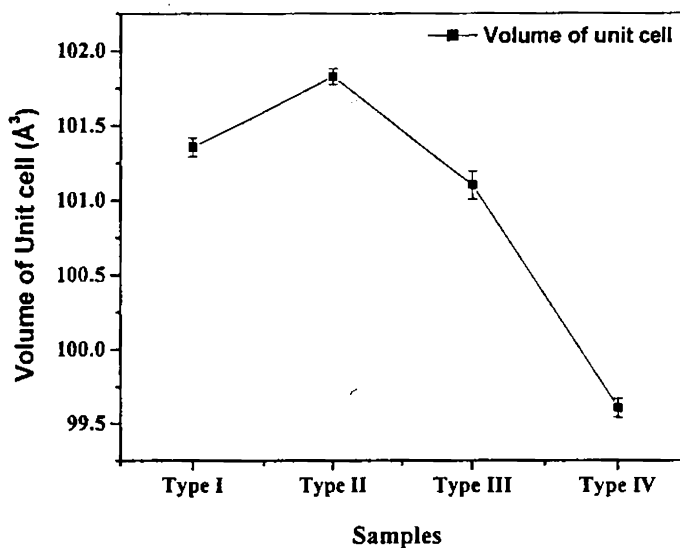
Fig. 3.10 Variation of volume of unit cell with increase of Cu in CdS samples.

3.4.1.3 Photothermal Studies

3.4.1.3a Thermal diffusivity measurement

Fig. 3.12 shows the log amplitude versus square root of frequency plot for "Type I" to "Type IV" samples. The initial steep decrease, which is due to thermal contribution because of optical absorption of the sample was fitted linearly to obtain the thermal diffusivity value. Detailed procedure is explained in chapter 1 (section 1.5.1).

Thermal diffusivity was found to decrease from 0.42 cm^2/s for "Type I" sample to 0.16 cm^2/s for "Type II" sample. On further increasing Cu

doping, the value of thermal diffusivity increased attaining a maximum value of 0.32 cm²/s for "Type IV" sample as shown in Fig. 3.11. Decrease in thermal diffusivity for "Type II" sample could be due to the thermal barriers existing between the grain [87]. XRD studies indicated decrease of grain size in "Type II" sample making the effect of this thermal barrier prominent and for "Type III" and "Type IV" samples grain size was found to be increasing.
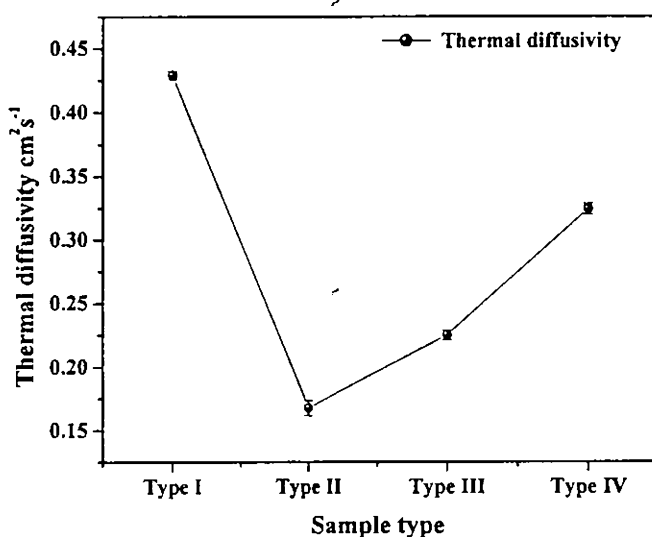
Fig. 3.11 Plot for thermal diffusivity for various Cu concentrations into CdS

3.4.1.3b Non contact mobility measurement

Mobility of the sample was determined by non-contact process using photothermal deflection spectroscopy as described in chapter 1 (section 1.5.2). Fig. 3.12(a), (b), (c) and (d) show the plots of (log amplitude versus $\sqrt{f}$) "Type I", "Type II", "Type III" and "Type IV" samples respectively. The plots exhibit an initial steep linear decrease between the frequency regime $\sqrt{f} = 5$ to

20 √Hz followed by series of humps between frequency regime from √f = 20 and 30 √Hz.

(a)

(b)

(c)

(d)
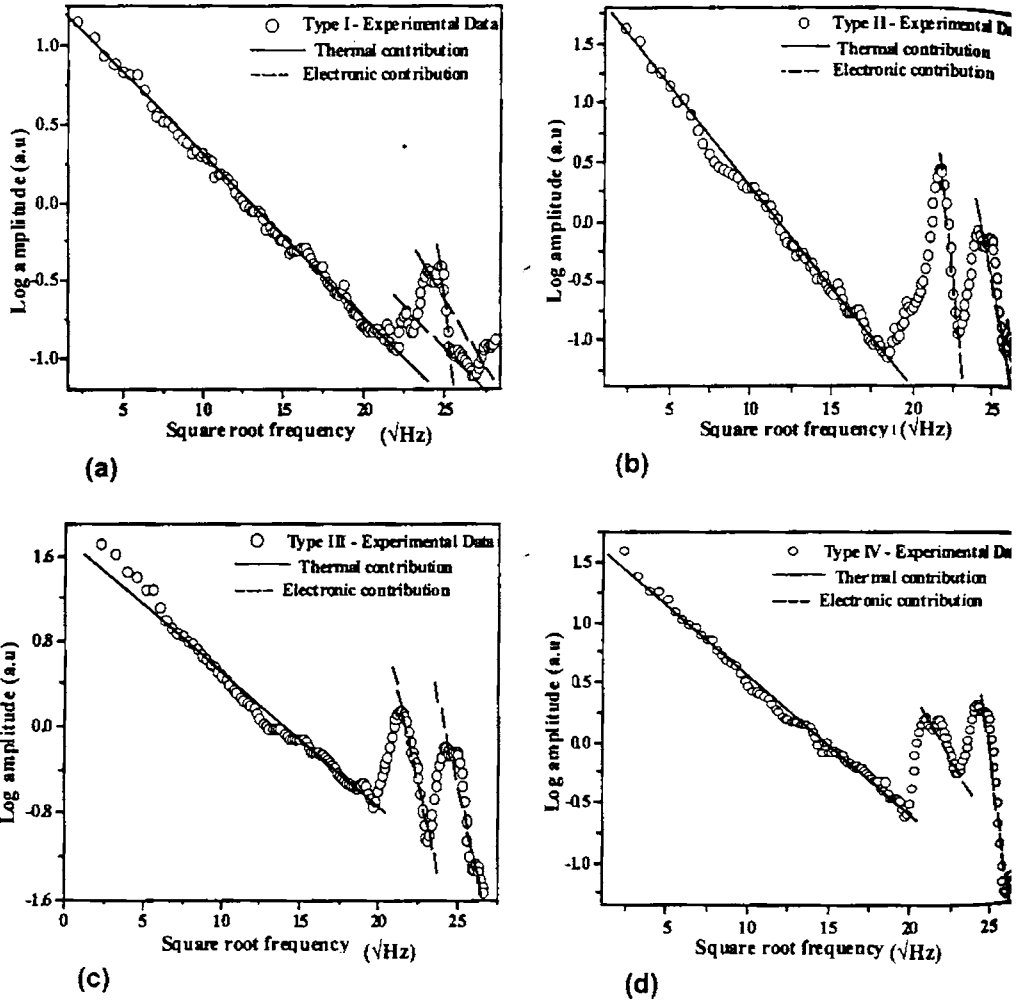
Fig. 3.12 Log amplitude versus square root of frequency curve of Cu doped CdS samples. These curves were used for calculating the thermal and electronic property of the sample

Series of humps observed after 20 √Hz might be due to complex interaction of photo generated minority carries. To calculate mobility, electronic diffusivity was first calculated within the frequency regime from √f = 20 and 30 √Hz. This value was used in Einstein-Smoluchowski relation which coupled the mobility μ and the diffusion coefficient D (As discussed earlier in chapter 1, section 1.5.2) and hence mobility value for the thin film sample was determined.

Mobility decreased initially from 9.5 $cm^2V^{-1}s^{-1}$ for "Type I" to 2.37 $cm^2V^{-1}s^{-1}$ for "Type II" sample and then there occurred a drastic increase to 16.8 $cm^2V^{-1}s^{-1}$ for further Cu doping. Fig. 3.13 shows the calculated mobility plot for different Cu doped CdS samples. The variation of mobility was found to be very similar to the variation observed for the grain size (Fig. 3.9).
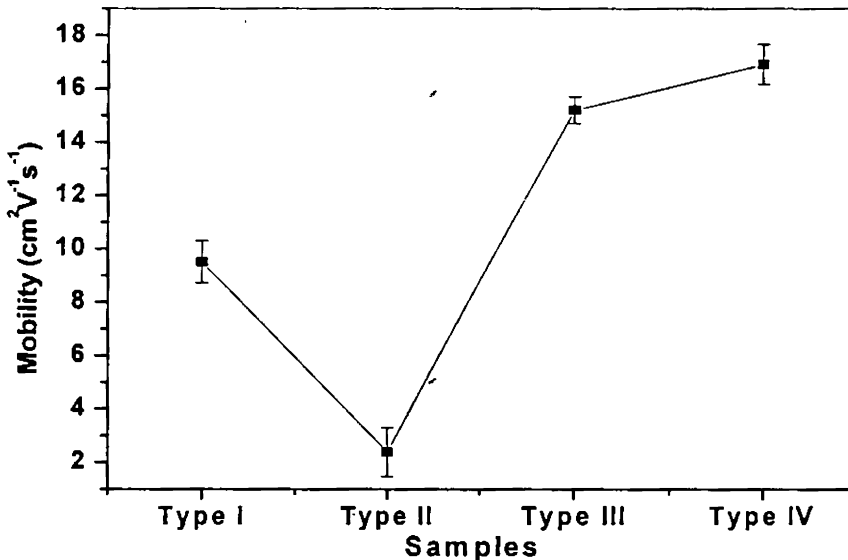
Fig. 3.13 Mobility variation for Cu doped CdS samples

Grain size of "Type II" sample was found to be decreased very much. Similarly mobility also decreased for this sample. On increasing the Cu doping concentration both grain size and mobility increased. It is quite evident that larger grain size will always lead to higher mobility.

The mobility values of evaporated CdS thin films prepared for solar cell applications were in the range 0.1 to 10 cm^{2}V^{-1}s^{-1} [90, 91, 92, 37]. The values of mobility obtained using PDS in the present work were in close coincidence with those reported earlier.

3.4.1.3c Non destructive thickness measurement

Thickness of the samples was determined using curve fitting method as described in chapter 1 (section 1.4). This was done assuming a three layer model. The top layer was the Cu diffused layer (l_1), while middle layer was Cu free CdS layer (l_2) and the bottom layer, pure SnO$_2$ layer (l_3). Schematic of the model is shown in Fig. 3.14. Modulated pump beam is irradiated on layer (l_1). The thermal waves, generated due to non-radiative transition because of optical absorption, travel through (l_1) to (l_3) through (l_2). Fig. 3.15 is a typical graph of photothermal deflection amplitude versus chopping frequency for "Type IV" sample, which was used to do theoretical curve fitting to determine the film thickness. Thickness obtained through theoretical fitting is tabulated in Table 3.4.
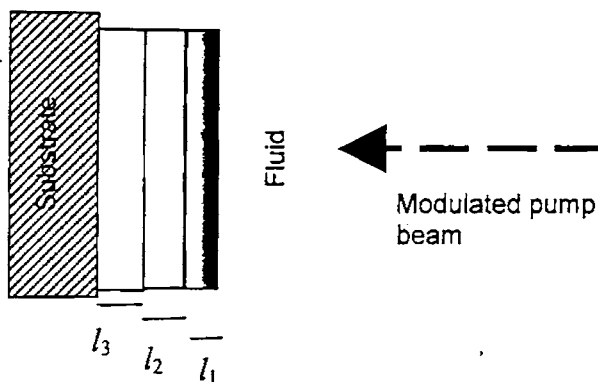
Fig. 3.14 Schematic of the model of sample used for thickness determination in the curve fitting method.
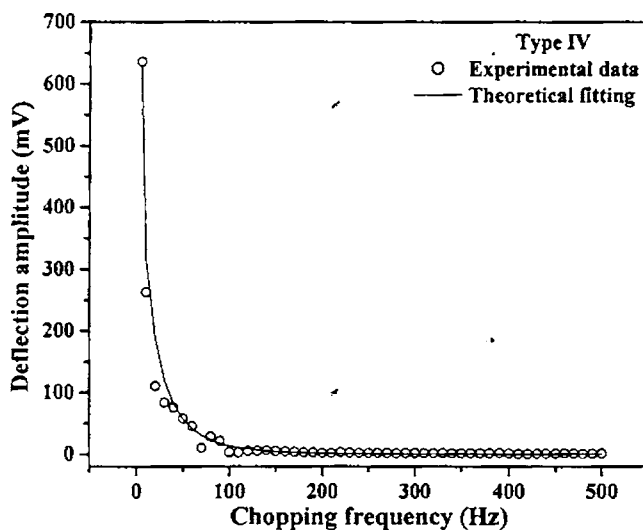
Fig. 3.15 Graph showing deflection amplitude versus chopping frequency of "Type IV" Cu doped CdS sample. This was one of the curve which was used for calculating the thickness of sample using curve fitting method.

Sample	Copper diffused layer thickness (l_1) (µm)	Bottom layer thickness (l_2) (µm)	SnO₂ layer thickness (l_3) (µm)	Error Bar (µm)
Type II	0.259	0.862	0.52	± 0.011
Type III	0.482	0.621	0.52	± 0.040
Type IV	0.491	0.723	0.52	± 0.013

Table 3.4 Values of thickness of Cu diffused region in CdS thin films, determined using curve fitting method.

X-ray photoelectron spectroscopy (XPS) was used earlier for depth profiling "Type III" sample showed that Cu distribution on top layer of CdS is uniform and there existed n-CdS layer below the p-CdS:Cu layer which was free of Cu atoms [93]. Thickness measured earlier using Ellipsometry [88] and XPS technique on similar kind of sample indicated that thickness of Cu diffused layer is ~500 nm. Thickness values obtained from PDS studies were coinciding well with those obtained from Ellipsometry and XPS technique.

As the Cu doped region had become p-type, it formed a junction with the lower n-CdS and the junction so formed was found to be very stable. V_{oc} and I_{sc} values of the samples prepared remained more or less constant for about ten months [67] without any protective layer.

3.4.2 Ion implanted CdS thin film samples

3.4.2a Studies on Ar$^+$ ion implanted CdS

3.4.2a.1 Optical absorption studies

Variation in energy band gap of Ar$^+$ implanted samples was studied by the same method as described earlier in section 3.4.1.1. The energy band gap decreased with increase in dosage for 100 keV Ar$^+$ ion implantation. Fig. 3.16 is the plot for E$_g$ versus Ar$^+$ ion implanted in CdS for various dosages.
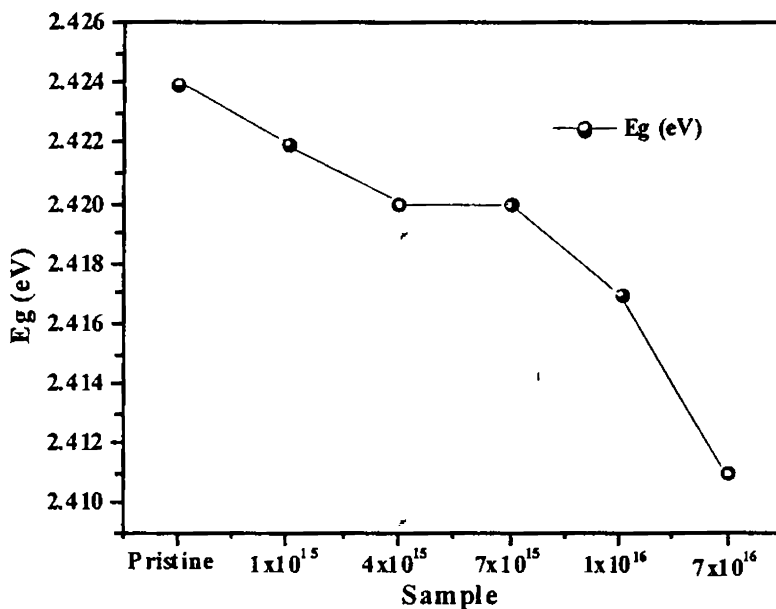

Fig. 3.16 Energy band gap variation for Ar$^+$ implanted CdS samples

Observed decrease in energy band gap may be due to the creation of defect levels within the band gap that lead to an increase in absorption coefficient.

3.4.2a.2 X-Ray Diffraction studies

XRD peaks of Ar^+ ion implanted samples indicated that CdS had hexagonal orientation and there were no peaks corresponding to CdO. The c-axis of crystallites was mostly oriented perpendicular to the substrate. Six prominent planes were identified and these were (100), (002), (101), (110), (103) and (112). It was found that peak corresponding to (103) plane decayed with increase in dosage except for samples irradiated with a dosage of $1x10^{16}$ Ar^+ ions/cm^2. Fig. 3.17 is the XRD pattern for Ar^+ implanted CdS samples.
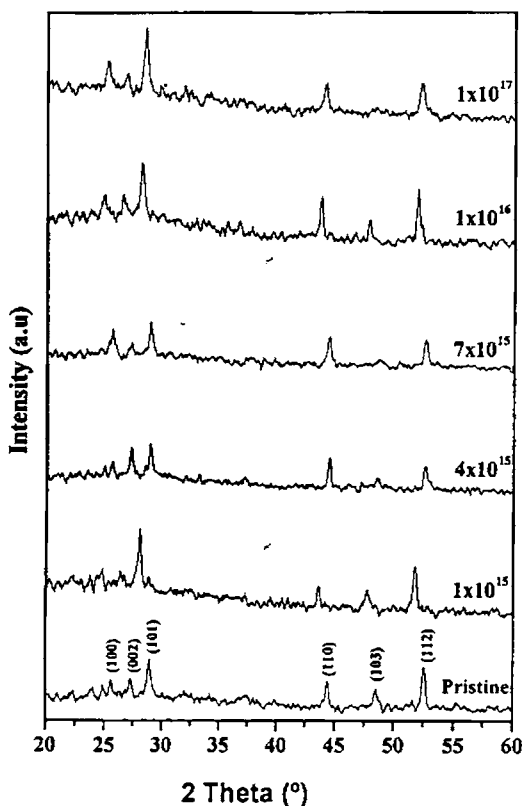
Fig. 3.17 XRD pattern for Ar^+ ion implanted CdS samples.

Implantation with Ar^+ ions is likely to produce vacancies and interstitials causing lattice damage, defect clusters such as argon bubbles and dislocation loops. Narayanan *et al* [62] had reported argon bubble formation for Ar^+ implantation in CdS. Mady *et al*. [95] reported the formation of zinc clusters in ZnS films due to nitrogen irradiation. From the XRD data, we could neither observe any indication of Cd cluster formation or any other phase formation after implantation. So we could only suspect Ar bubble formation.

Lattice strain calculated from the XRD data showed a drastic decrease for $1x10^{16}$ Ar^+ ions/cm^2 implanted sample. Fig. 3.18 depicts the variation of lattice strain with dosage of Ar^+ ion in CdS samples. Grain size was also calculated using Debye-Scherrer formula for the (110) peak from the XRD pattern and is plotted in Fig. 3.19. Grain size gradually decreased as dosage increased from $1x10^{15}$ to $1x10^{16}$ ions/cm^2. In the case of pristine samples, grain size was ~16 nm and for sample irradiated with a dose of $1x10^{16}$ ions/cm^2 the grain size was ~10 nm. But there was a sudden increase in grain size at the dose of $1x10^{17}$ ions/cm^2 (~24 nm).
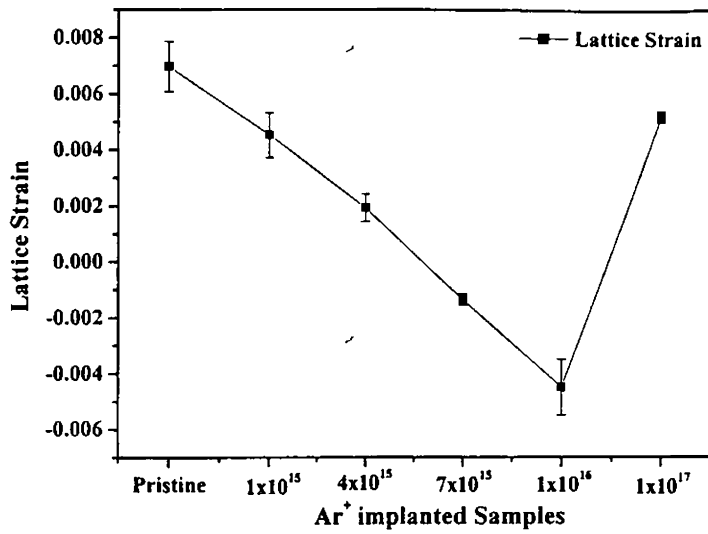
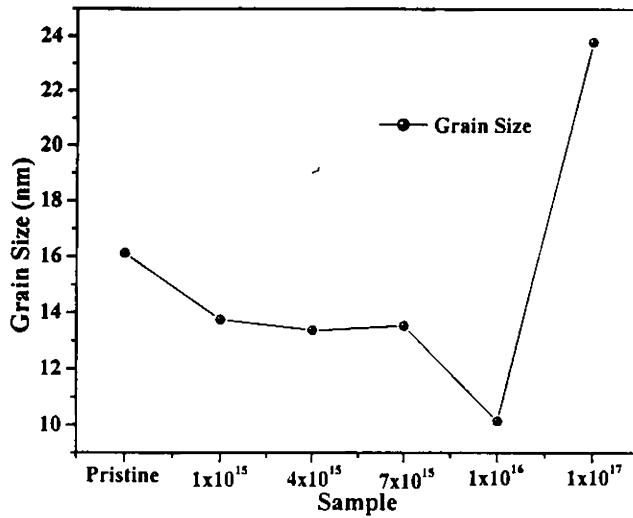Fig. 3.18 Lattice strain for Ar⁺ implanted CdS samples.

Fig. 3.19 Grain size for Ar⁺ implanted CdS samples.

Fig. 3.20 shows the variation of volume of the unit cell on Ar^+ implantation. Unit cell volume calculated from XRD pattern showed a more or less stable value upto a dose of $7x10^{15}$ ion/cm^3. Sudden increase was observed for $1x10^{16}$ Ar^+ ions/cm^2. The drastic decrease in strain for $1x10^{16}$ Ar^+ ions/cm^2 could be due to an increase in volume of the unit cell, causing a relaxation in strain. It is to be specifically noted that changes in unit cell volume and lattice strains occurred for sample irradiated with a dosages of $1x10^{16}$ Ar^+ ions/cm^2. It is for this sample the XRD peak corresponding to (103) plain re-appeared.
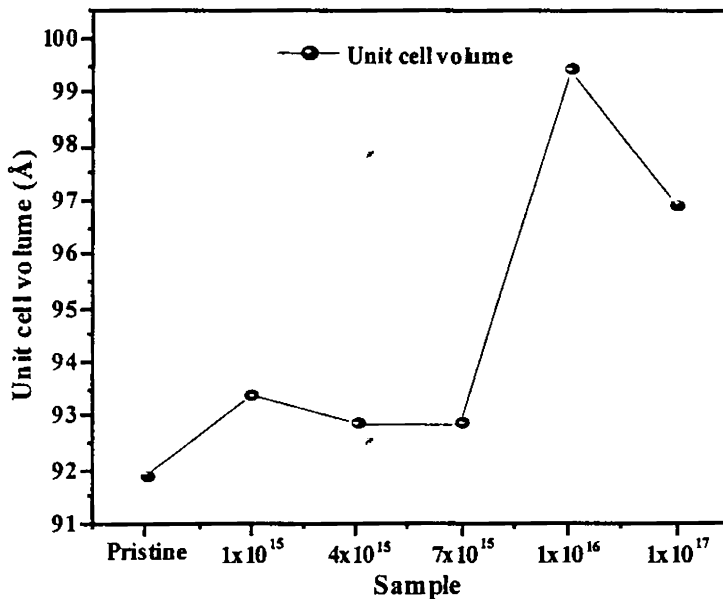
Fig. 3.20 Unit cell volume for Ar^+ implanted CdS samples.

3.4.2a.3 Photothermal Studies

3.4.2a.3a Thermal diffusivity measurement

Fig. 3.21 shows the variation in thermal diffusivity for various dosages of Ar^+ implantation in CdS. Detailed procedure for measuring thermal diffusivity is discussed in chapter 1 (section 1.5.1). The thermal diffusivity value was found to increase linearly with the increase in ion dosage. Increase in absorption due to ion implantation could be due to the increase in defects created by high energy ions, leading to enhanced probability of non radiative transition. This might be resulting in the increase of thermal diffusivity.
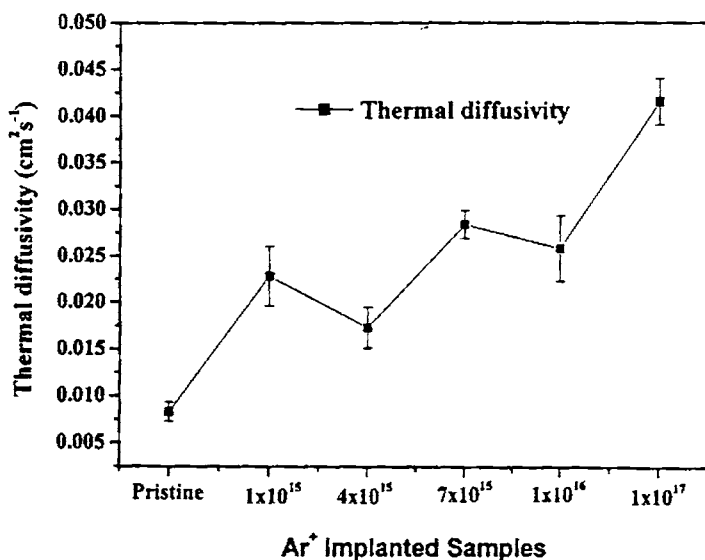
Fig. 3.21 Thermal diffusivity for Ar^+ implanted CdS samples.

3.4.2a.3b Non destructive thickness measurement

Depth of Ar^+ ion penetration into CdS was determined using PDS. Detailed procedure for depth profilometery was discussed in chapter 1 (section

1.4). From SRIM calculation, it was found that Ar^+ did not penetrate into SnO_2 layer. Thus two layer model was sufficient for theoretical modelling, in our case, l_1 being the damaged CdS layers due to Ar^+ implantation and l_2 the undamaged CdS layer. Fig. 3.22 shows the photothermal deflection amplitude versus chopping frequency curve for Ar^+ implanted CdS thin films for a dose of $7x10^{15}$ ions /cm^2 that was used for curvefitting. All other samples were depth profiled using same method. Thickness of Ar^+ implanted layer, obtained by curve fitting, is tabulated in Table 3.5.
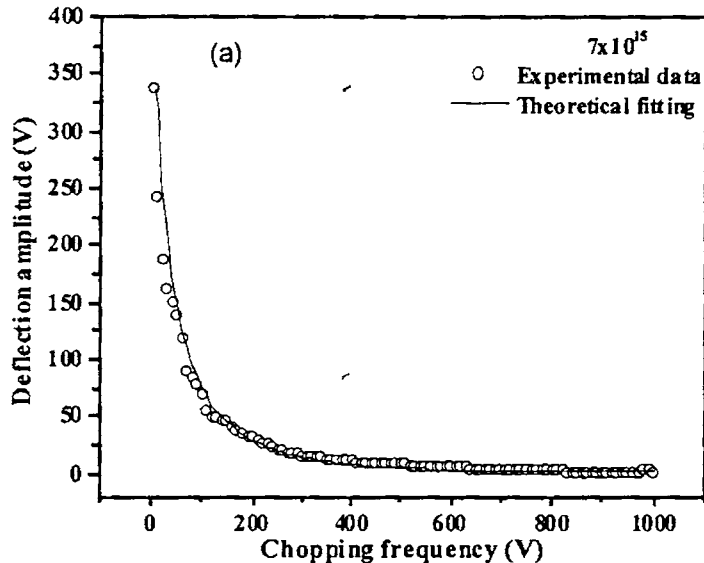
Fig. 3.22 Deflection amplitude versus chopping frequency curve for 100 keV Ar^+ ion implanted CdS sample for a dosage of $7x10^{15}$ ions/cm^2. This was one of the curves, which was used for calculating the thickness of sample using curve fitting method.

Sample (Ar$^+$ ions/cm^2)	Ar$^+$ ion implanted layer thickness (l_1) (µm)	Bottom pure CdS layer thickness (l_2) (µm)	Error Bar
Pristine	–	1.02	± 0.0011
1x10^{15}	0.082	0.919	± 0.0042
4x10^{15}	0.083	0.916	± 0.0060
7x10^{15}	0.083	0.916	± 0.0140
1x10^{16}	0.084	0.915	± 0.0051
1x10^{17}	0.084	0.915	± 0.0022

Table 3.5 Penetration depth of 100 keV Ar$^+$ ion in CdS thin films determined using the curve fitting method (PDS technique)

It was observed that thickness values of Ar$^+$ ion implanted layers, obtained from PDS studies for various dosages, coincide well with SRIM calculated values given in Table 3.1.

3.4.2b Studies on Cu$^+$ ion implanted CdS

3.4.2b.1 Optical absorption studies

Energy band gap was calculated from $(\alpha h v)^2$ Vs hv curve. It was found that there was an increase in energy band gap initially to 2.448 eV for very low dosage of 1x10^{13} Cu$^+$ ions/cm^2. But for further increase in dosage, the band gap was remaining almost constant. This was followed by a steep increase to 2.473 eV at 5x10^{15} Cu$^+$ ions/cm^2. Fig.3.23 is the plot for Eg versus Cu$^+$ implantation for various dosages in CdS thin film sample.
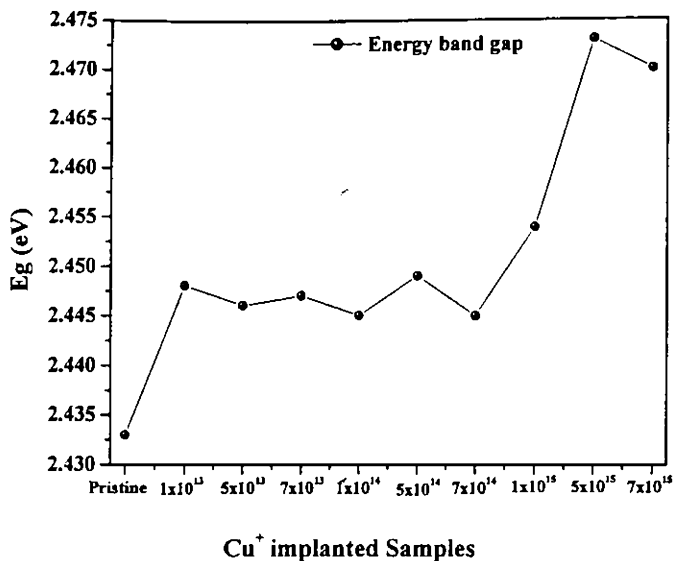
Fig. 3.23 Energy band gap variation for Cu^+ implanted CdS Samples

The observed increase in energy band gap could not be explained from the studies and was not clearly understood. There was no such drastic reduction in grain size leading to the increase of band gap. No cluster formation was observed. But $Cd_{10}Cu_3$ phase appeared from a dose of $1x10^{15}$ ions/cm^2. Band gap was also increasing from this dose. Probably this may be the reason for increase of band gap.

3.4.2b.2 X-Ray Diffraction studies

Fig. 3.24 depicts results of XRD analysis of Cu^+ implanted CdS samples. XRD peaks indicate that CdS had hexagonal orientation. The *c*-axis of crystallites was mostly oriented perpendicular to the substrate. Seven prominent planes were identified and they were (100), (002), (101), (102),

125

(110), (103) and (112) in the case of pristine samples. The peak at $2\theta = 47.81°$ might correspond to (103) CdS_{Hex}, ($20\bar{2}$) CuO, (131) $Cd_{10}Cu_3$. It was found that peak corresponding to $2\theta = 47.81°$ decayed with increase in dosage and reappeared for samples irradiated with a dosage of $1x10^{15}$ Cu^+ ions/cm². This peak was then found for very high dosages of $5x10^{15}$ Cu^+ ions/cm² and $7x10^{15}$ Cu^+ ions/cm². Since implantation was done under high vacuum of 10^{-6} torr, the possibility of formation of ($20\bar{2}$) CuO could be ruled out. In case of pristine there was no chance of Cu contamination. Hence, this peak definitely was due to (103) CdS with Hexagonal orientation. Since the $2\theta = 47.81°$ peak decayed due to Cu^+ implantation its reappearance for the dose of $1x10^{15}$ Cu^+ ions/cm² indicated that this peak might correspond to (131) $Cd_{10}Cu_3$ plane. Mady *et al* [95] had observed the formation of zinc clusters in ZnS films due to nitrogen irradiation.
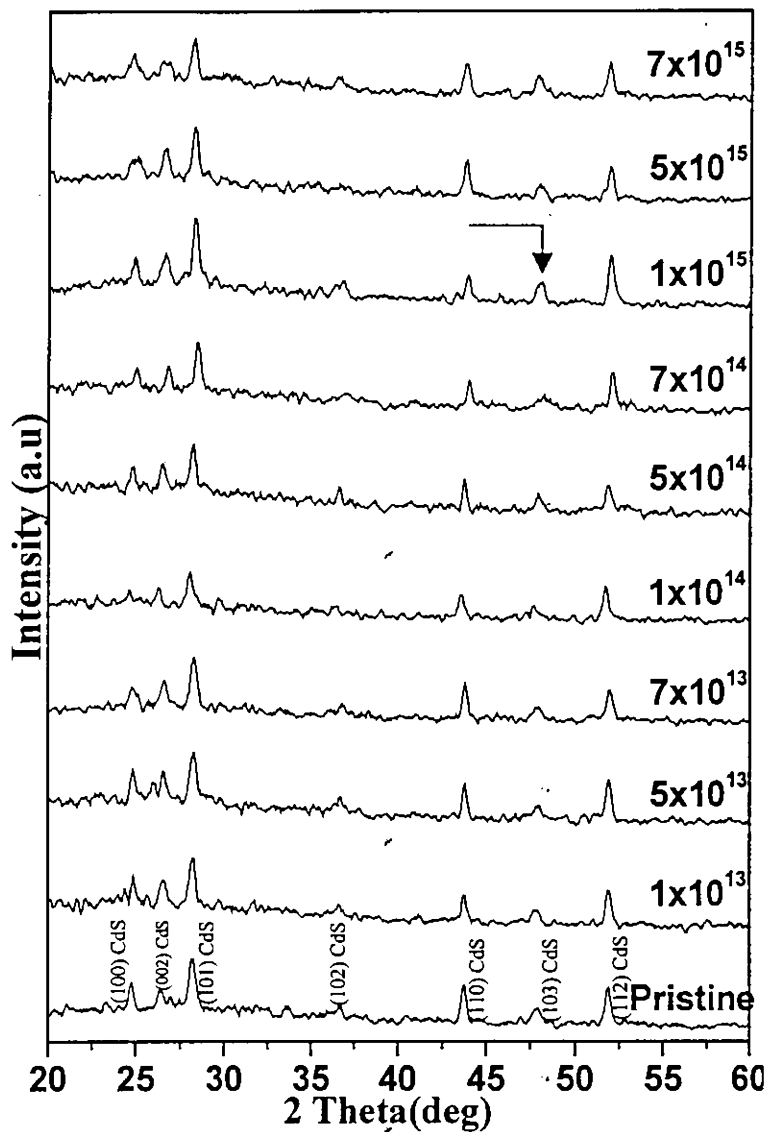
Fig. 3.24 XRD pattern for Cu⁺ implanted CdS samples (arrow mark indicates the re-appearance of (103) peak)

Fig. 3.25 depicts the lattice strain variation of Cu^+ implanted CdS for various dosages. Lattice strain calculated from XRD data showed a decrease initially for initial dosage of $1x10^{13}$ ions/cm^2 and increased for higher dosages from $5x10^{13}$ ions/cm^2. Not much variation was observed for further increase in dosage till $7x10^{14}$ ions/cm^2. Finally there was a drastic decrease in lattice strain for $1x10^{15}$ ions/cm^2. It should be noted that this sample showed the reappearance of $2\theta = 47.81°$ peak.
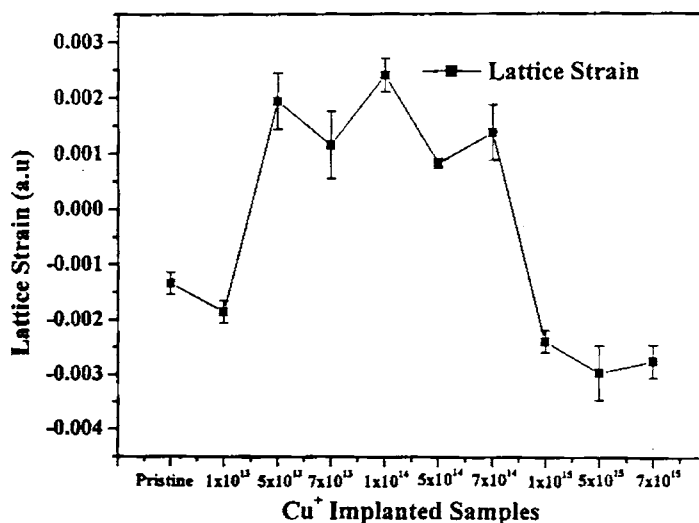
Fig. 3.25 Lattice strain variation for Cu^+ implanted CdS samples

Fig 3.26 depicts the grain size variation of Cu^+ implanted CdS. Grain size was calculated using Debye-Scherrer formula for (101) peak from the XRD pattern. Grain size remained almost unaffected till a dosage of $1x10^{14}$ ions/cm^2. From here onwards the grain size was found to increase for increase in dosage and attained a maximum value of 15.28 nm for $1x10^{15}$ ions/cm^2.
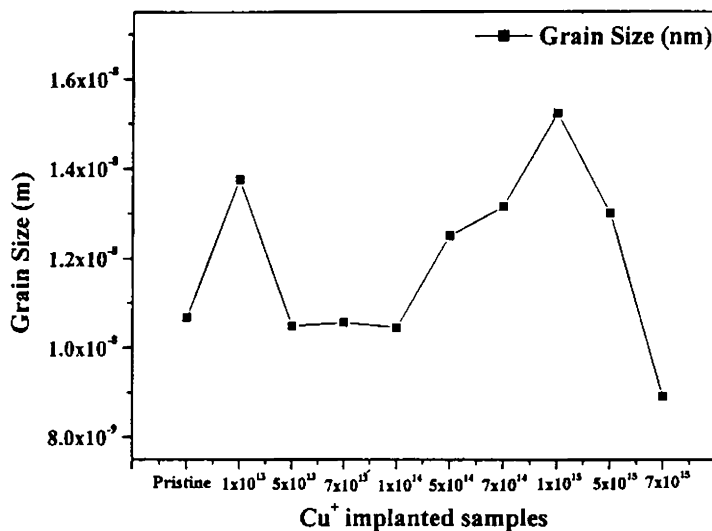
Fig. 3.26 Grain size variation for Cu^+ implanted in CdS.

It is to be specifically noted that changes in lattice strains and grain size occurred for sample irradiated with a dosages of 1×10^{15} Cu^+ ions/cm^2. Band gap also showed a drastic change from this dosage onwards. As stated earlier, the appearance of $Cd_{10}Cu_3$ phase, which also occurred at this dose, may be behind these changes.

3.4.2b.3 Photothermal Studies

3.4.2b.3a Thermal diffusivity measurement

  Thermal diffusivity calculated from linear portion of log amplitude versus square root of chopping frequency is plotted in Fig. 3.27 for various dosages of Cu^+ implantation. Detailed procedure for determining the thermal diffusivity is discussed in chapter 1 (section 1.5.1). The thermal diffusivity

values increased with dosage. It showed maximum value of 0.0169 cm^2/s for $1x10^{15}$ ions/cm^2 and decreased for higher dosages.
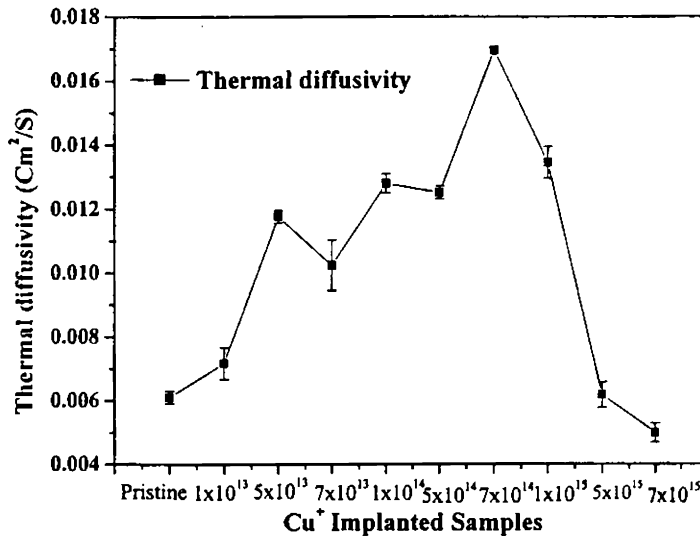

Fig. 3.27 Thermal diffusivity variation for Cu$^+$
implanted CdS samples with dosages.

Here also the decrease $1x10^{15}$ ions/cm^2 appeared to be critical as in the case of band gap, grain size and strain values.

3.4.2b.3b Non destructive thickness measurement

Fig. 3.28 shows the photothermal deflection amplitude versus chopping frequency curve for Cu$^+$ implanted CdS thin films for a dose of $5x10^{13}$ ions /cm^2. Using SRIM calculation, it was found that 1 MeV Cu$^+$ did not reach SnO$_2$ layer. So we used two-layer model as before (section 3.4.2a.3b) for depth profiling. Detailed procedure for depth profiling was discussed in chapter 1 (section 1.4). Here l_1 is the thickness of damaged CdS

layers due to Cu^+ implantation and l_2 is the thickness of the undamaged CdS layer. Thus two layer model was sufficient for the calculation. All other samples were depth profiled using same method. Thickness of these Cu^+ implanted layers obtained by curve fitting is tabulated in Table 3.6.
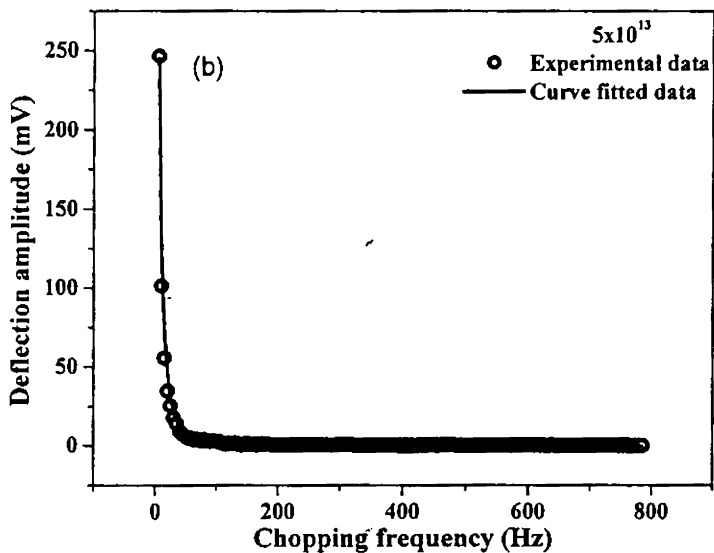

Fig. 3.28 Deflection amplitude versus chopping frequency curve for $5x10^{13}$ ions/cm^2 Cu^+ implanted CdS samples.

Sample (Cu$^+$ ions/cm^2)	Cu$^+$ ion implanted layer thickness (l_1) (μm)	Bottom pure CdS layer thickness (l_2) (μm)	Error Bar
Pristine	-	1.020	± 0.018
1x10^{13}	0.461	0.530	± 0.060
5x10^{13}	0.493	0.512	± 0.012
7x10^{13}	0.452	0.541	± 0.050
1x10^{14}	0.481	0.511	± 0.032
5x10^{14}	0.476	0.538	± 0.015

Table 3.6 Values of penetration depth of 1 MeV Cu$^+$ ion in CdS thin films determined using the curve fitting method (PDS technique)

It was observed that the thickness values obtained from PDS studies for Cu$^+$ ion implanted layers for various dosages coincided well with SRIM calculated values, as seen in Table 3.2.

3.4.2c Studies on He$^+$ ion implanted CdS

3.4.2c.1 Optical absorption studies

Energy band gap was calculated from $(\alpha h v)^2$ versus hv curve. Fig. 3.29 is plot of energy band gap variation of He$^+$ ion implanted CdS samples for various accelerating voltages. It was found that there was a slight decrease in energy band gap initially from 2.456 eV (for pristine) to 2.432 eV for low energy implantation of 60 keV He$^+$ ions/cm^2. Energy band gap then increased to a more or less steady value. The overall variation in the band gap is very small and probably the fact that the He$^+$ ion might not be able to create serious damage, was the reason behind this.
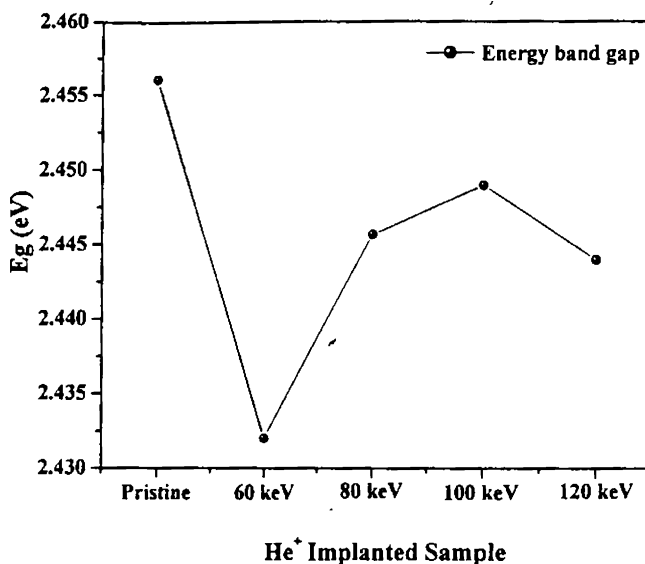
Fig. 3.29 Energy band gap variation of He^+ implanted CdS samples.

3.4.2c.2 X-Ray Diffraction studies

Fig. 3.30 shows variation in XRD peaks due to He^+ implantation. XRD pattern indicated that CdS had hexagonal orientation. The c-axis of crystallites was mostly oriented perpendicular to the substrate. Seven prominent planes were identified and they were (100), (002), (101), (102), (110), (103) and (112). An additional peak corresponding to $2\theta = 38.02°$ in the case of pristine samples coincided well with (200) CdO peak as per JCDPS value. Probably peak did not appear for implanted samples. Thus this could be from surface oxide layer and during the process of implantation this might have been sputtered off.

Fig. 3.31 is the lattice strain variation of He^+ implanted CdS thin films for various accelerating energies. Lattice strain calculated from XRD data increased upto 80 keV and then decreased for 100 keV.
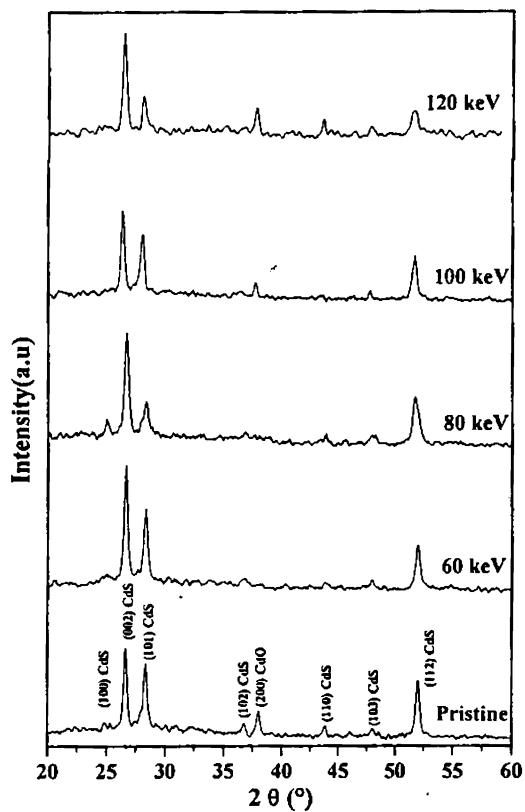

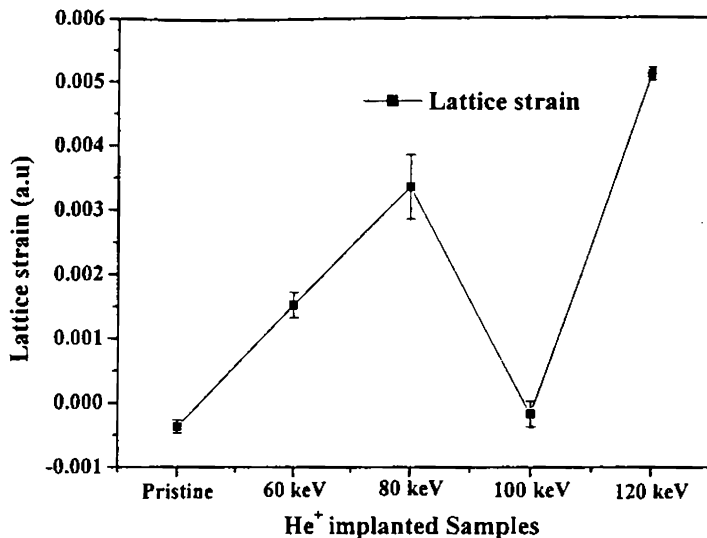Fig. 3.30 XRD diffraction pattern for He^+ implanted CdS samples for various energies.

Fig. 3.31 Lattice strain variation for He$^+$ implanted CdS samples for various energies.

Fig. 3.32 depicts the grain size variation for He$^+$ implanted CdS sample for various accelerating energies. Grain size was calculated using Scherrer's formula. Here one can see a general increase in grain size with accelerating voltage indicating that there was not much severe damage to grain / lattice. A small decrease was found at 100 keV. This might be due to the fact that He$^+$ had comparatively very small size and hence could not create much damage to lattice.
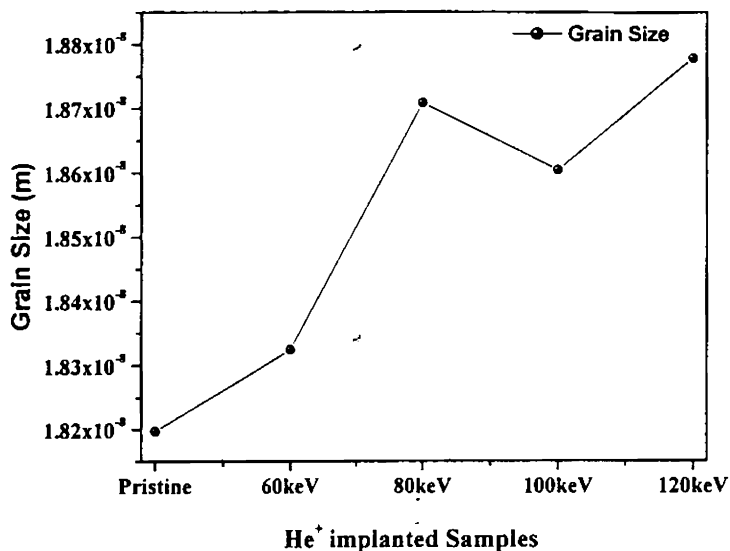
Fig. 3.32 Variation of grain size of He$^+$ implanted CdS samples with increase in accelerating voltage.

3.4.2c.3 Photothermal studies

3.4.2c.3a Thermal diffusivity measurement

Thermal diffusivity calculated from linear portion of log amplitude versus square root of chopping frequency is plotted in Fig. 3.33 for various accelerating voltage of He$^+$ ions. Detailed procedure for determining the thermal diffusivity is discussed in chapter 1 (section 1.5.1). Thermal diffusivity values generally decreased with increase of ion energies. But it showed an increase in the case of sample irradiated with He$^+$ ions of energy 100 keV. This may also be indicating the low level damage created by He$^+$ ions.
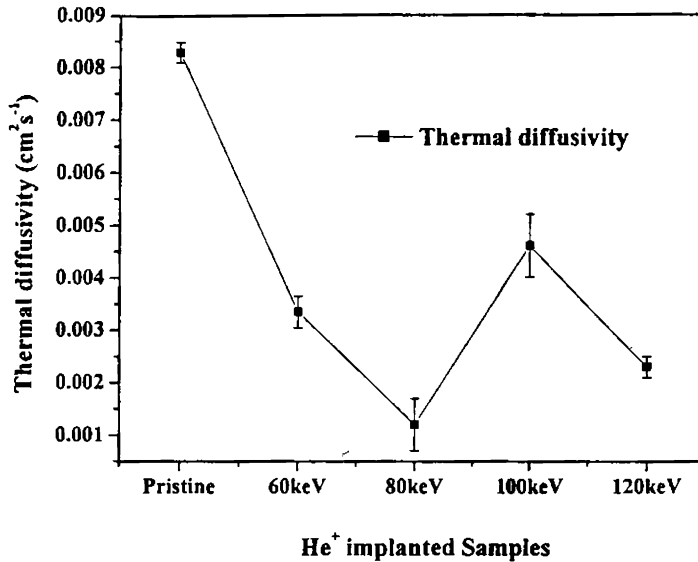
Fig. 3.33 Variation of thermal diffusivity of He^+ implanted CdS samples with accelerating voltage.

3.4.2c.3b Image mapping of ion implanted damage profile

Ion implantation damage distribution profile is roughly Gaussian as observed from SRIM calculation profile depicted in Fig. 3.3, 3.4 and 3.5. Understanding the damage distribution created by the energetic ions in the target helps us in tailoring semiconductor sample for its best usage. Hence, we performed one dimensional scanning of the sample across the implantated portion by moving the pump beam along a line. A layout of the experiment is shown in Fig. 3.34.
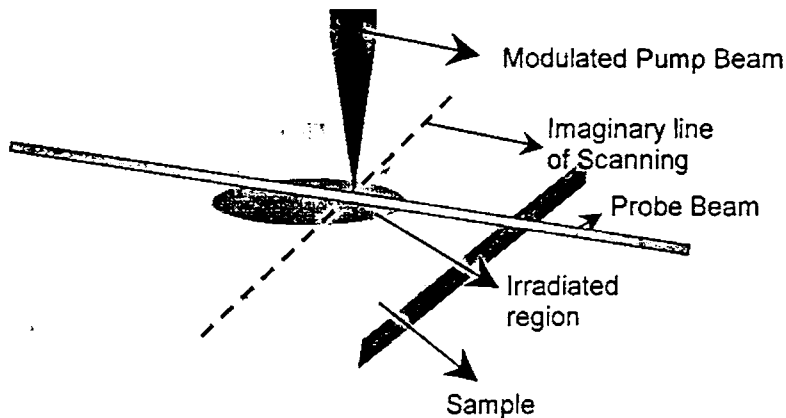
Fig. 3.34 Schematic of layout for imaging measurements.

The pump beam was modulated at a fixed chopping frequency of 5 Hz. Using this fixed chopping frequency, the amplitude of photothermal deflection was measured for different samples irradiated using He^+ ions accelerated at different voltages. For an increase in accelerating voltage, the depth of implantation into the sample increased resulting in the increase of thickness of damaged region. Hence the amplitude of deflection of PDS signal from this region increased considerably. As the pump beam was moved from unirradiated to irradiated region there was a sudden increase in the PDS signal. From this one could get an idea of the depth of implanted region. Data obtained from photothermal deflection method was plotted as a graph of deflection amplitude versus scanned distance for various accelerating voltages (Fig. 3.35). Signal collected from unirradiated portion of the sample shows minimum deflection amplitude. As we reach the implanted region, a sudden increase was observed that resulted in large value of photothermal deflection amplitude. The signal then saturated as we move inside the implanted region.

For increase in accelerating voltage the damage depth inside the sample also increased. We also observed that the strength of the signal was maximum for 120 keV and decreased for lower accelerating voltages and finally the signal was minimum for pristine sample.
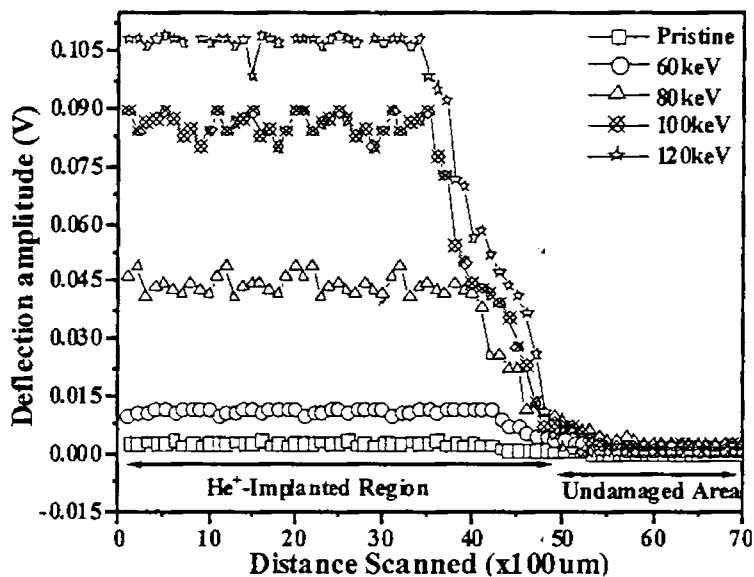

Fig. 3.35 Graph showing deflection amplitude at different distance; Line scanning done over the unimplanted and implanted region on He^+ implanted samples for various accelerating voltage

To study the implantation damage along the depth of the sample, 2-dimensional image was reconstructed from the PDS amplitude value for the pump beam chopping frequency of 5 Hz, 800 Hz and 3000 Hz. As already mentioned in chapter 1 (section 1.4) the penetration depth of thermal waves could be controlled by adjusting modulation frequency so as to get information about the damage created by the ions at different depth inside the sample. As

stated earlier, when chopping frequency is low (like 5 - 20 Hz), we get information from deeper region. But for high frequency (like 1000 – 3000 Hz) information from surface layer is obtained. The scanned area was 400 µm x 500 µm in steps of 50 µm over pristine, 60 keV, 120 keV He$^+$ implanted CdS thin films.

Fig. 3.36 shows the normalized two dimensional image plot for pristine sample for a constant pump beam chopping frequency of 5 Hz. A colour bar shown adjacent to the image plots is the reference of the normalized amplitude value. For low chopping frequency, as the PDS signal is from the depth of the sample, there is not much variation in the PDS amplitude for pristine sample. It can be seen that the pristine is almost defect free from this study.

Fig. 3.37 and Fig. 3.38 show the 2-dimensional PDS image plot for **pristine, 60 keV and 120 keV He$^+$** implanted CdS samples for 800 Hz and 3000 Hz respectively.
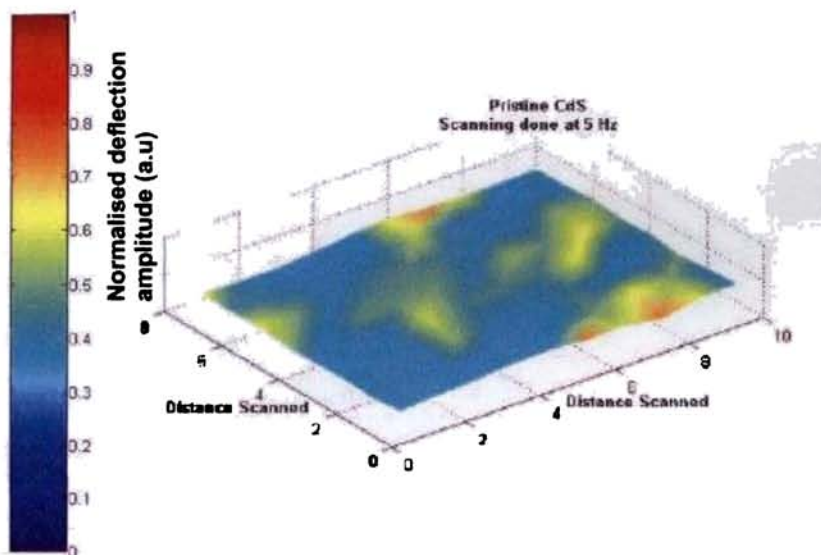
Fig. 3.36 Two dimensional image plot of pristine sample. This surface plot was generated using PDS amplitude values of a constant pump beam chopping frequency of 5 Hz (Figures showing minimum variation in the PDS amplitude signal).
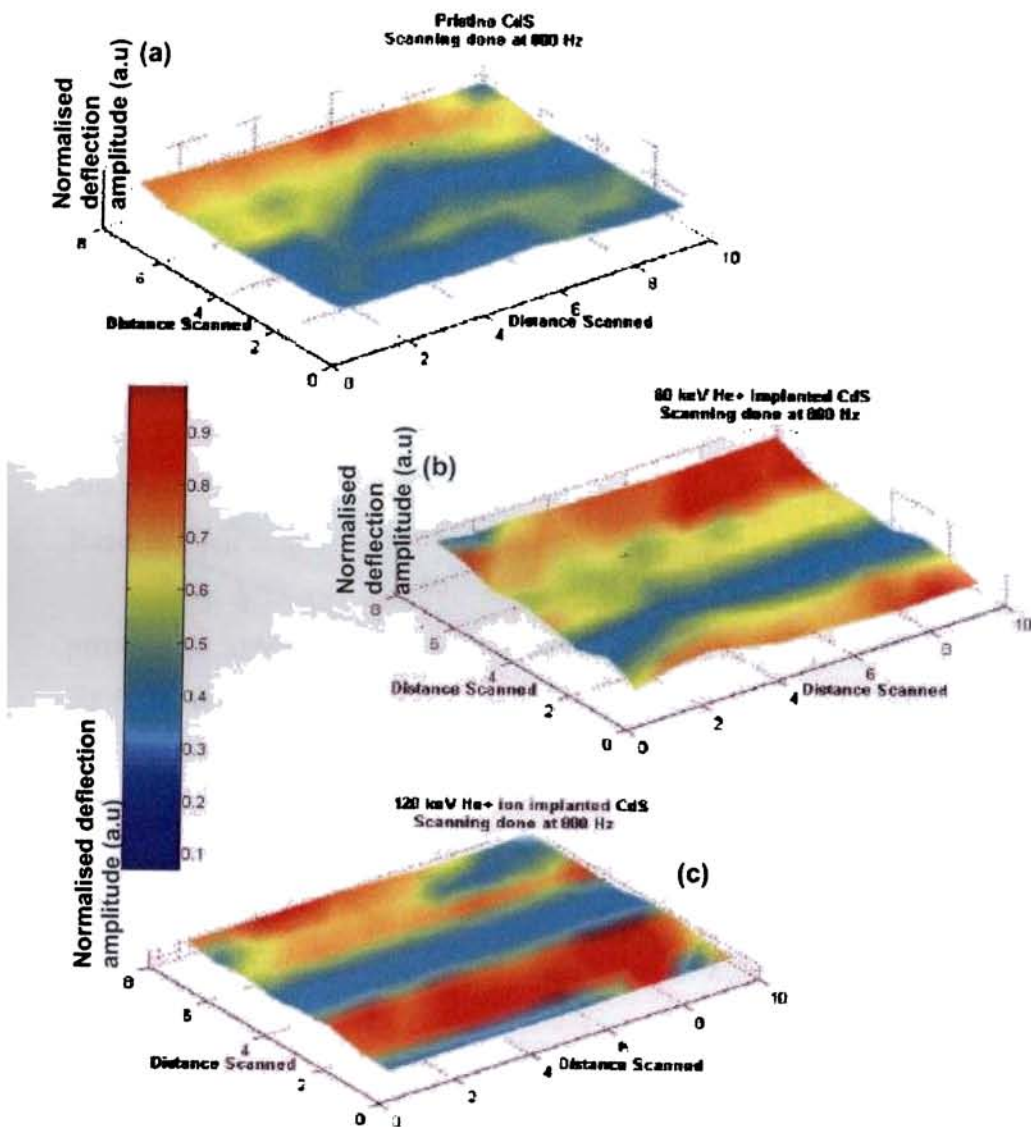
Fig. 3.37 Two dimensional image plot of pristine, 60 keV and 120 keV He⁺ ion implanted samples. This surface plot was generated using PDS amplitude values of a constant pump beam chopping frequency of 800 Hz (Fig. (c) shows maximum damage)
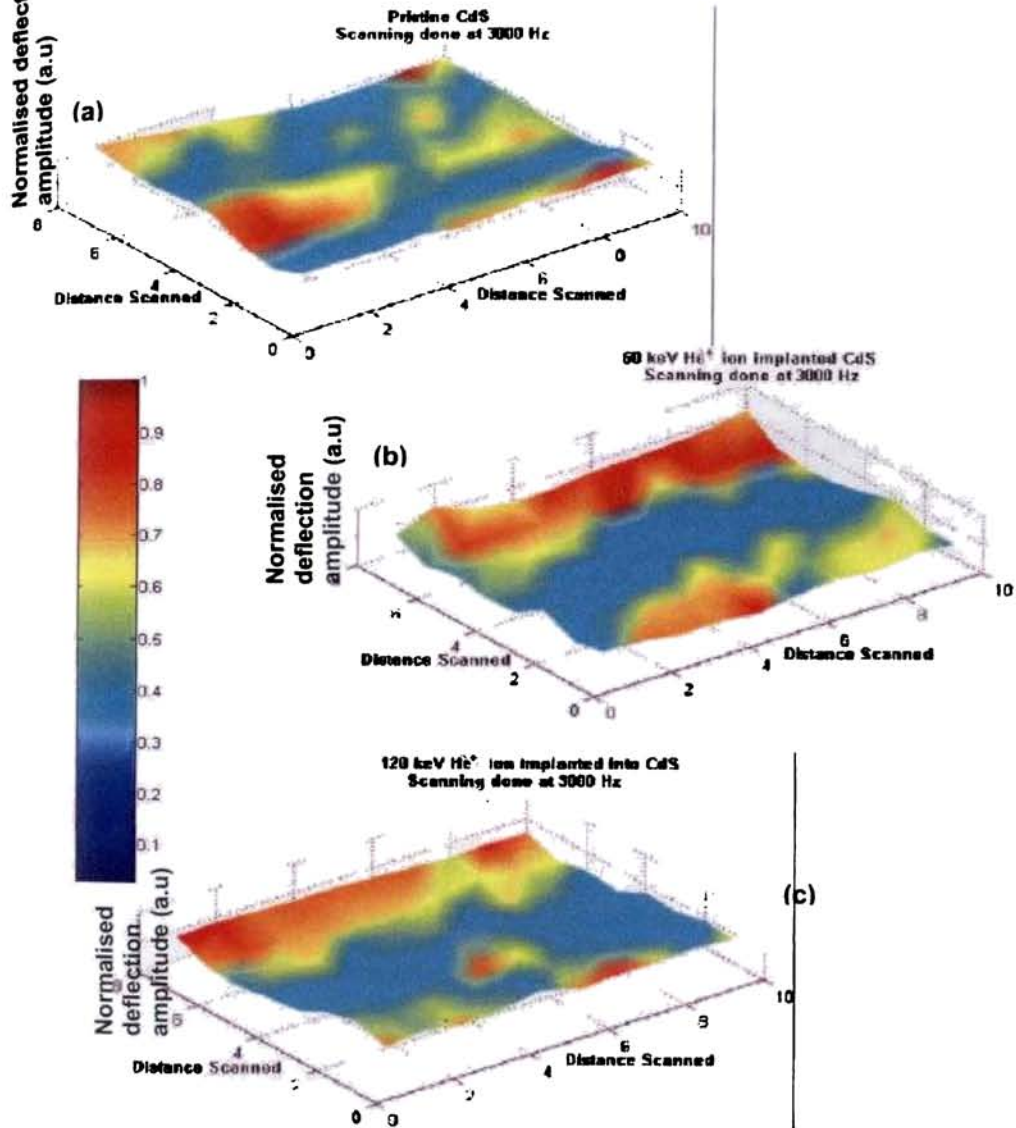
Fig. 3.38 Two dimensional image plot of pristine, 60 keV and 120 keV He⁻ ion implanted samples. This surface plot was generated using PDS amplitude values for a constant pump beam chopping frequency of 3000 Hz (In Fig. (b) and Fig. (c), the damage caused is visible).

On increasing the chopping frequency to 800 Hz, we get information from the central region of the film. But this region will be having minimum damage in the case of pristine and the one irradiated using He$^+$ ions accelerated with 60 keV. Of course the former sample will always have minimum damage. In the case of sample irradiated with 60 keV ion, the maximum damage will be created near the surface layer itself. Hence studies using 800 Hz will not give information about this. On the other hand samples irradiated using 120 keV ion will have maximum damage in the central region and hence PDS signal obtained from 800 Hz may contain information about this. It is observed that Fig. 3.37 (c) shows the maximum damaged area, whereas for 60 keV (Fig. 3.37 (b)) the damage is observed to be less and for pristine (Fig.(3.37) (a)) it is the least. It is to be noted here that Fig. 3.37(c) is for sample irradiated using 120 keV ion. As expected it had maximum damage in the central region. SRIM calculation also shows the same (Table 3.3).

On further, increasing the chopping frequency to 3000 Hz, the signal contribution was mostly from the topmost layer of the sample. At the surface, the ion just enters into the film in a direction perpendicular to the surface of the film with enough energy to pass through the layer and when this energetic ion comes to an immediate stop, excess energy is dissipated by dislocating the neighbouring bound atoms. This initiates the process of a cascade collision whose magnitude could be less as it reaches the surface. Hence the damage caused in this layer might be minimum. This could be the reason for decrease in damage, observed from Fig. 3.38 (b) and Fig. 3.38(c) for 60 keV and 120 keV samples respectively.

3.4.2c.4 Photoluminescence studies

Fig. 3.39 is the Photoluminescence (PL) spectrum of He^+ implanted CdS for various dosages. PL studies on unimplanted samples showed two peaks (P_I and P_{II}). P_I was a sharp peak at 2.37 eV and another (P_{II}) broad peak at 1.97 eV in our case.
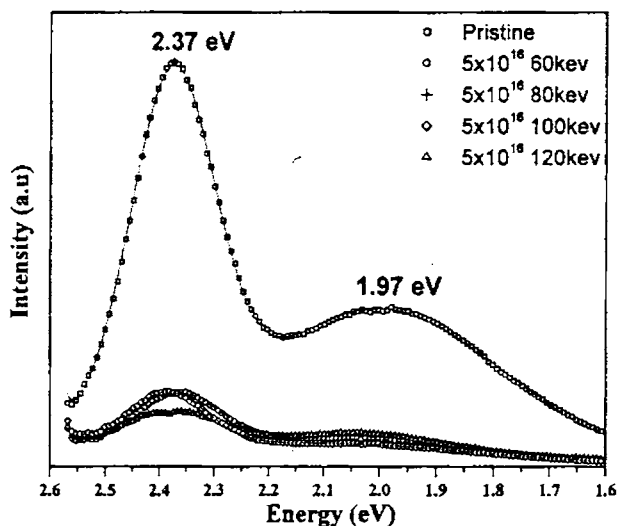

Fig. 3.39 PL spectrum of He^+ implanted CdS samples. PL spectrum of pristine sample is also given for comparision.

Earlier reports on Photoluminescence characterisation of CdS revealed that there were three emissions [96]. One was a well defined green emission with a maximum at 2.4 eV, attributed to direct band to band recombination [97]. The second one was a broad red emission centered around 1.6 - 1.7 eV and the third was a broad infrared emission centered around 1.2 - 1.4 eV [98, 99]. However, we did not observe the third peak. Peak height ratios (P_I/P_{II}) calculated for pristine and implanted samples was found to be almost constant

(~1.8), whereas P_I and P_{II} peak height decreased with increase in acceleration voltage.

Shiraki *et al* [101], Hiramoto *et al* [102] and Humenberger [103] proposed a self-activated center (SAC) model for the red emission, in which the emissive center was a Cd vacancy (V_{cd}) associated with a halogen impurity substituting an S atom. Lambe, Klick and Dexter [104] proposed Lambe-Klick model in which they attributed the red emission to electrons trapped in S vancancy (V_s) recombining with valence-band free hole.

3.5 Conclusion

CdS thin film samples, prepared using chemical spray pyrolysis, were studied to analyse the effect of Cu doping and ion implantation. In the case of Cu doped samples, both thermal diffusivity and mobility were found to decrease initially for small quantity of Cu doping. But these two increased with higher doping concentration. The grain size also showed an initial decrease and then an increase with Cu doping. Thus, it was observed that the grain size had a major role in determining the transport property of the material. Depth of diffusion of Cu atoms into CdS layer was also determined by non-contact depth profiling process. It was found out that the Cu atoms diffused to a depth of ~500 nm, which was also confirmed using XPS studies.

In case of ion implanted samples, penetration depth of different ions species into CdS thin film was determined through curve fitting, using as two layer model. In this model, the bottom layer was considered to be undamaged and the top layer was assumed to be damaged due to ion implantation. Values obtained for penetration depth of 100 keV Ar^+ ion and 1 MeV Cu^+ ion into

CdS layer of 1 μm thick, was found to coincide with the values obtained from SRIM calculation.

Distribution profile of the implanted ion in the sample was studied from 1-dimensional line scanning, performed over the implanted region of the sample. Depth of penetration was found to increase with increase in ion acceleration voltage. Two-dimensional imaging was done in order to understand the damage caused along the depth of the ion implanted sample. These results showed that the damage caused was somewhere near the central region of the sample.

Photoluminescence studies showed two peak at 2.3 eV and at 1.9 eV. The former due to direct band to band recombination and the latter due to electrons trapped in S vancancy recombining with valence-band free hole. Peak intensity of P_I and P_{II} reduced with increase in ion acceleration voltage, whereas P_I/P_{II} ratio was found to be constant.

PDS technique was used to determine the depth of Cu diffusion in CdS in the case of doped samples. For ion implanted samples, thickness of damaged layer due to implantation was also calculated. Ion distribution in the sample due to implantation could be studied and the damage caused could also be 2-dimensionally mapped along the depth.

References

[1] E.Gutsche and J.Voigt, *Proceedings of 7th International Conference on II-VI, Semiconducting Compunds*, held at New York, USA (1967) pp 755.

[2] M. Grus and A. Sikorska, *Physica B*, **266** (1999) 139.

[3] V. D. Vankar and K. L. Chopra, *Phys. Stat. Sol. (a)*, **45** (1978) 665.

[4] S. Vodjani, A. Sharifñai and M. Doroudian, *Electron. Lett.*, **9** (1973) 128.

[5] S. D. Sathaya and A.P.B. Sinha, *Thin Solid Films*, 37 (1976) 15.

[6] Alok K. Berry, P. M. Amirtharaj, Jack L. Booney and Don D. Martin, *Thin Solid Films*, **219** (1992) 153.

[7] B.K. Guptam, O.P. Agnihotri and A. Raza, *Thin Solid Films*, **48** (1978) 153.

[8] Inderjeet kaur, D.K. Pandya and K.L. Chopra, *J. Electrochem. Soc.*, **127** (1978) 943.

[9] K.L. Narayanan, K.P. Vijayakumar, K.G.M. Nair and G.V.N. Rao, *Bull. Mater. Sci.* **20** (1997) 287.

[10] M. A. Martinez, G. H. Herrero and M. T. Gutierrez, *Sol. Energy Mater. Sol. Cells*, **45** (1997) 75.

[11] B. T. Boike, G. S. Khripunov, V. B. Yurchenko and H.E. Ruda, *Ibid.*, **45** (1997) 303.

[12] J. Touskova, D. Kindl and J. Tousek, *Thin solid films*, 293 (1997) 272.

[13] A. Niemegeers and M. Burgelman, *J. Appl. Phys.*, **81** (1997) 2881.

[14] S. Durand, *Thin solid films*, **44** (1977) 43.

[15] N A Zeenath, K P Varkey and K P Vijayakumar, *J.Phys: Condens.Matter*, **10** (1998) 2053.

[16] I. Gunal and H. Mamikoglu, *Thin solid films*, **185** (1990) 1.

[17] Y. Kashiwaba, I. Kanno and T. Ikeda., *Jpn. J.Appl.Phys.*, **31** (1992) 1170.

[18] H. Chavez, M. Jordan, J. C. McClure, G. Lush and V. P. Singh, *J.Mater.Sci.Mater.Electron.*, **8** (1997) 151.

[19] *"Fundamentals of Solar Cells"*, ed. K.L.Chopra and I.Kaur, Plenum Press, New York (1983).

[20] G.F.J. Garlick, and M.J. Dumbleton, *Proc. Soc.* **B 67** (1954) 442.

[21] I. Broser and R. Broser, *J. Physique Rad.*, **8** (1956) 791.

[22] R. Heitz, A. Hoffmann, P. Thurian and I. Broser, *J. Phys.: Condens. Matter,* **4** (1992) 157.

[23] W.W.Anderson and J.T.Mitchell, *Appl. phys. lett.*, **12 (10)** (1968) 334.

[24] N.R. Parikh, D.A. Thompson, and G.J.C. Carpenter, *Rad. Eff.*, **98** (1986) 289.

[25] A.C.Boccara, D.Fournier, W.B.Jackson, and N.M.Amer, *Opt. Lett.,* **5** (1980) 377.

[26] Y. Bouizem, A. Belfedal, J.D. Sib and L. Chahed, *Solid State Commn.*, **126** (2003) 675

[27] P.K.Kuo, M.J.Lin, C.B. Reyes, L.D. Favro, R.L. Thomas, D.S. Kim, Shu Yi Zhang, L.J. Inglehart, D. Fournier, A.C. Boccara, and N. Yacoubi, *Can. J. Phys.,* **64** (1986) 1165.

[28] Daniele Fournier, Claude Boccara, Andrew Skumanich and Nabil M. Amer, *J. Appl.Phys.*, **59** (1986) 787.

[29] P. Grunow and M. Kunst, *J. Appl. Phys.*, **77** (1995) 2767.

[30] E. Gheeraert, A. Deneuville, E. Bustarret and F. Fontaine, *Diamond and related materials*, **4** (1995) 684.

[31] D.C. Reynolds, G. Leiss, L.L. Antes and R.E. Marbuger, *Phys. Rev.*, **96** (1954) 533.

[32] R. H. Bube, *J. Appl. Phys.*, **34** (1963) 2390.

[33] R. H. Bube, *J. Chem. Phys.*, **23** (1995) 18.

[34] A. Ashour, R.D. Gould, A.A. Ramdan, *Phys. Stat. Solidi (a)*, **125** (1991) 541.

[35] L. Hernandez, O. de Melo, O. Zelaya-Angel, R. Lozada-Morales and E. Puron, *J. Electrochem. Soc.*, **141** (1994) 3238.

[36] S.S. Kale, U.S. Jadhav and C.D. Lokhande, *Ind. Jnl. Pure and Appl. Phys.*, **34** (1996) 324.

[37] R.R. Chamberlin and H.S. Skarman, *J. Electrochem. Soc.*, **113** (1966) 86.

[38] C. Wu and R.H. Bube, *J. Appl. Phys.*, **45** (1974) 648.

[39] Yale Y. Ma and R.H. Bube, *J. Electrochem. Soc.*, **124** (1977) 1430.

[40] A. Palafox, G. Romero-Paredes, A. Maldonado, R. Asomoza, D.R. Acosta, J. Palacios-Gomez, *Sol. Ener. Mat. And Sol. Cell.*, **55** (1998) 31.

[41] I.W. Chow, Y.C. Lee and H. L. Kwok, *Thin solid films*, **81**(1981) 307.

[42] D. A. Cusano, *Solid State Electron.*, **6** (1963) 217.

[43] G. Mandel, *Phys. Rev.*, **134** (1964) A1073.

[44] R.H. Bube, *"Photoconductivity of Solids"*, Wiley, New York (1960).

[45] J.Woods and J.A.Campion, *J.Electron.Control*, **3** (1960) 243.

[46] H.G.Grimmeis and R.Memming, *J.Appl.Phys.*, **33** (1962) 2217.

[47] T.Abe, J. Sato, S. Ohashi, M. Wantanabe and Y. Kashiwaba, *Phys. Stat. Sol. (b)*, **2** (2002) 1015.

[48] P.J.Sebastian, *Appl. Phys.Lett.*, **62** (1993) 2956.

[49] S.Mathew, P.S.Mukerjee, and K.P.Vijayakumar, *Jpn.J.Appl.Phys.*, **34** (1995) 4940.

[50] E. Khawaja and S. G. Tomlin, *J. Phys. D: Appl. Phys.*, **8** (1975) 581.

[51] S.H.Wei, A.Zunger, *Phys. Rev.B*, **37** (1988) 8958.

[52] Sunny Mathew, P.S. Mukerjee and K.P. Vijayakumar, *Thin solid films*, **254** (1995) 278.

[53] K. L. Narayanan, R. Rajaraman, M.C. Valsakumar, K.G.M. Nair, and K. P. Vijayakumar, *Mat. Res. Bull.*, **34** (1999) 1729.

[54] Y.Shiraki, T.Shimada, and K.F.Komatsubara, *J.Appl. Phys.*, **43** (1972) 710.

[55] F.Chernow, G.Eldridge, G.Ruse, and L.Wahlin, *Appl. Phys. Lett.* **12** (1968) 339.

[56] W.W.Anderson, *Solid State Electron.* **11** (1968) 421.

[57] B.Tell and W. M. Gibson, *J. Appl. Phys.*, **40** (1969) 5320.

[58] Ratnasagar and M.P. Srivastava, *Phys. Lett. A*, **183** (1993) 209.

[59] M. Kitagawa and T. Yoshida, *Appl. Phys. Lett.*, **18** (1971) 41.

[60] V.Ruxandra and S.Antohe , *J. Appl. phys.*, **84 (2)** (1998) 727.

[61] A.L. Dawar, P.K. Shishodia, Gayatri Chauhan, Anilkumar and P.C. Mathur, *J. Appl.Phys.*, **67** (1990) 6214.

[62] K.L. Narayanan, K.P. Vijayakumar, K.G.M. Nair and R. Kesavamoorthy, *Phys. Stat.Sol. (a)*, **164** (1997) 725.

[63] G.Amarendra, K.L.Narayanan, G.Venugopal Rao, B.Viswanathan, and K.G.M.Nair, K.P.Vijayakumar, *J. Appl. Phys.*, **84 (8)** (1998) 4448.

[64] K. Senthil, D. Mangalaraj, Sa.K. Narayandass, R. Kesavamoorthy, G.L.N. Reddy, B. Sundaravel, *Physica B*, **304** (2001) 175.

[65] M.V.Yakushev, R.W.Martin, J.Krustok, A.V.Mudriy, D.Holman, H.W.Schock , R.D.Pilkington, A.E.Hill, R.D.Tomlinson, *Thin solid films*, **387** (2001) 201.

[66] B.M. Basol, V.K. Kapur and A. Halani, *Conf. Rec. 22nd IEEE Photovoltaic Specialist Conf.*, held at Las Vegas, New York, (1991) pp

893.

[67] K.P.Varkey and K.P.Vijayakumar, *Jpn. J. Appl. Phys.*, 36 (1997) L394.

[68] H.L. Kwok, *J. Phys. D: Appl. Phys.* 13 (1980) 1911.

[69] J. Dresner and F. V. Shallcross, *J. Appl. Phys.*, 34 (1963) 2390.

[70] S.A. Tomas, O.Vigil, J.J. Alvarado-Gil, R. Lozada-Morales, O.Zelaya-Angel, H.Vargas and A. Ferreira da Silva, *J. Appl. Phys.*, 78 (1995) 2204.

[71] Yu-Shen Yuang, Yang-Fang Chen, Yang-Yao Lee and Li-Chi Liu, *J. Appl. Phys.* 76 (1994) 3041.

[72] A. Salazar, A. Sanchez-Lavega and J. Fernandez, *J. Appl. Phys.* 65 (1989) 4150.

[73] K. N. Madhusoodanan and J. Philip, *Phys. Stat. sol. (a)*, 108 (1989) 775.

[74] M. Bertolotti, R. Li Voti, G. Liakhou and C. Sibilia, *Rev. Sci. Instrum.* 64 (1993) 1576.

[75] Kyrill L. Muratikov, Aleksei L. Glazov, and Heinz G. Walther, *High temperatures High pressure*, 31 (1999) 69.

[76] K. Friedrich, K. Haupt, U. Seidel and H.G. Walther, J. *Appl. Phys.* 72 (1992) 3756.

[77] S. Grauby, B.C. Forget, S. Hole, D. Fournier, *Rev. Sci. Instrum*, 70 (1999) 3603.

[78] T. Kawahara, M. Miyazaki, A. Kimura, Y. Okamoto, J. Morimoto and T. Miyakawa, *Appl. Phys. A*, 69 (1999) 343.

[79] R. Tilgner, J. Baumann and M. Beyfuss, *Can. J. Phys.*, 64 (1986) 1287.

[80] J. Baumann and R. Tilgner, *Can. J. Phys.*, 64 (1986) 1291.

[81] Haruo Fujimori, Yamato Asakura, Kazumichi Suzuki and Shunsuke Uchida, *Jpn. Jnl. Appl. Phys.*, 26 (1987) 1759.

[82] Ts. S. Velinov and K. P. Bransalov, *Phys. Stat. Sol. (a)*, 121 (1990) 555.

[83] H. G. Walther and V. Aleshin, *J. Appl. Phys.*, **86** (1999) 6512.

[84] Y. Nagasaka, T. Sato and T. Ushiku, *Meas. Sci. Technol.*, **12** (2001) 2081.

[85] Takashi Abe, Yasube Kashiwaba, Mamoru Baba, Jun Imai, and Hideyaki Sasaki, *Appl. Surface Science*, **175-176** (2001) 549.

[86] Susumu Keitoku, Hiromichi Ezumi, Hiroto Osono, and Mitsuo Ohta, *Jpn. J. Appl. Phys.*, **34** (1995) L138.

[87] G. Langer, J. Hartmann and M. Reichling, *Rev. Sci. Instrum.*, **68** (1997) 1510.

[88] Sunny Mathew, P.S. Mukerjee, and K.P. Vijayakumar, *Jpn. J. Appl. Phys.*, **34** (1995) 4940.

[89] Kodigala Subba Ramaiah, V. Sundara Raja, and A. K. Bhatnagar, *Semicond. Sci. Technol.*, **15** (2000) 676.

[90] K.L. Chopra and S.R. Das, *Thin film solar cells*, Plenum press-New york (1983).

[91] N.G. Dhere and N.R. Parikh, *Thin Solid Films,* **60** (1979) 257.

[92] S. R. Das, *Ph.D Thesis*, Indian Institute of Technology-Delhi (1978).

[93] K.P. Varkey, K. P. Vijayakumar, T. Yoshida, and Y. Kashiwaba, *Renewable energy*, **18** (1999) 465.

[94] K. Senthil, D. Mangalaraj, Sa. K. Narayandass, Byungyou Hong, Yonghan Roh, Cheon Seok Park and Junsin Yi, *Semicond. Sci. Technol.*, **17** (2002) 97.

[95] K.H.A. Mady, Z.S.Moustafa, M.S.Selim, A.A. Gabr, *J.Mater.Sci.*, **23** (1988) 2403.

[96] I.J. Ferrer, and P. Salvador, *J. Appl. Phys.*, **66** (1989) 2568.

[97] B. A. Kulp and R. H. Kelley, *J. Appl. Phys.*, **31** (1960) 1057.

[98] T. Shiraki, T. Shimada, and K. F. Komatsubara, *J. Appl. Phys.*, **45** (1972)

3554.

[99] C. N. Elsby and J. M. Meese, *J. Appl. Phys.*, **43** (1972) 4818.

[100] Mahuya Chakrabarti, Sreetama Dutta, S Chattapadhyay, A Sarkar, D Sanyal and A Chakrabarti, *Nanotechnology*, **15** (2004) 1792.

[101] T. Shiraki, T. Shimada, and K.F. Komatsubara, *J. Appl. Phys.*, **45** (1974) 3554.

[102] H. Hiramoto, K. Hashimoto, and T. Sakata, *Chem. Phys. Lett.*, **133** (1987) 440.

[103] J. Humenberger, G. Linnert, and K. Lischka, *Thin Solid Films*, **121** (1984) 75.

[104] J.J. Lambe, C.C. Klick, and D.L. Dexter, *Phys. Rev.*, **103** (1956) 1715.

Chapter 4

STUDIES ON INDIUM SULPHIDE THIN FILMS

4.1 Introduction

β-In$_2$S$_3$ is a semiconductor with a band gap of 2.0 – 2.8 eV having excellent photoconducting, photoluminescent properties that makes it a promising optoelectronic material [1]. This material had been used in the preparation of green and red phosphors and in the manufacture of picture tubes for colour televisions [6], dry cells [7] and heterojunctions to be used as photovoltaic devices [8].

In$_2$S$_3$ is a III-VI compound originating from II-VI compound semiconductor by replacing group II metals by group III elements [9]. It exists in three different forms viz., α, β and γ [10]. In this, α-In$_2$S$_3$ has cubic structure between 420 °C and 754 °C and γ-In$_2$S$_3$ has trigonal structure above 754 °C [11]. β-In$_2$S$_3$ has tetragonal structure below 420 °C and gets transformed into a layered structure at 740 °C [12, 13, 14]. Recently, there has been great interest in the optoelectronic properties of indium sulphide [15, 16].

Optical properties of In$_2$S$_3$ thin films depend mainly on the method of prepration and stoichiometry. It can be found that its band gap varies from 2.0 eV [17] to 2.8 eV [15]. This large band gap makes this material good candidate, to substitute CdS as buffer layer in thin film solar cells. This is a very effective replacement for cadmium containing buffer layer, in thin film solar cells to obtain more environmentally friendly photovoltaic technology and to improve the light transmission in the blue region due to wider band gap.

A number of techniques had been used to prepare this compound in thin film form such as organometallic chemical vapor deposition [18], spray pyrolysis [15, 19-21], thermal evaporation [22] and rf sputtering [23]. Among these, chemical spray pyrolysis (CSP) is a simple, low tech and cost effective technique, suitable for depositing large area films. Here one uses solution containing salts of the elements of the compound whose film is to be coated. Usually chlorides of metal elements are used. This results in unintentional introduction of chloride into the film. In the case of In_2S_3 films also, $InCl_3$ is usually used and this results in doping with chlorine. In order to avoid this, indium nitrate or indium acetate can be used as precursor. When nitrate is used substrate temperature can also be reduced. There are works going on in this direction [45]. Successive Ionic Layer Adsorption and Reaction (SILAR) is another recent technique for thin film deposition [28]. This technique has been used for depositing In_2S_3 films very recently [47] in our own lab.

In this chapter we describe the optical, electrical and thermal characterisation of In_2S_3 prepared using CSP and SILAR techniques. Characterisation is done using PDS technique.

4.2 Brief review of earlier works on In_2S_3 films and crystals

By around 1949 Hahn *et al* [29] studied the crystal structure of indium sulfide. This could probably be the earliest study on In_2S_3. By 1959 Rooymans *et al* [30] interpreted some extra lines in the XRD pattern indicating that In_2S_3 was in fact tetragonal. The tetragonal unit cell was formed by the superposition of three spinel blocks and a four-fold screw axis appeared as a result of indium

156

vacancy ordering. The same year Bube *et al* [31] and Syrbe *et al* [32] studied electrical properties of indium sulfide. By 1962 Gilles *et al* [33] studied photoconductivity of indium sulfide and observed that this compound behaved like compensated semiconductor when it was prepared using direct synthesis under a pressure of sulphur of order 5 to 10 atmospheres. The sample, so prepared, had dark conductivity at room temperature in the order 10^{-7} $\Omega^{-1}cm^{-1}$. When an illumination of 1000 lux was given the conductivity increased by five orders of magnitude. They also observed that Cu doping markedly increased the photosensitivity of this compound. Photoconductivity decay time was found to be in the order of 10^{-3} second. By 1965 Rehwald *et al* [12] published work on conduction mechanism of single crystal β-In$_2$S$_3$. They found that In$_2$S$_3$ samples, grown by chemical transport reaction, showed n-type conductivity and samples having high resistivity exhibited an exponential increase of Hall mobility with temperature. They explained this effect by assuming a mixed conduction and different scattering mechanisms for electrons and holes in the same temperature range. They also demonstrated that by heating, sulphur treatment and doping, the concentration and sign of charge carriers deviated from stoichiometric composition.

Herrero *et al* [34] prepared n-type β-In$_2$S$_3$ thin films having good crystallinity by chalcogenization of metallic electroplated indium. These thin films were found to be thermodynamically stable in the polysulphide electrolyte because its photodecomposition potential was more positive than the polysulphide redox couple potential. Asikainen *et al* [1] prepared β-In$_2$S$_3$ by atomic layer epitaxy using InCl$_3$ and H$_2$S as precursors. They observed that the films had a modified spinel structure in which one third of the tetrahedral metal sites remained empty and vacancies were ordered onto the 4$_1$ screw. The

photoresponse observed was reversible and recovery of conductivity occurred shortly after the sample had been re-exposed to light. Yu *et al* [10] prepared nanocrystalline powder of β-In_2S_3 through hydrothermal process. The particles were spherical in shape with a grain size of 13 nm. The same group [35] prepared nanocrystalline β-In_2S_3 by organothermal synthesis having the crystallite size of 7.7 nm. Lokhande etal [36] deposited In_2S_3 thin films using Chemical Bath Deposition (CBD) technique. From Transmission Electron Microscopy (TEM) results they found that the initial growth of the film on glass substrate was γ-In_2S_3 phase. Seyam [37] had studied the optical and electrical properties of indium monosulfide thin films prepared using thermal evaporation. He observed that films deposited at a substrate temperature of 473 K were homogeneous and stoichiometric. XPS results revealed the composition to be 50.76 % S and 49.24 % In. Barreau *et al* [38] synthesized wide band gap In_2S_3 using Physical Vapour Deposition (PVD) method. Energy band gap was found to be 2.8 eV. The observed band gap and the optical constants (n and k values) did not significantly depend on annealing temperature. The same group [39] did a comparative study on In_2S_3 films prepared using CBD and PVD In_2S_3. They found that, by annealing in appropriate conditions, PVD In_2S_3 films could be grown with similar properties of CBD In_2S_3. They also observed the presence of oxygen contamination that was infact advantageous. Choe *et al* [40] prepared β-In_2S_3 and β-In_2S_3:Co^{2+} single crystals grown by chemical transport reaction method, using In_2S_3, S, and ZnS as starting materials and ($ZnCl_2$+I_2) as transport agent. Optical studies were preformed in temperature range from 5 K to 300 K. Indirect and direct transitions of the films were also studied and they observed optical absorption peaks due to β-In_2S_3:Co^{2+}. Xiong *et al* [41] prepared In_2S_3

nanocrystals using solvent-reduction method. They also used cetyltrimethylammonium bromide (CTAB) as a modifier to shape the products. The product was found to be quantum confined. In_2S_3 nanoparticles, short nanowhiskers, nanorods and finger structured nanocrystals having stoichiometric composition could be prepared using this method.

Kim *et al* [42] coated $Co_xIn_2S_{3+x}$ thin films by CSP method having tetragonal structure of In_2S_3 and the films became amorphous above *x*=0.6. The energy band gap of these films decreased with increasing *x*. The same group [15] studied optical and structural properties of β-In_2S_3 prepared using CSP method. Kamoun etal [19] prepared InS films with composition close to that of In_2S_3 by an airless spray technique from spray solutions with composition ratio (y =$[In^{3+}][S^{2-}]$) varying from 0.43 to 0.6. Films having composition y = 0.6, were β-In_2S_3 having high crystalline quality. The same group [43] had deposited β-In_2S_3 and β-In_{2-x} Al_xS_3 using spray method on different substrates such as, pyrex glass, SnO_2/pyrex and steel. They reported that, nature of substrate and presence of Al atoms in the material contributed to the growth of deposited film. Best crystallinity for β-In_2S_3 was observed when deposited on SnO_2/pyrex. The best composition was obtained for In_2S_3 deposited on SnO_2 after annealing. Bhira *et al* [44] studied structural and photoelectrical properties of sprayed β-In_2S_3 thin films. Photoconductivity measurements carried out using visible light at different modulation frequency and bias voltages showed that the energy band gap was comparable to that of values obtained through optical absorption methods. Teny *et al* [21] had studied In_2S_3 thin film samples prepared using CSP method. Good control over the photosensitivity of these samples could be acheived by varying substrate temperature or In/S ratio. The same group [45] also prepared In_2S_3 thin film

samples using indium nitrate precursor in order to avoid chlorine contamination.

Mane *et al* [28] used SILAR method to deposit In_2S_3 thin films. These films were observed to be highly resistive (of the order 10^5 Ω cm). SEM images revealed that the films were homogeneous, pinhole free and without cracks. Ranjith *et al* [47] prepared β-In_2S_3 thin films using SILAR method. They did a comparative study with samples prepared using (CSP). X-ray diffraction (XRD) studies showed that the grain size for SILAR samples were very small (about 6.54 nm) when compared with CSP samples (24.91 nm).

Detailed study of the conduction mechanism in single crystal β-In_2S_3 was carried out by Rehwald *et al* [12]. They reported that conductivity was always n-type and no p-type conduction could be observed even when the samples were doped with copper or cadmium. Mirovsky *et al* [48] had done the thermodynamic studies of the photoelectrochemical behaviour of In_2S_3. Gasanly *et al* [49] studied Photoluminescence (PL) of InS single crystals in low temperature range (between 8.5 – 293 K). They observed three PL bands centered at 2.05 eV, 1.98 eV and 1.51 eV. These peaks were observed at 8.5 K. In this the last peak, centered at 1.5 eV, was very weak. On increasing the temperature, peak intensities decreased. Jayakrishnan *et al* [50] observed four peaks at 563 nm, 612 nm, 663 nm, and 840 nm. Qasrawi *et al* [51] identified defect levels in InS crystals using optical and electrical measurements. They assumed these levels to be due to the presence of native structural defects and strain in the films.

Hara *et al* [52] fabricated an electrochemical solar cell based on nanocrystalline In_2S_3/In_2O_3 thin film electrodes. They observed photon to electron conversion efficiency of 33 % at 410 nm while solar cell conversation

efficiency was 0.31%. Teny *et al* [53] fabricated $CuInS_2/In_2S_3$ thin film solar cell, fully using CSP method, having an efficiency of 9.5%.

We could not find any reported work of characterisation of In_2S_3 thin films, prepared using CSP or SILAR method using PDS technique. To the best of our knowledge, this could be the first kind of work in that direction.

4.3 Experimental Details

4.3.1 Preparation of In_2S_3 using SILAR method

Thin film samples of In_2S_3 were prepared using SILAR technique, in the following method. $InCl_3$ solution (0.01 M; pH ~4) was used as cationic precursor and Na_2S solution (0.01M; pH ~11) was the anionic precursor. Cleaned glass substrates were immersed in cationic precursor ($InCl_3$ solution) for a short time "s" seconds, which resulted in adsorption of Indium ions on the surface of the glass substrate. The substrate was then immersed in double distilled water for a short time "w" seconds. This was done to prevent homogeneous precipitation on the substrate during the film deposition. The substrate was then immersed in anionic precursor (Na_2S solution) for "s" seconds. As the last step, the substrate was again immersed in double distilled water for "w" seconds and this completed one "SILAR" cycle. Thin layer of film, coated over the substrate, was visible. During the process of dipping, sulfide ions were reacting with adsorbed indium ions on glass substrate, resulting in the formation of In_2S_3 layer. All these samples were deposited at room temperature. Uniform layer of good quality thin films was found to be coated after 100 cycles. To increase the film thickness, we repeated the process up to 300 cycles. Above 300 cycles, the film surface was observed to be

powdery. Water used for rinsing was removed after every ten SILAR cycles. For the film deposition, we used an indigenously designed microprocessor controlled set up. Using this, we could control dipping time as well as number of dips in precursors and water.

One set of samples prepared were named as 5s2w, 6s2w, 8s2w, 10s2w, 12s2w and 15s2w, where "s" indicates the dipping time in the precursor solution and "w" the dipping time in water. We called this as "Set 1" samples.

Another set of samples were prepared by varying dipping time in water (2 to 15 seconds) and constant (2 second) rinsing time in solution. We selected best samples for PDS studies from this set and they were "2s2w" and "2s6w". These were samples from "Set 2". These samples were latter annealed at 400 °C for 1 hour in vacuum at 10^{-5} Torr. Annealed samples were named as "A2s2w" and "A2s6w".

4.3.2 Preparation of In_2S_3 thin film samples having various atomic concentrations of indium and sulphur using CSP technique

In_2S_3 samples, having various thicknesses, were prepared by spraying the solution of indium chloride (In_2Cl_3) and thiourea $(CS(NH_2)_2)$ over a hot glass substrate kept at 300 °C. Atomic concentration of In:S in the solution was kept constant at 2/5. By increasing the volume of spray solution we could increase sample thickness. Volume of solution sprayed was 400 ml, 600 ml, 800 ml and 1000 ml. Rate of spray was kept at 20 ml/min for all cases. Detailed description of sample preparation is given elsewhere [21]. Samples thus prepared were named as "400", "600", "800" and "1000". These samples were annealed at 400 °C for 1 hour in vacuum maintained at 10^{-5} Torr. Annealed samples were named as "A400", "A600", "A800" and "A1000".

In$_2$S$_3$ samples, with various In/S ratio, were prepared by varying the molar concentration of InCl$_3$ and (CS(NH$_2$)$_2$) for In/S ratio varying between 2/1 to 2/8. Quantity of spray solution taken was 400 ml in all the cases.

In$_2$S$_3$ thin films were also prepared using indium nitrate (In(NO$_3$)$_3$) and thiourea (CS(NH$_2$)$_2$) as precursor solutions. Indium to sulphur ratio was varied by varying molar concentrations of precursor solutions for In/S ratios ranging from 2/1 to 2/8. This was done be maintaining the molarity of indium nitrate at 0.025 M and by varying the molarity of thiourea. Detailed description of the sample preparation is given elsewhere [45]. Total volume of the solution sprayed was 400 ml and the rate of spray was 20 ml/min in all cases, keeping the substrate at 300 °C, with air as the carrier gas. These samples are named in terms of In/S ratio.

4.4 Results and Discussion

4.4.1 In$_2$S$_3$ thin film samples prepared using SILAR method
4.4.1.1 Structural and optical properties

The direct band gap of In$_2$S$_3$ thin films prepared using SILAR method was estimated by plotting $(\alpha h \nu)^2$ versus hν and extrapolating the linear portion near the onset of absorption edge to the energy axis. Band gap value showed linear decrease from 2.54 eV to 2.26 eV with increase in dipping time in solution for 5s2w to 15s2w in "Set 1" samples. Similar trend was observed for unannealed and annealed samples in "Set 2" also.

XRD studies showed that all these samples should either be amorphous or polycrystalline in nature. Only after annealing, the samples showed weak peaks corresponding to β-In$_2$S$_3$. In "Set 1", the crystalline quality

for "10s2w" was found to be better (Fig. 4.3). When it comes to "Set 2", they were all observed to be amorphous in nature and after annealing, only "A2s2w" showed peaks corresponding to β-In$_2$S$_3$. Enhancement of β In$_2$S$_3$ peak after annealing could be due to orderly rearrangement of cationic vacant sites [11].

4.4.1.2 Photothermal studies

Understanding the microstructural, thermal and transport properties for these thin films are important because SILAR is a new method for thin film preparation and hence there are not much reports this type of samples. As PDS technique generates thermal waves within the sample, understanding its propagation within the materials gives an idea of thermal and transport property. Moreover, it is non-contact and non-destructive. Thermal diffusivity and mobility of these sample is determined using the procedure described in chapter 1 (section 1.5.1 and 1.5.2 respectively).

4.4.1.2a Thermal diffusivity measurement

Fig. 4.1 gives variation of thermal diffusivity of "Set 1" SILAR samples having different dipping timing in solution. Thermal diffusivity was observed to be maximum for "10s2w" showing a value 0.357 cm^{2}s^{-1}. The value was found to decrease with increase in dipping time in solution. From XRD pattern it was observed that "10s2w" showed relatively good crystalline quality (Fig. 4.3). Fig. 4.2 shows the variation in thermal diffusivity for annealed SILAR samples from "Set 2". Thermal diffusivity values measured for unannealed samples was very low. Samples after annealing had better thermal diffusivity compared to the unannealed samples. Thermal diffusivity

values calculated for "A2s2w" sample was found to be 0.167 cm^2s^{-1} and was the maximum. Thermal diffusivity was found to decrease linearly for "A2s2w" and "A2s6w" reaching a minimum of 0.136 cm^2s^{-1}. High thermal diffusivity for "A2s2w" could be due to its improved crystalline quality (Fig. 4.4). However, if we compare Fig. 4.3 and Fig. 4.4, one can see that crystallinity is much better for annealed samples. But thermal diffusivity values of annealed sample is much lower than that of "Set 1" samples. This is not clearly understood.
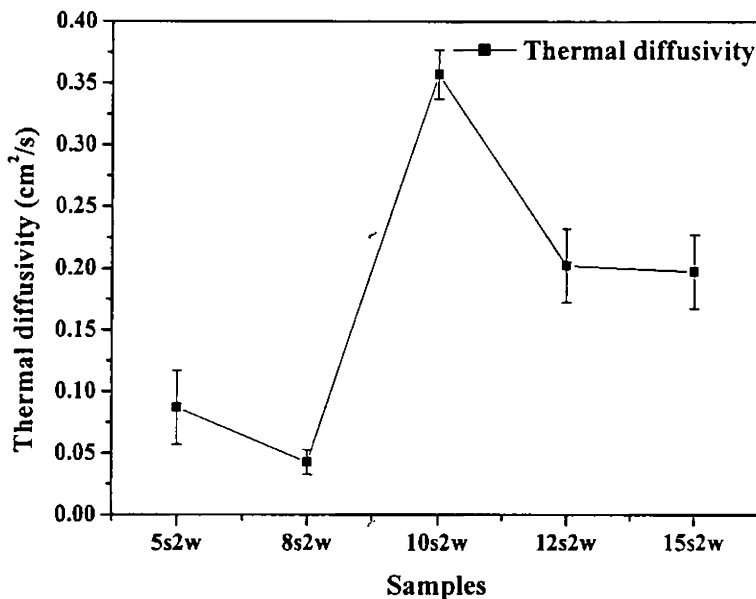
Fig. 4.1 Variation in thermal diffusivity value of "Set 1"samples prepared using SILAR method
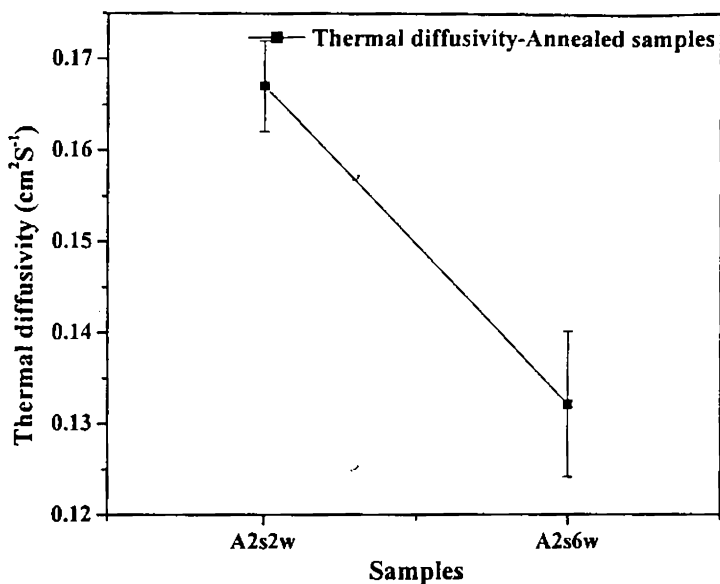
Fig. 4.2 Variation in thermal diffusivity value of "Set 2" annealed samples prepared using SILAR method
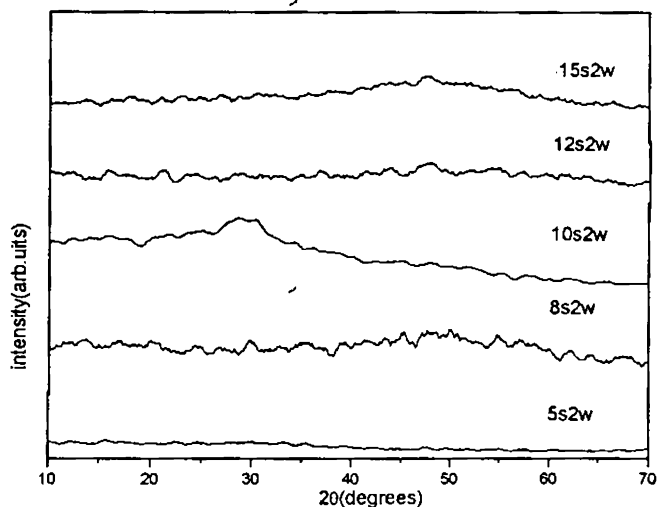
Fig. 4.3 XRD pattern of In_2S_3 thin film ("Set 1") sample prepared using SILAR method.
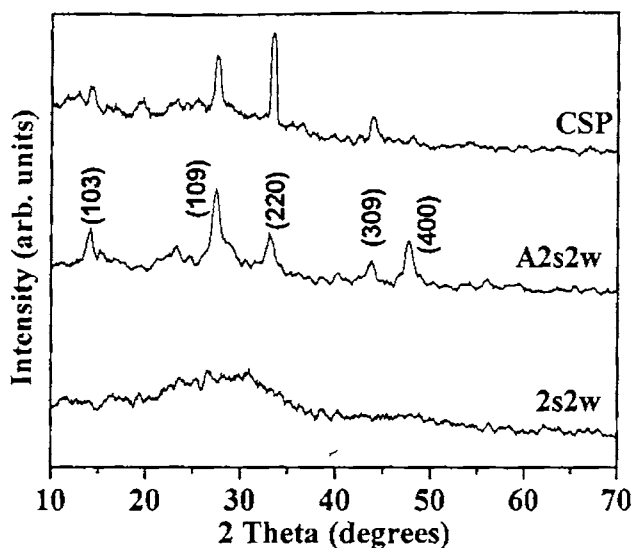
Fig. 4.4 XRD pattern of In_2S_3 thin films "2s2w" and "A2s2w" in "Set 2" samples prepared using SILAR method. XRD pattern of a sample prepared using CSP technique is also shown for comparison.

4.4.1.2b Mobility measurement

Fig. 4.5 shows the variation in mobility of "Set 1" SILAR samples. Mobility value was found to be low for "5s2w" and "8s2w", which was ~1 $cm^2V^{-1}s^{-1}$. The value showed a sudden increase for "10s2w" sample. This sample had the maximum mobility value of 6.478 $cm^2V^{-1}s^{-1}$. But on increasing dipping time in solution the mobility value decreased. From XRD pattern, it was observed that "10s2w" sample had better crystalline quality (Fig.4.3). This sample also showed high value for photoresponse $(I_L-I_D)/I_D$ ~2.1. (Where, I_L - Current measured while illuminating the sample and I_D - Dark current).

For short dipping time in solution the film growth could not have been completed. During SILAR cycle there occured a transition between the growth of a compact adherent and homogeneous film, and a porous layer containing a large amount of trapped solution [54]. As the porous grown mechanism occured, growth of the inner compact layer stopped almost completely. This could be probably the reason for decrease in mobility for sample with long dipping time in solution. Dipping time of 10 seconds in solution and 2 seconds in water should have been the ideal condition for the preparation of In_2S_3 using SILAR method.

Fig. 4.6 shows the variation in mobility of annealed SILAR samples from "Set 2". Mobility value was found to be maximum, showing a value of 1.61 $cm^2V^{-1}s^{-1}$ for "A2s2w" sample. The value was found to decrease to ~0.2 $cm^2V^{-1}s^{-1}$ for "A2s6w". Decrease in mobility for these two samples could be due to its poor crystalline quality. As observed from XRD, (Fig. 4.4) high value of mobility for "A2s2w" sample could be due to its better crystalline structure which might enhance the transport of photogenerated charge carriers through the sample. Here also one can see that the mobility of "Set 1" samples is much higher than that of "Set 2" and this is not understood from the present studies.
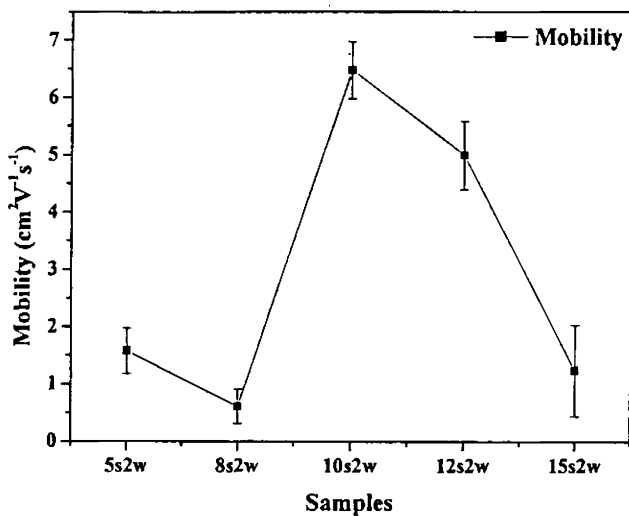
Fig. 4.5 Variation in mobility value with time
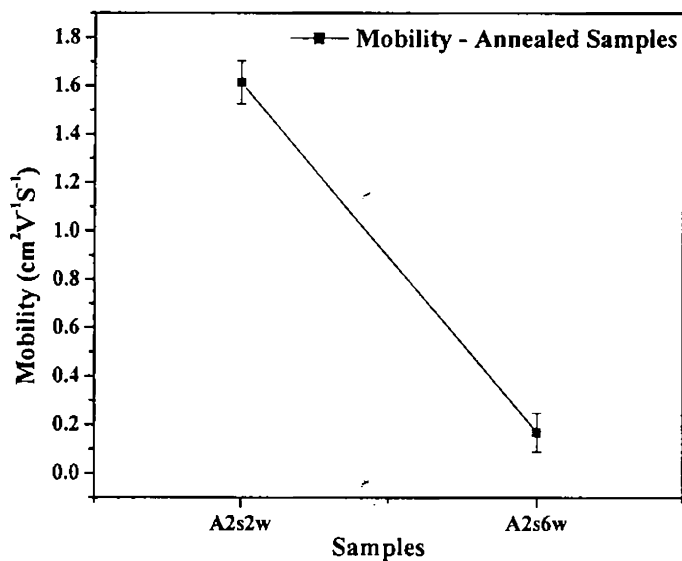of dipping in solution of "Set 1" samples

Fig 4.6 Variation in mobility value of "Set
2"(annealed) samples

4.4.2 In$_2$S$_3$ thin film samples having different sample thicknesses

4.4.2.1 Structural and optical properties

Samples having different thicknesses were studied to know their optical absorption. It was found that the band gap had steep increase from 2.659 eV for sample "400" to 2.881 eV for "600". But further increase in the thickness of the samples by increasing the volume of spray solution did not result in an increase of the band gap. Instead it remained more or less a constant upto sample prepared by spraying 1000 ml. On annealing, the band gap was found to decrease. The highest band gap was observed for "A400" sample with a value of 2.491 eV. This gradually reduced to 2.158 eV for "A1000". The observed decrease in band gap after annealing could be due to increase in grain growth.

Results from transmission spectrum showed that annealing caused an increase of the absorption coefficient of the films. It was observed that "A1000" sample showed the least transmission of about 6 % amongst both unannealed and annealed samples, whereas "400" showed the highest transmission of about 65 % amongst unannealed samples.

XRD pattern showed that compound formed was β-In$_2$S$_3$ with tetragonal orientation. Reflection from (103), (220) and (309) planes were observed (Fig. 4.12). (103) and (309) peaks were observed to be very weak. Crystalline quality was observed to be very poor for "400" sample. This improved with increase in thickness. The intensity of (220) peak was also found to increase with thickness and "1000" sample showed the maximum intensity for (220) peak. This peak height was found to increase with annealing.

170

In terms of crystalline quality, "A1000" was found to be the best. Fig. 4.7 is plot showing variation of lattice strain of annealed samples having various thicknesses. Lattice strain calculated from XRD data showed a gradual decrease for annealed samples for "A400" to "A800" and a steep decrease for "A1000". When crystallinity is better the strain should be less and, this could be the reason for the drastic decrease in lattice strain for "A1000" sample. Grain size was calculated using Scherrer's formula. Fig. 4.8 is the plot showing grain size variation of annealed samples. Grain size was observed to increase from 24.3 nm for "A400" to a maximum value of 27.9 nm for "A1000" sample.
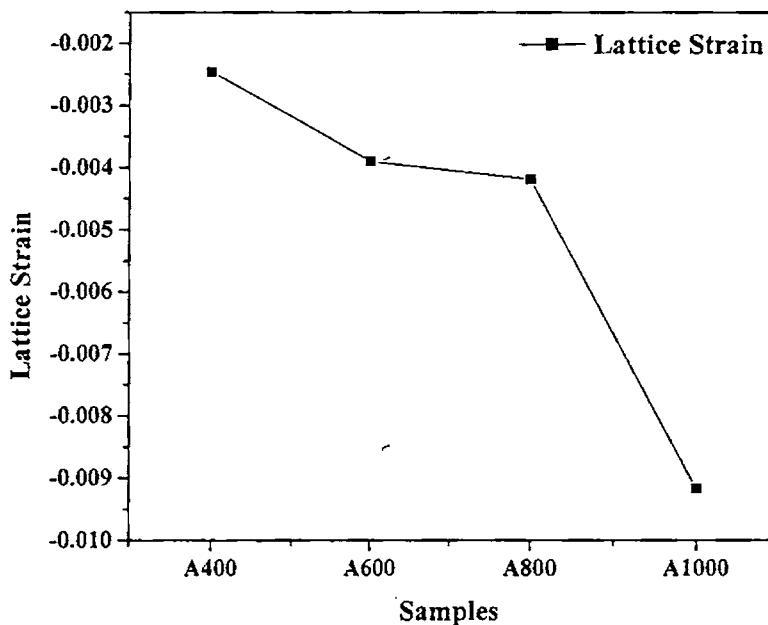

Fig. 4.7 Graph showing lattice strain of annealed In_2S_3 samples prepared using CSP techniques by spraying different volumes of solution to increase sample thickness.
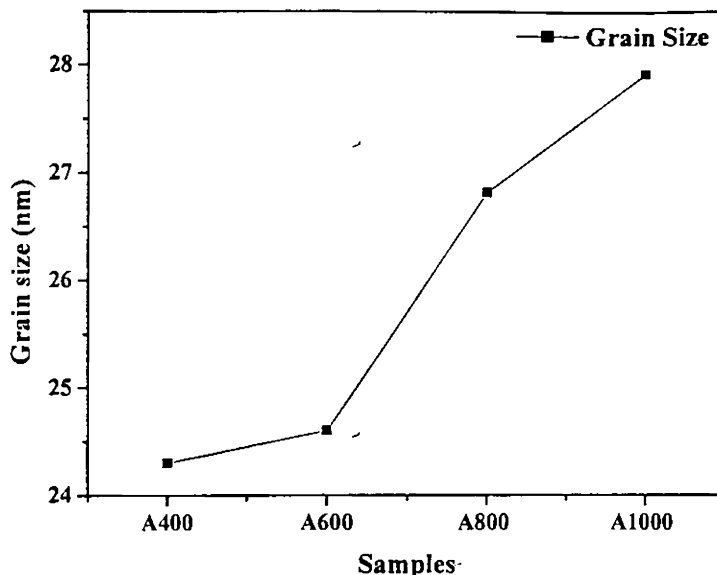
Fig. 4.8 Graph showing grain size of annealed
In₂S₃ samples prepared using CSP techniques
by spraying different volumes of solution to
increase sample thickness.

4.4.2.2 Photothermal Studies

PDS technique was used to determine the thermal diffusivity and
mobility of In_2S_3 samples having various thicknesses. The procedure used for
thermal diffusivity and mobility determination was as described in chapter 1
(section 1.5.1 and section 1.5.2 respectively).

4.4.2.2a Thermal diffusivity measurement

Fig. 4.9 is a typical plot, showing log amplitude versus square root of
chopping frequency for "A1000" In_2S_3 sample. Both thermal and electronic
contribution could be clearly distinguished in this sample. Thermal diffusivity
was determined from the slope of the curve in the low frequency range.

Variation in thermal diffusivity of samples having various thicknesses is as shown in Fig. 4.10. Thermal diffusivity value was observed to stay constant at 0.02 cm^2/s for "400", "600" and "800". A sudden increase was observed for "1000" sample attaining a value of 0.1066 cm^2/s. Thermal diffusivity values of annealed sample are shown in Fig. 4.11. It was observed that generally the thermal diffusivity value increased with annealing. Here also, the sample "A1000" showed the maximum thermal diffusivity value. It is worth pointing out here that both "1000" and "A1000" samples are having good crystallinity as revealed by the XRD pattern (Fig. 4.12). This may be the reason for high thermal diffusivity exhibited by these two samples. On comparison between Fig. 4.10 and Fig. 4.11 one can see that annealed sample had better thermal diffusivity.
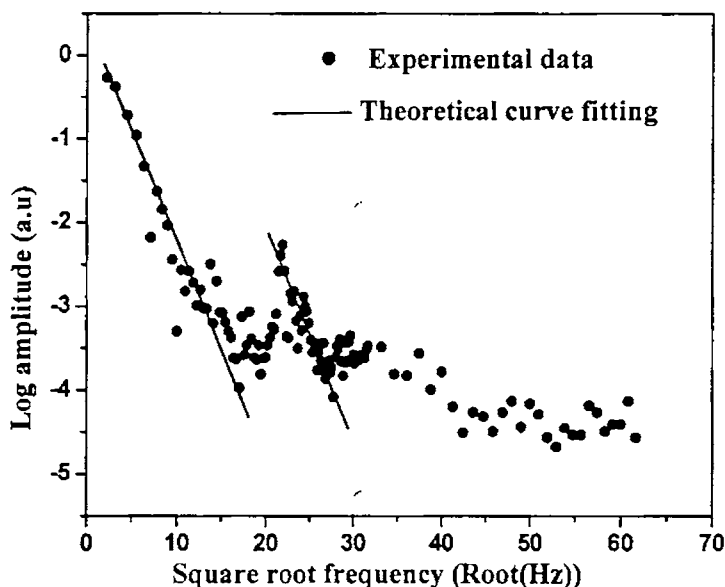

Fig. 4.9 Graph showing log amplitude versus
√f for "A1000" In$_2$S$_3$; a typical curve used for
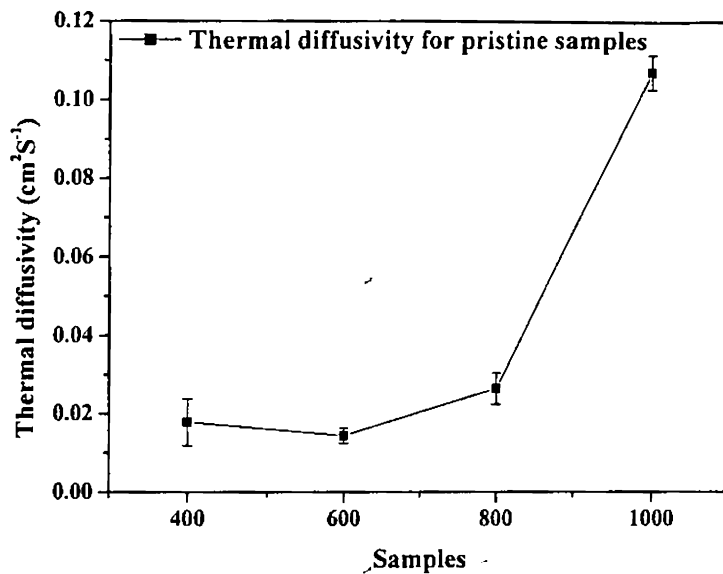calculating thermal diffusivity and mobility.

Fig. 4.10 Thermal diffusivity of unannealed In$_2$S$_3$ samples having different thicknesses.
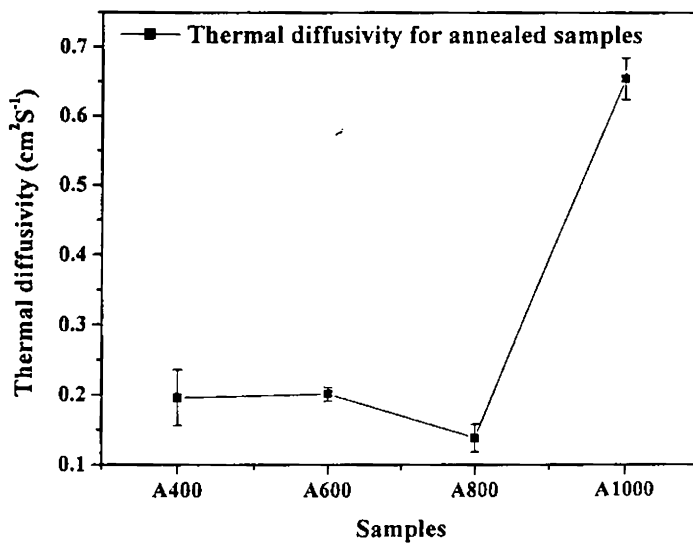

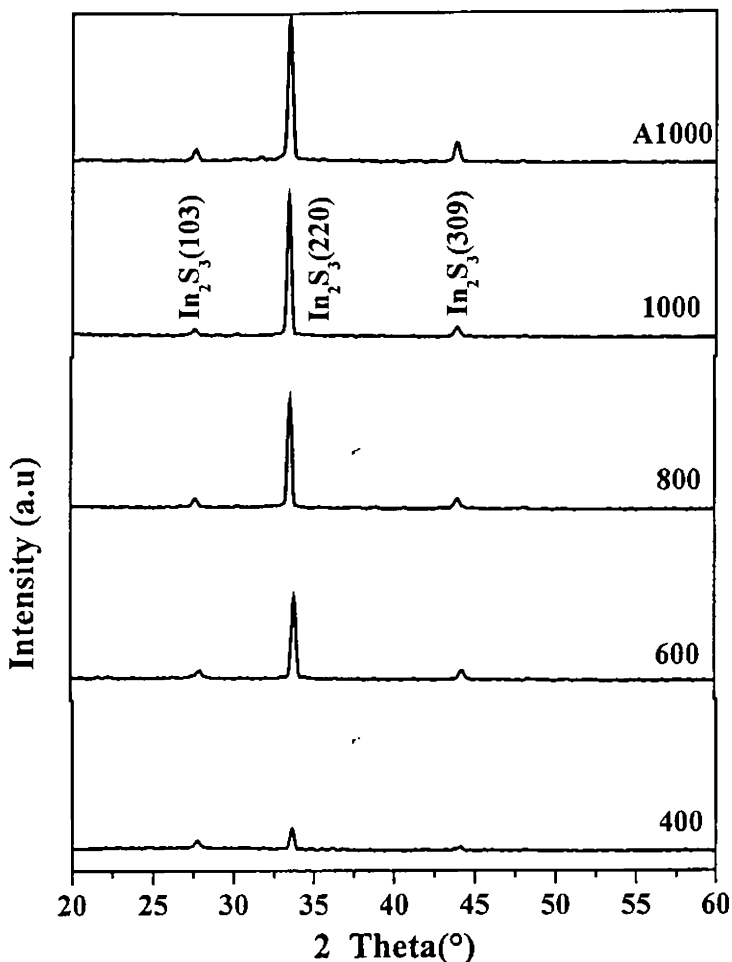Fig. 4.11 Thermal diffusivity of annealed In$_2$S$_3$ samples having different thicknesses

Fig. 4.12 XRD pattern of In_2S_3 thin film
sample prepared with different thicknesses.

4.4.2.2b Mobility measurement

Fig. 4.13 shows the plot for mobility variation for pristine In_2S_3 samples. Mobility values were found to be almost constant for "400", "600" and "800" (between 5.25 $cm^2V^{-1}s^{-1}$ and 6 $cm^2V^{-1}s^{-1}$). However, for "1000" there occurred a drastic increase reaching a value of 7.51 $cm^2V^{-1}s^{-1}$. Fig. 4.14

shows the plot for mobility variation for annealed In_2S_3 samples prepared for various thicknesses. The mobility did not improve much on annealing for "A400", "A600" and "A800". However, a drastic increase was observed for "A1000" reaching a value of 11.17 $cm^2V^{-1}s^{-1}$. From XRD pattern (Fig. 4.12) it was observed that this sample had maximum intensity for (220) peak.

The reason for this could be, reduction in grain boundary scattering due to better grain size and minimum lattice strain in the case of "A1000". As annealing enhanced the grain growth and preferable orientation of the crystal, it is natural for "A1000" to show an increase in mobility.
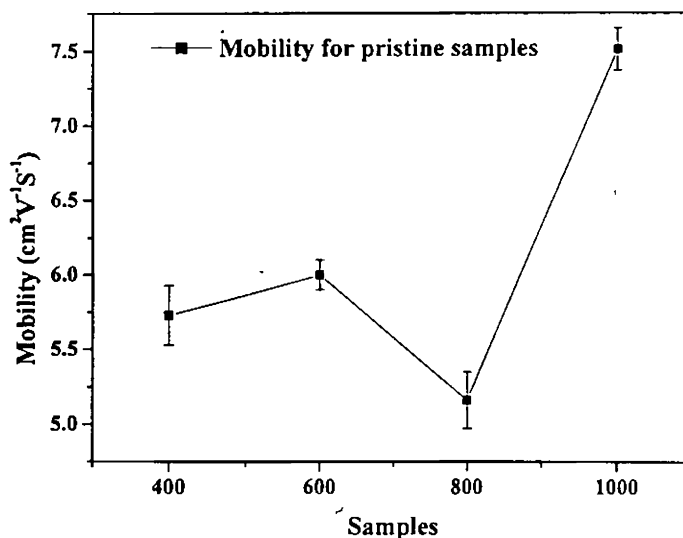

Fig. 4.13 Mobility values of unannealed In_2S_3 samples having different thicknesses.
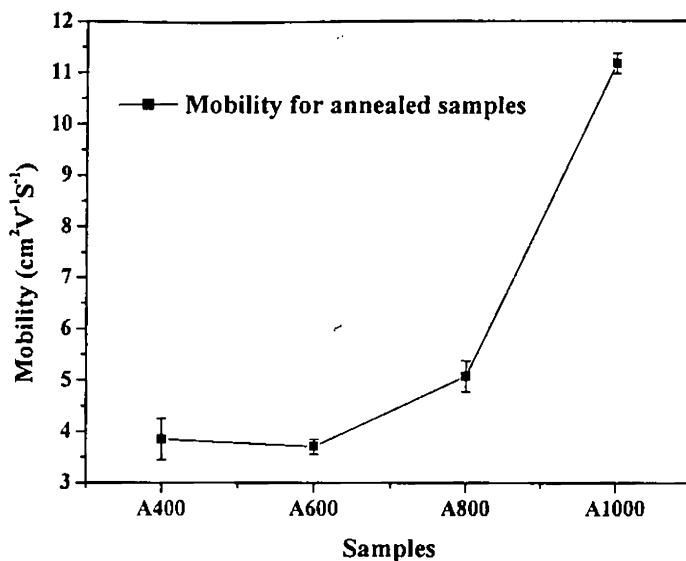
Fig. 4.14 Mobility values of annealed In_2S_3
samples having different thicknesses.

4.4.2.2c Thickness measurement

Thickness of the samples calculated using curve-fitting method was as
described in Chapter 1 (section 1.4). In the present case, the curve fitting was
done, assuming single layer model. An absorbing layer (l_1) coated over that of
backing layer / glass substrate (which was assumed to be non-absorbing). This
structure was immersed in the fluid medium. Schematic of the model is shown
in Fig.4.15. Modulated pump beam irradiated over this absorbing layer
resulting in thermal wave generation inside the material due to optical
absorption.

Fig. 4.16 shows the plot for typical photothermal deflection amplitude
versus chopping frequency for pristine In_2S_3 samples having different
thicknesses. These curves used for theoretical curve fitting to determine the

film thickness. Multiparameter least square fitting procedure was done to optimize the experimental result. From the experimental PDS data, it was clearly observed that, as the volume of spray solution was increased the deflection amplitude was found to increase for very low chopping frequency. Thickness obtained through theoretical fitting is tabulated in Table 4.1 and the thickness measured by Stylus method is also given for comparison. These two values were coinciding very much.
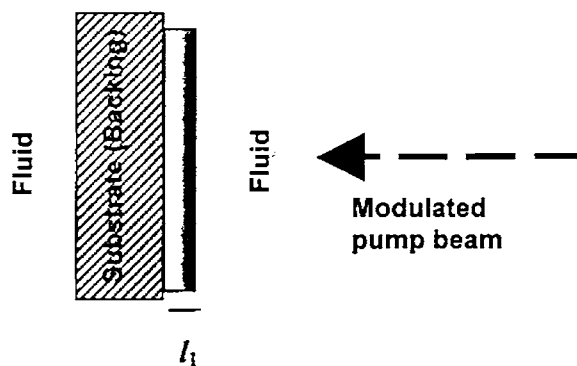

Fig. 4.15 Schematic representation of the model used for determination of thin film thickness.

Samples	Thickness measured using PDS method (l_1 µm)	Error bar	Thickness measured using Stylus method (µm)
400 ml	0.96	± 0.012	1.00
600 ml	2.02	± 0.082	2.05
800 ml	2.15	± 0.057	2.11
1000 ml	3.94	± 0.011	4.10

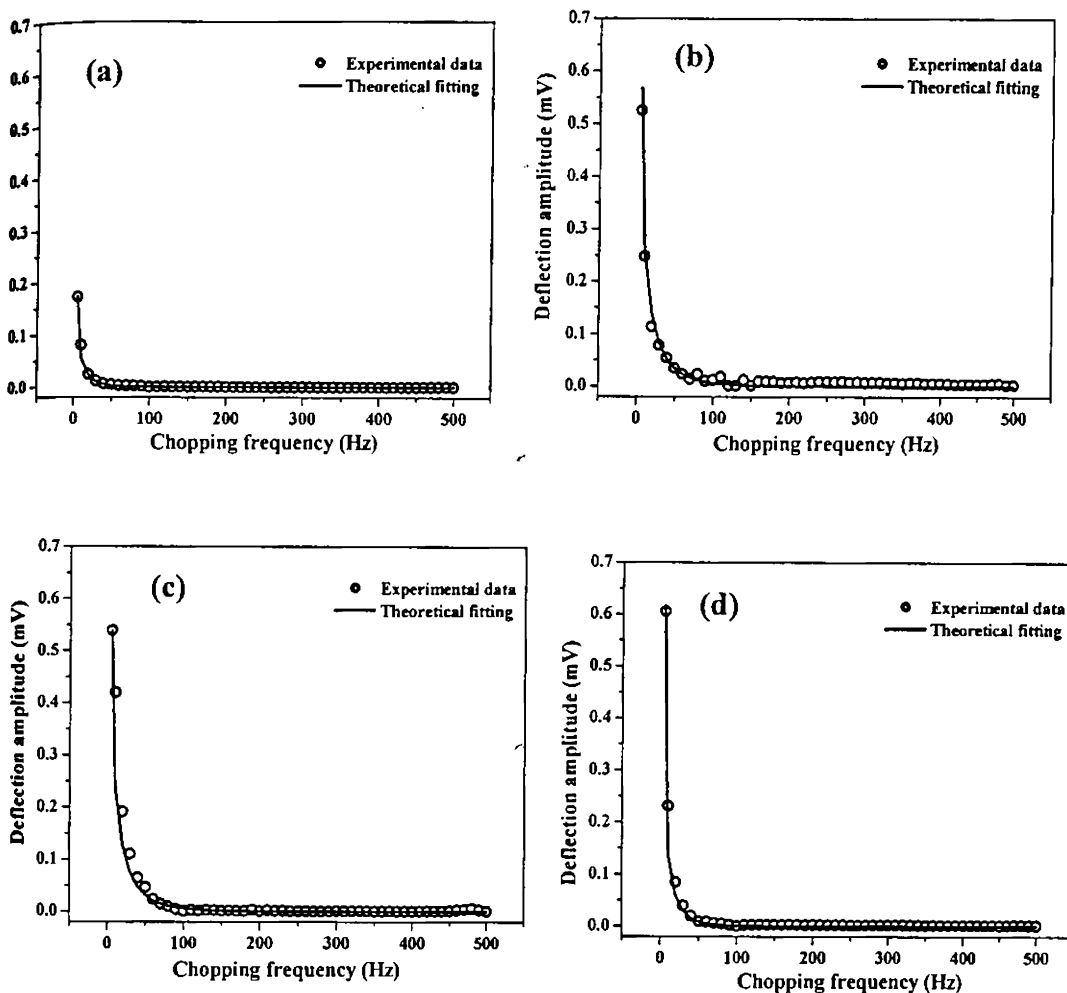Table 4.1 Tabulated value of the measured thickness of In_2S_3 samples having different thicknesses.

Fig. 4.16 Photothermal deflection amplitude versus chopping frequency of unannealed In2S3 samples having different thicknesses; these plots were used for theoretical curve fitting for the determination of the thin film thickness.

179

4.4.3 In$_2$S$_3$ thin film samples prepared with various atomic concentration of indium and sulphur using chloride as precursor

4.4.3.1 Structural and optical properties

The energy band gap was calculated from $(\alpha h v)^2$ versus hv plot. The bandgap of the sample with an In/S ratio of 2/3 was found to be 2.67 eV. On decreasing the sulphur concentration to 2/1 the bandgap was found to increase to 2.81 eV and on increasing the sulphur concentration to 2/8 it was found to decrease to 2.64 eV. The wider band gap may be due to poor crystallinity and / or due to presence of oxygen [39]. XPS studies done earlier on 2/2 samples showed that samples having very low sulphur concentration had oxygen in excess [21].

XRD studies showed β-In$_2$S$_3$ phase with good crystallinity and preferential orientation along the (220) plane except for those having very low sulphur concentration (Fig. 4.21). The characteristic peaks of β-In$_2$S$_3$ were found to appear for samples having an In/S ratio of 2/2. The sample with an In/S ratio of 2/3 showed good crystallinity and orientation along the (220) plane. Increase in the sulphur concentration, resulted in increase of intensity of the peak corresponding to (220) plane. This increase was observed up to an In:S atomic concentration of 2/5. Further increase in the sulphur concentration, resulted in the decrease of XRD peak intensity. Optical transmission studies shows that the percentage of transmittance decreased from 85% to 55% when the In/S ratio varied from 2/1 to 2/8, in the wavelength range 350-1200 nm.

Fig. 4.17 shows the variation of the lattice strain with the variation in atomic ratio of different samples. Lattice strain calculated from the XRD data

showed that strain was minimum for 2/5 sample, where as it increased for and high sulphur concentration samples. Intensity of (220) peak for 2/5 sample was found to be maximum, and hence preferred orientation of grain growth could be the reason for minimum lattice strain. Grain size was calculated using Debye – Scherrer formula. Fig.4.18 is the plot showing variation of the grain size. Grain size was also observed to be maximum for 2/5 sample, as the (220) peak intensity was found to be maximum from XRD studies for this sample. Grain size was found to decrease for low and high sulphur concentration. This could be because 2/5 showed good crystallinity amongst these samples. Oxygen contamination could be one reason for decrease in grain size for samples with low sulphur concentration, while crystal degradation could be the reason with high sulphur concentration.
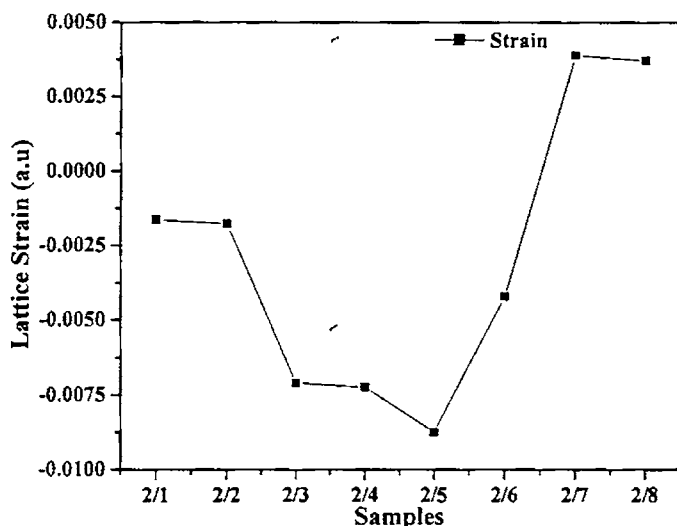

Fig. 4.17 Lattice strain of In_2S_3 thin film sample having different sulphur concentration (prepared using chloride as precursor).
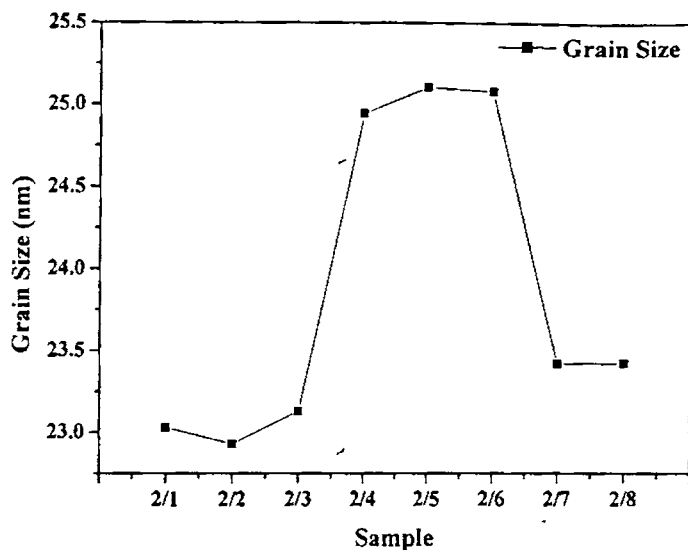
Fig. 4.18 Grain size of In_2S_3 thin film sample having different sulphur concentration (prepared using chloride as precursor).

4.4.3.2 Photothermal studies

Thermal diffusivity and mobility of the In_2S_3 samples were determined using the procedure described earlier in chapter 1 (section 1.5.1 and 1.5.2 respectively).

4.4.3.2a Thermal diffusivity measurement

Thermal diffusivity variation due to the variation in atomic concentration of In_2S_3 prepared using chloride as precursor solution was studied (Fig. 4.19). Samples with low sulphur concentration showed low value of thermal diffusivity. The value was almost constant (about 0.04 cm^2s^{-1}) for samples having In/S ratio of 2/1 to 2/4. But for 2/5 sample, the thermal diffusivity value showed a drastic increase attaining a maximum of

0.0956 cm^{2}s^{-1}. For further increase in sulphur concentration (2/6 to 2/8 samples), the thermal diffusivity again showed a decrease to 0.041 cm^{2}s^{-1}. As the crystallinity, grain size and microstructure of the material influenced thermal transport property of the material, maximum thermal diffusivity observed for 2/5 sample was expected as this sample showed good crystalline quality.

Fig. 4.19 Thermal diffusivity of In$_2$S$_3$ thin film sample having different sulphur concentration (prepared using chloride as precursor).

4.4.3.2b Mobility measurement

As mobility is an important parameter controlling electronic transport, one among the transport property, we used PDS technique for studying the variation in mobility for various atomic concentration of In to S and Fig. 4.20 is the plot for mobility variation. Mobility value was found to be almost stable around 5 cm^{2}V^{-1}s^{-1} for low In/S concentration samples (2/1 to 2/3). The value

was found to show a sudden increase for 2/4 sample to 13 $cm^2V^{-1}s^{-1}$ on further increase in sulphur concentration for 2/5 the value increased to 17.5 $cm^2V^{-1}s^{-1}$. This value was found to be maximum. Further increase of sulphur concentration resulted in the decrease of mobility. Better crystallinity of this sample might be the reason for high mobility.
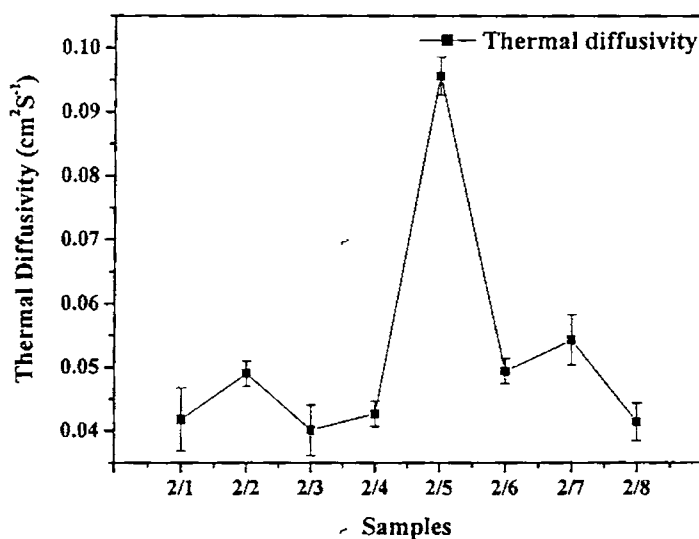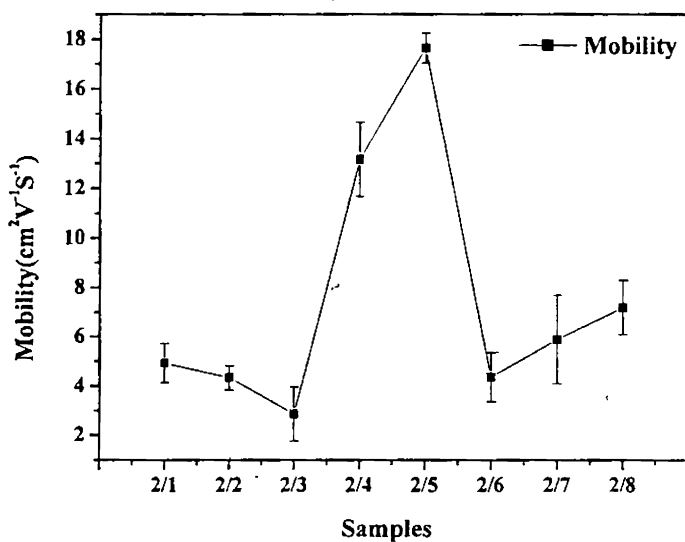

Fig. 4.20 Mobility of In_2S_3 thin film sample having different sulphur concentration (prepared using chloride as precursor).
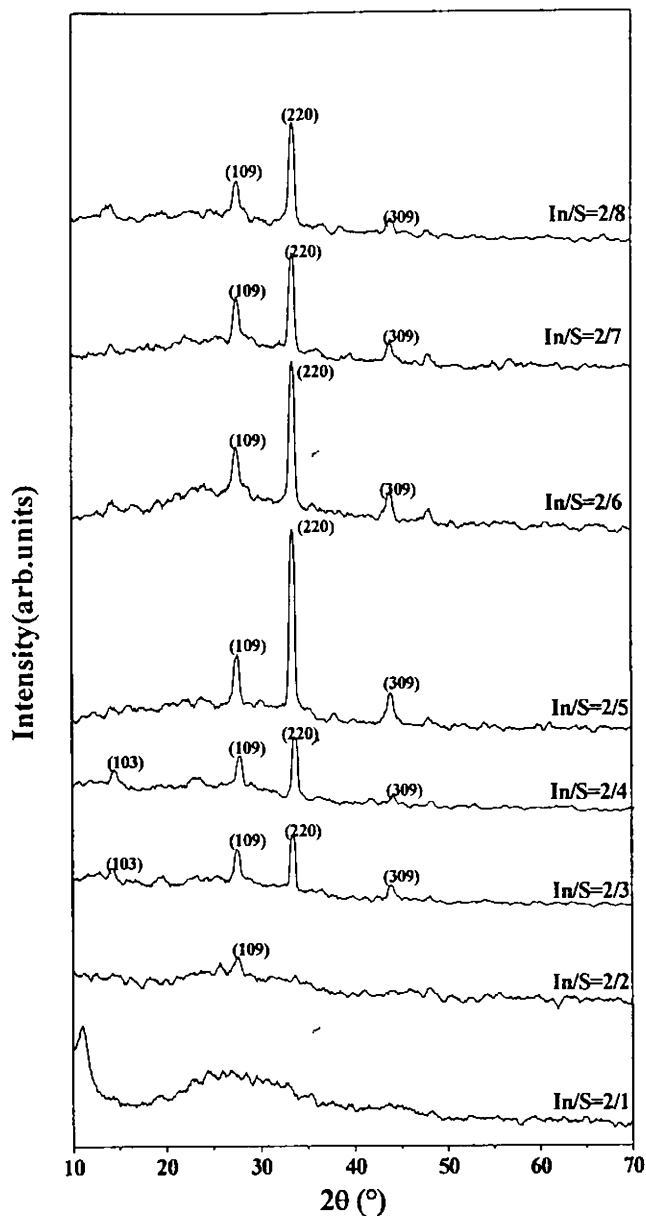
Fig. 4.21 XRD pattern for In$_2$S$_3$ samples having various In to S prepared using Chloride as precursor solution [21].

Eventhough the crystalline quality played a major role in controlling to mobility of charge carriers, oxygen impurty observed though XPS studies should also be a reason for the decrease for low sulphur concentration samples. Since oxygen is not present for high sulphur concentration, crystalline degradation should be the only reason.

4.4.4 In_2S_3 thin film samples prepared with various atomic concentration of indium and sulphur using nitrate as precursor

4.4.4.1 Structural and optical properties

From the plot of $(\alpha hv)^2$ versus hv, band gap was calculated for all In_2S_3 samples. The band gap showed a steady decrease with increase in sulfur concentration. 2/1 showed the highest band gap value of 2.95 eV. The observed increase in band gap for low sulfur concentration could be due to the presence of secondary phases as observed in XPS studies.

From XRD pattern [45], it was observed that only 2/3 sample exhibited good crystalline property. There were five distinguished peaks corresponding to (103), (109), (220), (309) and ($22\overline{1}2$ or 400) orientations of β-In_2S_3. Except for this sample, all other samples were observed to be highly amorphous. In the case of samples having sightly high sulphur concentration, the XRD pattern showed a peak along (103) plane, which was very weak. Further increase in sulphur concentration result in change of orientation to (109) from (103) plane. This plane was observed for samples above 2/6. Two additional peaks corresponding to (103) and (400) also appeared on increasing the sulfur

concentration. Grain size was calculated using Debye – Scherrer formula. It was observed that 2/3 showed the maximum grain size of 28 nm.

4.4.4.2 Photothermal studies

In this case also we used PDS technique for studies on thermal diffusivity and mobility variation. These were determined using the procedure described earlier in chapter 1 (section 1.5.1 and 1.5.2 respectively).

4.4.4.2a Thermal diffusivity measurement

Thermal diffusivity variation of samples having various atomic concentration of indium to sulphur, prepared using nitrate as precursor, is plotted in Fig. 4.22. The value was found to be maximum for 2/3 sample (around 0.24 cm^2s^{-1}) and decreased for high sulphur concentration falling down to 0.1 cm^2s^{-1}. Similarly, low thermal diffusivity value was observed for samples with low sulphur concentration.
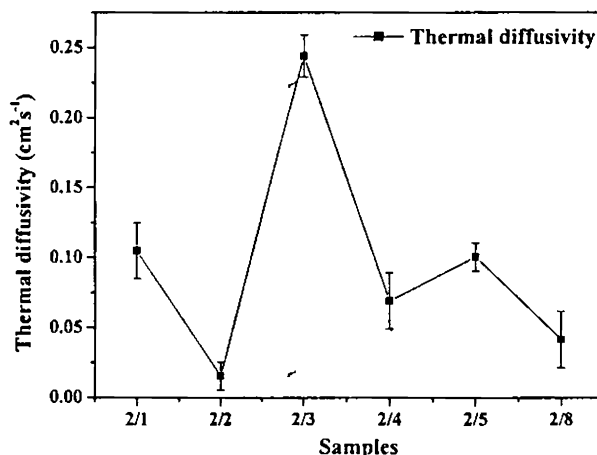

Fig. 4.22 Graph showing variation of thermal diffusivity of In_2S_3 samples prepared with different sulphur concentration using nitrate as precursor.

4.4.4.2b Mobility measurement

Fig. 4.23 is the plot depicting mobility variation of sample having various indium to sulphur ratio prepared using nitrate precursor. Mobility value was found to be around $1 \, cm^2V^{-1}S^{-1}$ for 2/1 and 2/2 samples. But for 2/3 sample it increased to around $7.45 \, cm^2V^{-1}S^{-1}$, which was the maximum. On further increasing the sulphur concentration, mobility again decreased.

From XPS studies, it was found that atomic concentrations of indium and sulphur were almost equal for 2/3. Moreover, XRD analysis indicated that only thin sample was having good crystal quality and these two factors may be the reason for high value of mobility [45]. Lower value of mobility for rest of the samples could be due to their amorphous nature as indicated in XRD studies.
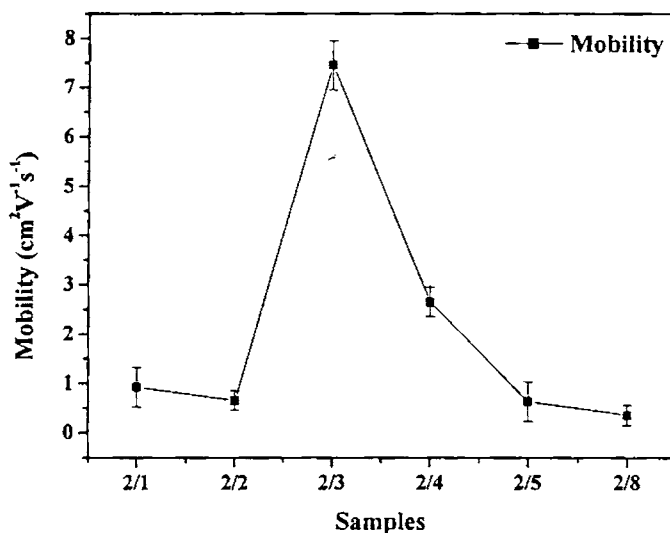

Fig. 4.23 Graph showing variation of mobility of In_2S_3 samples prepared with different sulphur concentration using nitrate as precursor.

4.5 Conclusion

In$_2$S$_3$ thin film samples, prepared using SILAR and CSP techniques, were analysed to know the details of their thermal and transport properties. For SILAR prepared samples, thermal diffusivity and mobility was found to be maximum for sample having more dipping time in solution (10s2w). This sample also showed comparatively good crystalline quality, as observed from XRD studies. For another set of samples which was prepared by keeping dipping time in solution constant and varying the rinsing time in water, it was found that sample having equal dipping time in water and solution (2s2w) showed a high value of thermal diffusivity and mobility. Annealing these sample enhanced the grain size, and both the thermal and mobility values were also found to increase.

In$_2$S$_3$ thin film samples having various thicknesses (prepared using CSP technique) were also studied to know about the variation of their transport properties. Depth profiling was done on these samples using PDS technique. Thickness values obtained were found to coincide well with Stylus method. For increasing the sample thickness amount of spray solution was increased in steps of 200 ml. Thermal diffusivity and mobility values were maximum for the thickest sample. These values were increasing with annealing temperature also.

In$_2$S$_3$ thin film samples were also prepared using chloride and nitrate as precursor solution. Thin films prepared using chloride precursor solution were found to have high thermal diffusivity and mobility values. When nitrate was used as precursor solution, only the sample having In/S ratio 2/3 showed high value of thermal and mobility values. From our studies we observed that 2/5

sample, obtained by using chloride precursor, showed a mobility value of 17.5 $cm^2V^{-1}s^{-1}$ and that of 2/3 sample prepared using nitrate as precursor showed a mobility value of 7.45 $cm^2V^{-1}S^{-1}$. Hence in our observation 2/5 sample prepared using chloride as precursors exhibited good electrical property.

References

[1] T. Asikainen, M. Ritala, M. Leskela, *Appl. Surf. Sci.,* **82/83** (1994) 122.

[2] R.B. Hall, J.B. Meakin, *Thin Sol. Films*, **63** (1979) 203.

[3] J. Britt, C. Ferekides, *Appl. Phys. Lett.,* **62** (1993) 2851.

[4] B. Dimmler, H.W. Schock, *Prog. Photovoltaic Res. Appl.,* **4** (1996) 425

[5] D. Braunger, D. Hariskos, T. Waltre and H.W. Schock, *Sol. Energy Mater. Sol. Cells,* **40** (1996) 97.

[6] T. Takahara, N. Matsoura, and N. Inoue, *Ger. Offen.* 2.850.491: *see Chem. Abs. No* 67384a, **91** (1979) 8.

[7] E. Dalas, and L. Kobotiatis, J. *Mater. Sci.,* **289** (1993) 6595.

[8] E. Dalas, S. Sakkopoulos, E. Vitoratos, and G. Maroulis, *J. Mat. Sci.,* **28** (1993) 5456.

[9] J. Herrero and J. Ortega, *Sol. Energy Mater.,* **17** (1988) 357.

[10] S.Yu, L. Shu, Y. Qian, Y. Xie, J. Yang, and L. Yang, *Mat. Res. Bull.,* **33** (1998) 717.

[11] D. Diehl and R. Nitsche, *J. Cryst. Grow.,* **20** (1973) 38.

[12] W. Rehwald and G. Harbeke, *J. Phys. Chem. Solids.,* **26** (1965) 1309.

[13] J. M. Giles, H. Hatwell, G. Offergeld, and J. Van Cakenberghe, *Phys. Stat. Sol.,* **2** (1962) K73.

[14] R. Diehl and R. Nitsche, *J. Cryst. Grow.,* **28** (1975) 306.

[15] W. T. Kim and C. D. Kim. J. *Appl. Phys.,* **60** (1986) 2631

[16] R. Normura, S. Inazawa, K. Kanaya, and H. Matsuda, *Appl. Organomet. Chem.,* **3** (1989) 195.

[17] J.George, K.S.Joseph, B.Pradeep, and T.I.Palson, *Phys. Stat. sol. (a),* **106** (1988) 123.

[18] R.Nomura, K.Konishi, and H.Matsuda, *Thin solid films,* **198** (1990) 339.

[19] N.Kamoun, R.Bennaceur, M.Amlouk, S.Belgacem, N.Mliki, J.M.Frigerio and M.L.Theye, *Phys. Stat. sol. (a),* **169** (1998) 97.

[20] N.Bouguila, H.Bouzouita, E.lacaze, A.Belhadj amara, H.Bouchriha, and A.Dhouib, *J. Physique III,* 7 (1997) 1647.

[21] Teny Theresa John, S. Bini, Y. Kashiwaba, T. Abe, Y. Yasuhiro, C. Sudha Kartha and K.P. Vijayakumar, *Semicond. Sci. Technol.,* **18** (2003) 491.

[22] A.A.El Shazly, D.Abdeldady, H.S.Metoually, and M.A.M.Segmam, *J.Phys: Condensed Matter,* 10 (1998) 5943.

[23] H.Ihara, H.Abe, S.Endo, and T.Irie, *Solid state commun.,* **28** (1970) 563.

[24] M. A. Martinez, G. H. Herrero and M. T. Gutierrez, *Sol. Energy Mater. Sol. Cells,* **45** (1997) 75.

[25] B. T. Boike, G. S. Khripunov, V. B. Yurchenko and H.E. Ruda, *Ibid.,* **45** (1997) 303.

[26] J. Touskova, D. Kindl and J. Tousek, *Thin solid films,* **293** (1997) 272.

[27] A. Niemegeers and M. Burgelman, *J. Appl. Phys.,* **81** (1997) 2881.

[28] R.S. Mane and C.D. Lokhande, *Mat. Chem. and Phys.,* 78 (2002) 15.

[29] H. Hahn and W. Klinger, *Z. anorg. Chem.,* **260** (1949) 97.

[30] C.J.M. Rooymans, *J. Inorg. Nucl. Chem.,* **11** (1959) 78.

[31] R. H. Bube and W.H. McCarroll, *J. Phys. Chem. Solids,* **10** (1959) 333.

[32] G. Syrbe and Ch. Kleint, *Z. Naturf.,* **14a** (1959) 754.

[33] J.M. Gilles, H. Hatwell, G. Offergeld and J. Van Cakenberghe, Short notes *"Union Carbide European Research Associates, Brussels",* (1962) K77.

[34] J. Herreo and J. Ortega, *Sol. Energy Mater.,* **17** (1988) 357.

[35] Shu-Hong Yu, Lei Shu, Yong-Sheng Wu, Jian Yang, Yi Xie and Yi-Tai Qian, *J. Am. Ceram. Soc.,* **82(2)** (1999) 457.

[36] C.D. Lokhande, A. Ennaoue, P.S. Patil, M. Giersig, K. Diesner, M. Muller, H. Tributsch, *Thin Solid Films,* **340** (1999) 18.

[37] M.A.M. Seyam, *Vacuum,* **63** (2001) 441.

[38] N. Barreau, S. Marsillac, J.C. Bernede, T. Ben Nasrallah and S. Belgacem, *Phys. Stat. Sol. (a),* **184** (2001) 179.

[39] N. Barreau, J.C. Bernede, H. El Maliki, S. Marsillac, X. Castel and J. Pinel, *Solid State Commn.,* **122** (2022) 445.

[40] Sung-Hyn Choe, Tae-Hwan Bang, Nam-Oh Kim, Hyung-Gon Kim, Choong-Il Lee, Moon-Seog Jin, Seok-Kyun Oh and Wha-Tek Kim, *Semicond. Sci. Technol.,* **16** (2001) 98.

[41] Yujie Xiong, Yi Xie, Guoan Du and Xiaobo Tian, *J. Mater. Chem.,* **12** (2002) 98.

[42] Wha-Tek Kim, Chang-Sun Yun, Hae-Mun Jeong and Chang-Dae Kim, *J. Appl. Phys.,* **60** (1986) 2357.

[43] N. Kamoun, S. Belgacem, M. Amlouk, R. Bennaceur, J. Bonnet, F. Touhari, M. Nouaoura and L. Lassabatere, *J. Appl. Phys.,* **89** (2001) 2766.

[44] L. Bhira, H. Essaidi, S. Belgacem, G. Couturier, J. Salardenne, N. Barreaux and J.C. Bernede, *Phys. Stat. sol. (a),* **181** (2000) 427.

[45] Teny Theresa John, C. Sudha Kartha, K.P. Vijayakumar, T. Abe and Y. Kashiwaba, *Appl. Surf. Sci.* (In press)

[46] G. Laukaitis, S. Lindroos, S. Tamulevicius, M. Leskela and M. Rackaitis, *Appl. Surf. Sci.,* **161** (2000) 396.

[47] R. Ranjith, Teny Theresa John, C. Sudha Kartha and K.P. Vijayakumar, *Proc. DAE SSP symposium* held at Jiwaji University, Gwalior, India

(2003) fp62.

[48] Y. Mirovsky, R. Tenne, D. Cahen, G. Sawatzky, M. Polak, J. *Electrochem. Soc.*, **132** (1985) 1070.

[49] N.M. Gasanly and A. Aydinli, *Solid Stat. Commn.*, **101** (1997) 797.

[50] R. Jayakrishnan, Teny Theresa John, C. Sudha Kartha, K.P. Vijayakumar, T. Abe and Y. Kashiwaba, *J. of Lum.*, (communicated).

[51] A. F. Qasrawi and N.M. Gasanly, *Semicond. Sci. Technol.*, **17** (2002) 1288.

[52] K. Hara, K. Sayama, H. Arakawa, *Sol. Energy Mater. Sol. Cells,* **62** (2000) 441.

[53] Teny Theresa John, Meril Mathew, C. Sudha kartha, K. P. Vijayakumar, T. Abe and Y. Kashiwaba, *Sol. Ener. Mat. and Sol. Ener.* (In press)

[54] D.Lincot, R.O.Borges, *J.Electrochem. Soc.*, **139** (1992) 1880.

Chapter 5

STUDIES ON UNDOPED AND ION IRRADIATED ZnO THIN FILMS

5.1 Introduction

Zinc oxide (ZnO) emerged as one of the most promising optoelectronic materials due to its attractive optical and electrical properties, high chemical and mechanical stability, eco-friendly nature and abundance. Moreover, it is a low cost material compared with the most currently used TCO materials like ITO and SnO_2 [1]. During past few decades, ZnO had been used in many optoelectronic devices. For example, highly oriented piezoelectric zinc oxide films find great use in many acousto-optic components, such as acousto-optic modulators which are used in optical switching, Q-switching and mode locking of lasers. The light emitting property of ZnO is the result of its large exciton binding energy (60 meV). Another advantage of this material is that there are well developed bulk and epitaxial growth processes [2]. Moreover, it plays an important role in realizing blue and ultraviolet light-emitting diodes and lasers. Due to its large band gap, ZnO is suitable for the fabrication of high-temperature, high-power devices with application, just as GaN. Further practical advantages of ZnO include amenability to conventional wet chemical etching, which is compatible with Si technology [3].

Properties of ZnO films such as crystallite orientation, grain size, layer resistivity, carrier mobility or optical transparency are influenced by fabrication techniques and processing parameters [4]. These films were

195

prepared using sputtering [5, 6], reactive thermal and electron beam evaporation [7], pulse laser deposition [8, 9], spray pyrolysis [10, 11, 12, 13], chemical vapor deposition [14, 15] sol-gel [16], atomic layer deposition [17], and molecular beam epitaxy [18, 19, 20]. Among these, the spray pyrolysis technique received good attention because of its simplicity, low tech nature and it does not require a high vacuum apparatus. Moreover, it can be adapted easily for production of large area films especially for display devices [21]. However, film reproducibility remains a problem, despite considerable research into ZnO deposition [22].

Suitable doping can increase the conductivity of the ZnO thin films. This is achieved by replacing Zn^{2+} with atoms of higher valence such as indium [23], aluminium [24] and gallium [25]. Presently a lot of research is going on to convert this material into p-type as this can lead to the fabrication of unique pn junction, which will be an important device in the semiconductor technology [26]. The difficulties of p-type doping in ZnO arises from various reasons such as, the deep acceptor level preventing easy low thermal excitation of holes, low solubility of the dopant and/or induction of self-compensating processes on doping [26].

Study of the modification of optical, electrical and piezoelectric properties by ion beam bombardment is motivated by the potential use of the ZnO in irradiation environment such as space application [27, 2].

In our work, we prepared ZnO thin films using spray pyrolysis method for different thicknesses and irradiated 120 MeV Au_{197} ions using Pelletron accelerator. Doping was also carried out using Indium. These samples were analysed using PDS technique and the results are presented in this chapter.

5.2 Brief review of earlier works done on ZnO

In 1959, Thomas was the first to report [28] on the enhancement of n-type activity in ZnO by doping In. Considerable efforts were made to increase electrical and optical property of ZnO thin films there after [29, 30, 31].

Cruz *et al* [32] prepared sulphur doped ZnO thin films using chemical bath deposition. These thin films showed red and green luminescence. Jayaraj *et al* [33] studied electrical and optical properties of ZnO thin films, prepared using rf magnetron sputtering. The films showed an average transmission of about 85 % in the visible range. They also studied effect of various substrate temperatures and target-to-substrate distances. The best film properties, in terms of conductivity and transmission, were obtained for a substrate temperature at 423 K and for substrate to target distance of 1.5 cm. Wang *et al* [34] deposited ZnO films on Si substrate using rf magnetron sputtering. From Photoluminescence (PL) studies, they observed two peaks, a strong violet emission located at 402 nm and a weak ultraviolet emission at 384 nm.

Pushparajah *et al* [35] studied the physical properties of spray pyrolysed (pure and doped) ZnO thin films, as a function of substrate temperature and Li concentration. Best films were obtained for $T_s = 400$ °C with conductivity 6.3×10^{-3} Ω^{-1} cm^{-1} and mobility of 104 cm^{2}V^{-1}s^{-1}. They also observed that transmission of these films decreased as Li concentration increased. Resistivity was also found to increase by 3 orders. Nunes *et al* [1] studied effects of different dopant elements on the properties of ZnO thin films. They observed that films doped with 1 at% of In showed maximum change in the electrical property with a resistivity value of 1.9×10^{-1} Ωcm.

197

Studenikin *et al* [36] studied optical and electrical properties of undoped ZnO films grown by spray pyrolysis using Zinc nitrate solution. They also observed a critical temperature, T_c = 180 °C, below which the thermal decomposition of ZnO did not occur or was incomplete. Films prepared above T_c showed strong preferred orientation of polycrystals along the *c*-axis, while the films grown below T_c showed a powder like, non oriented polycrystalline structure. Time-resolved luminescence and photoconductivity were also studied. El Hichou *et al* [22] studied undoped ZnO and F-doped $ZnF_xO_{(1-x)}$ (x=5 at%) films prepared by spray pyrolysis technique. They observed that doping with fluorine kept the optical absorption threshold unchanged. They observed intensive blue-green light emission (λ = 520 nm) and a red emission (λ = 672 nm) for undoped ZnO sample and the presence of fluorine gave rise to a new light emission corresponding to λ = 454 nm and lead to a more homogeneous re-partition of the emitting centers. J.M. Bian *et al* [37] prepared N-In codoped p-type ZnO films using ultrasonic spray pyrolysis. They also conducted electrical studies on these films and observed that incorporation of indium caused a change in the chemical state of nitrogen, which promoted the formation of p-type conduction.

Minegishi *et al* [31] fabricated p-type ZnO at room temperature by chemical vapour deposition, through N doping using NH_3. The films showed poor reproducibility, high resistance of ~100 Ω cm and low carrier concentration of ~ 1×10^{16} cm^{-3}. Ning *et al* [38] and Hiramatsu *et al* [39] observed that doping of Al, Ga or In increased its electron conductivity without affecting the optical transmission. Kolb *et al* [40] observed doping of Li increased its resistivity. Yamamoto *et al* [41], using theoretical calculations proposed, that codoping of donor and acceptor dopants in ZnO could lead to

the formation of p-type ZnO. Joseph *et al* [26] could observe p-type behaviour in ZnO thin films, prepared using codoping method. They were able to fabricate p-type ZnO films by N doping. These films showed resistivity of 5×10^5 Ω cm and carrier density of 2×10^{10} cm^{-3}. Low resistivity films were prepared using codoping, with Ga as donor and N as acceptor. These films were observed to have resistivity of 2 Ωcm and carrier density of 4×10^{19}cm^{-3}.

'Zu *et al* [42] fabricated ZnO thin films by pulsed laser deposition. These films showed stimulated emission at room temperature. Ohta *et al* [43] fabricated a transparent light emitting diode using p-SrCu$_2$O$_2$/n-ZnO heterostructure. Purica *et al* [4] studied the optical and structural properties of ZnO thin films, prepared using chemical vapor deposition (CVD). Energy band gap of these thin films was quite high (3.47 eV) when compared to that of bulk (3.2 eV). Xu *et al* [44] studied the electronic structure and spectral properties of ZnO using "full potential linear Muffin tin orbital" method. Naoki *et al* [45] studied the band-edge emission of undoped and doped ZnO single crystals at room temperature. They observed an increase in carrier concentration for Al doped ZnO samples. It had a negative effect on PL peak which was assumed to be caused by donor to free hole recombination. Auret *et al* [46] observed the presence of four electron traps, from Deep level transient spectroscopic studies, on vapour grown single crystal ZnO over which Schottky barrier diodes were fabricated. They observed two major levels situated at 0.12 eV and 0.57 eV below the conduction band. Ratheesh *et al* [47] studied the effect due to fluorine doping on structural, electrical and optical properties of ZnO thin films. From PL studies, they observed a single broad peak at 517 nm for undoped sample while three additional peaks appeared for fluorine-doped film. Electrical resistivity and photosensitivity were decreased
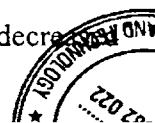
considerably on doping. Temperature dependent conductivity studies revealed that prominent shallow donor levels are Zn in interstitial and regular lattice positions. Wacogne *et al* [48] performed in-situ measurement of film thickness and optical losses, using interferometric method. They observed that the losses were not only due to absorption in the film, but were also a result of the scattering of light by the columnar structure of sputtered films. By their method, the maximum film thickness that could be measured was 32.85 µm.

Kohiki *et al* [49] observed an enhancement in conductivity of zinc oxide by implanting it with 100 keV H^+ ion. Look *et al* [2] studied electron irradiation damage in ZnO and post annealing effects. They found that the activation energy of the dominant donor produced by the irradiation was about 30 meV. Matsunami *et al* [27] studied the structural, optical and electrical properties of 100 keV Ne ion irradiated in ZnO thin films (grown on MgO). They observed that films (with *a*-axis orientation) showed an increase in grain size and rearrangement of their orientation after irradiation. They also found that the resistivity increased by three order of magnitude for small dose. Kono *et al* [50] observed nanoparticles of Cu formed in ZnO substrate, by negative Cu ion implantation, using an acceleration voltage of 60 keV.

We could not find any reported work of characterisation of ZnO thin films, (prepared using CSP or on ion irradiated) using PDS technique. To the best of our knowledge, this could be the first kind of work in that direction.

5.3 Experimental Details

In the present work, ZnO thin films were prepared by spraying a solution of 0.6 M Zinc acetate dissolved in ethanol and water taken in the ratio

1:1. A set of samples was prepared by spraying various volumes of spray solution from 50 ml to 300 ml keeping the substrate at 400 °C. Detailed description of the sample preparation is given elsewhere [13].

Films of about 1 cm^2 area were irradiated with 120 MeV Au_{197} ions using 15UD Pelletron tandem accelerator installed at Nuclear Science Centre - New Delhi, on a set of samples (thickness ~0.5 μm) with dosages ranging between $1x10^{12}$ to $3x10^{13}$ ions / cm^2. Beam current was maintained around 1 nano ampere. Ion beam was focused to a spot of 1 mm diameter and then scanned over 1 cm × 1 cm area using a magnetic scanner. In our case, high energy was selected to have the range of the ions to few microns so that no ions are implanted in the film and there will be defects only due to the irradiation.

5.4 Results and Discussion

5.4.1 ZnO thin film samples prepared for various thicknesses

5.4.1.1 Structural and optical properties

Energy band gap (Eg) of the samples were estimated by plotting $(\alpha h\upsilon)^2$ versus $h\upsilon$ and extrapolating the linear portion near the onset of absorption edge to the energy axis in the wavelength range 300 to 900 nm. The measured Eg values showed a steady increase with increase in sample thickness from 3.26 eV for "50 ml" sample to 3.35eV for "200 ml" sample. For further increase in the film thickness the Eg value was found to decrease slightly, to 3.29 eV. Initial low value of Eg could be due to poor crystallinity of the film, as revealed by the XRD (Fig. 5.5).

From the XRD pattern, a strong peak located at $2\theta = 34.4°$, corresponding to (002) plane, was observed. Another weak peak located at $2\theta = 36.15°$, corresponding to (101) plane, was also observed. The (002) peak for "50 ml" and "300 ml" samples were found to be very weak. The crystallite size was estimated using Debye – Scherrer formula. Grain size of 270 nm was observed for "200 ml" sample and this was found to be the maximum value. The grain size also steadily increased with thickness of the sample.

The increase in grain size for "200 ml" could be due to good crystalline quality, as (002) peak intensity was found to be maximum for this sample, which was evident from XRD pattern [13]. Observed increase in (002) peak with increase in film thickness could be due to the fact that the grains with lower surface energy becomes larger as the film grows. This showed that (002) texture of the film might form easily [33]. Fig. 5.1 shows the lattice strain variation for ZnO samples calculated from XRD pattern. It was seen that the lattice strain was least for "200 ml" sample. This indicated that "200 ml" sample was formed with good crystalline quality.
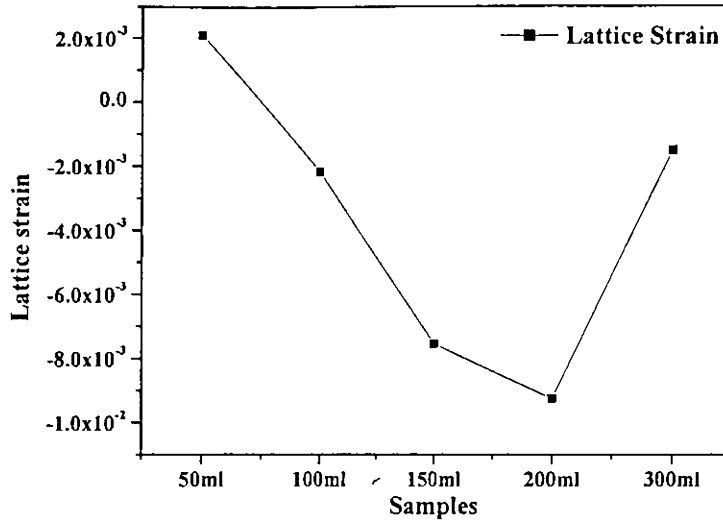
Fig. 5.1 Plot for variation of lattice strain for ZnO samples prepared for various sample thicknesses

5.4.1.2 Photothermal studies

All the ZnO thin film samples were analysed using the existing PDS setup. The only change was that, as ZnO is a wide band gap material, we used 300 nm line from Xe-arc (Oriel) lamp after passing the light beam through a monochromator. Beam optics was adjusted by setting the wavelength at 532 nm.

5.4.1.2a Thermal diffusivity measurement

Fig. 5.2 is the typical log amplitude versus square root of chopping frequency plot. We used this curve for the determination of the thermal and electrical property of the thin films. The procedure used was explained earlier, in chapter 1 (section 1.5.1). Fig. 5.3 shows the variation of thermal diffusivity for ZnO samples having various thicknesses.

Thermal diffusivity values show a decrease from 0.021 cm^2s^{-1} for "50 ml" sample to 0.009 cm^2s^{-1} for "100 ml" sample. On further increasing the sample thickness the thermal diffusivity value was found to increase to 0.022 cm^2s^{-1} for "200 ml". However, for sample sprayed for "300 ml" showed a decrease of 0.016 cm^2s^{-1}.
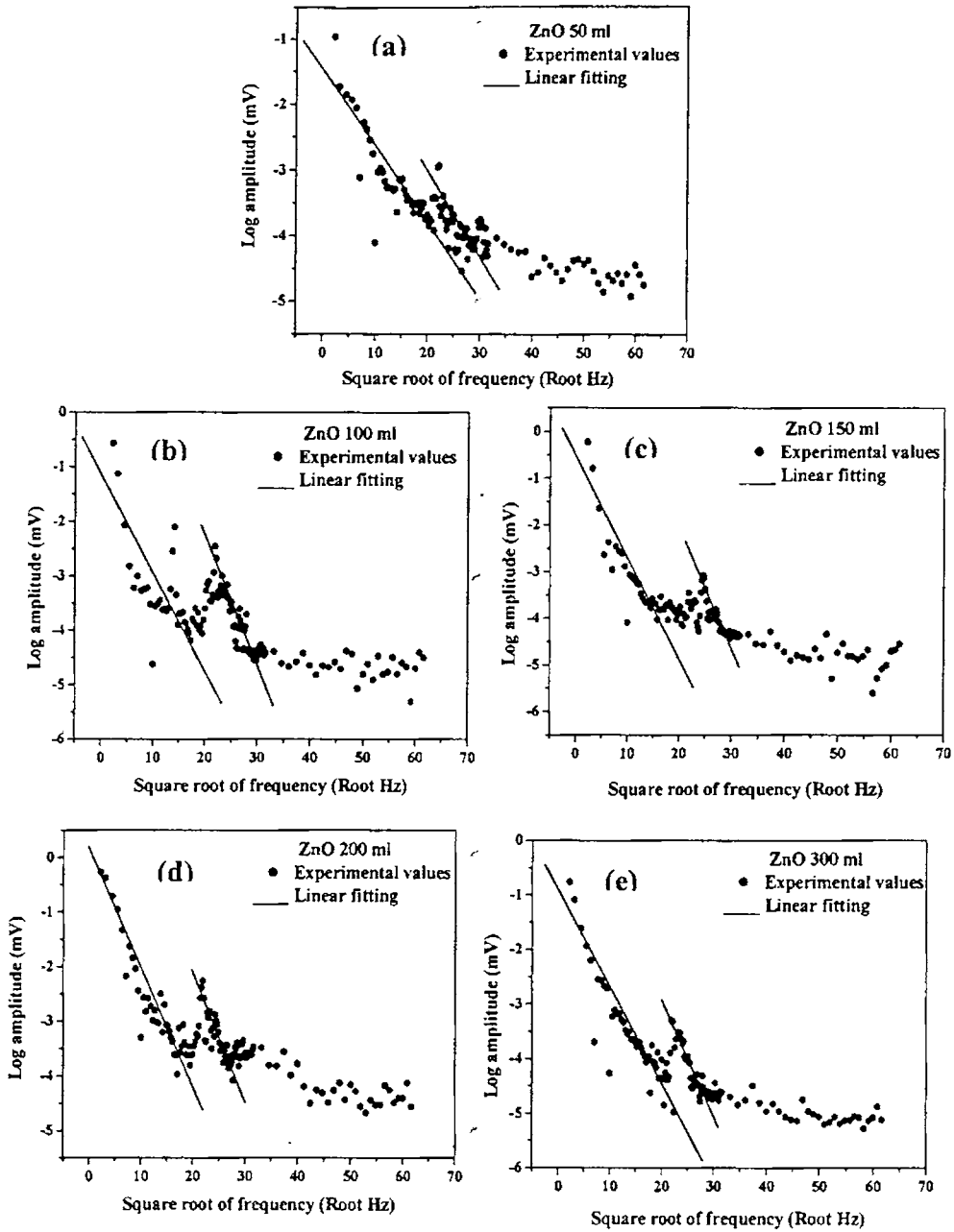
Fig.5.2 Log amplitude versus square root of frequency plot for ZnO samples prepared with various thicknesses.

Variation of thermal diffusivity with film thickness can be explained on the basis of density of film. When the thickness is very low as in case of 50 ml spray, the film has an island structure making density very low and hence a higher thermal diffusivity. But on increasing the film thickness by increasing the spray volume, the density increases. This makes thermal conductivity low. But as the thickness increases further, the increase of grain size may be overcoming the effect due to increase in grain size and hence the thermal diffusivity increased very much.
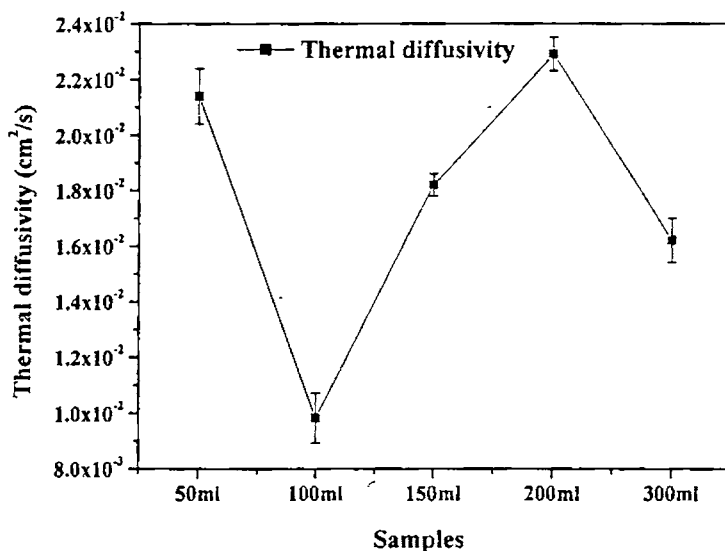

Fig.5.3 Plot for variation in thermal diffusivity for ZnO samples prepared for various thicknesses.

5.4.1.2b Mobility measurement

Fig. 5.4 shows the graph, depicting variation in mobility of samples having various thicknesses. Tabulated mobility value of these samples are

shown in Table 5.1. This was calculated using Einstein-Smoluchowski relation. Calculation was done using the procedure described earlier in chapter 1 (section 1.5.2). Mobility showed an increase and attains a maximum value of 16.1 $cm^2V^{-1}s^{-1}$ for "200 ml" samples. This value agrees with the reported value [33,51, 52-54].

Increase in mobility observed with increase in volume of spray solution could be due to improvement in crystalline quality. The (002) peak intensity increased with the volume of spray (i.e. with film thickness), which was observed from XRD pattern shown in Fig. 5.5. The grain size calculated using Debye-Scherrer's formula also showed an increase with volume of spray solution (Fig. 5.6). Then understanding the mechanism of mobility became an important factor. Mobility of charge carriers within a material can be understood this way.
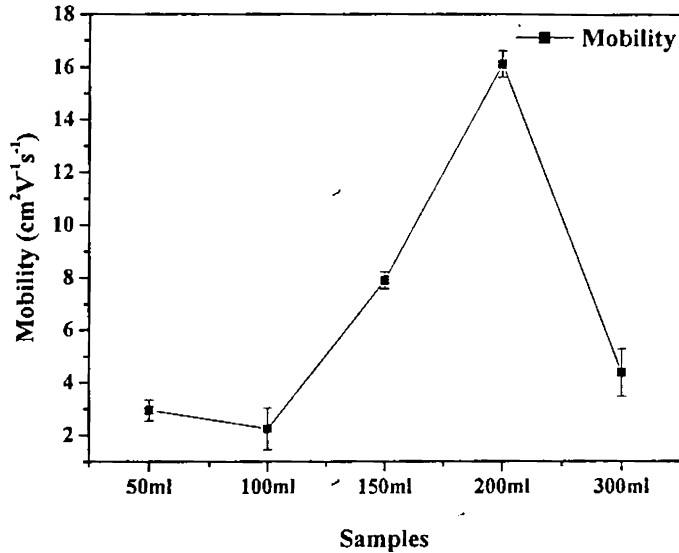
Fig.5.4 Mobility variation for ZnO thin films
prepared for various sample thickness.

The grain boundaries have an inherent space charge region due to the interface and band bending occurs that results in the potential barriers to the charge transport. Volger [55] proposed a model, which consisted of an inhomogeneous conductor consisting of series connected, separately homogeneous domains of high and very low conductivity. The high conductivity domains were the grains itself, and the low conductivity domains were the grain boundaries. This model represented a polycrystalline semiconductor in which ohmic transport of the carriers dominated. A schematic representation is shown in Fig. 5.7. Then mobility can be expressed as [64],

$$\mu = \mu_g \left\{ \left[1 + \left(l_2 / l_1 \right) \exp\left(q\phi_b / kT \right) \right]^{-1} + \left(l_2 / l_1 \right) \right\}, \quad \ldots\ldots\ldots\ldots\ldots\ldots\ldots(5.1)$$

Where,

l_1 - grain size,

l_2 - boundary width,

μ - Hall mobility,

μ_g – Bulk grain mobility,

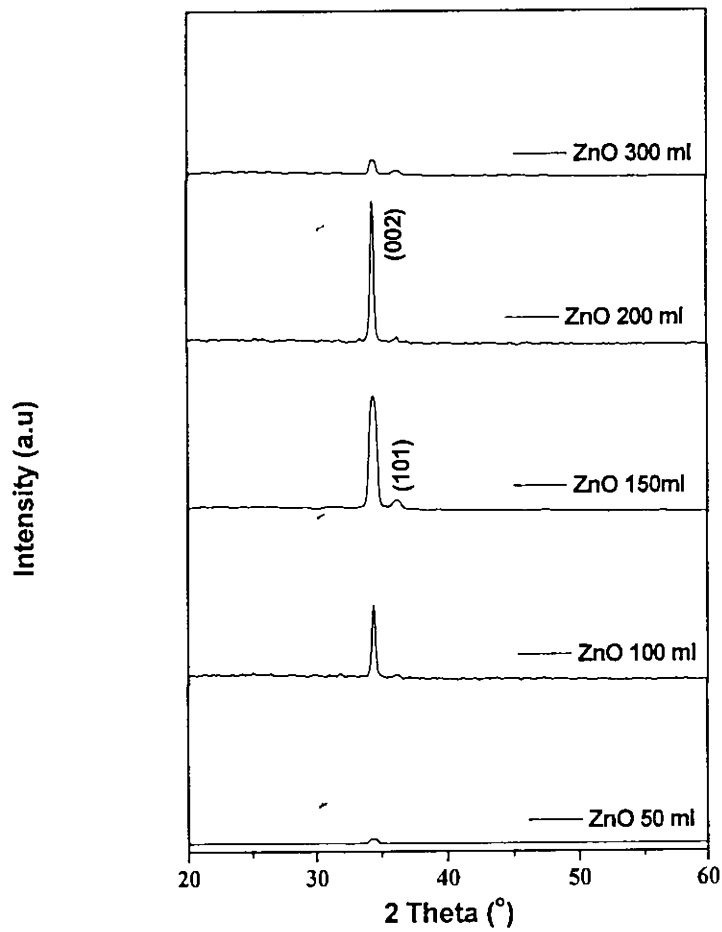ϕ_b - Barrier potential,

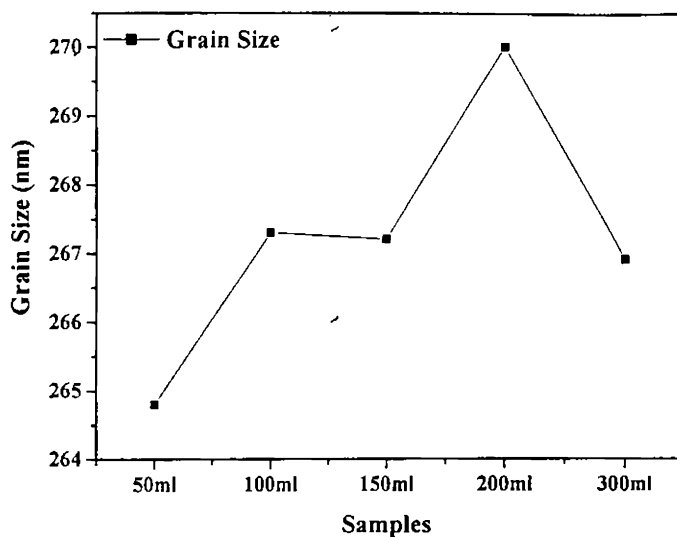Fig.5.5 XRD pattern for ZnO samples prepared for various thicknesses

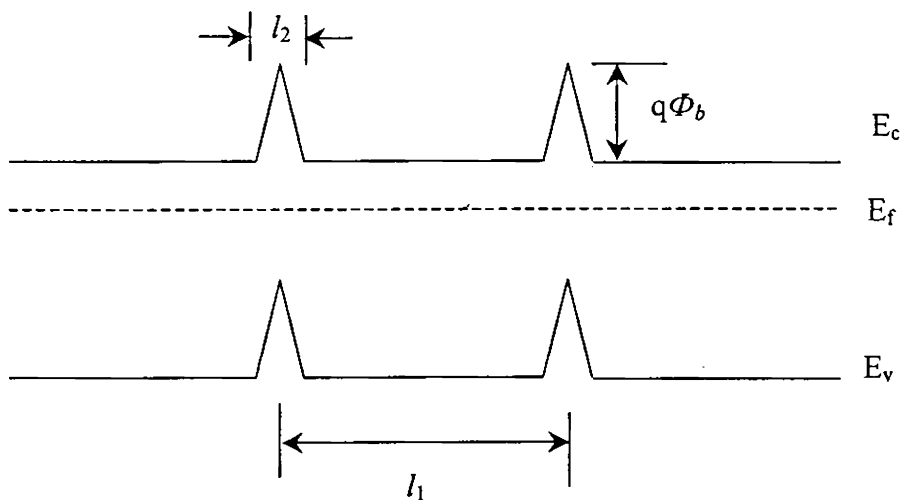Fig.5.6 Grain size yariations for various thicknesses of the sample

Fig. 5.7 Energy band representation of a polycrystalline crystalline semiconductor thin film with grain size l_1 and grain boundary width l_2. Grain boundary barrier potential is $q\Phi_b$.

Moreover, there occurs a possibility of grain boundary trapping. A large concentration of active trapping sites are present at the grain boundary which, in turn captures free carriers [56, 57 and 58], and as a result, the charge states at the grain boundaries become potential barriers and these barriers limit the transport of carriers between grains. Hence the mobility will be low for samples whose grain size is small, as there will be large number of grains in the sample. This could be the reason for decrease in mobility for samples of low thickness.

Hence from the above argument it is clear that as grain size increased (or l_1 increased) mobility would naturally increase. In the PDS measurement here, we found the same thing; sample prepared by spraying had maximum grain size, and it has maximum mobility also.

Samples	Mobility measured using PDS		Other references
	curvefitting ($cm^2V^{-1}s^{-1}$)	Error Bar	
ZnO 50 ml	2.95	± 0.42	-
ZnO 100ml	2.24	± 0.81	-
ZnO 150ml	7.90	± 0.32	-
ZnO 200ml	16.10	± 0.52	[33], [51],[52- 54]
ZnO 300ml	4.37	± 0.90	-

Table 5.1 Tabulated value of mobility of ZnO thin film samples. The value was calculated using PDS technique and references are also given for comparison.

5.4.1.2c Thickness measurements

Optical techniques are usually the preferred method for measuring thickness of transparent thin films because these are accurate, nondestructive, and require little or no modification of sample. Most commonly used optical measurements are spectral reflectance, ellipsometry and recently PDS measurements. Spectral reflectance measures the amount of light reflected from a thin film over a range of wavelengths, with the incident light normal to the sample surface. Ellipsometry measures the reflectance at non-normal incidence and at two different polarizations [63]. Variable Angle Monochromatic Fringe Observation (VAMFO) is also a simple nondestructive method for measuring the refractive index and thickness of transparent films on reflecting substrates. Fringe counting could be laborious and this can have errors [59]. As PDS technique uses thermal wave propagation for thin film characterization, this is not affected by light scattering. One can confidently use it even for the characterisation of transparent or opaque films.

Thicknesses of the samples were calculated using the curvefitting method in PDS technique as described in chapter 1 (section 1.4). Curve fitting was done assuming single layer model. Backing layer was glass substrate, which was assumed to be non absorbing. But film coated over this backing layer was absorbing. The whole system was immersed in fluid medium. This constituted the model for our theoretical analysis. Schematic representation of the model is as shown in Fig. 5.8. Modulated pump beam, when irradiated over the absorbing layer, generates thermal waves due to non-radiative transition in the film. The thermal waves so generated propagates through this layer to the surface of the sample and we obtain the PDS signal. This is plotted as graph, showing variation of signal for different frequencies (Fig. 5.9). Curve

212

fitting was done on these graphs using one layer model as shown in Fig. 5.8. Thickness of the samples determined by this way, is tabulated in Table 5.2. Thickness measured for "200 ml" using Stylus method is also given for comparison. It can be seen that PDS value coincided well with the Stylus data. Multiparameter least square fitting procedure was done to optimize the experimental result. Since thickness was an input parameter, we could derive it from many trials from the best fitted curve. From the experimental PDS data it was clearly observed that for increase in volume of spray solution, there was an observed increase in the deflection amplitude for very low chopping frequency. For low chopping frequency, the signal is from the bottom most layer of the sample, resulting in increase in deflection amplitude for increase in sample thickness.
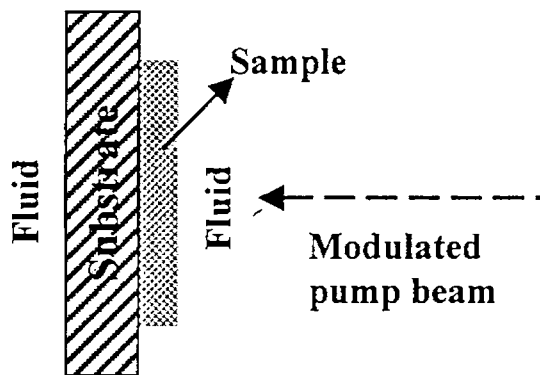

Fig. 5.8 Schematic representation of the model used for thin film thickness determination.
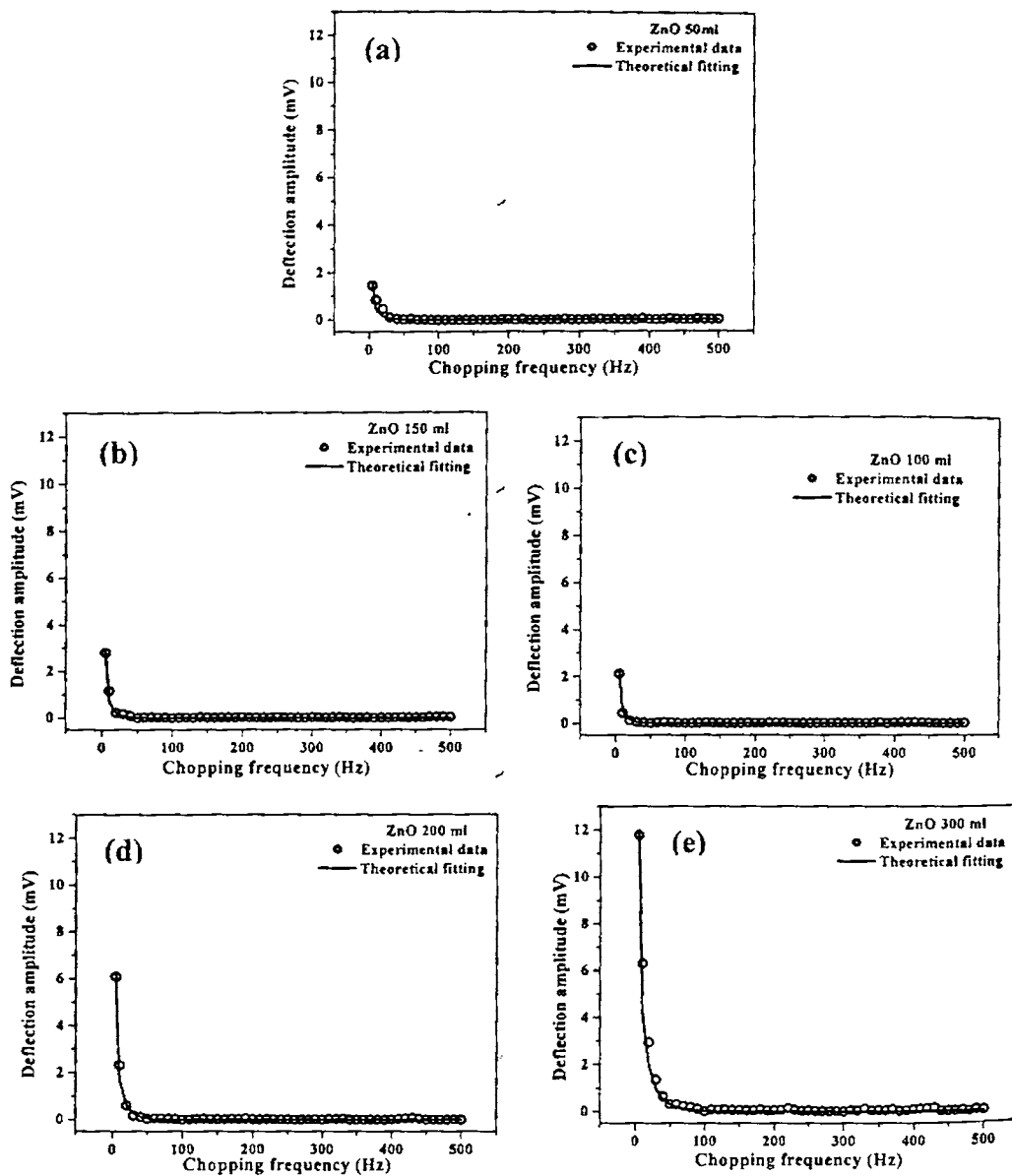
Fig.5.9 Typical deflection amplitude versus chopping frequency plot for ZnO samples used for determining thickness through curvefitting method.

Samples	Thickness measured using PDS		Thickness measured (µm) using stylus method
	curvefitting (µm)	Error Bar	
ZnO 50 ml	0.17	± 0.011	-
ZnO 100ml	0.20	± 0.032	-
ZnO 150ml	0.32	± 0.116	-
ZnO 200ml	0.57	± 0.012	0.563
ZnO 300ml	0.73	± 0.024	-

Table 5.2 Tabulated value of thickness calculated using PDS method for ZnO samples prepared with different volume of spray solution. Measurement from stylus for "200 ml" sample is also given for comparison.

5.4.2 ZnO thin film samples irradiated with 120 MeV Au$_{197}$ ions

5.4.2.1 Structural and optical properties

XRD pattern of ion irradiated ZnO samples showed a systematic decrease in intensity of (002) plane for dosages of $1x10^{13}$ and $3x10^{13}$ ions/cm^2. Peak corresponding to (101) plane also decreased with increase of ion dosage. Fig. 5.10 is the XRD pattern for both pristine and irradiated samples. Lattice strain was also calculated from XRD data. Lattice strain increased with ion dosage. Fig.5.11 shows the lattice strain of pristine and irradiated samples. Grain size was calculated using Debye Scherrer formula from the XRD data and this decreased with ion dosage. Fig.5.12 is the plot depicting variation in grain size of pristine and irradiated samples for various dosages.

Ion irradiation or ion implantation causes stress due to the bombardment of energetic ions into the target and hence there is an observed increase in lattice stain in irradiated ZnO samples. On ion implantation, the strain tensor related to the density variation from ρ to $\rho+\Delta\rho$ can be express as,

$$\varepsilon_\rho = -\frac{\Delta\rho}{\rho}\left(1-\exp\left(-\frac{\Phi}{\Phi_\rho}\right)\right), \dots\dots\dots\dots\dots\dots\dots\dots\dots\dots\dots\dots\dots\dots(5.2)$$

where

Φ_ρ - is the characteristic dose of densification.

Φ – Ion dose.

Strain tensor for whole of the material can be expressed as the sum of thermal component, density component and intrinsic strain component,

$$\varepsilon\left(x,\Phi\right) = \varepsilon_T + \varepsilon_\rho + \varepsilon_i, \dots\dots\dots\dots\dots\dots\dots\dots\dots\dots\dots\dots\dots\dots(5.3)$$

As a result, stress distribution versus depth is not uniform and follows the distribution of implanted ions [62].

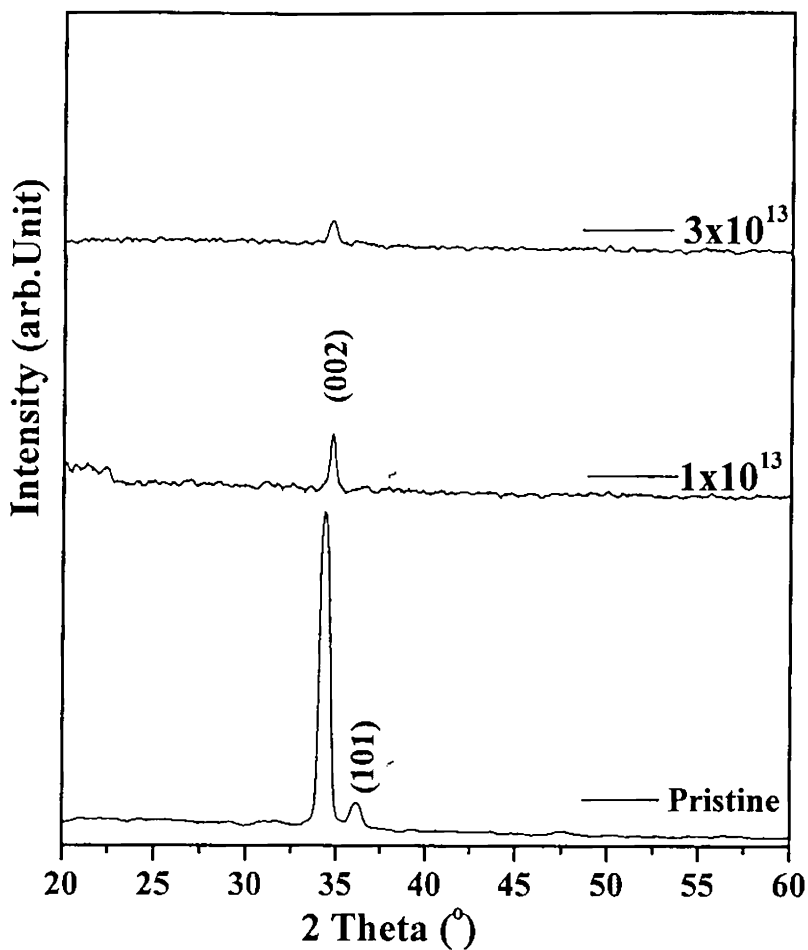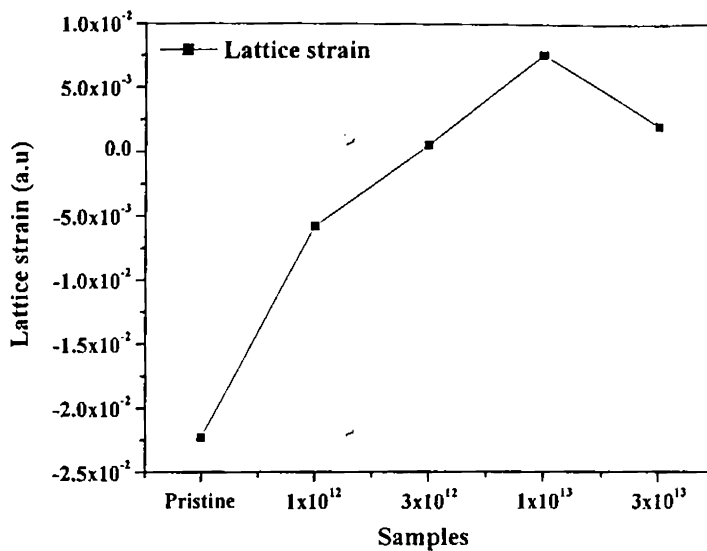Fig. 5.10 XRD pattern for 120 MeV Au_{197} ion irradiated ZnO samples.

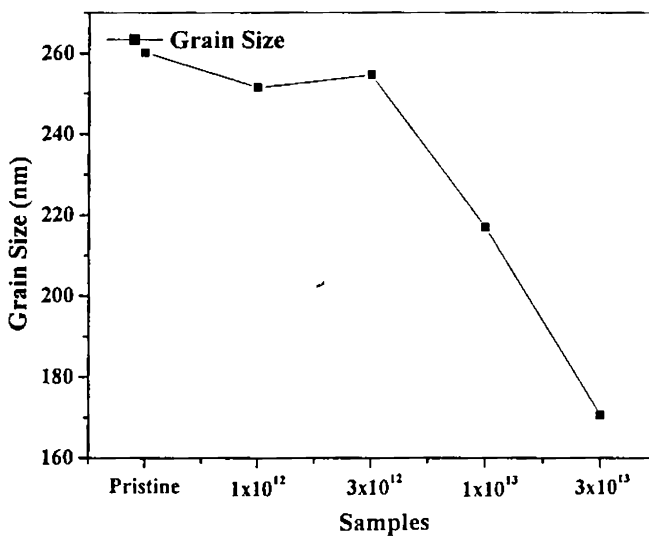Fig. 5.11 Lattice strain for120 MeV Au_{197} ion irradiated ZnO samples.

Fig. 5.12 Grain size variation for120 MeV Au_{197} ion irradiated ZnO samples

5.4.2.2 Photothermal studies

All the irradiated thin films were analysed using the existing PDS setup. As ZnO is a wide band gap material, we used 300 nm line from a Xe-arc (Oriel) lamp source, as the pump beam, after passing the light beam through a monochromator (Oriel). Pump beam irradiating the sample surface was focused to an area of 1x1.5cm^2. Beam optics was adjusted by setting the wavelength at 532 nm.

5.4.2.2a Thermal diffusivity measurement

Variation in thermal diffusivity of pristine and irradiated samples is as shown in Fig. 5.13. The calculated value of thermal diffusivity showed a steep decrease with increase of ion dosage. The value decreased from 0.023 cm^{2}s^{-1} for pristine sample to 0.016 cm^{2}s^{-1} for irradiated sample of dosage 1x10^{13} ions /cm^2. Thus, we can conclude that the thermal diffusivity decreased with ion irradiation. This decrease could be attributed to the bond breaking or rupturing due to impinging of energetic ions. More the time of exposure of the target to ion beam, more is the damage. However, there are reports on self annealing of dangling bonds [27] occurring due to exchange of high energy during the process. Increase in lattice strain and decrease in grain size (Fig. 5.11 and Fig. 5.12) in the present study also supports the decrease of thermal diffusivity.

By definition, thermal diffusivity is the capacity of the material to transport or allow the diffusion of thermal energy. In our work, measurement of thermal diffusivity was done by generating thermal waves within the sample and detecting it at the sample surface. As thermal wave propagation depends on the microstructural property of the material, any change in the regularity of

the material structure could be identified. This is been used for studying the presence of damage due to ion irradiation.

We could not find reports on thermal diffusivity studies on ZnO thin films and this could be the first work carried out on ion irradiated transparent conducting oxide material, such as ZnO thin films, to the best of our knowledge.
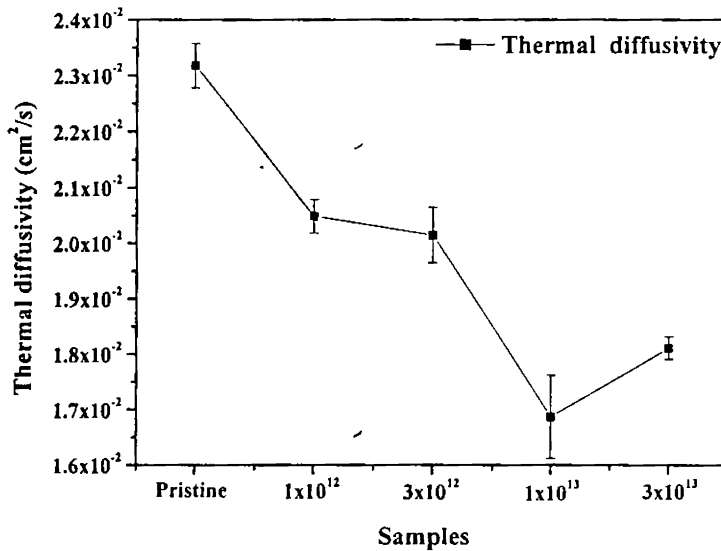

Fig. 5.13 Graph showing variation of thermal diffusivity of prisitine and irradiated samples for various dosages.

5.4.2.2b Mobility measurement

Fig. 5.14 is plot for log amplitude versus square root of frequency for pristine and ion irradiated ZnO thin film samples. The second slope in these curves, which is due to the photogenerated carriers [56] was used to determine

the mobility of the sample. Details of mobility calculation is given in chapter 1 (section 1.5.2).

Mobility values calculated were found to decrease with irradiation dosage as shown in Fig. 5.15. The values ranged from 12.2 $cm^2V^{-1}s^{-1}$ (for pristine sample) to 1.93 $cm^2V^{-1}s^{-1}$ (for irradiated sample of dose $3x10^3$ ions/cm^2). Mobility value of 9.5 cm^2/Vs was reported for irradiated film by Shigemi *et al* [49] for 100 keV H^+ ion implanted in ZnO thin films upto a fluence of 10^{15} to 10^{17} ions/cm^2. Decrease in mobility should be due to increase in defects caused by irradiation making mean free path of photogenerated charge carriers small. Moreover, there is degradation in grain size also (section 5.4.1.2b).
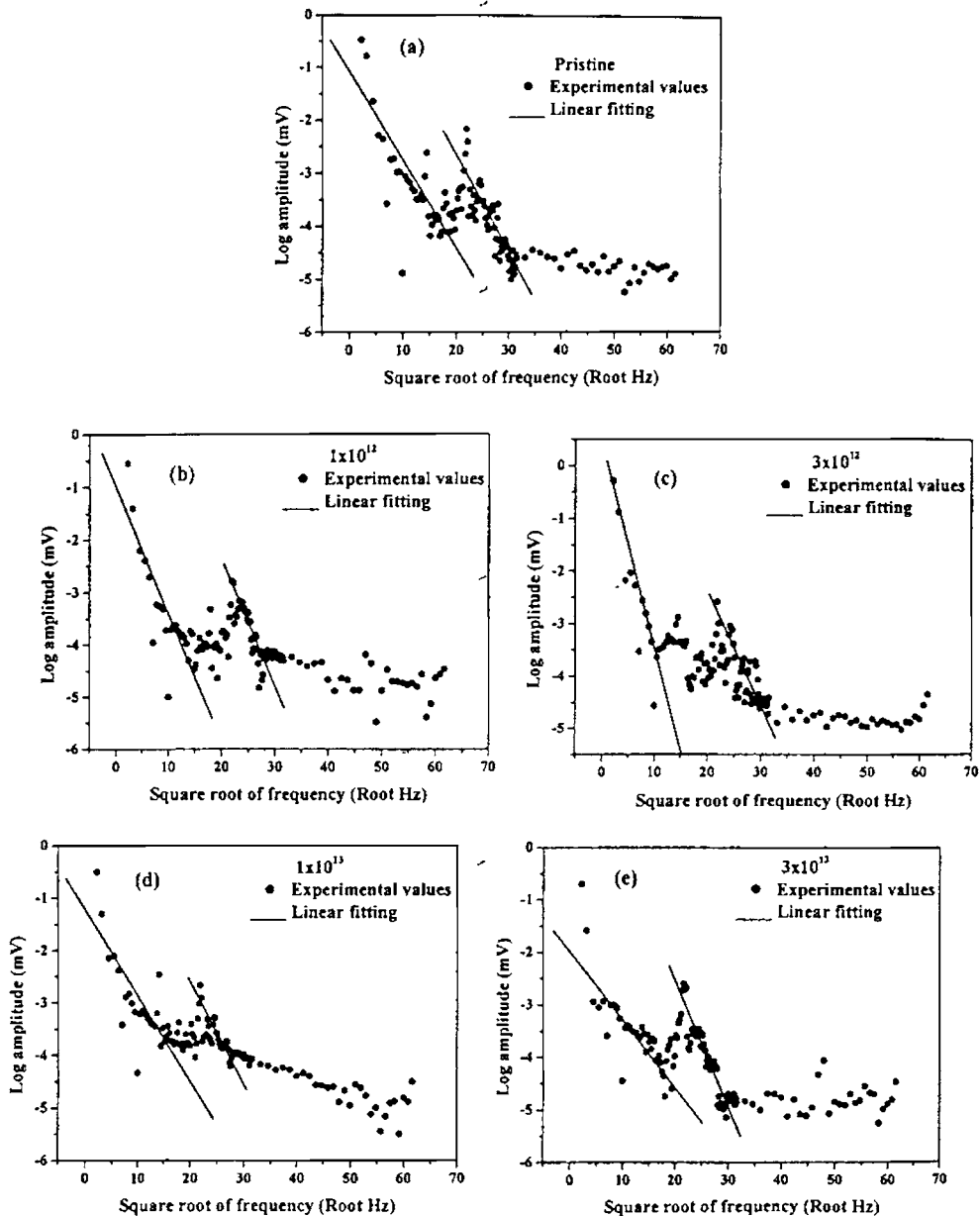
Fig. 5.14 Log amplitude versus square root of frequency curve for prisitine and ion irradiated ZnO thin film samples.
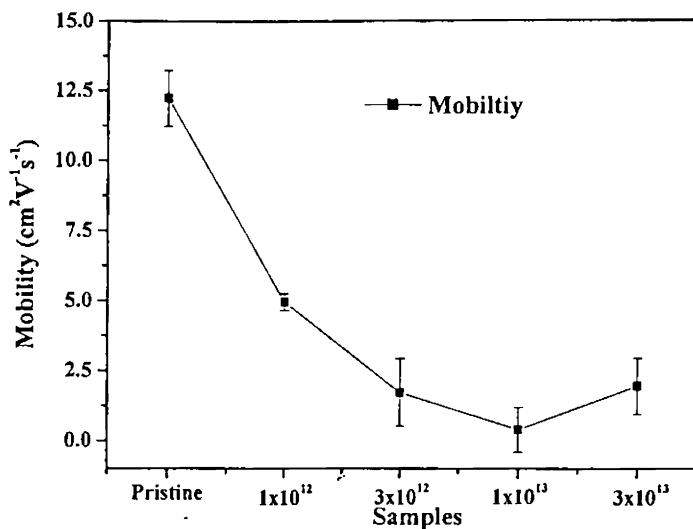
Fig. 5.15 Graph showing variation of mobility
of prisitine and irradated samples.

5.5 Conclusion

Thermal diffusivity and carrier mobility of ZnO films were determined using PDS techinque. Samples prepared using different volumes of spray solutions were studied and it was observed that, "200 ml" sample showed the maximum thermal diffusivity and mobility value. The crystalline property was also found to be good for the sample from XRD studies. Film thickness was also measured using PDS technique. The data obtained was found to coincide with the value from Stylus method.

Ion irradiated ZnO thin film samples were studied using PDS technique to know the thermal and transport properties. It was observed that ion irradiation caused degradation of the material microstructure. From XRD

pattern (002) peak intensity was found to decrease drastically with increase in ion dosage. Lattice stain calculated showed an increase with ion dosage and the grain size calculated from the XRD data showed a decrease with ion dosage. Both thermal diffusivity and mobility were observed to show a sharp decrease due to ion irradiation. These effects were attributed to damage caused due to ion irradiation.

References

[1] P. Nunes, E. Fortunato, P. Tonello, F. Braz Fernandes, P. Vilarinho, R. Martins, *Vacuum*, **64** (2002) 281.

[2] D. C. Look, D. C. Reynolds, and J. W. Hemsky, R. L. Jones and J. R. Sizelove, *Appl.Phys. Lett.*, **75 (6)** (1999) 811.

[3] M. J. Vellekoop, C. C. G. Visser, P. M. Sarro, and A. Venema, *Sens. Actuators A,* **A21-A23** (1990) 1027.

[4] M. Purica, E. Budianu, E. Rusu, M. Danila, R. Gavrila, *Thin solid films*, **403 – 404** (2002) 485.

[5] W. Li ., *J. Vac. Sci. Technol.*, **A 18** (2000) 2295.

[6] K. K. Kim, J. H. Song, H. J. Jung, and S. J. Park, *J. Appl. Phys.*, **87** (2000) 3573.

[7] H. Z. Wu, K. M. He, D. J. Qui, and D. M. Huang, *J. Cryst. Growth*, **217** (2000)131.

[8] S. H. Bae, S. Y. Lee, B. J. Jin, and S. Im, *Appl. Surf. Sci.*, **154** (2000) 458.

[9] X. W. Sun and H. S. Kwok, *J. Appl. Phys.*, **86** (1999) 408.

[10] K. N. Yoon and J. Y. Cho, *Mater. Res. Bull.*, **35** (2000) 39.

[11] F. Paraguay, W. Estrada, D. R. Acosta, E. Andrade, and M. Miki-Yoshida, *Thin Solid Films*, **350** (1999) 192.

[12] S. A. Studenikin, N. Golego, and M. Cocivera, J. *Appl. Phys.*, **84** (1998) 2287.

[13] P. M. Ratheesh Kumar, C. Sudha Kartha, K. P. Vijayakumar, F. Singh, D. K. Avasthi, T. Abe, Y Kashiwaba, G. S. Okram, M. Kumar, and Sarvesh Kumar, *J. Appl. Phys.* (Inpress).

[14] W. Li., *Nucl. Instrum. Methods Phys. Res. B*, **169** (2000) 59.

[15] W. Li., *Surf. Coat. Technol.*, **128** (2000) 346.

[16] T. Nagase, T. Ooie, Y. Nakatsuka, K. Shinozaki, and N. Mizutani, *Jpn. J. Appl.Phys.*, **Part 2 39** (2000) L713.

[17] A. Yamada and M. Konagai, *Solid State Phenom.*, **67-68** (1999) 237.

[18] Y. F. Chen, D. Bagnall, and T. F. Yao, *Mater. Sci. Eng.*, **B 75** (2000) 190.

[19] K. Iwata, P. Fons, S.Niki, A.Yamada, K. Matsubara, K. Nakahara, and H. Takasu, *Phys. Status Solidi (a)*, **180** (2000) 287.

[20] T. Makino, *J. Cryst. Growth*, **214** (2000) 289.

[21] S. A. Studenikin, N. Golego, and M. Cocivera, *J. Appl. Phys.*, **83** (1998) 2104.

[22] A. El Hichou., A. Bougrine., J. L. Bubendorff, J. Ebothe, M. Addou, and M. Troyon, *Semicond. Sci. Technol.*, **17** (2002) 607.

[23] H. Gomez, A. Maldonado, J. Palacios-Gomez, *Thin Solid Films*, **293** (1997) 117.

[24] A F Aktaruzzaman, G L Sharma, L K Malhotra, *Thin Solid Films*, **198** (1991) 67.

[25] A. Tiburcio-Silver, A. Sanchez-Juarez, A. Avila-Garcia, *Sol Energy Mater and sol. Cells.*, **55** (1988) 3.

[26] Mathew Joseph, Hitoshi Tabata and Tomoji Kawai, *Jpn. J. Appl. Phys.*, **38** (1999) L1205-L1207.

[27] N. Matsunami, M. Itoh, Y. Takai, M. Tazawa, M. Sataka, *Nucl. Instrum. Methods Phys. Res. B*, **206** (2003) 282.

[28] D. G. Thomas, *J.Phys. & Chem. Solids*, **9** (1959) 31. .

[29] J. J. Lander, *J.Phys. & Chem. Solids*, **15** (1960) 324.

[30] Y.Sato and S.Sato, *Thin solid films*, **281-282** (1996) 445.

[31] K. Minegishi, Y. Koiwai, Y. Kikuchi, K. Yano, M.Kasuga and A.

Shimizu, *Jpn. J. Appl. Phys.*, **36** (1997) L1453.

[32] Cruz-Vazquez, F. Rocha-Alonzo, S.E. Burruel-Ibarra and M. Inoue, *Superficies y Vacio*, **13** (2001) 89.

[33] M.K.Jayaraj, Aldrin Antony and Manoj Ramachandran, *Bull. Mater. Sci.*, **25 (3)** (2002) 227.

[34] Q. P. Wang, D. H. Zhang, Z. Y. Xue, X. T. Hao, *Appl. Surf. Sci.*, **9172** (2002) 1.

[35] P Pushparajah, Abdul Kariem Arof and S Radhakrishna, *J. Phys. D: Appl. Phys.*, **27** (1994) 1518.

[36] S.A.Studenikin and Michael Cocivera, *J. Appl. Phys.* **918** (2002) 5060.

[37] J. M. Bian, X. M. Li, X. D. Gao, W. D. Yu, and L. D. Chen, *Appl. Phys. Lett.*, **84 (4)** (2004) 541.

[38] Z. Y. Ning, S. H. Cheng, S. B. Ge, Y. Chao, Z. Q. Gang, Y. X. Zhang and Z. G. Liuet, *Thin Solid Films*, **307** (1997) 50.

[39] H. Hiramatsu, K. Imaeda, H. Horio and M. Nawata, *J. Vac. Sci. & Technol., A,* **16** (1998) 669.

[40] E. D. Kolb and R. A. Laudise, *J. Am. Ceram. Soc.*, **49** (1966) 302.

[41] T. Yamamoto and H. K. Yoshida, *Jpn. J. Appl. Phys.*, **38** (1999) L166.

[42] P. Zu, Z.K. Tang, G. K. L. Wong, M. Kawasaki, A. Ohtomo, H. Koinuma, and Y. Segawa, *Solid State commn.*, **103** (1997) 459.

[43] H. Ohta, K. Kawamura, M. Orita, M. Hirano, N. Sarukura and H. Hosono, *Appl. Phys. Lett.*, **77** (2000) 475.

[44] P.S. Xu, Y.M. Sun, C.S. Shi, F.Q. Xu, H.B. Pan, *Nimb. Instr. and Meth. in Phys.Res. B,* **199** (2003) 286.

[45] Naoki Ohashi, Takashi Sekiguchi, Kouichiroh Aoyama, Takeshi Ohgaki, and Yoshihiro Terada, Isao Sakaguchi, Takaaki Tsurumi, Hajime Haneda,

J. Appl. Phys., **91** (6) (2002) 3658.

[46] F. D. Auret, S. A. Goodman, M. J. Legodi, and W. E. Meyer, D. C. Look, *Applied Phys. Lett.*, **80** (2002) 8.

[47] P. M. Ratheesh Kumar, C. Sudha Kartha, K. P. Vijayakumar, F. Singh, D. K. Avasthi, *Mat. Sci. and Engg. B* (In press).

[48] B.Wacogne, C.N.Pannell, M.P.Roe, and T.J.Pattison, *Appl. Phys. Lett.*, **67** (2) (1995) 161.

[49] Shigemi Kohiki, Mikihiko Nishitani, Takahiro Wada and Takashi Hirao, *Appl. Phys. Lett.*, **64** (21) (1994) 2876.

[50] K. Kono, S. K. Arora, N. Kishimoto, *Nucl. Instrum. Methods Phys. Res. B*, **206** (2003) 291.

[51] Y. W. Heo, S. J. Park, K. Ip, S. J. Pearton and D. P. Norton, *Appl. Phys. Letts.*, **83** (2003) 1128.

[52] S. Major, A. Banerjee, and K.L. Chopra, *Thin solid films*, **108** (1983) 333.

[53] M. G. Ambia, M.N. Islam, and M. Obaidul Hakim, *Sol. Energy Mater. Sol. Cells*, **28** (1992) 103.

[54] J. De Marchant and M. Cocivera, *Chem. Mater.*, 7 (1995) 1742.

[55] J. Volger, *Phys. Rev.* **9** (1956) 1023.

[56] T.I. Kamins, *J. Appl. Phys.*, **42** (1971) 4357.

[57] P. Rai Choudhury and P.L. Hower, *J. Electrochem. Soc.*, **120** (1973) 1761.

[58] J.Y.W. Seto, *J. Electrochem. Soc.*, **122** (1975) 701.

[59] W. A. Pliskin, E. E. Conrad, *IBM Journal of Research and Development*, **8** (1) (1964) 43.

[60] E. Weber, T. Cacciato, A. Polman, *J. Appl. Phys.* **78** (7) (1995) 4723.

[61] L. Tamulevičius, S. Puodžiukynas, L.Matiukas, *Phys. Stat. Sol.(a)*, **96**

(1986) K157.

[62] Sigitas Tamulevicius, Ignas Pozela, Judita Puiso, *Mat. Sci.,* **10 (2)** (2004) ISSN 1392.

[63] Sunny Mathew, *Ph.D Thesis,* cochin University of Science and Technology – Cochin (1994).

[64] *"Polycrystalline and Amorphous Thin films and Devices",* Ed. Lawerence L. Kazmerski, Academic press Inc. New York (1980).

Chapter 6

PDS FOR INDUSTRIAL APPLICATION

6.1 Introduction

Finished materials, products and equipments, which fail to achieve their design requirements or projected life, due to undetected defects, may require expensive repair or early replacement. Such defects may also cause unsafe conditions or could lead to catastrophic failure, as well as loss of revenue due to unprecedented plant shutdown. Thus material analysis through Non-Destructive Testing (NDT) becomes very important. NDT can be applied in each stage of an item's construction to understand materials homogeneities or to determine its quality [1].

NDT, Non-Destructive Evaluation (NDE), Non-Destructive Inspection (NDI) are the terms commonly used in connection with the techniques that are based on the application of physical principles employed for the purpose of determining characteristics of material/components/systems, for detecting and assessing the inhomogeneties and harmful defects without impairing the usefulness of the material/components/systems. In other words, it is used for the examination of materials and components in such a way that, it allows materials to be examined without changing or destroying their usefulness. NDT of engineering materials, components and structures has steadily increased in recent years because of the all-round thrust for improving material quality and performance reliability.

The concept of component design strives towards greater efficiency and improved performance. This can be achieved by employing materials with

acceptable but minimum level of defects analysed through quality testing. NDT can be used to find out the size and to locate superficial as well as subsurface flaws and defects. Welded joint, cracks, porosity, voids, inclusions, etc., can be examined using NDT.

Performance of surface hardened parts is a major issue in automotive and aerospace industries. There is, therefore, a strong need to improve the quality control by introducing new measurement systems which allow for non-destructive, non-contact hardness profile measurement as an alternative to the presently used destructive inspection method [2]. Table 6.1 is the list of the merits and demerits of NDT with respect to destructive techniques.

Non-Destructive tests	Destructive tests
Advantages	**Limitations**
1. Tests are made directly on the object. 100% testing on actual components is possible.	Tests are not made on the objects directly. Hence correlation between the sample specimen used and object needs to be proved
2. Many NDT methods can be applied on the same part and hence many or all properties of interest can be measured	A single test may measure only one or a few of the properties
3. In-service testing is possible	In-service testing is not possible
4. Repeated checks over a period of	Measurement of properties over a

	time are possible	cumulative period of time cannot be possible
5.	Very little preparation is sufficient	Preparation of the test specimen is costly
6.	Most test methods are rapid	Time requirements are generally high
	Limitations	**Advantages**
7.	Measurements are indirect. Reliability is to be verified	Measurements are direct and reliable
8.	Usually qualitative measurements	Usually quantitative measurements
9.	Skilled judgments and experience are required to interpret indications	Correlation between test measurements and material properties are direct

Table 6.1: List of merits and demerits of NDT
with respect to destructive techniques.

6.2 The commonly used NDT methods

(i)   Liquid penetration inspection:

This technique is based on the ability of a liquid to be drawn into a "clean" surface-breaking flaw by capillary action. After a period of time (called the "dwell"), excess surface penetrant will be removed and a developer will be applied. This acts as a "blotter" and it draws the penetrant from the flaw to reveal it's presence. Major demerit of this technique is that this gives information about cavities that are open to the surface only. Very viscous liquids become unsuitable as penetrants, because they do not flow. Moreover, coloured penetrants require good white light while fluorescent penetrants need to be used in darkened conditions with an ultraviolet "black light".

(ii)   Eddy current:

This technique uses magnetic lines of force, when an energised coil is brought near to the surface of a metal component. Due to magnetic induction, the lines of force get distorted by the presence of a flaw. Major disadvantages of these technique is that, as Eddy current testing is an electromagnetic technique, it can only be used on conductive materials. Surface irregularities and scratches can also give misleading indications. Therefore it is necessary to ensure very careful preparation of the surface before magnetic particle testing is to be undertaken.

(iii)   X-Ray and Gamma rays detection:

The x-ray or gamma rays, is allowed to pass through the material to be inspected, and is then captured on a film. This film, when processed, gives an

image with a series of grey shades between black and white. The choice of type of radiation to be used, as to whether X-Ray or gamma ray, depends on thickness of the material to be tested. Major disadvantage with this method is that, X-rays and gamma rays are very hazardous. Special precautions must be taken when performing radiography. Hence the operator should use appropriate barriers and warning signals to ensure that there are no hazards to personnel.

(iv)   Ultrasonic detection:

It is based on the principle that, ultrasonic waves produced inside any material, could propagate through the material, since solid materials are good conductors of sound waves. The waves are not only reflected at the interfaces but also by internal flaws such as material separations, inclusions, etc,. This is one of the most popular NDT and is the "present day quality testing tool".

(v)   PDS technique

PDS technique is one among the NDT tool. It works on the principle of understanding thermal wave generation and propagation within the material. The thermal wave is generated inside the material through optical absorption. Since this technique uses laser beam, localized information to an area of μm range can be derived. Moreover this makes it non-destructive. Companies such as Jenoptik, PHOTOTHERM in Europe and Thermawave InC. in US, have started to manufacture apparatus based on PDS technique, for quality control (mainly of silicon wafers) which are based on optically and thermally modulated optical reflection from semiconductors [3]. This is for measuring thickness of surface coating like paint etc,. Lot of effort has gone in for the

transfer of technology from laboratory scale to industrial plant scale. This was because, it requires additional optimization comprising of cost considerations, security and reliability aspects. Most importantly the device has to work under the special conditions dictated by the industrial demands, with considerable reduction of the available measuring time [3].

In the present study, we attempt to show the use of PDS tool for industrial application. We tried to study the quality of welded joint, to determine the thickness of paint coated over a substrate and to understand the homogeneity of polymer doped with various filler components.

6.3 Review

Gibkes *et al* [4] had developed a trace gas detector using photothermal technique for industrial application. It uses either a tunable laser adjusted to an absorption line of the trace molecule or spectrometer to scan the whole absorption spectrum. The advantage of this detector is that it can be adapted to different gases by changing simply a narrow band IR-filter in the front of the excitation beam. The use of limited number of electronic, mechanical and optical components makes the system reliable and less sensitive to environmental changes.

Busse *et al* [5] measured thickness of paint, using modulated photothermal radiometry, as this was an appropriate method for remote and nondestructive evaluation of thickness and the thermal properties of thin films / coatings deposited on thick substrates. A 48-μm-thick layer of grey paint on brass was investigated. The measurements were performed with the Photothermal Microscope (model PTM1) made by PHOTOTHERM -

236

Germany [6]. Wu *et al* [7] investigated turbine blades for hidden defects using this technique. They used combination of Lock-in technique and commercial IR-thermography. This allowed a fast, remote and nondestructive inspection of components. Even at low modulation frequencies (0.03 Hz) the measurement time was within 3 minutes.

Walther [8] inspected rough steel surface using photothermal technique. He used an effective layer model and compared his results with experimental data. He also observed that the signal corresponds to the spatially averaged surface temperature, if the diameter of the heating spot was larger than the correlation length (which is the mean lateral distance between characteristic hills or valleys of the rough surface) and fulfills the conditions of one dimensionality. He had also published another work, which was based on the equivalent layer model. The effect of roughness induced thermal wave dispersion was studied on hardened steel. He could successfully demonstrate the validity of the theory by comparing calculations with photothermal radiometric measurements [9].

Pandey *et al* [10] studied polymeric materials using photothermal techniques. Thermal diffusivity values for polymer materials such as, Biaxially oriented polypropylene film (BOPP), Tubular Quinched polypropylene film (TQPP), Carbon fibers, fullerene and composite ceramics were determined using this technique.

6.4 Experimental Details

6.4.1 Welded joint

Two individual Steel plates (MS EN8) of dimension 2 x 1 inch and of thickness 5 mm were welded along a "V" Groove using a 3 mm welding rod, maintained at 120 Amp current, with an input voltage of 440 V. Protruding surface at this joint, after welding, was grounded and polished, so that the joint becomes visually invisible. Fig. 6.1 shows the schematic of the welded joint. This joint was analyzed using PDS technique, and was also tested using mechanical testing methods.

Debris at the surface was thoroughly washed and finally rinsed with acetone. For PDS studies, sample was loaded in the sample cell immersed in CCl_4 solution. Chopped laser beam from a semiconductor diode laser (NdYAG - CASIX) of wavelength 532 nm and of power 25 mW was used as the pump beam. Pump beam scanning was done over an area of 600 x 1000 μm^2 within the welded portion for two different chopping frequencies of 250 Hz and 3000 Hz.
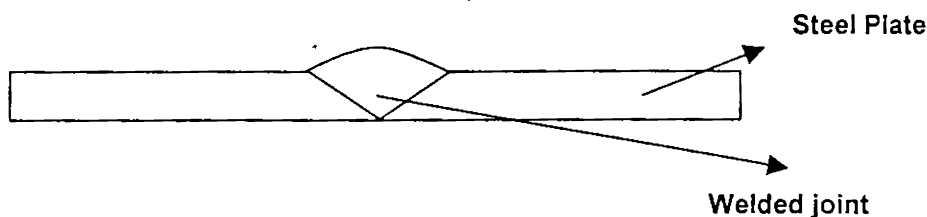
Steel Plate

Welded joint

Fig. 6.1 Schematic representation of the welded joint.

6.4.2 Thickness of paint

A layer of black paint was coated over a glass substrate using an artist brush. Fig. 6.2 is the schematic of paint coated over glass substrate. Thickness was calculated using gravimetric method, to be ~0.8 mm.

The painted substrate of dimension 1 x 5 cm was mounted in the sample cell. Chopped laser beam from a semiconductor diode laser (NdYAG - CASIX) of wavelength 532 nm and of power 25 mW was used as the pump beam. CCl_4 was not used as the coupling medium this time, as we observed that the painted layer got eroded when dipped in this liquid. For surface imaging, scanning was done over an area of 800 x 1000 μm^* at a fixed chopping frequency of 3200 Hz, so as to reconstruct a two-dimensional image of the paint coated area over the substrate. To determine the thickness, PDS data was collected over a range of chopping frequency of 5 Hz to 700 Hz. We used one layer model for curvefitting, as the painted layer was absorbing layer (l_1) and the substrate was non-absorbing (l_2). Detailed description of thickness calculation is given in chapter 1 (section 1.4).
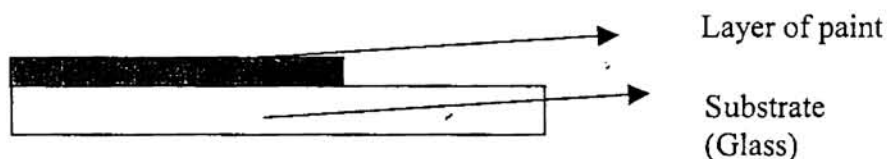

Layer of paint

Substrate
(Glass)

Fig. 6.2 Schematic of painted substrate

6.4.3 Effects of filler in Polymer material

The sample used for this measurement was developed for encapsulating or potting heat generating devices. Polyurethane (PU) prepared

from Empeyol sp 101 and MDI Cosmonate LK obtained from Manali petrochemicals, Chennai, was used as the polymer matrix. Required amount of SP 101 and Cosmonate LK were taken in the ratio of 100:30. This proportion was thoroughly mixed and filler components were added immediately. The composition was kept in continuous stirring condition till the filler got dispersed in the polymer. Entrapped air was removed by applying vacuum. This mixture was then poured into the mould for casting and left for 24 hours.

Unlike any conventional methods, where the sample is directly heated, PDS method is based on the principle of generation of thermal waves within the material by optical excitation. The thermal waves so generated traverse through the material, which in turn is governed by the material's thermal property. Thus, a direct relation could be obtained and the thermal diffusivity of the material could be determined nondestructively for PU doped with various fillers such as Mica, Boron Nitrate (BN), Zinc Oxide (ZnO), Aluminium Oxide (Al_2O_3). Samples were identified with running numbers as "1 to 9" and the sample detail is tabulated in Table (6.2).

Sample Id	Sample
1	PolyUrethane(PU)
2	PU+Mica
3	PU+BN(1g)
4	PU+BN(0.1g)
5	PU+ZnO(1g)
6	PU+BN(0.5g)+Mica(0.5g)
7	PU+BN(0.5g)+Silica(0.5g)
8	PU+Silica(1g-precipitate)
9	PU+BN(0.1g)+ZnO(0.9g)
10	PU+BN(0.1g)+Al2O3(0.9g)
11	PU+Al$_2$O$_3$(1g)
12	PU+Silica(1g-Ultrafine)
13	PU+BN+ZnO(2.5g)

Table 6.2 Details of undoped and doped PU polymer samples

The samples used for PDS studies were cut in a disc shape of 1cm radius. Chopped laser beam from a semiconductor diode laser (NdYAG - CASIX) of wavelength 532 nm and of power 25 mW was used as the pump beam. In this case too we did not use CCl_4, as CCl_4 was observed to degrade the polymer material. Details of thermal diffusivity measurement is described in chapter 1 (section 1.5.1).

6.5 Results and Disscussion

6.5.1 Welded joint

Two-dimensional PDS amplitude plots obtained for two different chopping frequencies of 250 and 3000 Hz is as shown in Fig. (6.3). It was observed that for 3000 Hz the signal was almost uniform. When the chopping frequency was decreased to 250 Hz, non uniformity in the PDS amplitude signal was observed.

For low chopping frequencies the signal is from the bottom layer of the sample and as the chopping frequency is increased the signal contribution is only for the surface. Thus, the non uniformity in PDS amplitude signal for 250 Hz could be due to hidden damage such as, entrapped air-pocket or unwelded portion inside the welded portion.
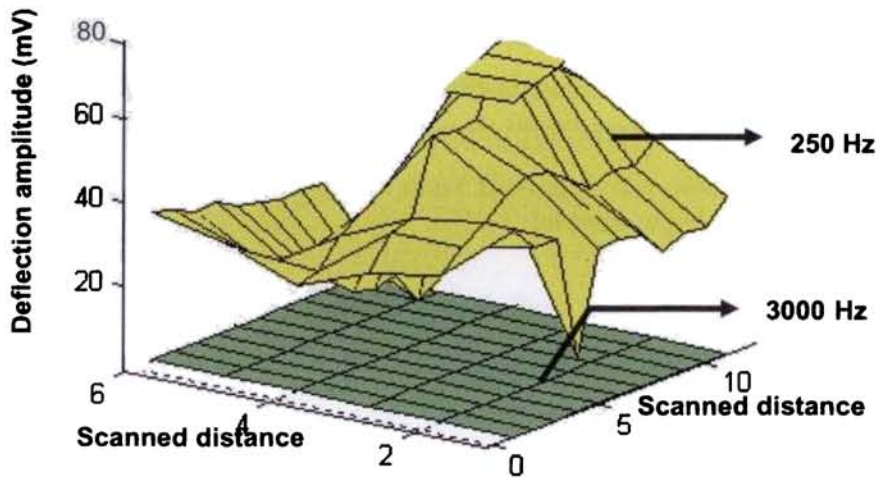
Fig 6.3 PDS analysis of welded joint; Two dimensional Plot.

242

6.5.2 Thickness of Paint

Fig. 6.4 is a two dimensional image plot of PDS amplitude from paint coated over glass substrate. The data presented is for normalized PDS amplitude signal and the surface seems to be rough (Colour bar is given at the side is for indication). The irregularities in the plot represents roughness of painted portion. Thickness of this layer was also calculated using the curvefitting method, assuming a one layer model, the value was calculated to be ~0.72 mm. Fig. (6.5) is the PDS amplitude versus chopping frequency curve used for the determination of the paint thickness. Experimental data was curvefitted with the theoretically generated values. This study was for online monitoring of surface finishing of painted layer during mass.
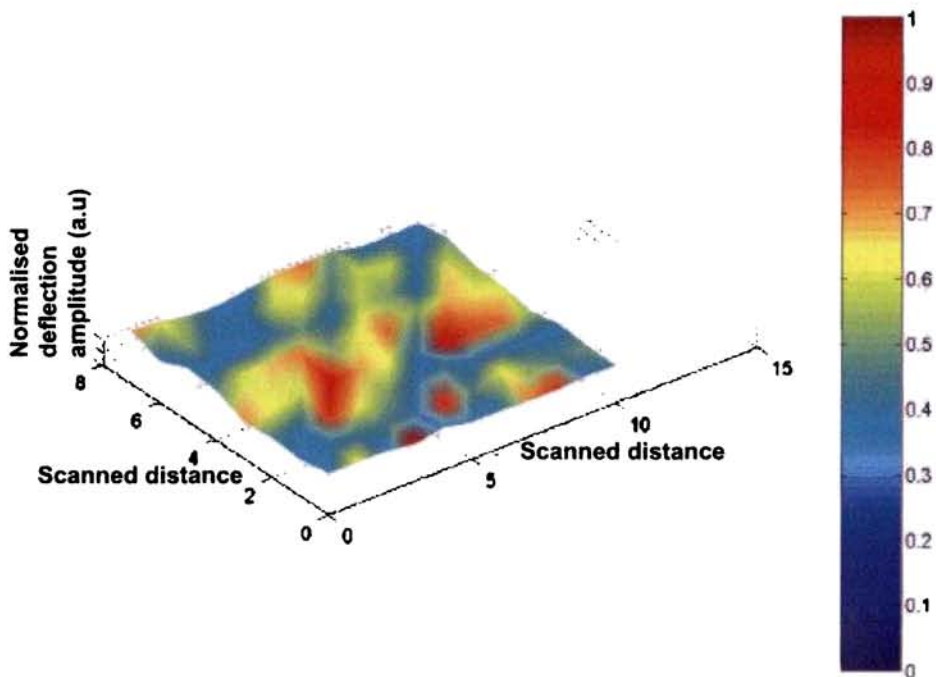

Fig. 6.4 Two dimensional image plot of surface of paint coated layer over a glass substrate.
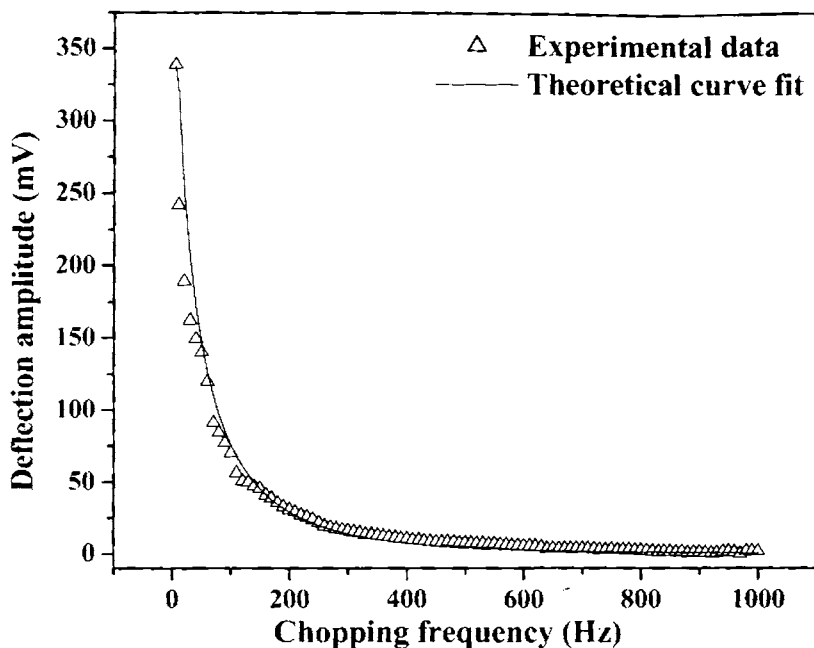
Fig. 6.5 PDS amplitude versus chopping frequency of painted layer over glass substrate.

6.5.3 Effect of filler in Polymer material

Fig. (6.6) is the typical log amplitude versus square root of chopping frequency of PU (which is the base material) and PU doped with Mica. Thermal diffusivity was determined using linear curvefitting of the experimental data. Thermal diffusivity of all other materials was determined the same way and the values are tabulated in Table (6.3). It was found that "sample 9" (PU doped with (0.1g) BN and (0.9g) ZnO) showed the maximum thermal diffusivity value of 0.4115 (10^{-6} m^2 /s) and the least was observed for "sample 1" (pure PU) of value 0.00113 (10^{-6} m^2 /s). Fig. (6.7) is the

normalised thermal diffusivity value for PU polymer samples. This gives a comparison study among the samples.

Thermal diffusivity is directly related to thermal conductivity (α) by the equation,

$$\alpha = \frac{k}{\rho c}, \dots\dots\dots\dots\dots\dots\dots\dots\dots\dots\dots\dots\dots\dots\dots\dots\dots\dots\dots(6.1)$$

Where,

k – Thermal conductivity,

ρ – Density of the material,

c – Specific heat.

The improvement in thermal diffusivity from the base material is largely related to the volume fraction of filler, and it's thermal conductivity. The type of thermally conductive filler, including its size, shape, and dispersion, determine the thermal conductivity of the mixture. Spherical fillers have the least impact on viscosity increase, but also have the least impact on thermal conductivity improvement. When particles interact in such a way that a structured network is formed, thermal conductivity is enhanced. Some of the spheroid filler particles agglomerate forming a network and facilitate heat conducting through the material [11]. It also depends on the aspect ratio of the filler and it's maximum packing fraction.
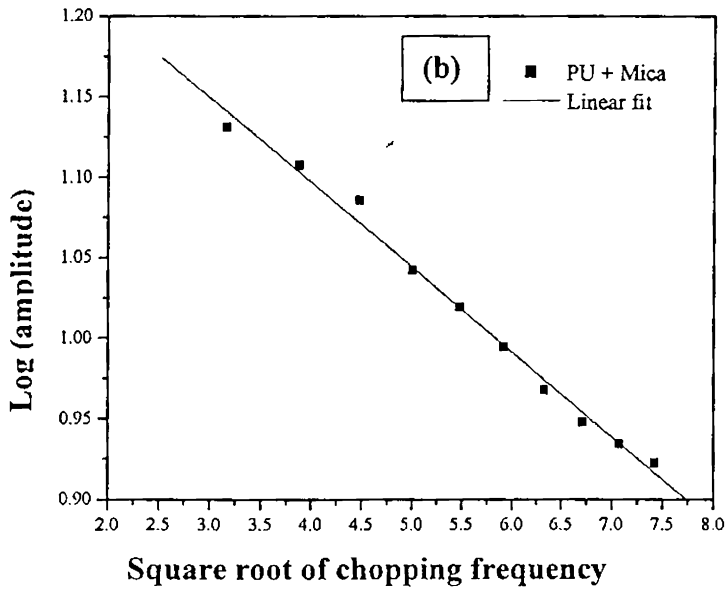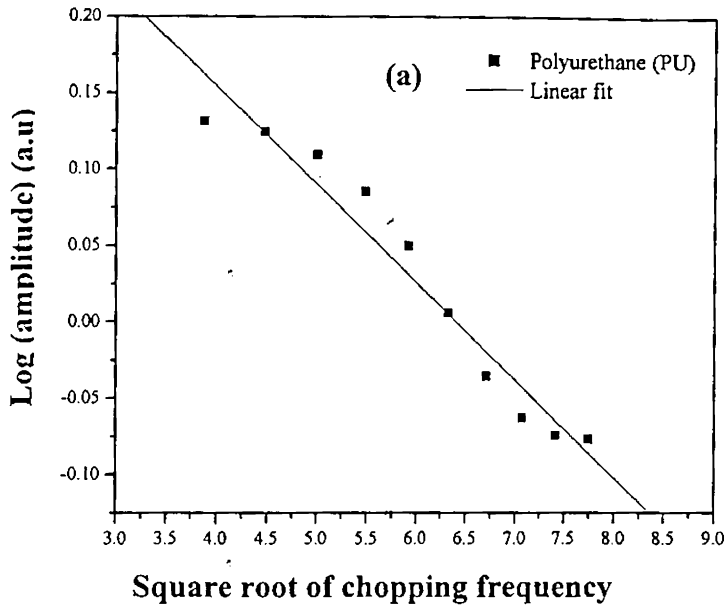
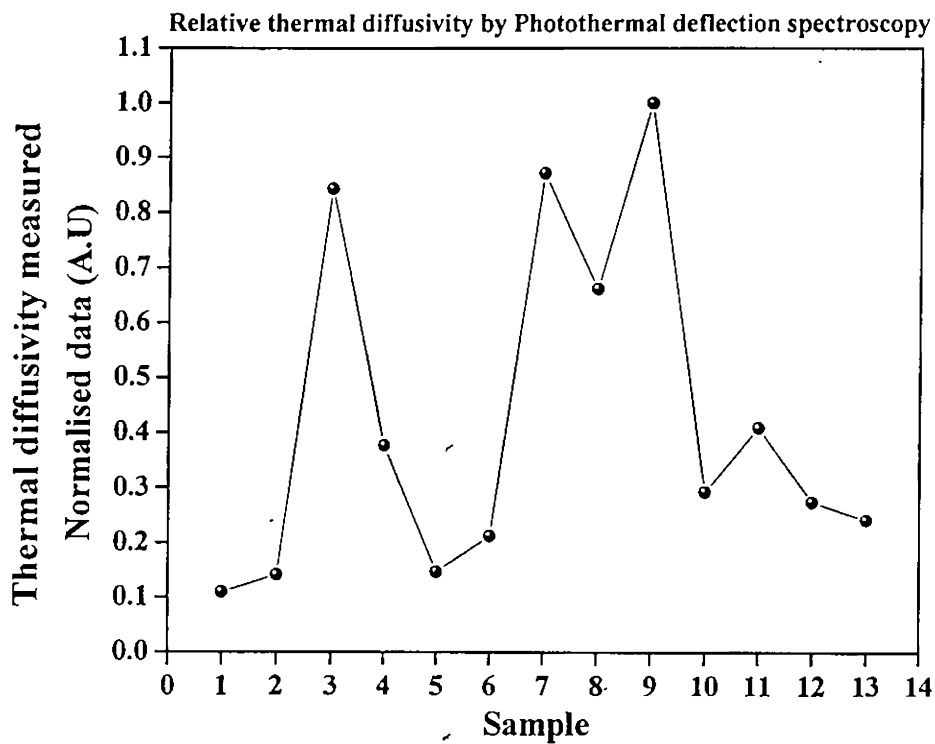Fig. 6.6 Depicts the log amplitude versus square root of frequency for polymer samples

Fig. 6.7 Normalised thermal diffusivity values
of polymer samples

Sample Id	Thermal diffusivity ($\times 10^{-6} m^2/s$)
1	0.00113
2	0.02561
3	0.2951
4	0.1112
5	0.0313
6	0.0503
7	0.3513
8	0.2879
9	0.4115
10	0.09034
11	0.1122
12	0.0615
13	0.0485

Table 6.3 Tabulated value of thermal diffusivity for PU and PU doped with various fillers

6.6 Conclusion

Welded joint was studied using PDS technique. Entrapped air-pocket or defect caused during the process of welding could be non-destructively detected. A layer of paint coated over a glass substrate was studied for its surface texture. Thickness of this layer of paint was also determined using PDS curve fitting method. Thermal diffusivity of polyurethane, before and after

248

adding filler components was also determined. Polyurethane doped with boron nitride and zinc oxide had the highest thermal diffusivity value and was found to be the best candidate amongst other filler combinations such as, Alumina, Mica, and Silica.

Reference

[1] Baldev Raj, T. Jayakumar, M. Thavasimuthu, *"Practical Nondestructive testing"*, Narosa Publishing House – New Delhi (1997).

[2] T.T.N Lan, H.G. Walther, *J. Appl. Phys.*, **80** (1996) 5289-5291.

[3] Josef Pelzl, "Photothermal methods: From basic research to industrial application", *European Thematic Network*, **Issue 1** (1998) 7.

[4] Jürgen Gibkes, Dr. Isabel Delgadillo-Holtfort, Bruno K. Bein, AG Solid State Spektroskopy lab, Ruhr-Univ. Bochum, *European Thematic Network*, **Issue 1** (1998) 6

[5] G.Busse, *Phys. Acoust.* **XVIII** (1988) 403.

[6] H.G.Walther, U.Seidel, W.Karpen, and G.Busse, *Rev. Sci. Instrum.* 63 **(11)** (1992) 5479.

[7] D. Wu, G. Zenzinger, W. Karpen and G. Busse, *Mat. Sci. Forum*, **210-213** (1996) 289

[8] H.G. Walther, *J. Appl. Phys.*, **89** (2001) 2939

[9] H.G. Walther, *Appl. Surf. Sci.*, **193** (2002) 156

[10] G.C. Pandey, A.C. Boccara and D. Fournier, *Proc. On 14th world conference on Non-Destructive Testing*, held at New Delhi (1996) 1511.

[11] L.E., Nielsen, *Ind. Engg.Chem., Fundam.*, **13(1)** (1947) 19.

Chapter 7

SUMMARY AND CONCLUSIONS

In the present work PDS technique was used for studying the optical, thermal and electrical properties of different semiconducting thin film materials. In this we have included wide band gap transparent material like ZnO and opaque materials like CdS and In_2S_3. Studies were mainly to measure film thickness carrier mobility and thermal diffusivity. Along with this, other structural and optical studies were also done.

First study was conducted on CdS film prepared using CSP technique. CdS been used widely in opto electronics and microelectronics due to its good optical and electrical properties. It is well known for its tendency to form nonstoichiometic compound having excess cadmium leading to n-type conductivity. Pure or undoped CdS films generally show high electrical resistivity. So doping or ion implantation technique is adopted for improving the electrical property of this material. Cu doped and ion implanted CdS thin films were studied to know the thermal, optical and transport properties, using PDS technique. Both thermal diffusivity and mobility were found to decrease initially for small quantity of Cu doping. These two parameters were found to increase with higher doping concentration. Similarly, grain size showed an initial decrease and then an increase with Cu doping. Thus, it was observed that the grain size had a major role in determining the transport property of the material. Depth of diffusion of Cu atoms into CdS layer was also determined by using PDS technique. It was found out that the Cu atoms diffused to a depth of ~500 nm, which was also confirmed using XPS studies. In the case of ion

implanted samples, penetration depth of different ions species into CdS thin film was determined through curve fitting using as two layer model. In this model, the bottom layer was considered to be undamaged and the top layer was assumed to be damaged due to ion implantation. Values obtained for 100 keV Ar^+ ion and 1 MeV Cu^+ ion penetration into CdS layer of 1 μm thick was found to coincide with the values obtained from SRIM calculation. Distribution profile of the implanted ion in the sample was studied from one-dimensional line scanning performed over the implanted region of the sample. Depth of penetration was found to increase with increase in ion acceleration voltage. Two-dimensional mapping was also done in order to understand the damage caused along the depth of the ion implanted sample. These results showed that the damage caused was somewhere near the central region of the sample. Photoluminescence studies showed two peaks at 2.3 eV and at 1.9 eV. The former was due to direct band to band recombination and the latter was due to electrons trapped in S vancancy recombining with valence-band free hole. Peak intensity of these two peaks were found to reduce with increase in ion acceleration voltage, whereas the peak ratio was found to be constant.

Second study was on β-In_2S_3. It is a semiconductor with a band gap of 2.0 − 2.8 eV having excellent photoconducting and photoluminescent properties that makes it a promising optoelectronic material. This large band gap makes this material good candidate, to substitute CdS as buffer layer in thin film solar cells. In the present work this sample was prepared using CSP and SILAR. In CSP technique, we used precursor solution containing indium chloride / indium nitrate and thiourea. It was observed that introduction of chloride into the film could be avoided by using indium nitrate as precursor.

The use of $InCl_3$ for sample preparation usually resulted in chlorine doping. When nitrate was used substrate temperature could also be reduced. In_2S_3 thin film samples prepared using SILAR and CSP techniques were analysed to know the details of their thermal and transport properties. Thickness values obtained using PDS were found to coincide well with Stylus method. Thermal diffusivity and mobility values were found to be maximum for the thickest sample. These values were increasing with annealing temperature. For SILAR prepared samples, thermal diffusivity (0.357 cm^2/s) and mobility (0.478 cm^2/Vs) was found to be maximum for sample having more dipping time in solution (10s2w). This sample also showed comparatively good crystalline quality. For another set of samples, which was prepared by keeping dipping time in solution constant and varying the rinsing time in water, it was found that sample having equal dipping time in water and solution (2s2w) showed a high value of thermal diffusivity and mobility. Annealing these samples enhanced the grain size, and both the thermal and mobility values were also found to increase. When nitrate was used as precursor solution, only the sample having In/S ratio 2/3 showed high thermal diffusivity and mobility values. Samples having In/S ratio 2/5 prepared by using chloride precursor showed a mobility value of 17.5 $cm^2V^{-1}s^{-1}$ and that of 2/3 sample prepared using nitrate as precursor showed a mobility value of 7.45 $cm^2V^{-1}S^{-1}$. Hence, 2/5 sample prepared using chloride as precursors exhibited good electrical property.

We selected ZnO for the next study, due to its attractive optical and electrical properties, high chemical and mechanical stability, eco-friendly nature and abundance, has emerged as one of the most promising

optoelectronic materials. ZnO is suitable for the fabrication of high-temperature, high-power devices with application, just as GaN. Further practical advantages of ZnO include amenability to conventional wet chemical etching, which is compatible with Si technology. Suitable doping can increase the conductivity of the ZnO thin films. Conversion of this material into p-type can lead to the fabrication of unique transparent pn junction. In the present work, samples were prepared using CSP technique. ZnO thin film samples prepared using different volumes of spray solutions were studied and it was observed that samples sprayed for "200 ml" showed the maximum thermal diffusivity (0.0254 cm^2/s) and mobility (16.1 cm^2/Vs) value. The crystalline property was also found to be good for this sample from XRD studies. PDS technique was used to determine the thickness of the samples. The data obtained was found to coincide with the value obtained from Stylus method. Ion irradiated ZnO thin film samples were also studied using PDS technique to know the thermal and transport properties. Studies on thermal properties of ZnO thin film using PDS will be the first work as there was no reports found in this area. For 120 MeV Au^+ irradiated ZnO thin film sample, the XRD pattern showed (002) peak intensity to decrease drastically with increase in ion dosage. Lattice stain calculated showed an increase with ion dosage and the grain size decreased with ion dosage. Both thermal diffusivity and mobility were observed to show a sharp decrease due to ion irradiation.

PDS has found applications in the estimation of coating thicknesses, characterization of layered samples and also to detect hidden patterns inside opaque and strongly scattering samples. We studied a welded joint and found a region having hidden defect. Online paint thickness monitoring could also be

done using PDS technique. In the present work, we analysed painted layer using PDS technique. Homogeneity of bulk polymer material was studied after doping it with filler components. Thermal property of this material was also determined. The advantage of PDS over other techniques is that, as the pump beam is from a laser source, after focusing, the area of sample irradiation could be restricted to a few μm.

In this work we have shown that PDS technique can be readily used for measurement of film thickness, thermal diffusivity and carrier mobility. Measurements were done on opaque and transparent semiconductors. Moreover values were found to be agreeing with earlier reported values obtained using other techniques.

Future scope

We had developed 3-layer model, which helps in studying the thermal wave propagation in the sample. This can be used to understand the material property such as thickness of the sample and thermal property exclusively for to one particular layer, in case of functionally graded materials.

When it comes to doped or ion implanted samples, restricting sample to 6-layers was found to be highly insufficient. Thus an n-layer modelling should be developed, which is expected to provide information for small variation in optical and thermal properties of a material for a small change in modulation frequency of the pump beam.

For depth profiling studies, thermal and optical parameters of the sample are an important input values and the thickness is derived from curvefitting method after modelling the sample that contains certain number of layers. For rapid determination of sample thickness, a software containing

bank of material parameters with iterative curve fitting programs can be developed. The software can start curvefitting after a minimum required number of experimental data are recorded. Thus a simultaneous online thickness measurement could be possible. This same program could also be used to find the unknown compounds formed, as the known materials parameters are already stored in the data bank.